Insights from Primary Immunodeficiencies: Investigating the Role of GIMAP6 in the Immune System



Brittany N. Chao
Merton College
University of Oxford

A thesis submitted for the degree of
Doctor of Philosophy
Trinity 2018

Abstract

While molecular, cellular, and animal models play a vital role in immunological research, the study of patients with inborn errors of immunity provides a unique opportunity to elucidate the direct importance of specific genes in the human immune system. In this thesis, I have investigated the disease etiology of four sets of patients believed to have novel primary immunodeficiencies (PIDs) using whole exome sequencing coupled with *in vitro* and *in vivo* assays of both patient cells and model systems. In one patient, I confirmed a mutation in *DNMT3B*, a DNA methyltransferase known to cause a previously identified PID. I next investigated whether a homozygous missense mutation in *TICAM2*, a toll-like receptor signaling adaptor, might underlie the disease of a patient with recurrent pneumonia. In collaborative project, I then examined the potential role of a newly described PID-associated gene, GTPase of the immunity-associated protein 5 (*GIMAP5*), in autophagy and metabolism. GIMAP5 is a member of a family of conserved GTPases with a poorly understood role in leukocyte development and survival. Stemming from the work on the GIMAP5 cohort, I identified a patient presenting with splenomegaly and autoimmunity who has a novel homozygous missense mutation in *GIMAP6*. The majority of this thesis focuses on verification of *GIMAP6* as a PID-associated gene and investigation of its molecular function. Using both patient cells and knockout mouse models, I demonstrated an autophagic defect in GIMAP6-deficient T cells, implicating GIMAP6 as a regulator of autophagy. Furthermore, I determined that *Gimap6* knockout mice have early mortality due to microangiopathic kidney disease. I demonstrated that this renal disease was not immune-mediated therefore implying that GIMAP6 has a novel role in endothelial cell function. The work presented in this thesis thus highlights both the challenges of studying PIDs and the promise of these diseases to help elucidate the mechanisms of human immunity and therapies for PID patients.

Declaration

This thesis is submitted to the University of Oxford in support of my application for the degree of Doctor of Philosophy. The work described here was performed when I was a graduate student in the NIH OxCam program under the supervision of Dr. Michael Lenardo, Prof Andrew McMichael, and Prof Katja Simon. All of the work presented in this thesis is the result of my own work unless otherwise stated. No part of my thesis has been accepted or is currently being submitted for any degree, diploma, or other qualification in the University of Oxford or elsewhere.

Publications

Chao BN, Baldwin WH, Healey JF, Parker ET, Shafer-Weaver K, Cox C, Jiang P, Kanellopoulou C, Lollar P, Meeks SL, Lenardo MJ. Characterization of a genetically engineered mouse model of hemophilia A with complete deletion of the F8 gene. J Thromb Haemost. 2016; 14(2):346-55.

Lu W, Karuppagounder SS, Springer DA, Allen MD, Zheng L, **Chao B,** Zhang Y, Dawson VL, Dawson TM, Lenardo M. Genetic deficiency of the mitochondrial protein PGAM5 causes a Parkinson's-like movement disorder. Nat Commun. 2014; 5:4930.

Acknowledgements

First, I would like to thank my amazing trio of supervisors, Michael Lenardo, Andrew McMichael, and Katja Simon. Mike, Andrew, and Katja are all brilliant scientists and mentors, and I have been fortunate to be able to learn from and work with not just one, but with all three. Each has shared their own wisdom and advice with me, and I have learned so much from each of them. I cannot say how much I have appreciated their support. Without them, I would not be the scientist I am today.

I have been privileged to be able to work at two wonderful institutions and in three incredible labs, as well as have a close relationship with two other lab groups. Therefore, I would like to thank the members of the Lenardo and Su labs at the NIH and the McMichael, Simon, and Borrow labs at Oxford. These groups are comprised of intelligent scientists who are also wonderful people. I could always count on them to be willing to help me however they could, whether it was giving advice on experiments, helping me practice presentations, or staying up with me until 3 in the morning to help me finish processing my samples. From Oxford, I would like to specially thank Hanlin Zhang, Simon Brackenridge, Ghada Alsaleh, Elaine Thomson, Gerry Gillespie, Dingxi Zhou, Tom Partridge, Isabela Pedroza-Pacheco, Elena Brenna, Lee Garner, Ane Ogbe, and Lucy Walters for all their support. From the Lenardo and Su labs, I would like to thank Alex Leney-Greene, Ann Park, Helen Su, Yu Zhang, Chrysi Kanellopoulou, Wei Lu, Lixin Zheng, Bernice Lo, Helen Matthews, Juan Ravell, Carrie Lucas, Anthony Venida, Giulia Notaragenlo, Drew Camrie, Jill Fritz, Aaron Morawski, Kim Shafer-Weaver, Moses Murdock, Ping Jiang, and many others for being great friends and colleagues. I could not ask to work with a better set of people.

My work could not be done without the help from many generous collaborators, including Dr. Avi Rosenberg, Prof. Richard Cornall, Dr. Elizabeth Soilleux, Dr. Katherine Bull,

and Dr. Errin Johnson. This work begins in the clinic, and so I also would like to thank the physicians and scientists who have worked with me and have provided excellent care to all of our patients, especially Deniz Cagdas and Ahmet Ozen.

I would also like to thank the top-notch facilities at the NIH and Oxford, as well as the institutes themselves for hosting me. Merton College has been a huge support outside of lab throughout my degree, and I am proud to be a member of such a prestigious college. For their generous financial funding, I would like to say my appreciation for Merton, Merck, the NIH-OxCam program, and the International Biomedical Research Alliance. I would like to further thank the NIH OxCam program itself, for I would not have had this amazing experience without the existence of this exceptional program.

Lastly, I would also like to thank my family and friends for their unwavering support, guidance, and love.

List of Abbreviations

4EBP1	Eukaryotic translational initiation factor 4E binding protein 1
5-mc	5-methylcytosine
ACD	Acid citrate dextrose
ACK	Ammonium-chloride-potassium
AGO1	Argonaute-1
AID	Activation-induced cytidine deaminase
AIHA	Autoimmune hemolytic anemia
AIM	Atg8 interacting motifs
AK7	ADENYLATE KINASE 7
ALPS	Autoimmune lymphoproliferative syndrome
AMPK	AMP-activated protein kinase
AP	Alkaline phosphatase
AP1	Activator protein 1
APC	Antigen presenting cell
APS	Anti-phospholipid syndrome
Baf	Bafilomycin A1
BCR	B cell receptor
BNIP3L	BCL2/adenovirus E1B-interacting protein 3-like
BSA	Bovine serum albumin
CADD	Combined Annotation Dependent Depletion
Cas9	CRISPR-associated protein 9
CD40L	CD40 ligand
CDS	Coding sequence
CFSE	Carboxyfluorescein succinimidyl ester
CGG	Chicken gamma globulin
CHIA	Acid mammalian chitinase
CLR	C-type lectin receptors
CRISPR	Clustered Regularly Interspaced Short Palindromic Repeats
CTLA4	Cytotoxic T-lymphocyte associated protein 4
CTV	Cell trace violet
CVID	Common variable immune deficiency
DAMP	Damage-associated molecular pattern
DAPI	4’,6-diamidino-2-phenylindole
DC	Dendritic cells
DEPTOR	DEP domain containing mTOR-interacting protein
DN	Double negative thymocytes
DNA	Deoxyribonucleic acid
DNMT3B	DNA methyltransferase 3 beta
DP	Double positive thymocytes
EBV	Epstein-Barr Virus
EDTA	Ethylenediaminetetraacetic acid

ELISA	Enzyme-linked immunosorbent assay
ELISpot	Enzyme-linked immunospot
ENAM	Enamelin
ENTPD3	Ectonucleoside triphosphate diphosphohydrolase 3
ENU	N-ethyl-N-nitrosourea
EOMES	Eomesodermin, xenopus, homolog of
ESCRT	Endosomal sorting complexes required for transport machinery
EV	Empty vector
FAO	Fatty acid oxidation
FBS	Fetal bovine serum
FO	Follicular B cell
FOXO	Forkhead box O
FOXP3	Forkhead box P3
FSC	Forward scatter
G domains	Guanine nucleotide-binding domains
GABARAP	GABA [gamma-aminobutyric acid] type A receptor associated protein
GABARAPL2	GABA [gamma-aminobutyric acid] type A receptor associated protein like 2
GAP	GTPase-activating protein
GATE-16	Golgi-associated ATPase enhancer of 16 kDa
GC	Germinal center
GC	Germinal center
GEF	Guanine exchange factor
GFP	Green fluorescent protein
GIM	GABARAP interacting motif
GIMAP	GTPase of the immunity-associated protein
gMFI	Geometric mean fluorescence intensity
GOF	Gain of function
GOLD	Golgi dynamics domain
GRM2	glutamate metabotropic receptor 2
gRNA	Guide RNA
GWAS	Genome-wide association study
HLA-DR	Human leukocyte antigen-antigen D related
HSC	Hematopoietic stem cell
HSPG2	Heparan sulfate proteoglycan 2
I.P.	Intraperitoneally
I.V.	Intravenous
IAN	Immune-associated nucleotide binding proteins
IBD	Inflammatory bowel disease
ICF	Immunodeficiency, centromeric region instability, and facial anomalies syndrome
ICS	Intracellular cytokine staining
IFN	Interferon
IKK	Inhibitor of kappa B kinase
IL	Interleukin

IMPC	International Mouse Phenotyping Consortium
IRAK	IL-1R-associated kinase
IRF	Interferon regulatory factor
ITP	Immune thrombocytopenia
IVIG	Intravenous immunoglobulin treatment
KCNK10	POTASSIUM CHANNEL, SUBFAMILY K, MEMBER 10
KLRG1	Killer lectin inhibitory receptor 1
KO	Knockout
KOMP	Knockout Mouse Project
LAMTOR	Late endosomal/lysosomal adaptor, MAPK, and mTOR activator
LATAIE	LRBA deficiency with autoantibodies, regulatory T cell defects, autoimmune infiltration, and enteropathy
LC3	Microtubule-associated protein 1A/1B light chain 3
LIR	LC3-interacting region
LOF	Loss of function
LPS	Lipopolysaccharide
LRBA	Lipopolysaccharide-responsive and beige-like anchor protein
LRR	Leucine-rich repeats
Luc	Luciferase
MAL	MyD88 adaptor-like
MAPK	Mitogen-activated protein kinase
MCF2L2	MCF.2 Cell Line Derived Transforming Sequence-Like 2
MHC	Major histocompatability complex
mLST8	mammalian lethal with Sec13 protein 8
MMRRC	Mutant Mouse Resource & Research Centers
MQ	Milli-Q
MSMD	Mendelian susceptibility to mycobacterial diseases
mTOR	Mechanistic target of rapamycin
mTORC	Mechanistic target of rapamycin complex
MyD88	Myeloid differentiation primary response 88
MZ	Marginal zone
NC	Normal control
NF-κB	Nuclear factor kappa-light-chain-enhancer of activated B cells
NGS	Next generation sequencing
NIAID	National Institutes of Allergy and Infectious Disease
NIH	National Institutes of Health
NK	Natural killer cell
NKT	Natural killer T cell
NLR	NOD-like receptors
NOD2	Nucleotide-binding oligomerization domain-containing protein 2
NP	4-Hydroxy-3-nitrophenylacetyl (NP)
NPC1	Niemann-Pick disease type C1
OXPHOS	Oxidative phosphorylation

PAMP	pathogen-associated molecular patterns
PBMC	Peripheral blood mononuclear cell
PBS	Phosphate buffer saline
PC	Pearson's coefficient
PCR	Polymerase chain reaction
PD-1	Programmed cell death protein 1
PFA	Paraformaldehyde
PHA-P	phytohemagglutinin-P
PI3K	Phosphatidylinositol 3-kinase
PI3P	Phosphatidylinositol 3-phosphate
PID	Primary immunodeficiency
PIP_3	Phosphatidylinositol (3,4,5)-triphosphate
PLA	Proximity ligation assay
PLEKHH2	Pleckstrin homology domain-containing protein, family H, member 2
PPP1R9A	Protein phosphatase 1, regulatory subunit 9A
PRAS40	Proline-rich AKT substrate of 40 kDa
Protor 1/2	Protein observed with rictor 1
PRR	Pattern recognition receptor
PVDF	Polyvinylidene difluoride
q-PCR	Quantitative polymerase chain reaction
RAB	Ras-related protein
Rag1	Recombination activating 1
Raptor	Regulatory associated protein of mTOR complex 1
RBC	Red blood cell
Rheb	Ras homolog enriched in brain
Rictor	Rapamycin-insensitive companion of mTOR
RIP	Receptor-interacting protein
RISC	RNA-induced silencing complex
RLR	Retinoic acid-inducible gene (RIG)-I-like receptors
RNA	Ribonucleic acid
RT	Room temperature
RT-PCR	Real-time polyermase chain reaction
S6K	Ribosomal protein S6 kinase
SAM	S-adenosylmethionine
SARM	Sterile-alpha and armadillo motif containing protein
SARS-CoV	Severe Acute Respiratory Syndrome coronavirus
SCID	Severe combined immunodeficiency
SCN11A	Sodium channel, voltage-gated, type XI, alpha subunit
SHIP1	SH-containing inositol 5’ phosphatase 1
Sin1	SAPK-interacting protein 1
SKY	Spectral karyotyping
SLE	Systemic lupus erythematosus
SNARE	soluble N-ethylmaleimide-sensitive factor attachment protein receptor
SNP	Single-nucleotide polymorphism

SNV	Single nucleotide variants
SP	Single positive thymocytes
SSC	Side scatter
STAT3	Signal transducer and activator of transcription 3
STED	Stimulated emission depletion microscopy
STX17	Syntaxin 17
T7E1	T7 endonuclease I
TAG	TRAM adaptor with GOLD [Golgi dynamics] domain
TAK1	TGF-β-activated kinase 1
TBK1	TANK binding kinase 1
T_{CM}	T central memory
TCR	T cell receptor
TD	T cell-dependent
T_{EFF}	Effector T cell
T_{EM}	T effector memory
T_{EMRA}	T effector memory RA
TFEB	Transcription factor EB
Tfh	Follicular helper T cell
TGF-β	Transforming growth factor beta
Th	T helper cell
TI	T cell-independent
TICAM1	TIR domain-containing adapter molecule 1
TICAM2	TIR domain-containing adapter molecule 2
TIDE	Tracking of Indels by Decomposition
TIR	Toll/Interleukin-1 receptor
TIRAP	TIR domain containing adaptor protein
TLR	Toll-like receptor
TMED7	Transmembrane emp24 protein transport domain containing 7
T_N	Naïve T cell
TNF	Tumor necrosis factor
Toc	Translocon on the outer chloroplast membrane
TPPII	Tripeptidyl peptidase II
TRAF	TNF-receptor associated factors
TRAFAC	Translation Factors
TRAM	TRIF related adaptor molecule
Treg	Regulatory T cells
TRIF	TIR domain-containing adapter inducing interferon-b
TRIM	Tripartite motif
TSC2	Tuberous sclerosis complex 2
ULK1	unc-51-like autophagy activating kinase 1
Veh	Vehicle
WES	Whole exome sequencing
WGS	Whole genome sequencing

WT	Wildtype
XIAP	X-linked inhibitor of apoptosis

Table of Contents

Abstract ..... ***I***

Declaration ..... ***II***

Publications ..... ***III***

Acknowledgements ..... ***IV***

List of Abbreviations ..... ***VI***

Chapter 1: Introduction ***1***

1.1 Primary immunodeficiencies **1**
1.1.1 Advances from the study of primary immunodeficiencies 2

1.2 Innate immunity **5**
1.2.1 Pathogen recognition 5
1.2.2 Human primary immunodeficiencies in the innate immune system 9

1.3 Adaptive immunity **11**
1.3.1 T cells 12
1.3.2 B cell activation 16
1.3.2 Immunological memory 17
1.3.3 Adaptive immune senescence and exhaustion 18
1.3.4 Lessons from primary immunodeficiencies in the adaptive immune system 19

1.4 Autophagy in the adaptive immune system **22**
1.4.1 Autophagic function 23
1.4.2 The autophagic process 24
1.4.3 Autophagy regulation 26
1.4.4 Autophagy in the adaptive immune system 31
1.4.3 Autophagy in primary immunodeficiencies 33

1.5 Thesis summary **35**

Chapter 2. Materials and Methods ***37***

2.1 Human samples **37**
2.1.1 Human subjects and whole exome sequencing 37
2.1.2 Processing of whole blood 37
2.1.3 Human activation assays 38
2.1.4 Karyotyping 38

2.2 Mice **39**
2.2.1 Mouse strains and husbandry 39
2.2.2 Tissue and serum/plasma processing 40
2.2.3 Genotyping of Gimap6 KO mice 41
2.2.4 Bone marrow chimera 42
2.2.5 NP-CGG immunization 42
2.2.6 B cell depletion 43
2.2.7 Blood and plasma analysis 43
2.2.8 Mouse activation assays 43

2.3 Cell culture **44**
2.3.1 General cell culture 44
2.3.2 Creation of CRISPR Jurkat lines 44
2.3.3 Transfection of 293T cells 47

2.4 Flow-based assays **47**
2.4.1 General flow cytometric staining 47

2.4.2 Mouse peripheral blood staining 48
2.4.3 Intracellular cytokine staining 48
2.4.4 Proliferation assays 49
2.4.5 LC3-II staining 49
2.4.6 MitoSox and MitoTracker staining 50
2.4.7 FOXP3 staining 50

2.5 Microscopy 54
2.5.1 Confocal and STED microscopy 54
2.5.2 Proximity Ligation Assay (PLA) 55
2.5.3 Mouse histology 57
2.5.4 Transmission electron microscopy 57
2.5.5 Kidney immunoglobulin staining 58

2.6 PCR 61
2.6.1 Transformations 61
2.6.2 RT-PCR 61

2.7 ELISAs and other *in vitro* assays 62
2.7.1 Cytokine ELISAs 62
2.7.2 Luciferase assay 63
2.7.3 NP-CGG ELISA 64
2.7.4 NP-CGG ELISpot 65
2.7.5 Serum antibody ELISAs 66
2.7.6 Anti-nuclear antibody (ANA) assay 66

2.8 Western blot 66

2.9 Statistics 68

Chapter 3. Investigation of causative mutations in novel Mendelian immune diseases 70

3.1 Introduction 70
3.1.1 Whole exome sequencing 70

3.2 Results 74
3.2.1 Identification of patient with a homozygous mutation in DNA methyltransferase 3 beta (DNMT3B) resulting in Immunodeficiency, Centromeric instability, and Facial anomalies (ICF) syndrome 74
3.2.3 Investigation of novel TICAM2 variant as causal mutation underlying patient 1414's disease 87
3.2.3 Inherited disease caused by mutations in GIMAP5, a lysosomal protein with a possible role in metabolism 101

3.3 Discussion 113
3.3.1 Identification of ICF patient 113
3.3.2 Mutation in TICAM2 identified as possibly inactivating but not pathogenic 116
3.3.3 GIMAP5 as a protein involved in lysosomal function 118
3.3.4 Use of single patients in studying Mendelian Disease 121

Chapter 4. Characterization of a patient with a homozygous missense mutation in GIMAP6 and of a mouse model for GIMAP6 deficiency 122

4.1 Introduction 122
4.1.1 The GIMAP family of proteins 122
4.1.2 GIMAP1 123
4.1.3 GIMAP2 123
4.1.4 GIMAP3 123
4.1.5 GIMAP4 124
4.1.6 GIMAP5 124
4.1.7 GIMAP6 125
4.1.8 GIMAP7 125
4.1.9 GIMAP8 125
4.1.10 GIMAP9 126

4.2 Results **126**
4.2.1 Identification of a novel GIMAP6 variant in a primary immunodeficiency patient 126
4.2.2 Immunophenotyping of patient T cells 133
4.2.3 Immunophenotyping of T cells in Gimap6$^{-/-}$ mice 138
4.2.4 Immunophenotyping of Gimap6$^{-/-}$ competitive bone marrow chimeras 146
4.2.5 Investigating B cell responses in Gimap6$^{-/-}$ mice 152

4.3 Discussion **156**
4.3.1 Identification of mutation in GIMAP6 as a potential disease-causing variant 156
4.3.2 The role of GIMAP6 in T cell activation 157
4.3.3 Changes in T cell populations in Gimap6 KO mice 158
4.3.4 Role of GIMAP6 in B cells 160

Chapter 5. Loss of GIMAP6 results in defective autophagy in T cells ***162***

5.1 Introduction **162**
5.1.1 Potential role of GIMAP6 in autophagy 162

5.2 Results **163**
5.2.1 Gimap6$^{-/-}$ mice have an autophagic defect in lymphocytes 163
5.2.2 T cells from patient 1467 have reduced autophagy after activation 175
5.2.3 GIMAP6$^{-/-}$ Jurkat lines have no detectable difference in autophagy 178

5.3 Discussion **186**
5.3.1 The role of GIMAP6 in autophagy in murine lymphocytes 186
5.3.2 Germline deletion of GIMAP6 in Jurkat T cells does not result in an autophagy defect 188
5.3.3 Autophagy in patient T cells 190

Chapter 6. Loss of germline Gimap6 in mice results in early mortality due to progressive kidney disease ***192***

6.1 Introduction **192**

6.2 Results **192**
6.2.1 Gimap6 KO mice have early mortality 192
6.2.3 Renal disease in KO mice 193
6.2.3 Renal disease in Gimap6$^{-/-}$ mice appears to be non-hematopoietic in origin 203

6.3 Discussion **209**
6.3.1 Early mortality in KO mice 210
6.3.2 Etiology of microangiopathy and other potential GIMAP6-expressing cells 212

Chapter 7. Discussion ***216***

7.1 GIMAP6: mouse vs human differences **216**

7.2 GIMAP6—Current understanding and working models **222**

7.3 Therapeutic prospects **225**

7.4 Identification of novel PIDs **227**

References ***230***

Appendix ..... ***i***

Chapter 1: Introduction

1.1 Primary immunodeficiencies

Primary immunodeficiencies (PIDs) are a group of disorders with diverse clinical presentations caused by hereditary or *de novo* genetic changes affecting immune function. These diseases are now also called inborn errors of immunity because they can encompass disease states such as autoimmunity, abnormal lymphoid homeostasis, aberrant immune regulation, defects in innate immunity, and immune cell cancer predisposition besides simply deficient immune responses. PIDs are extremely rare individually, with ~20% originally identified in only a single patient (*1*). Yet, in aggregate they present a significant health risk. PIDs overall are more common than originally thought, with an estimated prevalence ranging from 6-90 cases per 100,000 people (*2*). However, PIDs are likely greatly underdiagnosed for several reasons. As of 2017, 354 distinct PIDs have been identified that are caused by mutations in 344 different genes (*3*). As might be expected, the diversity in genetic underpinnings leads to a huge variety in clinical presentations, ranging from susceptibility to different diseases to malignancies to inflammatory conditions, and can often have non-immunological presentations including developmental delays, mental retardation, albinism, skeletal dysplasia, and a wide range of other symptoms (*3*). Furthermore, mutations in the same gene can result in quite different phenotypes. For example, signal transducer and activator of transcription 3 (STAT3) loss of function (LOF) mutations cause autosomal dominant Hyper IgE syndrome with increased susceptibility to candidiasis and bacterial disease, but STAT3 gain of function (GOF) results in autoimmunity and lymphoproliferation

(*4*). However, an increased awareness of PIDs and rapidly advancing new technologies have led to an exponential increase in identified PIDs in the past decade.

In particular, the advent of next generation DNA sequencing (NGS), or massively parallel DNA sequencing, has revolutionized the field of PIDs and medical genetics in general. Developed in the first decade of the twenty-first century, this technology permits the determination of millions of short-read DNA sequences simultaneously (*5*–*7*). Since the first application of NGS to human genomics, the number of single genes associated with specific PIDs has more than doubled, from ~150 in 2007 to over 350 in 2017 (*3*, *8*, *9*). The study of PIDs has greatly enhanced our understanding of the human immune system.

1.1.1 Advances from the study of primary immunodeficiencies

Traditionally, cell lines and animal models have been utilized to explore immune function. Both types of conventional models are useful in allowing for comprehensive reverse genetic approaches, in which genes are selectively knocked out or knocked in to determine function. One advantage with animal models is that reverse genetics can be done on an organismal scale—something obviously impossible to do in humans. Unbiased forward genetic approaches, such as identification of naturally occurring mutations in mice or N-ethyl-N-nitrosourea (ENU) screens, have been useful in identifying new genes and pathways in immunity. For example, the importance of the apoptosis-inducing protein FAS in lymphoproliferative diseases was first identified in the MRL/lpr strain of mice, in which retrotransposonal insertion into the *FAS* gene resulted in a loss of expression (*10*); this finding supported the later identification of *FAS* mutations as a major cause of autoimmune lymphoproliferative syndrome (ALPS) in humans (*11*–*13*). Approximately 80% of human genes

have 1:1 orthologs in mice, and phenotypes in mice often correlate well with those in humans, making animal studies a valuable tool (*14*–*16*).

While animal models have been tremendously important in learning fundamentals of immunology, studying human patients has several unique advantages. PIDs have been likened as "experiments of nature" that allow for insight into the role of genes in the complex human context. Along with obvious differences between mice and humans, experimental mice are inbred populations that do not easily encompass the extensive genetic diversity seen in humans. It is also known that different backgrounds can have drastically different phenotypes with the same mutation, yet it is rare for labs to use multiple strains (*16*). For example, MRL mice with the *lpr* mutation are models for lupus nephritis, but the same mutation in C57BL/6J mice causes no renal disease (*17*). Additionally, while knock-ins are occasionally made, knockouts are more common and often remove or disrupt the entire gene(*15*). On the other hand, many of the human genetic diseases identified are caused by missense mutations, which can affect different parts of a protein's structure and lead to hypomorphs and gain-of-functions with varying phenotypes (*18*). Null mutations in *RAG1*, for example, cause a severe combined immunodeficiency (SCID) with a loss of T and B cells, whereas hypomorphs can present as several diseases, including Omenn syndrome, atypical SCID, or granulomatous disease (*19*). Further, mice live in tightly regulated settings which do not reflect the many environmental factors, particularly microorganisms, experienced by people on a daily basis. Nor do experimental infections fully recapitulate those seen in humans; indeed, many relevant infections, such as malaria, human immunodeficiency virus (HIV), and tuberculosis, are human-tropic and thus do not naturally infect mice (*20*). A large number of PIDs confer disease susceptibility to a very narrow range of pathogens, whereas mutant mice are often vulnerable to a wider range of experimental ones (*21*). This

discrepancy highlights the importance of the co-evolution of humans and their diseases and the layers of redundancy that has created in human immunity. Therefore, studying natural infections in PID patients allows identification of the critical pathways involved in protection against specific pathogens in human beings.

Along with improving our understanding of human immunity, the study of PIDs allows for unique therapeutic opportunities. Traditionally, PID treatment has involved hematopoietic bone marrow transplants, intravenous immunoglobulin (IVIG), or corticosteroids (*22*–*24*). Identification of the molecular mechanism of patients' diseases allows for precision medicine as well as proof of concept studies. For example, deficiency in lipopolysaccharide-responsive and beige-like anchor protein (LRBA) in LATAIE disease (LRBA deficiency with autoantibodies, regulatory T cell defects, autoimmune infiltration, and enteropathy) was shown to reduce surface expression of the T cell co-inhibitory receptor CTLA4 (cytotoxic T-lymphocyte associated protein 4), resulting in autoimmunity and humoral immunodeficiency. Treatment of patients with abatacept, a CTLA4-immunoglobulin fusion protein that inhibits T cell activity, improved their symptoms (*25*). The success of abatacept therapy suggests that drugs that directly modulate the mutated genes or affected pathways could be ground-breaking therapies for PID patients. These treatments, including potentially gene therapies, that are first successfully demonstrated used in the treatment of PIDs may lead the way for other future clinical therapeutics (*26*, *27*).

Together, the study of cell and animal models of immunity along with human PID allows for deep insight into human immunology, including identification of novel immune genes and their function. In this thesis, I present four sets of primary immunodeficiency patients which I studied to identify the causal genes underlying their disease as well as the function of some of the poorly characterized proteins. The rest of this chapter will give a

background on the relevant pathways discussed in the following chapters, with a particular focus on autophagy, which is the major pathway examined in the work presented here.

1.2 Innate immunity

The innate immune system provides a rapid, first-line, broad defense against infection. Along with barrier protection and secretion of antimicrobials, the innate immune system has several other functions. The complement system attacks the membrane of infectious agents, signaling engulfment by phagocytic cells such as macrophages and neutrophils, thus resulting in destruction of the pathogen as well as producing anaphylatoxins to modulate immunity (*28*, *29*). Clearance is further accomplished through direct lysis by cells like natural killer (NK) cells that can detect virally infected cells and some tumors (*30*). Innate cells are also key in inflammatory responses, producing mediators such as cytokines and leukotrienes to recruit other immune cells and direct immune responses (*31*). Further, cells such as dendritic cells and macrophages play an important role in the initiation of the adaptive immune response through presentation of antigens in highly specialized ways (*32*), which will be discussed further in **Section 1.3**.

1.2.1 Pathogen recognition

The innate immune system's capability to recognize a diverse range of pathogens is bestowed by expression of pattern recognition receptors (PRRs)(*33–36*). These PRRs recognize conserved microbial motifs called pathogen-associated molecular patterns (PAMPs) and initiate signaling cascades leading to inflammatory responses when bound to their cognate ligand. There are four known families of PRRs: retinoic acid-inducible gene (RIG)-I-like receptors (RLRs), NOD-like receptors (NLRs), C-type lectin receptors (CLRs), and

Toll-like receptors (TLRs). RLRs and NLRs are both cytoplasmic receptors that recognize intracellular pathogens, with RLRs particularly important in viral defenses and NLRs for intracellular bacteria (*37*, *38*). CLRs are a large group of transmembrane and soluble proteins that bind carbohydrates and function in fungal defenses (*39*). TLRs will be discussed in greater detail below.

1.2.1.1 TLR family of proteins

The TLR family, a group of type I transmembrane proteins, were the first discovered PRRs (*33–35*). There are thirteen mammalian TLRs, with ten in humans. Each recognizes different microbial ligands via N-terminal leucine-rich repeats (LRRs) and then interacts with other proteins through cytoplasmic TIR (Toll/interleukin-1 receptor) domains to propagate downstream signaling (*40*). TLR ligands include bacterial products such as lipopolysaccharide (LPS), which is recognized by TLR4, and viral nucleotides like double-stranded RNA in the case of TLR3.

1.2.1.2 TLR signaling

The TLRs require intracellular adaptors in order to transmit signaling cascades. There are five known adaptors: MyD88 (myeloid differentiation primary response 88); TICAM1 (TIR domain-containing adapter molecule 1), also known as TRIF (TIR domain-containing adaptor inducing IFN-β); TICAM2, also called as TRAM (TRIF-related adaptor molecule; TIRAP (TIR domain containing adaptor protein), or MAL (MyD88 adaptor-like); and SARM (sterile-alpha and armadillo motif containing protein) (*41–45*).

All TLRs except TLR3 can use the classical MyD88-dependent signaling pathway. TLR3 and endosomal TLR4 and possibly TLR2 use a TICAM1-dependent pathway. Upon TLR stimulation, MyD88 is either directly associated with TLR TIR domains or, in the case of TLR4

and TLR2, recruited by TIRAP (*44*, *46*, *47*). Illustrated with TLR4 (**Fig. 1.1**), MyD88 then interacts with IRAK4 (IL-1R-associated kinase 4), allowing for activation of IRAK1 and 2 and subsequent recruitment of TRAF6 (TNFR-associated factor 6) and other ubiquitin protein ligases (*48*). Together, these ligases activate the TGF-β-activated kinase 1 (TAK1) protein complex which initiates the NF-κB pro-inflammatory pathway. TAK1 also activates the MAPK pathway, resulting in AP-1 (activating protein 1) translocation to the nucleus to activate expression of other pro-inflammatory genes (*49*).

The TRIF-dependent pathway differs from the MyD88 pathway by inducing a type I interferon response (**Fig. 1.1).** TLR3 binds directly to TICAM1, whereas endosomal TLR4 require TICAM2 for TICAM1 recruitment (*50*, *51*). TICAM1 interacts with both TRAF6 and TRAF3 (*52*). Also recruited are RIP1 and RIP3, which together with TRAF6 result in NF-κB and AP-1 activation (*53*). On the other hand, TRAF3 activatation of TBK1 and IKKi leads to translocation of interferon regulatory factor 3 (IRF3) to the nucleus where it induces the type I interferon response (*54*, *55*).

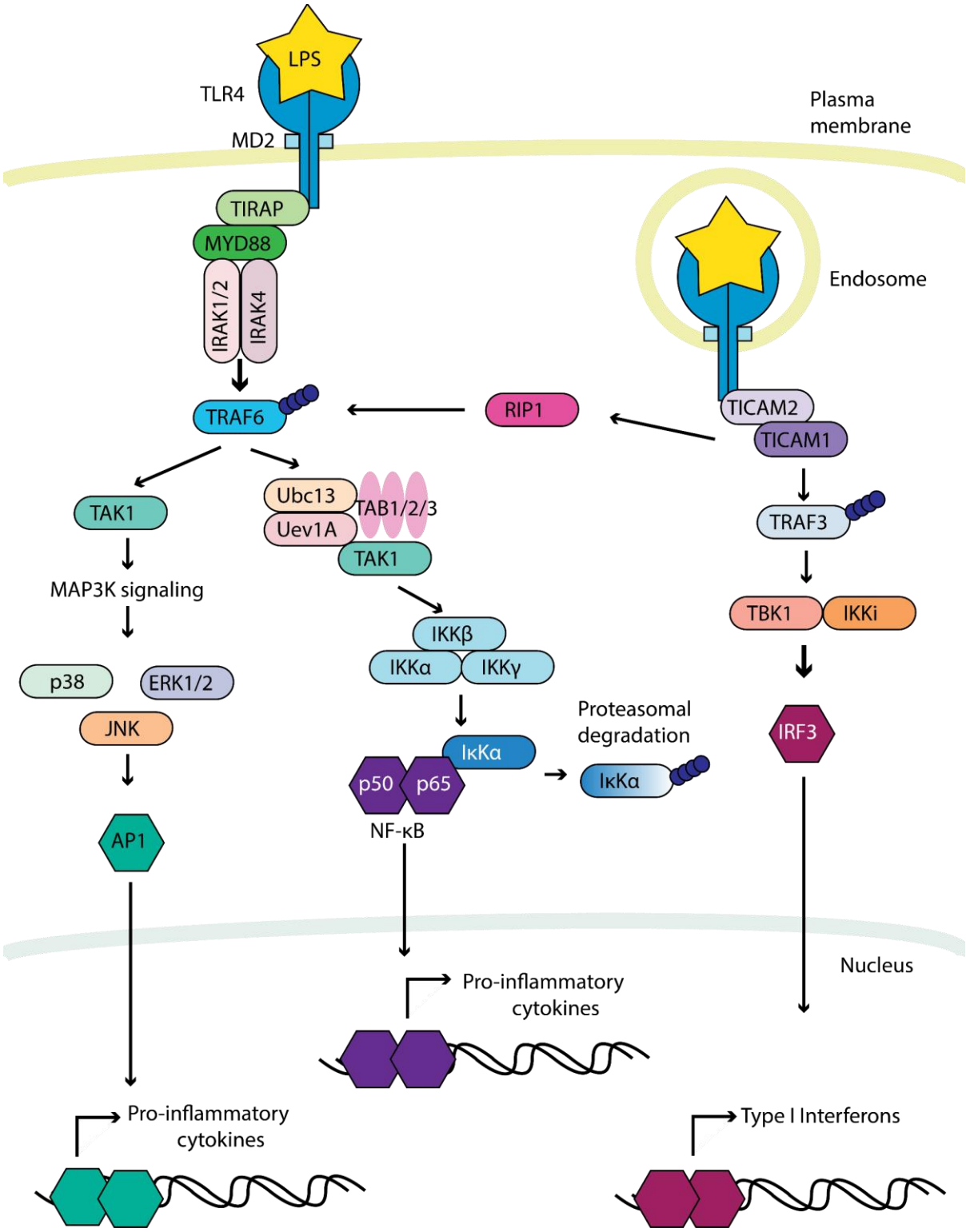


Fig. 1.1. The TLR4 signaling pathway. The TLR4 signaling pathway uses both the MyD88- and TICAM1-dependent signaling pathways. When bound to LPS with the help of LBP and CD14, TLR4 recruits MyD88 with the TIRAP adaptor protein. Activated IRAK proteins recruits TRAF6. Through TAK1 signaling, TRAF6 results in AP-1 and NF-κB translocation into the nucleus. AP-1 and NF-κB upregulate transcription of pro-inflammatory cytokines and genes encoding other important features of immune cell responses. Endocytosed TLR4 initiates TICAM1-

signaling through recruitment by the adaptor protein TICAM2. Along with activating TRAF6 through the RIP1 signaling, TICAM1 interacts with TRAF3, which leads to downstream activation of IRF3. IRF3 upregulates transcription of type I interferons. Blue circles represent ubiquination. Adapted from (*56*).

1.2.2 Human primary immunodeficiencies in the innate immune system

PIDs caused by defects in innate immunity more typically result in immunopathologies such as allergy and autoimmunity, than in broad susceptibility to disease (*57*). While there is no doubt to the importance of the innate immune system, this skewing of PID phenotypes does suggest a certain level of redundancy in the function of its individual components.

LOF mutations in innate immunity often show very narrow phenotypes, confined to a susceptibility in a limited number of pathogens in specific tissues or at particular points in life (**Table 1.2**). For example, though MyD88 is involved in almost all TLR responses, its deficiency causes increased susceptibility to primarily certain pyogenic bacterial infections (*58*, *59*). Similarly, several PIDs in innate signaling pathways result in a narrow Mendelian susceptibility to mycobacterial diseases (MSMD). Identification of the causal genes in these diseases are largely in the IL-12/IFN-γ pathway, such as *IRF8*, *STAT1*, *IL12B* and its receptor (*IL12RB1*), and the components of the IFN-γ receptor (*IFNGR1* and *2*), which revealed the critical role of IFN-γ in mycobacterial control (*60*–*65*).

More commonly, PIDs stemming from mutations in innate genes lead to autoimmunity and inflammatory conditions (**Table 1.2**). The type I interferonopathies, which are a broad group of autoinflammatory conditions characterized by the eponymous type I interferon response, are caused by a variety of gene defects affecting PRR and cytokine signaling (*66*). Though there are several monogenic deficiencies that lead to a systemic lupus erythematosus (SLE) phenotype, the majority are associated with innate immune pathways,

such as complement, nucleic acid sensing and degradation, and type I interferon (*67*). Similar to monogenic SLE, other autoimmune or inflammatory conditions can be attributed to dysregulation of innate immunity; congenital inflammatory bowel disease (IBD), for example, can results from defects in immunity, barrier integrity, or phagocytosis, or from hyperactivation of inflammatory pathways (*68*). Genome wide association studies (GWAS) of multigenic diseases like SLE, IBD, rheumatoid arthritis, multiple sclerosis, type I diabetes, and other autoimmune conditions have also identified single-nucleotide polymorphisms (SNPs) in genes involved in innate immunity, highlighting the contribution of these to immunopathologies (*69*–*73*).

Table 1.1. Overview of major phenotypes and pathways in innate immunity-associated primary immunodeficiencies

Phenotype	Major pathways involved	Selected causal genes
Susceptibility to bacteria	TLRs, complement	*MyD88*; *TIRAP*; *C3*; *C5* (Susceptibility to *Neisseria* infections)
Susceptibility to parasites and fungi	IL-17	*IL17F*; *IL17RA*
Susceptibility to viruses	TLR, RLR, Type I interferons	*TLR3* (HSE); *STAT1*; *IFIH1*
Susceptibility to mycobacterial disease (MSMD)	IL-12/IFN-gamma	*IFNGR1*; *IL12B*; *IRF8; STAT1*
Recurrent inflammation (recurrent fever)	Inflammasome, inflammatory cytokine signaling	*MEFV* (Familial Mediterranean fever); *TNFRSF1A* (TRAPS)
Systemic inflammation with urticaria rash	NLR, inflammasome, inflammatory cytokine signaling	*NLRP3* (CAPS/Muckle Wells syndrome); *NLRP1*
Auto-inflammatory	Proteasome, inflammatory response	*PSMB8* (CANDLE); *COPA*

Phenotype	Major pathways involved	Selected causal genes
Type I interferonopathies	Type I interferon signaling	*TREX1* (Aicardi-Goutieres syndrome); *TMEM173* (STING-associated vasculopathy, infantile-onset)
Sterile inflammation	IL-1 signaling, PRR	*NOD2* (Blau syndrome); *IL1RN* (DIRA); *ADAM17*
SLE-like syndrome	Complement	*C1Q; C1R*; *C2*; *C4A*
Atypical hemolytic Uremic Syndrome	Complement	*C3* GOF; *CFH*; *THBD*
Neutropenia	Ribosome biogenesis, apoptosis, stress responses, cell metabolism, intracellular trafficking (*74*)	*SBDS* (Schwachman-Diamond syndrome); *LAMTOR2*; *WAS* GOF (X-linked neutropenia)
Leukocyte adhesion deficiency (LAD)	Integrin signaling	*ITGB1* (LAD I); *SLC35C1* (LAD II)
Chronic granulomatous disease	Respiratory burst	*NCF1*; *CYBB*
Functional defects in phagocytes	Hematopoiesis, GM-CSF signaling	*GATA2* (MonoMac syndrome); *CSF2RA* (Pulmonary alveolar proteinosis)

HSE= Herpes simplex encephalitis; TRAPS= TNF receptor-associated periodic syndrome; DIRA=Deficiency of the interleukin 1 receptor agonist; CAPS= Familial Cold Autoinflammatory Syndrome; GOF= gain of function; SLE= systemic lupus erythematosus; GM-CSF=granulocyte-macrophage colony-stimulating factor; STING=stimulator of interferon genes. Adapted from (*75*, *76*).

1.3 Adaptive immunity

The adaptive immune system is distinct from the innate by its ability to form highly specific responses to a wide variety of antigens and to generate immunological memory. The two major classes of effector cells in adaptive immunity are B and T lymphocytes. B cells and T cells develop in the bone marrow and thymus, respectively(*77*, *78*). B cells recognize epitopes through the B cell receptor (BCR) and produce antibodies(*79*). T cells utilize the T cell receptor (TCR) and consist of two subsets, that have, broadly speaking, different

functions: CD8 T cells which are involved in cytolytic immunity, particularly to viruses, and CD4 T cells that provide help to other immune cells and initiate and regulate immune responses(*80*).

1.3.1 T cells

1.3.1.2 The T cell receptor

Antigen specificity is determined by the TCR, which binds to peptides presented by major histocompatibility complex (MHC) molecules. The TCR consists of alpha and beta chains (or gamma and delta chains in the case of the innate-like gamma-delta T cells) in complex with the CD3-delta, -epsilon, -gamma, and -zeta invariant chains (*81–83*). During thymic development, gene rearrangement of the variable (V), diversity (D), and joining (J) segments of the TCR chains mediated by the recombination activating genes 1 and 2 (RAG1 and RAG2) generates a diverse TCR repertoire (*84–87*). The developing T cell-progenitors, called thymocytes, first undergo positive selection for the ability of their rearranged TCR to bind to MHC on cortical thymic epithelial cells (TEC) and thus receive survival signals (*88–90*). To establish central tolerance, autoreactive T cells are then eliminated through negative selection. During this process, self-antigen is presented on medullary TEC, which display tissue-restricted self-antigens in part due to expression of autoimmune regulator (AIRE), or on other thymic antigen presenting cells (APCs) (*90*, *91*). Cells that are strongly autoreactive undergo apoptosis (*90*, *92*, *93*).

1.3.1.2 T cell activation

Three signals are required for activation of naïve T cells. The first involves recognition of MHC-presented antigen by TCR. All nucleated cells express MHC class I (MHC

I) molecules that canonically present endogenous antigenic peptides, though exogenous antigens can also be displayed through cross-presentation. MHC I displayed antigen is recognized by CD8 T cells. On the other hand, CD4 T cells bind to exogenous antigens displayed by homologous MHC II molecules expressed on professional APCs such as B cells, macrophages, and dendritic cells. The interaction of TCR and its CD4 or CD8 co-receptor with the MHC molecule (Signal 1) propagates a downstream signaling cascade that leads to transcriptional and metabolic changes in the T cell allowing for its activation, proliferation, and effector functions (*94*).

However, TCR engagement alone results in an unresponsive state called anergy; both co-stimulation (Signal 2) and cytokines (Signal 3) are needed for full effector function (*95*–*98*). The major co-stimulatory molecule is CD28, which binds to CD80 and CD86 on APCs(*99*). CD28 signaling drives several key pathways, including the PI3K/Akt/mTOR metabolism pathway, as well as enhancing cytokine and chemokine production, survival, and T cell proliferation (*100*–*102*).

Conversely, interactions between CD28 family members and their ligands can also provide inhibitory signals important for tolerance and prevention of autoimmunity (*102*). CTLA4 is a homolog of CD28 with a higher affinity for CD80 and CD86 (*103*, *104*). CTLA4 is upregulated after T cell activation, and controls T cell responses by competing for ligands to act as an immune checkpoint inhibitor and suppress effector responses (*104*–*106*). Another key inhibitor is PD-1, which binds to PD-L1 and PD-L2 and acts to regulate the immune response in the periphery (*107*). Co-stimulation and co-inhibition thus function in peripheral tolerance.

Lastly, cytokine signaling (Signal 3) is important for T cell clonal expansion and differentiation. In CD8 T cells, IL-12 and type I interferons have been identified as sources of signal 3, with IL-1 playing a similar role for naïve CD4 T cells (*98*, *108*).

1.3.1.3 T cell function

T cells function in both cell-mediated and humoral immune responses. CD8 T cells are particularly important for defense against intracellular pathogens, as well as tumor surveillance. Activation of CD8 T cells results in the release of cytotoxins including perforin, granulysin, and granzymes as well as antiviral cytokines, leading to apoptosis of the infected cell (*109*–*111*).

CD4 T cells participate in a wide variety of activities, including humoral immune responses and immune regulation. Upon activation, the presence of specific cytokines drives the differentiation of CD4 T cells into various subsets of helper cells (Th) to fulfill different functions (**Table. 1.2)** (*112*)**.** Th1 and Th2 were the first discovered subsets (*113*). Th1 cells are generally involved in protection against intracellular infections and aid in the activation of cytotoxic CD8 T cells, whereas Th2 cells participate in allergic responses and protection against extracellular pathogens(*114*). IL-12 induces Th1 differentiation driven by expression of the master regulator T-bet and STAT4; likewise, IL-4 promotes Th2 differentiation and expression of the transcription factors GATA3 and STAT6 (*115*–*119*). Each subset selectively produces effector cytokines, the most characteristic of which are IFN-γ and TNF-α in Th1 cells and IL-4, -5, and -13 in Th2 cells (*113*). Since the discovery of the Th1 and Th2 subsets, several other CD4 T helper subsets have been determined, each of which has its own promoters of differentiation and effector functions, which are summarized in **Table 1.2** (*112*, *120*). Polarization towards specific Th subsets is associated with various immunopathologies (*120*).

One specialized subset of CD4 T cells called regulatory T cells (Tregs) play an important role in immune suppression and tolerance (*121–123*). Unlike the other Th subsets, Tregs are generally formed in the thymus, though can also be induced in the periphery, and are typically distinguished by their expression of CD25 and the transcription factor FOXP3 (*124–127*). Tregs dampen immune responses through several different mechanisms including: secretion of inhibitory cytokines such as TGF-β, IL-10, and IL-35; expression of inhibitory molecules such as CTLA4 that can compete for ligands presented by APCs and block co-stimulation of naïve T cells; and direct killing of target cells through induction of apoptosis or secretion of granzyme and perforin (*128*).

Table 1.2 CD4 Helper T cell subsets

Subset	Differentiation cytokines	Major transcription factor	Effector functions	Signature cytokines
Th1	IL-12	T-bet, STAT4	Cell-mediated immunity, intracellular pathogens, antigen presentation	IFN-γ, TNF-α
Th2	IL-4	Gata3, STAT6	Humoral immunity, allergy, certain extracellular pathogens (parasites, bacteria)	IL-4, IL-5, IL-13
Th9	TGF-β + IL-4	PU.1	Mucosal immunity, autoimmunity, and cancers	IL-9
Th17	TGF-β + IL-6	RORγt, STAT3	Tissue inflammation, protection against bacteria and fungi, autoimmunity, cancer	IL-17, IL-22
Th22	IL-6	?	T cell proliferation, tissue inflammation, elimination of extracellular parasites, allergy	IL-22
Tfh	IL-6, IL-21, B cell interaction	Bcl-6	B cell help, autoimmunity, immunodeficiency, and malignancy	IL-21
Treg	TGF-β	Foxp3, STAT5	Immune tolerance/suppression	TGF-β, IL-10

Modified from (*129*).

1.3.2 B cell activation

B cells directly bind to antigen through the BCR, which consists of membrane immunoglobulin (IgM or IgD on naïve B cells) in complex with the Igα/Igβ signaling protein heterodimer (*130*, *131*). Like T cells, diversity and antigen specificity of B cells is conferred by the BCR through V(D)J recombination of the heavy and light chain loci of the immunoglobulin gene, giving each B cell a narrowly-defined specificity (*132*, *133*).

B cells develop in the bone marrow and then circulate the body until activated through either T cell-independent (TI) or -dependent (TD) means. There are two types of TI antigens: 1) mitogens that intrinsically activate B cells without needing T cell help or BCR recognition, usually through TLR signaling; and 2) large highly repetitive molecules that promote crosslinking of multiple BCRs on mature B cells, such as bacterial capsule polysaccharides (*134*). TI responses generally produce low affinity, poly-reactive IgM, though they are also capable of inducing some class-switching and possibly differentiation into memory cells, especially with cytokine help (*134*–*136*). In general, TI activation is typical of unconventional B cells, namely B-1 and marginal zone (MZ) B cells, whereas conventional B-2 cells participate in TD reactions. Unconventional B cells fulfill innate-like roles, allowing for more rapid IgM responses against pathogens than typical humoral responses (*137*). B-1 cells reside primarily in the peritoneal and pleural cavities and produce the majority of natural antibodies, which circulate in the blood of healthy individuals prior to exposure of cognate antigen(*138*). Similarly, MZ B cells produce poly-reactive immunoglobulin which protects against blood-borne pathogens and apoptotic cells in the splenic marginal sinus. MZ B cells also undergo TD activation, and are capable of capturing and delivering antigen to conventional B cells in the follicle (*139*, *140*).

TD responses are promoters of high-affinity humoral immunity in conventional B cells. Like with T cell activation, TD B cell activation requires co-stimulation and cytokine signals in addition to BCR binding that are provided by helper T cells, particularly T follicular helper cells (Tfh)(*137*). Recognition of antigen by the BCR triggers internalization of the captured antigen where it is degraded into peptides that can be loaded onto MHC II to be presented to T cells resulting in their activation (*141*, *142*). Cognate T cells then express the co-stimulatory ligands like CD40L and cytokines such as IL-4, IL-21, and IFN-γ that stimulate B cell activation and proliferation. In the germinal center (GC), T cell help results in a high-affinity antibody response by mediating affinity maturation. This occurs in the dark zone through rounds of somatic hypermutation mediated by activation-induced cytidine deaminase (AID) and in the light zone through clonal selection that favors higher affinity cells (*143*, *144*). During an acute immune response B cells cycle between the light and dark zones of the germinal center, resulting in their ability to produce progressively higher affinity antibodies. Additionally, T cell cytokines drive immunoglobulin class-switching from IgM to other isotypes, also with the help of AID, each of which has different effector functions (*144–146*). Activated B cells differentiate into three types of cells: short-lived plasmablasts, which secrete antibody for a short period of time before dying; long-lived plasma cells, which migrate to the bone marrow and continue expressing antibody without further antigen exposure; and memory B cells, which will recirculate in the body providing lasting protection against future challenges (*147*).

1.3.2 Immunological memory

Immunological memory allows for a quicker and stronger anamnestic response if an antigen is encountered again— a hallmark of the adaptive immune system that also serves as the basis for vaccination. At the end of immune responses, the majority of effector B and T

cells undergo apoptosis and are eliminated (*148*). However, a small portion of B and T cells become memory cells, which provide long-lived, antigen-specific responses to the encountered stimulus. Memory B and T cells have quicker activation, proliferation, and effector function in response to re-encountered antigen than naïve cells (*148*).

The two major classes of memory T cells are T effector memory (T_{EM}) and T central memory (T_{CM}), though tissue-resident (T_{RM}) and stem cell-like (T_{SCM}) memory T cells have gained increasing attention (*148*). T_{EM} and T_{CM} reside in different locations, with T_{CM} generally trafficking through secondary lymphoid organs (SLO) and T_{EM} through non-lymphoid tissue. Supporting this function, T_{CM} but not T_{EM}, express the SLO-homing chemokine receptors CCR7 and CD62L (*149*). In response to antigens, T_{CM} rapidly produce Il-2, IL-4, IFN-gamma, TNF-α, and CD40L; T_{EM} secrete pro-inflammatory cytokines and cytolytic agents including IL-4, IL-5, IFN-gamma, and perforin (*148*).

1.3.3 Adaptive immune senescence and exhaustion

Immune senescence and exhaustion are immunoregulatory processes that occur during chronic immune activation. Clonal expansion is a tactic for increasing the number of antigen-specific lymphocytes available during challenge; senescent cells have reduced proliferative ability partially due to shortened telomeres and decreased telomerase activity. DNA damage initiated by factors such as reactive oxygen species (ROS) or Tregs can also induce senescence (*150*, *151*). Senescent T cells are pro-inflammatory, producing high levels of cytokines such as IFN-gamma and TNF-alpha (*152*). While senescent cells are typically terminally-differentiated T cells, exhausted T cells are hypo-responsive T cells. Chronic inflammation and antigen exposure, such as during chronic infection or autoimmunity, leads to a reduction in effector functions and an increased expression in inhibitory receptors, such

as PD-1 (*153*). Unlike senescent cells, exhaustion is a reversible state, which is a highly targeted area of therapy for oncology (*154*).

1.3.4 Lessons from primary immunodeficiencies in the adaptive immune system

PIDs caused by genetic defects in the adaptive immune system almost equally cause disease susceptibility and immunopathologies, and sometimes both concurrently (*75*, *155*). As with PIDs involving the innate immune system, PIDs involving the adaptive system are quite diverse, but most generally result in antibody defects, defects of cellular and humoral immunity (combined immunodeficiencies [CID]), or immune dysregulation often with autoimmunity (*75*). Since Col. Ogden Bruton recognized the first PID in agammaglobulinemia patients in 1952, defects in the adaptive immune system have provided insight into the roles of immune-specific and non-specific genes in the human immune system (*156*).

The study of PIDs have increasingly demonstrated that genes not classically considered “immune” genes have critical roles in immunity. This is particularly evident in a category of severe CID (SCID) caused by a dramatic loss in T cell numbers or function often in conjunction with depletion of B and/or NK cells which typically results in death within a child’s first year if not treated (*157*). Dr. Elo Giblett in 1972 was the first person to identify a specific causal protein in PID: a loss of adenosine deaminase (ADA) as a cause of SCID (*158*). Her discovery was ground-breaking not only for determining a molecular cause of PID, but also because it showed that a ubiquitously expressed protein involved in non-immune-specific pathways (purine metabolism in the case of ADA) could profoundly affect the immune system (*159*). Since then, a wide range of pathways have proven critical for immune homeostasis and function, ranging from ubiquitous pathways such as DNA methylation and repair, vesicle

trafficking, and proteasome degradation to immune-specific pathways like TCR and BCR signaling, cytokine signaling, and immune cell development (*76*). The complexity of the mechanisms underlying PIDs is highlighted in the diversity of pathways involved in their pathogenesis and by the range of phenotypes observed (**Table 1.2)**.

Table 1.2 Overview of major phenotypes and pathways in a selection of adaptive immunity-associated PIDS

Phenotype	Major pathways involved	Selected causal genes
SCID T-B+	T cell activation, homeostasis, and development, TCR and cytokine signaling	*IL2RG* (γc deficiency); *CD3D*
SCID T-B-	Purine metabolism, BCR and TCR generation	*RAG1, RAG2, ARTEMIS*; *ADA*
CID with low CD4 or CD8 cells	MHC signaling, TCR signaling	*CIITA* (MHC-II deficiency); *CD8A*; *TAP1* (MHC-I deficiency)
CID with low B cells	Cytoskeleton, NF-KB signaling, B cell proliferation	*DOCK8*; *IL-21*; *MAP3K14* (NIK deficiency)
CID with low immunoglobulin	NF-κB signaling; Co-stimulation; Isotype switching	*CARD11; BCL10; CD40*
CID with normal immunoglobulin	TCR signaling, co-stimulation, NF-κB signaling	*TRAC* (TCRα deficiency); *OX40; MALT1*
CID with congenital thrombocytopenia	Cytoskeletal and immunologic synapse	*WAS* (Wiskott-Aldrich syndrome); *WIPF1*
CID with DNA repair defects	DNA repair	*DNMT3B* (ICF1); *NBS1* (Nijmegen breakage syndrome); *POLE1*
CID with thymic defects and additional congenital anomalies	Transcriptional regulation	*22q11.2DS* (DiGeorge syndrome); *CHD7* (CHARGE syndrome)
CID with immuno-osseous dysplasias	Chromatin remodeling, mitochondrial RNA processing, cell cycling, glycosylation, splicing	*RMRP (*Cartilage Hair Hypoplasia); *SMARCAL1* (Schimke syndrome) *RNU4ATAC*

Phenotype	Major pathways involved	Selected causal genes
CID with Hyper-IgE	STAT3 signaling, glycosylation, epithelial cell function	*STAT3* (Job's syndrome); *SPINK5* (Comel-Netherton syndrome); *PGM3*
CID with dyskeratosis congenita	Telomere maintenance	*DKC1* (Dyskeratosis congenita); *STN1* (COATS plus syndrome); *SAMD9* GOF
CID with Vitamin B12 and Folate metabolism defects	Vitamin B12 and folate transport and processing	*TCN2*; *SLC46A1*; *MTHFD*
CID with anhidrotic ectodermaldysplasia with immunodeficiency	NF-κB signaling	NEMO; IKBA (EDA-ID)
CID with other associated or syndromic features	Calcium signaling, autophagy, NFKB signaling, purine metabolism, methylation	*ORAI1; EPG5* (Vici syndrome); *KDM6A* (Kabuki syndrome)
Hypogammaglobulinemia with absent B cells	BCR signaling, B cell development	*BTK* (X-linked agammaglobulinemia); *IGHM; BLNK*
Hypogammaglobulinemia with CVID phenotype	B cell activation, NF-KB signaling, metabolism	*CD19; NKB1; IKZF1; PTEN*
Hyper-IgM syndromes	DNA repair, CSR	*AICDA; UNG; MSH6*
Isotype or light chain deficiencies with generally normal numbers of B cells	Immunoglobulin formation, unknown	*IGKC (*Kappa chain deficiency); most are unknown (Selective IgA deficiency; Selective IgM deficiency, etc)
High B cell numbers due to constitutive NFKB activation	NF-κB signaling	*CARD11* GOF
Familial hemophagocytic lymphohistiocytosis (FLH)	Secretory vesicles, perforin	*PRF1 (*Perforin deficiency); *STX11; UNC13D*
Hemophagocytic lymphohistiocytosis with hypopigmentation	Vesicle trafficking	*LYST* (Chediak Higashi syndrome); *RAB27A* (Griscelli syndrome type 2); *AP3B1* (Hermansky Pudlak syndrome type 2)

Phenotype	Major pathways involved	Selected causal genes
Susceptibility to EBV	TCR signaling, costimulation, proliferation, apoptosis	*MAGT1* (XMEN); *ITK; CD27; XIAP* (XLP2)
Autoimmune lymphoproliferative syndrome (ALPS)	Apoptosis	*CASP8; TNFRSF6; FADD*
Autoimmunity with Treg defects	Treg differentiation and function	*FOXP3* (IPEX); *IL2RA; CTLA4*
Autoimmunity with or without lymphoproliferation	STAT3 signaling, immune tolerance, ubiquination, peptide degradation, TCR signaling	*AIRE* (APECED); *ITCH; ZAP70; LRBA*
Immune dysregulation with colitis	IL-10 signaling	*IL10; IL10RA; NFAT5*

CID= combined immunodeficiency; SCID= severe combined immunodeficiency; CHARGE= Coloboma, heart anomaly, choanal atresia, retardation, genital and ear anomalies; TCR= T cell receptor; BCR= B cell receptor; COATS plus= Cerebroretinal microangiopathy with calcifications and cysts; EDA-ID= Anhidrotic ectodermal dysplasia with immune deficiency; CSR= class switch recombination; XMEN= X-linked immunodeficiency with magnesium defect, Epstein-Barr virus infection, and neoplasia; XLP= X-linked lymphoproliferative syndrome; Immunodysregulation, polyendocrinopathy, and enteropathy, X-linked; APECED= Autoimmune polyendocrinopathy-candidiasis-ectodermal dystrophy; GOF= gain of function. Adapted from (*75*, *76*).

1.4 Autophagy in the adaptive immune system

The two major degradative pathways in eukaryotic cells are the ubiquitin-proteasome system and autophagy. Proteasomes are protein complexes that contribute to proteostasis, or cellular protein homeostasis, by proteolytic degradation of damaged or unwanted proteins recognized typically through polyubiquitin chains (*160*). The second pathway, autophagy is also involved in proteostasis, as well as other forms of protein and organelle degradation. During my investigation of PID patients, autophagy was implicated in the function of two candidate genes (*GIMAP5* and *GIMAP6*), and thus is the focus of much of this thesis. Autophagy, its regulation, and its role in the immune system is discussed in greater detail below.

1.4.1 Autophagic function

Autophagy is a highly conserved catabolic process in which cellular components such as damaged organelles and aggregated protein are targeted for degradation in the lysosome and recycled for further use in the cell. There are three major types of autophagy: microautophagy, chaperone-mediated autophagy, and macroautophagy. Microautophagy refers to the direct uptake of cytoplasmic content by invagination of lysosomes, endosomes, or vacuoles (*161*–*163*). Chaperone-mediated autophagy is a form of selective autophagy in which specific chaperones recognize substrates bearing a KFERQ-like motifs and bind to LAMP2A, leading to direct translocation into the lysosome (*164*–*167*). Macroautophagy, which is henceforth referred to as "autophagy", involves the formation of distinct double-membrane structures called autophagosomes which deliver cellular content to lysosomes using a well-characterized set of conserved autophagy (ATG) proteins**.**

Previously considered a bulk form of degradation, the selectivity of autophagy has become increasingly appreciated (*168*, *169*). During starvation, cytoplasmic components are likely non-selectively degraded for nutrients. However, autophagy is also important in cellular homeostasis and quality control. Through various adaptor proteins, autophagy can selectively eliminate damaged or excess organelles, including ER and mitochondria (*170*). Degradation of mitochondria, called mitophagy, is especially important in preventing the accumulation of reactive oxygen species (ROS), which can damage cells and reduce survival (*171*–*173*).These adaptor proteins also help with proteostasis by targeting aggregated proteins to the autophagosome for degradation (*174*, *175*). The importance of autophagy in cell longevity is particularly noticeable in long-lived quiescent cells, such as neurons and memory lymphocytes.

1.4.2 The autophagic process

The autophagic process involves several core protein complexes. In response to stimuli, the unc-51-like autophagy activating kinase 1 (ULK1) preinitiation complex forms at the site of autophagosome biogenesis (*176*, *177*). The ULK1 complex initiates autophagy by recruiting and activating a Class III phosphatidylinositol 3-kinase (PI3K) complex, which produces the lipid phosphatidylinositol 3-phosphate (PI3P). Membranes enriched in PI3P are the site of nucleation, and recruit proteins such as the WIPI proteins, which interact with the ATG12-ATG5-ATG16L complex involved in phagophore expansion (*178–180*). The transmembrane protein ATG9 also seems to be essential for autophagosome biogenesis and is thought to be involved in membrane recruitment, though its precise role is unclear (*181*).

Two ubiquitin-like protein conjugation systems are involved in autophagosome expansion. Formation of the ATG12-ATG5-ATG16L complex requires the conjugation of ATG12 to ATG5 mediated by the E2-like ATG10 and E1-like ATG7 followed by binding of ATG16L to form a complex that functions as an E3-like ligase (*182–184*). The other ubiquitin-like reaction involves the ATG8 proteins, which consists of 7 homologues in humans, including microtubule-associated protein 1A/1B light chain 3 (LC3) which is typically used as a marker for autophagosomes. After proATG8 is cleaved by ATG4 to form the inactive ATG8-I, the E1-like ATG7 activates ATG8-I before transferring it to the E2-like ATG3 (*185*). ATG3 binds ATG8 to the phosphatidylethanolamine (PE) lipid moiety mediated by the E3-like ligase activity of the ATG12-ATG5-ATG16L complex (*185*, *186*). ATG8-PE (ATG8-II) inserts into autophagosomal membranes and is involved in membrane expansion. The Atg8 family also plays an important role in cargo specificity through their interactions with different adaptor proteins, such as SQSTM1/p62, BNIP3/Nix, and NCOA4 (*170*).

The mechanisms of autophagosome closure and lysosomal fusion have not yet been fully elucidated, but seems to involve a large array of characters. Though the Atg8 family does not seem to be required for autophagosomal closure, there is evidence that the Atg8 family is involved in the promotion of membrane fission, as well fusion of the autophagosome to the lysosome (*187*–*190*). The ESCRT (endosomal sorting complexes required for transport machinery) complex is likely also involved in membrane closure (*191*–*193*). Once closed, RAB7 plays a pivotal role in autophagosome trafficking to the lysosome by acting as a mediator between its interacting partners on the autophagosome and the kinesin and dynein motor proteins (*194*–*197*). Rab7 and other Rab proteins are also involved in autophagosome-lysosome fusion (*194*, *198*, *199*), where they coordinate with various tethering complexes such as the HOPS proteins and the soluble N-ethylmaleimide-sensitive factor attachment protein receptors (SNAREs)(*190*). Of particular importance is Syntaxin 17 (STX17), an autophagosomal SNARE that interacts with SNAP-29 and lysosomal VAMP8 to mediate fusion (*200*, *201*). Once fused to the lysosome, the autophagosomal contents are degraded by acidic hydrolases to basic metabolic building blocks such as amino acids, nucleotides, etc. and released back into the cell.

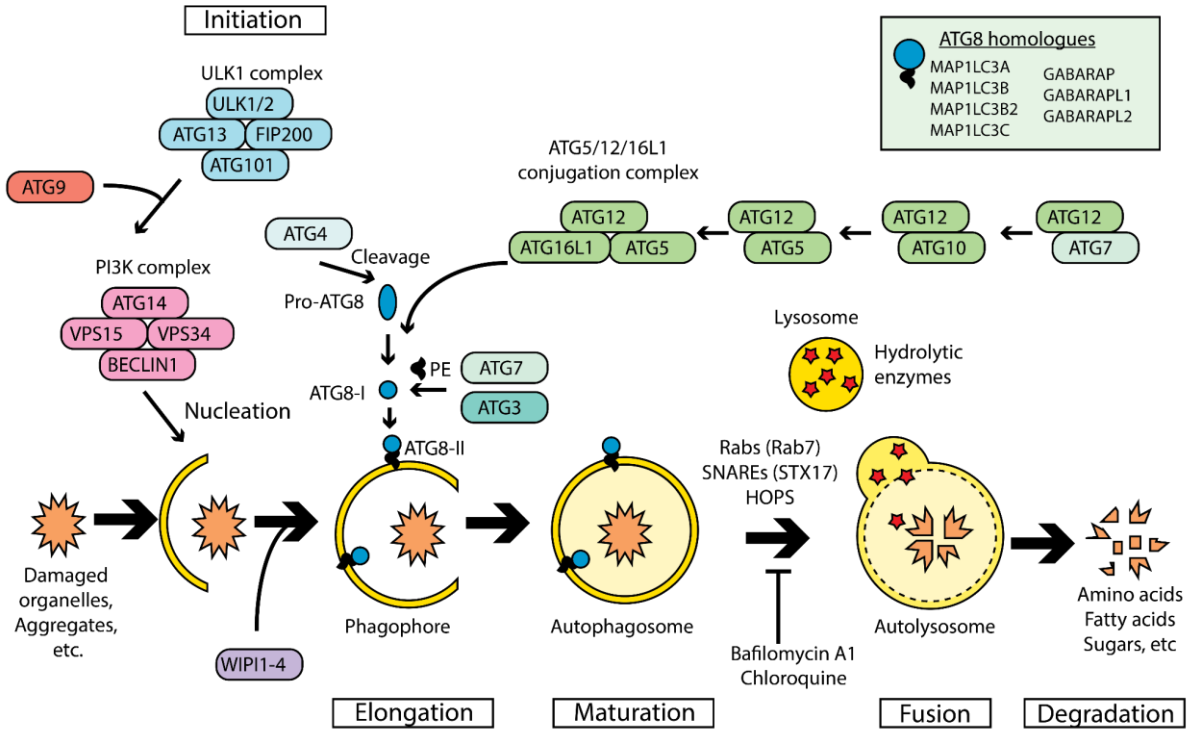


Fig. 1.2 The core autophagic process. Upon induction of autophagy through stress signals, the ULK1 complex is recruited to membranes where it activates a class I PI3K complex. The PI3K complex is involved in nucleation of phagophores. A ubiquitin-like reaction occurs to assemble the ATG5/ATG12/ATG16L1 conjugation complex, which aids ATG7 and ATG3 in another ubiquitin-like reaction used to lipidate ATG8 proteins. ATG8 has several human homologues, which is shown in the inset box. Lipidated Atg8 helps with expansion of the autophagosome before closure of the mature autophagosomal membrane. Rab, SNARE, and HOPS proteins are then involved in transport of the autophagosome and the fusion of the autophagosome to the lysosome. Once fused, hydrolytic enzymes from the lysosome degrade the autophagosomal contents, which can then be recycled back to the cell. Adapted from (*202*).

1.4.3 Autophagy regulation

Autophagy is at the nexus of growth, metabolism, and cell remodeling. It is regulated by many pathways involved in nutrient and stress sensing, as well as by specific immune signals.

1.4.3.1 Metabolic control with mTORC1 signaling

Autophagy regulation is closely linked to metabolism. Two major metabolic signaling pathways are linked in autophagy regulation: the mTORC and AMPK pathways. The mechanistic target of rapamycin (mTOR) is a serine/threonine kinase that senses cellular nutrient levels and controls anabolism and catabolism, thereby affecting growth, metabolism, and survival. mTOR is part of two signaling complexes. The first, mTOR complex 1 (mTORC1) is comprised of the scaffold protein regulatory-associated protein of mTOR (Raptor), mammalian lethal with Sec13 protein 8 (mLST8), and the inhibitory subunits proline-rich AKT substrate of 40 kDa (PRAS40) and DEP domain containing mTOR-interacting protein (DEPTOR). mTOR complex 2 (mTORC2), on the other hand, is composed of mLST8, DEPTOR, rapamycin-insensitive companion of mTOR (Rictor), Sin1 and Protor 1/2. mTORC2 is involved in cytoskeletal organization and survival, whereas mTORC1 functions largely in cell growth, proliferation, and metabolism (*203*).

Recruitment of mTORC1 to the lysosome is crucial for its function (*204*–*206*) (**Fig. 3.2)**. The Ragulator complex, which is comprised of late endosomal/lysosomal adaptor, MAPK, and mTOR activator 1-5 proteins (LAMTOR 1-5), serves as both a scaffold and GEF to Rag GTPases (*206*, *207*). RagA/RagB form heterodimers with RagC/RagD that interact with Raptor, thus recruiting mTORC1 to the surface of the lysosome when amino acids are present (*205*). mTORC1 can then be activated by the small GTPase Rheb (Ras homolog enriched in brain), which also localizes to the lysosome (*208*–*211*). Active mTORC1 can then enable catabolism and inhibit anabolism through phosphorylation of various downstream proteins, including eukaryotic translational initiation factor 4E-binding protein 1 (4EBP1) and ribosomal protein S6 kinase (S6K). Effects of mTORC1 signaling include repression of autophagy and increased synthesis of proteins and other macromolecules (*203*).

mTORC1 signaling regulates autophagy through phosphorylation of two major effectors: unc-51-like autophagy activating kinase 1 (ULK1) and transcription factor EB (TFEB). Under nutrient-rich conditions, mTOR inhibits ULK1 by phosphorylating it at Ser757 (*212*). When mTOR is inactivated, such as during starvation or treatment with mTOR inhibiting drugs like rapamycin and torin, ULK1 is then able to initiate autophagy. Autophagy can be further regulated by mTORC1 through phosphorylation of TFEB, a key transcription factor in autophagy, which prevents its nuclear translocation and thus activity (*213*, *214*).

1.4.3.2 AMPK

AMP-activated protein kinase (AMPK) is a sensor of the low energy supplies typical of starvation and is activated by increased ADP and AMP levels (*215*). AMPK indirectly promotes autophagy and downregulation of anabolism in multiple ways, including inhibiting of mTORC1 signaling through phosphorylation of TSC2 and Raptor (*210*, *216*). Additionally, AMPK enhances activity of a NAD^+-dependent deacetylase (SIRT1) that serves as another regulator of metabolism and autophagy (*217–219*). SIRT1 deacetylates autophagy proteins such as ATG5, ATG7, and ATG8, as well as forkhead box O (FOXO) transcription factors (*217*, *220*, *221*). FOXO proteins have diverse roles in metabolism, cell growth, and survival, and FOXO3 and FOXO1 have both been shown to promote autophagy (*222*). FOXOs are additionally regulated by AMPK through phosphorylation, enhancing their activity (*223*, *224*). AMPK also directly upregulates autophagy through activation of the ULK1 and PI3K complexes (*212*, *225*, *226*).

1.4.3.3 Growth factors and the PI3K/AKT pathway

Growth factors, such as insulin-like growth factor 1 (IGF1), generally regulate autophagy by activating class I PI3Ks (*227–229*). PI3K generates phosphatidylinositol (3,4,5)-

triphosphate (PIP_3), which then recruits AKT and PDK1 to the cell membrane via their pleckstrin homology domains, resulting in the activation of AKT through phosphorylation. AKT then activates the mTOR pathway by inhibiting TSC2 and PRAS40, which allows activation of Rheb, thereby indirectly downregulating autophagy (*230*, *231*). AKT can also phosphorylate the FOXO transcription factors, preventing their nuclear translocation (*232*, *233*). Withdrawal of growth factors can induce autophagy through increased activity of the FOXO transcription factors (*227*).

1.4.3.4 Innate immune signals

Autophagy is intimately associated with in innate immune functions, particularly cytokine responses and xenophagy, or the autophagy of pathogens. NOD1 and NOD2 can direct ATG16L1 to bacterial entry points for xenophagy (*234*). Other PRRs, including other NLR, RLRs, and TLRs, generally promote autophagy through multiple mechanisms, though a few, such as NLRP4, have been shown to be inhibitory (*235–240*). Similarly, damage-associated molecular patterns (DAMPs), which are intracellular molecules released by injured cells or activated immune cells and can be recognized by PRRs, also induce autophagy (*241*). This is in part due to NF-κB signaling, which can both reduce and augment autophagy through transcriptional regulation of autophagy-related genes (*242*).

Cytokines play an intricate role in autophagy regulation. Several cytokines induce autophagy, including IL-1, TGF-β, TNF-α, and IFN-γ; others inhibit, such as IL-10, IL-4, and IL-27 (*243–249*). However, the effect of cytokine signaling on autophagy seems to be context-dependent. For example, TGF-β promotes autophagy in multiple cell lines through various pathways such as TAK1, FOXO, and ROS signaling (*248*, *250–252*). However, it can also inhibit autophagy in endothelial cells by suppressing Beclin1 expression (*248*, *253*). Further,

autophagy itself can influence the production of pro-inflammatory cytokines, demonstrating the complex interactions between autophagy and cytokines to control immunity (*248*, *254*).

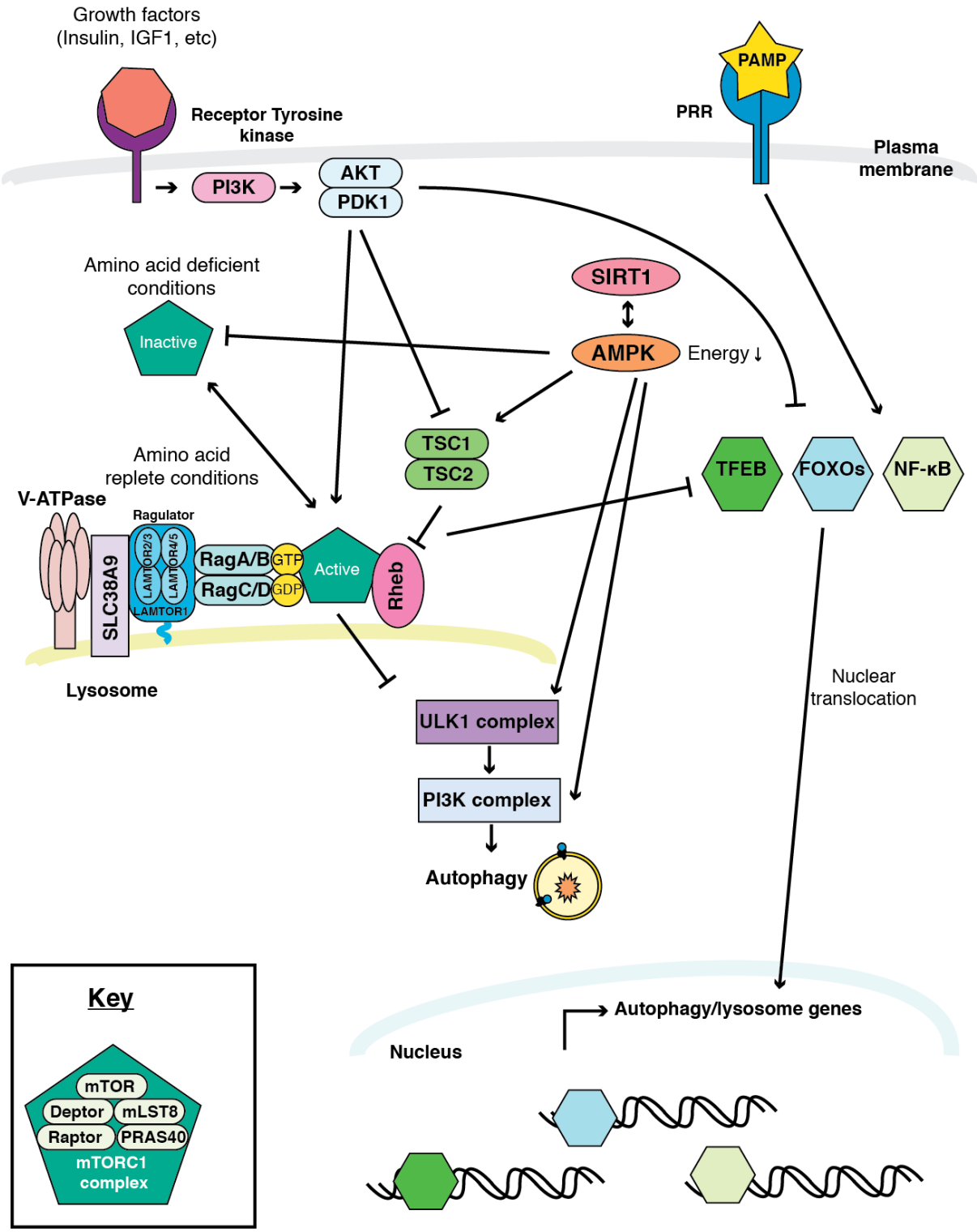


Fig. 1.3 Major autophagy regulatory pathways. Autophagy is regulated by multiple signals, including cytokines, growth factors, danger signals, and nutrient supplies. Class I PI3K, mTORC1, and AMPK signaling are three major signaling pathways that affect autophagy.

Multiple transcription factors, including TFEB, FOXOs, and NF-κB are involved in transcriptional regulation of autophagy. PRR= pattern recognition receptor; PAMP= pathogen-associated molecular pattern. Adapted from (*255*).

1.4.4 Autophagy in the adaptive immune system

1.4.4.1 Autophagy in T cells

Autophagy is involved in several stages of T cell development and differentiation (**Fig. 1.2.I)**. While T cell-specific deletion of autophagy genes does not greatly impact thymic development, autophagy does have a recognized role in peripheral T cell homeostasis and survival, and its abrogation results in T cell lymphopenia and homeostatic T cell proliferation (*256–259*). An accumulation of organelles likely contributes to apoptosis as an increase in mitochondrial and ER mass, as well as ROS, is observed in several models (*260–262*). TCR and common gamma-chain cytokine signaling upregulates autophagy (*263–265*), and autophagy-deficient T cells have reduced proliferation and cytokine production upon activation *in vitro* (*257*, *264*, *266*). However, *in vivo*, T cell responses appears functional, but autophagy defects cause impaired differentiation of memory cells with increased apoptosis during the contraction phase prior to memory formation (*256*, *267*, *268*). T cells rely on different metabolic programs depending on their state of activation. Upon activation, naïve T cells switch from utilizing primarily oxidative phosphorylation (OXPHOS) to aerobic glycolysis (*269*). Memory T cells, on the other hand, rely strongly on fatty acid oxidation (FAO) (*270*, *271*). Along with an accumulation of damaged mitochondria, autophagy-deficient memory T cells have impaired FAO (*256*, *267*, *268*). Supporting a role of autophagy in metabolic reprogramming, Tregs, which also utilize OXPHOS and FAO (*272*), are particularly sensitive to autophagy deficiency with generally decreased survival that may, in part, be due to a shift towards glycolysis (*258*, *273–275*).

Autophagy is also involved in CD4 T cell differentiation, though its specific importance to different subsets is less clear. Along with its role in Treg maintenance, deletion of *BECLIN1* in CD4 T cell resulted in reduced survival of Th1 and Th2 cells *in vitro* in one study (*276*). However, other studies showed no defects in Th1 or Th2 survival (*274*, *277*). Rather, one paper showed an increase in Th9 cells due to an accumulation of the Th9-associated transcription factor PU.1 secondary to inhibition of its autophagy-mediated degradation (*277*).

1.4.4.2 Autophagy in B cells

Autophagy similarly plays an important role in B cell homeostasis (**Figure 1.2.II).** B cells from chimeras transplanted with autophagy-deficient fetal liver have an arrest in development from the pro- to pre-B cell stage (*278*, *279*). However, as with T cells, conditional ablation of autophagy in B cells does not seem to affect homeostasis or survival of conventional B cells or humoral responses (*280*). On the other hand, survival is impaired for autophagy-deficient B-1 B cells (*280–282*). Unlike B-2 cells which are produced by bone marrow precursors, B-1 cells rely on self-renewal for maintenance (*283*, *284*); autophagy-deficient B-1 cells have impaired metabolism and accumulation of damaged mitochondria, fitting the paradigm of autophagy's role in metabolism and organelle homeostasis (*282*).

While conventional B cells have relatively low levels of constitutive autophagy, B-1, memory, and plasma cells have higher rates (*282*, *285*, *286*). Though differentiation into memory cells is unimpaired in B cells with conditional *Atg7* knockout, their survival is compromised, thus blunting secondary immune responses (*286*, *287*). Similarly, B cells differentiate normally into antibody-secreting plasma cells without autophagy, but have impaired long-term survival (*280*, *285*). Like memory cells, bone marrow plasma cells are long-

lived; both accumulate damaged organelles without autophagy (*285–287*). Plasma cells in particular have very high demands for protein production, and any impediment to autophagy results in enhanced ER stress and reduced capacity for sustained antibody production (*285*). The reduced survival in these subsets highlights the importance of autophagy in maintaining organelle quality in long-lived B cell lineages.

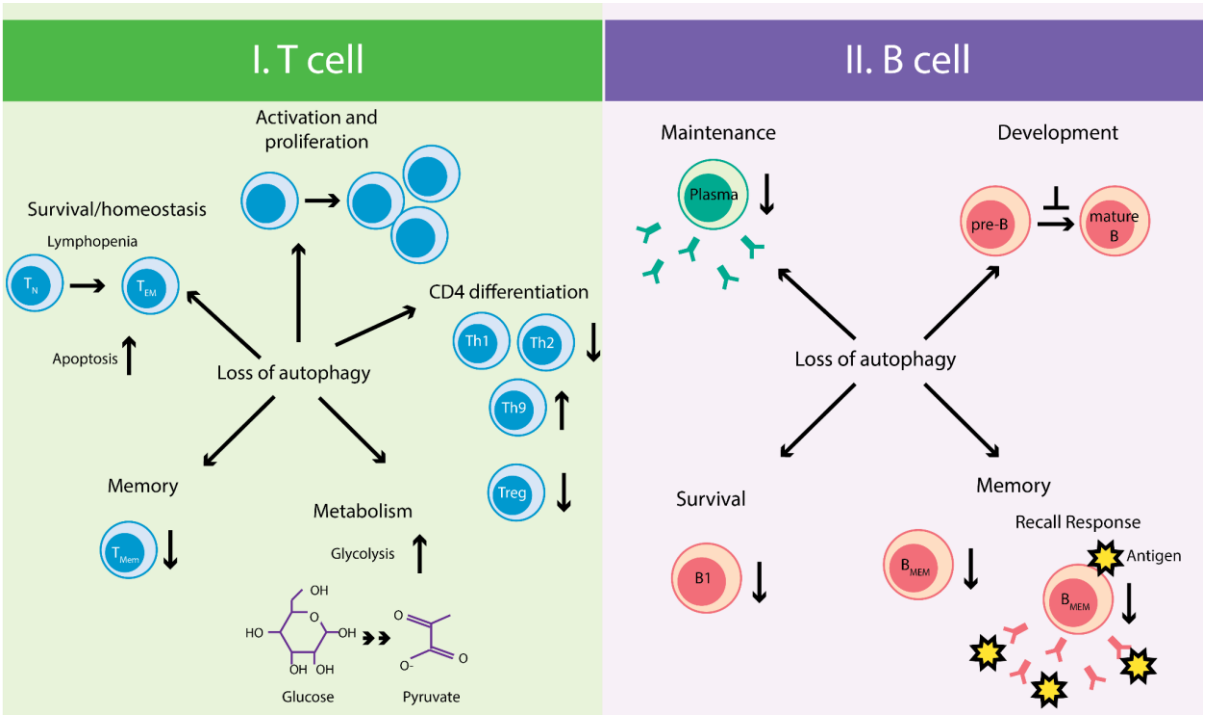


Fig. 1.4 Autophagy in the adaptive immune system. Loss of autophagy has multiple consequences in T (I) and B (II) cells, including survival and differentiation defects, decreased memory maintenance and formation, changes in metabolism, and effects on activation and proliferation.

1.4.3 Autophagy in primary immunodeficiencies

Congenital defects in autophagy are largely associated with neurological disorders, but there is growing evidence for their role in immunodeficiencies (*288*, *289*). For example, along with an increased lysosomal degradation of CTLA4 that can be prevented by treatment with the autophagy inhibitor chloroquine, LRBA deficiency also results in decreased

autophagy in B cells (*25*, *290*). Similarly, mutations in *EPG5,* a RAB7 effector involved in autophagosome-lysosome fusion and cargo delivery, result in Vici syndrome, a neurodevelopmental disorder that presents with CID (*291–294*). The molecular pathogenesis of tripeptidyl-peptidase II (TPPII) deficiency, which presents as CID with severe autoimmunity, also involves a form of autophagy. In this disease, compensatory lysosomal activity due to the loss of TPPII depletes hexokinase-2 through chaperone-mediated autophagy, thus leading to impaired glycolysis and cytokine production (*295*). Along with CIDs, autophagy is involved in several autoimmune and inflammatory conditions.

Autophagy has been strongly implicated in SLE and inflammatory bowel disease (IBD) pathogenesis, with SNPs in several autophagy genes, including *ATG16L1*, *NOD2*, *ATG5*, and *IRGM*, identified by GWAS (*71*, *296*, *297*). Fittingly, the majority of identified PIDs caused by genes related to autophagy occur in innate signaling and inflammation (*289*). As previously mentioned, some proteins involved in pathogen recognition like NOD2 and the TRIM (tripartite motif) proteins can directly recruit the autophagic machinery to their substrates, thus generating an autophagy response to PAMPS and DAMPs (*234*, *298*). Autophagy also has a complicated role in cytokine signaling, and is both regulated and regulates several innate immune pathways (*289*). For example, autophagy is involved in selectively degrading inflammasome components and substrates, including the adaptor protein ASC and pro-IL-1β, thus preventing excessive inflammation (*289*, *299*, *300*). However, the induction of autophagy in combination with inflammasome agonists can actually promote inflammasome-signaling (*301*, *302*).

Consistent with autophagy's role in innate immunity, several monogenic diseases that present with susceptibility to infection or inflammation are caused by genes associated with autophagy, including *NOD2*, *IFIH1*, *WAS*, *TRIM20, TNFRSF1A, IRF8*, *COPA, XIAP,* and *MyD88*

(*289*, *303–308*). For example, defects in NOD2-mediated xenophagy have been linked to IBD in both a lymphoproliferative syndrome caused by X-linked inhibitor of apoptosis (XIAP) deficiency and Niemann-Pick disease type C1 (NPC1), a lysosomal storage disorder (*309*). Similarly, autophagy and autoinflammation have been associated in Wiskott-Aldrich syndrome (WAS) patients, whose presentation includes with recurrent infections and often autoimmunity (*307*, *310*). A recent study demonstrated that WAS protein (WASp), a regulator of actin cytoskeleton mobilization, is involved in autophagosome recruitment as its deficiency leads to increased inflammasome signaling and dysfunctional xenophagy (*307*). While the functional process of autophagy has not been directly examined in many of the other PIDs named here, the associations of these genes with autophagy suggest it may play a role in the pathogenesis of multiple autoinflammatory diseases.

1.5 Thesis summary

The study of PIDs has greatly enhanced our understanding of the human immune system, its critical pathways, and its redundancies. In the future, identification of novel genes associated with PIDs can give insight into the pathways involved in a specific gene's function in the both the healthy and diseased immune system and thus potentially allow for new clinical therapies and application of precision medicine. However, as many PIDs begin with the identification of a single patient, it has become increasingly important to validate both the causality of candidate genes as well as the signaling pathways involved in pathogenesis. Methodical approaches using appropriate models are needed to rigorously establish the relationship between the gene and phenotype to convincingly prove the existence of a novel PID.

In this thesis, I aimed to identify and validate the etiological causes of three patients' diseases (Chapters 3 and 4). Of these patients, I confirmed in a patient whose disease gene was previously unknown, a previously identified PID called ICF (immunodeficiency, centromere instability, and facial anomalies) syndrome. In a second patient, I investigated but was unable to verify the causality of a variant in *TICAM2*, a TLR adaptor protein (Chapter 3). I then undertook collaborative work with other members of the Lenardo laboratory to investigate the role of *GIMAP5*, a member of a poorly characterized family of immune GTPases, in autophagy and metabolism (Chapter 3). From this work, we identified a patient with a homozygous variant in a related gene, *GIMAP6*, which is the focus of the majority of this thesis. In Chapter 4, I describe my work to characterize the patient's mutation and immune phenotype, as well as that of a knockout mouse model for the patient's disease. As *GIMAP6* has been implicated in autophagy, I hypothesized this pathway may be involved in the pathogenic mechanism underlying her disease. I therefore examined the effects of *GIMAP6* deficiency on autophagy in the both the patient and a mouse knockout model system and observed a defect in autophagic flux in patient and knockout mouse T cells (Chapter 5). Unexpectedly, germline deletion of *Gimap6* in mice resulted in a survival defect that appears to be caused by microangiopathic kidney disease (Chapter 6). Further work is needed to fully validate *GIMAP6* as monogenic cause of PID and clarify its role in the immunological and vascular systems. However, the work presented in this thesis supports the hypothesis that GIMAP6 is a regulator of autophagy associated with a novel PID.

Chapter 2. Materials and Methods

2.1 Human samples

2.1.1 Human subjects and whole exome sequencing

All patients (or their legal guardians) and their relatives provided written informed consent for enrollment in research protocol (06-I-0015) that was approved by the Institutional Review Board of the National Institute of Allergy and Infectious Diseases (NIAID), National Institutes of Health (NIH). Patient and control specimens were obtained under approved protocols.

Whole exome sequencing was done by Yu Zhang, Joshua McElwee, or Michael Leney-Greene (NIAID, NIH, Bethesda, MD, USA) as previously described (*311*). In short, genomic DNA was isolated from whole blood. Whole exome sequencing was performed using the SureSelect Human All Exon 50Mb Kit (Agilent) followed by HiSeq next-generation sequencing (Illumina). Sequenced reads were mapped to the hg19 human genome using the Burrows-Wheeler Aligner (*312*). Single nucleotide variant (SNV) and indel calling was done using the Genome Analysis Toolkit v.2 (GATK; www.broadinstitute.org/gatk) (*313*). SNV/indel calls were filtered for quality and annotated using Annovar (*314*). An in-house custom analysis pipeline was then used to filter and prioritize candidates.

2.1.2 Processing of whole blood

Blood was collected into either ethylenediaminetetraacetic acid (EDTA) or acid citrate dextrose (ACD) tubes (BD). Blood from patients was shipped at room temperature; blood from controls was drawn at the same time and kept at room temperature until both could be processed together. Peripheral blood mononuclear cells (PBMCs) were isolated from blood

by density-gradient centrifugation with Ficoll-Paque PLUS (GE Healthcare) at 2000 RPMI for 25 min with the centrifuge brake off. The cell interface was collected and washed twice in phosphate buffered saline (PBS). If there was still significant red blood cell (RBC) contamination, RBCs were lysed using ammonium-chloride-potassium (ACK) lysing buffer (Thermo Fisher Scientific) for 2 min before washing. Cells were counted and resuspended in complete RPMI (cRPMI) at $1x10^6$ cells/mL for downstream assays. cRPMI consisted of RPMI-1640 (Lonza), 10% fetal bovine serum (FBS), 2 mM glutamine, 50 mM 2-mercaptoethanol, and 100 U/mL each of penicillin and streptomycin and was used in all experiments with human cultures unless indicated otherwise.

2.1.3 Human activation assays

To activate T cells, PBMCs were stimulated with 1 μg/ml Ultra-LEAF purified anti-CD3 (clone HIT3α; Biolegend) and 1 μg/ml Ultra-LEAF purified anti-CD28 (clone CD28.2; Biolegend). To culture blasting T cells, activated T cells were washed and then cultured in complete RPMI-1640 medium supplemented with 100 U/ml recombinant human IL-2 (rhIL-2; R&D Systems). To activate B cells, PBMCs were cultured at 1 x 10^6 cells/mL in cRPMI at 37°C and 5% CO_2. Cells were stimulated with either 25 μg/mL of anti-IgM and 1 μg/mL of anti-CD40 or CpG and Il-4. To activate monocytes, PBMCs or enriched monocytes were activated with B5 Ultrapure LPS (tlrl-b5lps; Invivogen) for the times indicated.

2.1.4 Karyotyping

RBC lysis was performed on whole blood. Cells were then stimulated with 3 μg/mL phytohemagglutinin-P (PHA-P) (Sigma-Aldrich) at 1 million cells/mL for 96 hours. Karyotyping was then performed on Colcemid (Karyomax, Invitrogen) arrested cells by Sandra Burkett (National Cancer Institute, NIH, Frederick, Maryland, USA) as previously described (*315*).

2.2 Mice

2.2.1 Mouse strains and husbandry

The B6N(Cg)-*Gimap6*$^{tm1b(KOMP)Wtsi}$/J (referred to as *Gimap6* KO mice in this thesis) were created by the Knockout Mouse Project (KOMP) and bought from Jackson laboratories (*316–318*). They were created by insertion of a "knockout-first" trapping cassette and a promoter-driven selection cassette downstream of exon 1 of *Gimap6* and flanking of exons 2 and 3 with loxP sites(*316*, *318*, *319*). Subsequent breeding to a Cre-expressing mouse resulted in complete excision of exons 2 and 3 and generation of the B6N(Cg)-*Gimap6*$^{tm1b(KOMP)Wtsi}$/J mouse (**Fig. 2.1**).

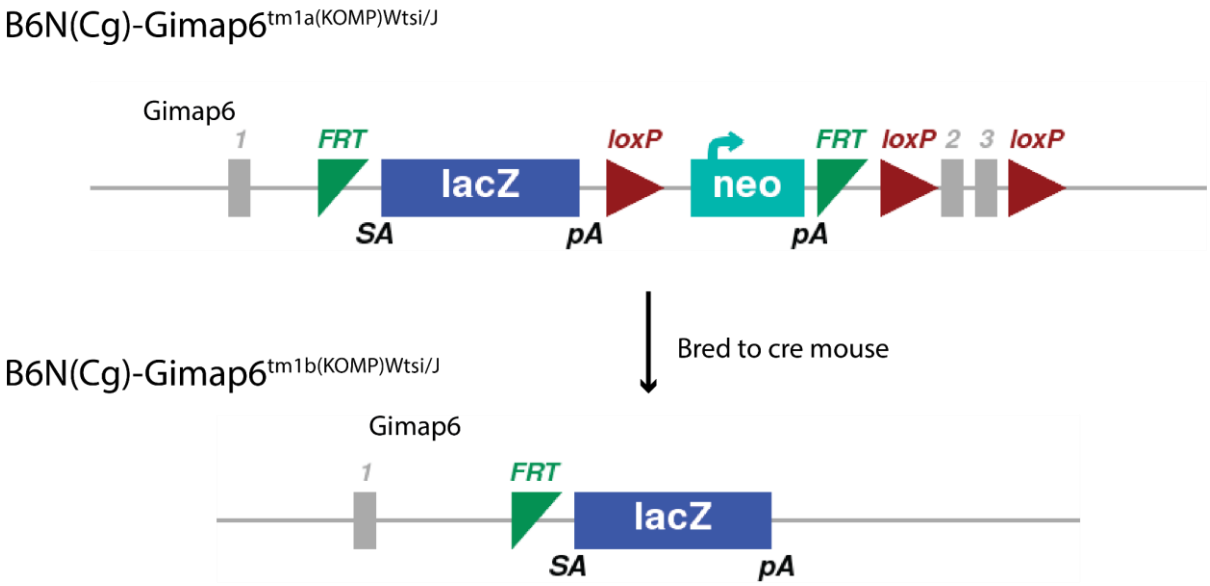


Figure 2.1. Diagram of *Gimap6* KO mice allele. B6N(Cg)-*Gimap6*$^{tm1a(KOMP)Wtsi}$/J mice were made by insertion of an IRES:*lacZ* trapping cassette and a floxed promoter driven neomycin (*neo*) at position 48704928 of Chromosome 6, with loxP sites flanking *Gimap6* exon 2 and 3. Breeding to a Cre-expressing transgenic mouse generated the B6N(Cg)-*Gimap6*$^{tm1b(KOMP)Wtsi}$/J mouse used in this thesis. sA=splice acceptor; pA= SV40 polyadenylation signal; neo= neomycin phosphotransferase; lacZ= gene encoding β-galactosidase. Figure modified from http://www.mousephenotype.org (*316*, *318*).

C57BL/6J-*Gimap5*^{m1Btlr}/Mmucd (GIMAP5^{Sphinx}) mice containing a G38C mutation in GIMAP5 were bought from the Mutant Mouse Resource & Research Centers (MMRRC) and bred in the NIH animal facility. B6.*Rag*$^{-/-}$ mice were originally supplied as a kind gift from Fiona Powrie (University of Oxford, Oxford, UK) and bred in University of Oxford animal facility. CD45.1 B6.SJL were purchased from the University of Oxford Department of Biomedical Services or Charles River Laboratories.

Mice were housed in pathogen free facilities and given food and water ad libitum. Gimap5^{Sphinx} mice were housed at the NIH animal facility (Bethesda, MD, USA). All other mice were housed at the Biomedical Services, University of Oxford (Oxford, UK). Heterozygous females and either heterozygous or homozygous males were used as breeders for the *Gimap6* KO colony. Age- and sex- matched mice were used as controls, with littermates used whenever possible. Mice were used between 8 and 35 weeks of age. All animal work performed at the National Institutes of Health (NIH) was carried out under a protocol approved by the National Institute of Allergy and Infectious Disease (NIAID) Animal Care and Use Committee. All animal work performed at the University of Oxford was approved by the local ethical review committee and performed under UK project license 30/3388.

2.2.2 Tissue and serum/plasma processing

Mice were euthanized by schedule 1 methods before organ collection. Organs for histology were either fixed for 24-48 hours with 4% paraformaldehyde (PFA) at 4^{o}C or snap frozen in liquid nitrogen. PFA fixed organs were then moved to 70% ethanol before further processing. Splenocytes were isolated by pressing spleens through a 70 μm cell strainer (Thermo Fischer Scientific) with a syringe plunger into complete RPMI (RPMI-1640 + 10% FBS + 100 U/mL penicillin and streptomycin + 2 mM Glutamax + 50 μM 2-Mercaptoethanol + 20

mM HEPES). This media was used for all mouse experiments unless otherwise stated. After centrifugation at 300xg, red blood cells (RBCs) were lysed using RBC lysis buffer (Biolegend) for 1-2 min. Cells were washed twice with PBS, resuspended in cRPMI and quantitated using a TC20 Automated Cell Counter (Bio-Rad).

Bone marrow was isolated from femur and tibia by crushing with a mortar and pestle in PBS with 0.1% BSA and 2 mM EDTA. Cells were then filtered through 70 μm cell strainers, spun down, and resuspended in PBS.

Serum and plasma were collected either through lateral tail vein bleeding or cardiac puncture into uncoated microcentrifuge tubes (serum) or lithium heparin microvette CB300 capillary tubes (Sarstedt). Serum was allowed to coagulate for 1-2 hours at 4^{o}C, and plasma was kept at 4^{o}C and processed within 2 hours. Samples were centrifuged at 5000xg for 10 min at 4^{o}C and the supernatant was carefully aspirated. It was then snap frozen on dry ice and stored at -20^{o}C until analysis.

2.2.3 Genotyping of Gimap6 KO mice

The genotyping protocol for *Gimap6* KO mice was modified from the protocol provided by Jackson Laboratory (https://www.jax.org). Earclips were digested in 50 μL of lysis buffer (200 mM NaCl, 5 mM EDTA, 100 mM Tris-HCl pH 7.4-8.5, 0.4% SDS) with 3 ul of 20 mg/mL Proteinase K (Qiagen) at 50^{o}C overnight. DNA was extracted by first adding 450 μL of water and 500 μL of isopropanol, centrifuging (8 min, 10,000 rpm at room temperature) and decanting, and then repeating with 70% ethanol. After decanting the ethanol from the DNA pellet, the sample was allowed to dry and then resuspended in 50 μl of water. PCR for genotyping used BioTaq DNA Polymerase (Bioline Reagents) according to manufacturer's instructions before samples were run on a 1.5% agarose gel. For the WT allele, the primer set

used was: Fw: 5'- CCT CAA TGC ACA GTT CAG GA -3'; Rv: 5'- CAG GGT AAA GTT ATT CCA CAC G -3'. For the mutant allele, the primer set used was: Fw: 5'- CGG TCG CTA CCA TTA CCA GT -3'; Rv: 5'- CGA GTG ATG GAC CCA AAA G -3'. 508 and 203 bp bands indicates a mutant or wild type allele, respectively.

2.2.4 Bone marrow chimera

A single cell bone marrow suspension was prepared as described in **Section 2.2.2**. Cells were resuspended at 2 million cells/100 µL in PBS. For mixed bone marrow chimeras, CD45.1+ SJL bone marrow was mixed at a ratio of 1:1 with either CD45.2+ GIMAP6$^{-/-}$ or GIMAP6$^{+/+}$ bone marrow. To avoid rejection, only bone marrow from female mice were used, as male recipients can receive bone marrow from either sex, but females can only receive from other females. Adult female SJL mice hosts were lethally irradiated at 450 cGy twice with four hours in between doses. One to two hours after the final irradiation dose, mice were injected in the tail vein with 200 µL of donor bone marrow suspension. Host mice were given antibiotic water (Baytril) for two weeks post irradiation.

2.2.5 NP-CGG immunization

50 µg 4-Hydroxy-3-nitrophenyl-chicken gamma globulin (NP-CGG) (N-5055D-5; Biosearch Technologies) per mouse dissolved in PBS was mixed 1:1 with an equivalent volume of Imject Alum adjuvant (Thermo Fisher) and mixed on a rotator at room temperature for 30 min. 200 µL (50 µg NP-CGG) was injected intraperitoneally (i.p.) per mouse on day 0. Similarly, a secondary immunization was performed on day 35. Peripheral blood samples were collected from the lateral tail vein on indicated days.

2.2.6 B cell depletion

8-12 week old mice were injected i.v. through the tail vein with 125 μg of anti-CD20 antibody (clone SA271G2, Biolegend) or Ultra-LEAF purified rat IgG2b, κ Isotype control (Biolegend) over two days (250 μg total) (*320*). B cell depletion was monitored approximately once a week, and further anti-CD20 antibody was administered when B cells began to recover. For all other injection, mice were injected intraperitoneally (i.p) with 250 μg anti-CD20 (clone 18B12, a kind gift from Mark Cragg and Martin Glennie) or InVivoMab mouse IgG2a isotype control (Bio X Cell) in PBS (*321*). Plasma was collected every other week for monitoring of urea, creatinine, and albumin levels.

2.2.7 Blood and plasma analysis

Blood was collected from the lateral tail vein of mice into lithium heparin-coated containers and stored on ice. For clinical chemistry on plasma, blood was then spun at 5000xg for 10 min at 4^{o}C, and the plasma was snap frozen until analysis. Plasma was typically diluted 1:3 and analyzed on the AU680 Analyser (Beckman-Coulter) by the Clinical Pathology Service Laboratory at MRC Harwell (Harwell, UK). For hematologic indices, whole blood was quantified on either a Sysmex KX-21N 3-part differential hematology analyzer or a Pentra ES 60 analyzer (Horiba Medical).

2.2.8 Mouse activation assays

To activate T cells, plates were coated with 1 μg/mL of anti-mouse CD3 (clone 17A2, Biolegend) in PBS at either 4^{o}C overnight or 37^{o}C for 2 hours. After washing with PBS, cells were added to the plates in media at 1 million cells/mL. Anti-mouse CD28 (clone 37.51,

Biolegend) was added at 1 μg/mL to the cell culture media if using splenocytes or was also bound to the plate as with the anti-CD3 antibody if using purified T cells.

For B cell activation and class switch assay, B cells were isolated using the Miltenyi Pan B cell II kit (130-104-443; Miltenyi) according to manufacturer's protocol. B cells were then stimulated in a 96-well flat bottom plate at 1 million cells/mL with 10 μg/mL LPS (Santa Cruz). B cells were incubated at 37°C for 1-5 days before staining.

2.3 Cell culture

2.3.1 General cell culture

Jurkats (clone E6-1) and derivative Jurkat lines were cultured in RPMI-1640 Medium (42401-018; Gibco) supplemented with 10% FBS (Sigma), Penicillin-Streptomycin (Sigma, P0781, 1:100), and 1X GlutaMax (35050-035; Gibco) in 5% CO_2 at 37°C unless otherwise stated. 293T and 293FT cells were cultured similarly, but in Dulbecco's Modified Eagle's Medium (DMEM) (42430-025; Gibco) instead of RPMI-1640.

2.3.2 Creation of CRISPR Jurkat lines

2.3.2.1 Design and cloning of gRNAs

gRNAs targeting the 5' end of *GIMAP6* exon 3 were designed and evaluated using the MIT CRISPR Design tool (http://crispr.mit.edu)(*322*)(**Table A5.1)**. Three of the top candidates were cloned into pSPgRNA (a gift from Charles Gersbach, Addgene plasmid #47108 (*323*). The GIMAP5 gRNA had previously been cloned and screened by M. Leney-Greene, but was re-cloned into pSPgRNA. To do this, 5 μg pSPgRNA was digested with the restriction enzyme BBSI (New England BioLabs, Inc) for 2 hours at 37°C according to manufacturer's guidelines. 1 μL of calf-intestinal alkaline phosphatase (CIP) (New England BioLabs, Inc) was added to the mix

for 90 min at 37°C. The digested plasmid was then run on a 1% agarose gel and extracted from the gel using the QIAquick Gel Extraction Kit (Qiagen). 10 μM of sense and antisense gRNA oligonucleotides (**Table 2.1**) were phosphorylated incubating with T4 Polynucleotide Kinase (New England BioLabs, Inc) at 37°C for one hour, then 95°C for 5 min, and then allowing to cool down to room temperature for a few hours. 1 μL of a 1:200 dilution of the phosphorylated oligonucleotides were ligated by adding 50 ng of gel purified pSPgRNA, 1 μL of 10X T4 Ligase buffer, 1 μL of T4 DNA Ligase to a 10 μL reaction and incubating at room temperature for 2 hours. The ligated vector was then transformed into competent *E. coli* as described in **Section 2.6.2.** Colonies were sequenced, and ones with the gRNA correctly inserted were used in downstream assays.

2.3.2.2 Screening of gRNAs

Plasmids containing the selected gRNAs were co-transfected into 293T cells with pCas9_GFP (a gift from Kiran Musunuru, Addgene plasmid #44719) as described in **Section 2.3.3**. Thirty-six hours after transfection, cells were harvested and DNA was extracted using QuickExtract (Epicentre Products) according to the manufacturer's protocol. The region around the targeted gRNA cutting site was amplified by PCR using the primers listed in **Table 2.1** and KOD Hot Start DNA polymerase (Merck Millipore) according to the manufacturer's instructions. The cycling conditions used were: 95°C for 2 min and then 40 cycles at 95°c for 20s, 60°C [GIMAP5] or 64°C [GIMAP6] for 10s, and 70°C for 15s. Afterwards, the PCR products were run on an agarose gel, excised, and purified using the NucleoSpin Gel and PCR Clean-up kit (Takara Bio).

The T7 Endonuclease I (T7EI) assay was performed by denaturing 200 ng of PCR product at 95°C for 5 min, then cooling at a ramp rate of -2°C/s to 85°C and at a rate of -

0.1°C/s from 85-25°C, and finally holding at 4°C. 1 μL of T7 endonuclease was added to each reaction for 15 min at 37°C. The DNA was run on a 1.5% agarose gel to check for cutting. gRNA 3 was used for creation of the GIMAP6 CRISPR lines.

2.3.2.3 Creating clonal lines and verification of KO

Low passage E6-1 Jurkats (a kind gift from S. Davis) were used to create the CRISPR lines. Using the Neon Transfection System (Thermo Fisher Scientific), 2 million cells suspended in buffer R were transfected with 20 μg each of pCas9_GFP and pSPgRNA at a pulse voltage of 1350 V, pulse width of 10 ms, and pulse number of 3. Cells were immediately dispensed into pre-warmed, antibiotic-free media for two days. After two days, live cells were stained with Aqua Live/dead (Thermo Fisher) for 20 min, washed, and then resuspended into sorting buffer (RPMI 1640 without phenol red, 25 mM HEPES, 1X glutaMAX, and 5% FBS). Live, green fluorescent protein positive (GFP+) cells were sorted into 40% FBS in complete RPMI using a Beckman Coulter MoFlo Legacy Sorter. Cells were then washed, resuspended in supplemented RPMI (as described in **Section 2.3.1** with the addition of 1x MEM non-essential amino acids solution [1854739; Gibco], 50 μM 2-Mercaptoethanol, 20 mM HEPES, and 1x sodium pyruvate [11360-038; Gibco]), and cloned by limiting dilution into 384-well plates. Cells were incubated at 37°C for up to two weeks. Lysates from clones that grew out were tested for GIMAP5 or GIMAP6 expression by western blot as described in **Section 2.8.** Genomic DNA was also extracted in the same way as was done for the T7 assay and underwent DNA sequencing using the Sanger method. Indels were determined using the Tracking of Indels by Decomposition (TIDE) web tool (https://tide.nki.nl)(*324*).

Table 2.1 Primers used in CRISPR cloning		
Section	**Use**	**Primer sequence**
Design and cloning of gRNAs	Oligonucleotides for cloning GIMAP6 gRNA1 into pSPgRNA	Fw: caccgCTGAGGCTCATTCTCATG Rev: aaacCATGAGAATGAGCCTCAGc
Design and cloning of gRNAs	Oligonucleotides for cloning GIMAP6 gRNA2 into pSPgRNA	Fw: caccgATGAGCCTCAGTCTCCTT Rev: aaacAAGGAGACTGAGGCTCATc
Design and cloning of gRNAs	Oligonucleotides for cloning GIMAP6 gRNA3 into pSPgRNA	Fw: caccgAAGACCCCAAGGAGACTG Rev: aaacCAGTCTCCTTGGGGTCTTc
Design and cloning of gRNAs	Oligonucleotides for cloning GIMAP5 gRNA3 into pSPgRNA	Fw: caccgCATTGAGGATTATCCTAG Rev: aaacCTAGGATAATCCTCAATGc
Screening of gRNAs	Amplification of GIMAP6 gRNA target region	Fw: AATTCCCTTCCTGCCTTCTTCC Rev: CTGGTTGTTGGTCTCTCGC
Screening of gRNAs	Amplification of GIMAP5 gRNA target region	Fw: AAGCTCTATTTGCCACAATCCAGA Rev: AGCTCTTGGGTATCGGCCTG

2.3.3 Transfection of 293T cells

293T cells were seeded the day before transfection and used at 50-80% confluence. Plasmids were transfected into 293T cells using GeneJuice (Merck Millipore) according to manufacturer's instructions. In short, GeneJuice was added to serum-free medium, vortexed, and incubated at RT for 5 min. An appropriate amount of plasmid was then added and incubated for 15 min. The mix was placed drop-wise onto the plated cells. Cells were used for analysis after being incubated for 24-48 hours at 37^{o}C. TurboFect (R0531;Thermo Fisher Scientific) was used instead of GeneJuice where mentioned.

2.4 Flow-based assays

2.4.1 General flow cytometric staining

Cells were surface stained with validated antibodies purchased from BD Biosciences, Biolegend, or eBioscience. If a viability dye was used, the cells were first washed with PBS and

stained with the dye in PBS for 15-20 min at 4°C before washing. If FC block was used, it was added with the viability dye. Cells were then surface stained for 30 min at 4°C in the dark with antibodies diluted in 50-100 μL of FACS buffer (5% FBS and 0.1% sodium azide in PBS). After washing, cells were fixed in 2-4% PFA, washed, and resuspended in PBS before flow cytometric analysis. Results from Chapter 3 and Chapters 4-6 were obtained using an LSR-II (BD) or an LSR Fortessa (BD), respectively, and analyzed by FlowJo 10.4. Variations in sample preparation are described in the following sections. Antibodies used in flow cytometry are shown in **Table 2.2.**

2.4.2 Mouse peripheral blood staining

RBCs from peripheral blood collected in a lithium-heparin microvette were lysed in 500 μL of RBC lysis buffer for 5 min on ice before 1 mL of 5% FBS in PBS was added to stop lysis. Cells were spun down and washed with PBS. All spins were at 300xg for 5 min at 4°C. Cells were stained with viability dye and surface antibodies diluted in PBS for 20 min at 4°C. They were then washed with PBS and fixed for 10 min in 4% PFA before washing and resuspension in PBS for flow analysis.

2.4.3 Intracellular cytokine staining

1 million PBMCs were activated with LPS for the indicated amount of time with 1X Brefeldin A solution (420601; Biolegend). They were then spun down for 5 min at 300xg and wash with PBS. Dead cells were stained with the viability dye Zombie Green (423111; Biolegend) for 5 min at RT in the dark. 5 uL Human TruStain FcX block (422301; Biolegend) was then added to the cells and incubated for 10 min at RT before staining with antibodies for surface markers for another 15 min. The cells were washed and spun down before

fixation with 100 µL of IC Fixation buffer (00-8222-49; eBioscience) for 30 min at RT in the dark. 200 µL of permeabilization buffer (00-8333-56; eBioscience) was added to the fixation buffer before the cells were centrifuged as before. The cells were then washed in permeabilization buffer. Antibodies against intracellular cytokines were diluted in permeabilization buffer and added to the cells for 30 min at RT. After washing, the cells were resuspended in FACS buffer for flow cytometric analysis.

2.4.4 Proliferation assays

After washing with PBS, cells were stained with 1 ml per 10 million cells of 5 µM of CellTrace Violet (Thermo Fisher Scientific) or 1 µM of CellTrace CFSE (Life Technologies) for 5 min at room temperature. A half volume of FBS was then added for 5 min at room temperature before 10 ml of media was added. After centrifugation (300xg, 5 min), cells were washed with cRPMI. They were then resuspended in media and used for downstream assays.

2.4.5 LC3-II staining

LC3-II staining was performed using the FlowCellect Autophagy LC3 Antibody-based Assay Kit (Merck Millipore). In brief, cells were incubated with 10 nM Bafilomycin A1 or vehicle (DMSO or 100% ethanol) for 2 hours at 37^{o}C before staining. All staining was done at 4^{o}C in the dark. After cells were stained with aqua live/dead in PBS for 15 min, the cells were washed and stained for surface markers for 20 min. Samples were then washed with assay buffer and then permeabilized by resuspending in 0.05% saponin before immediately centrifuging the cells and discarding the supernatant. The anti-LC3 antibody was then added for 30 min. Samples were then washed, fixed with 2% PFA for 10 min at RT, and then stored at 4^{o}C in PBS until acquired on the flow cytometer.

2.4.6 MitoSox and MitoTracker staining

Cells were stained with viability dye for 10 min at room temperature and washed before cells were stained for surface markers for 20 min at 4°C. After washing, cells were stained with 300 nM MitoTracker Green FM (Thermo Fisher Scientific) or 5 µM MitoSOX Red Mitochondrial Superoxide Indicator (Thermo Fisher Scientific) diluted in PBS with 5% FCS at 37C for either 25 min or 15 min respectively. Cells were washed with cold PBS, suspended in cold FACS buffer, and then immediately analyzed by flow cytometry.

2.4.7 FOXP3 staining

Splenocytes were washed in PBS and then stained with Aqua Live/dead stain (Life Technologies) and Trustain FC block (Biolegend) for 15 min at 4°C. After washing, antibodies against surface markers were added to the cells for 20 min at 4°C before another wash. FOXP3 fixation buffer (eBioscience) was then added for 15 min at RT, and the cells were washed in FOXP3 perm/wash buffer (eBioscience). Antibodies against intracellular markers were then added in perm buffer for 45 min at RT. After washing twice, samples were resuspended in PBS and run on the flow cytometer within a day.

Table 2.2. Antibodies and dyes used in flow cytometry

Target	Fluorophore	Clone	Reactivity	Company	Cat no
Annexin V	APC	N/A	N/A	Biolegend	640920
Annexin V	PE	N/A	N/A	Biolegend	640908
CD115 (CSF-1R)	PE-Cy7	RM4-4	Mouse	Biolegend	116012
CD11b	PE-Cy7	M1/70	Mouse	Biolegend	101215
CD127	BV785	A7R34	Mouse	Biolegend	135037
CD127	PE	A7R34	Mouse	eBioscience	12-1271-82
CD129 (CCR7)	PE	G043H7	Human	Biolegend	353204
CD14	Pacific Blue	M5E2	Human	Biolegend	301816
CD154 (CD40L)	APC	MR1	Mouse	Biolegend	106510
CD154 (CD40L)	PE	24-31	Human	Biolegend	310805
CD19	PerCP-Cy5.5	6D5	Mouse	Biolegend	115534

Table 2.2. Antibodies and dyes used in flow cytometry					
Target	**Fluorophore**	**Clone**	**Reactivity**	**Company**	**Cat no**
CD19	APC-Cy7	SJ25C1	Human	Biolegend	363009
CD19	Pacific Blue	SJ25C1	Human	Biolegend	363035
CD21	PE-Cy7	7E9	Mouse	Biolegend	123419
CD23	APC	B3B4	Mouse	Biolegend	101620
CD23	APC	B3B4	Mouse	Biolegend	101620
CD25	APC	3C7	Mouse	Biolegend	101910
CD25	AF700	PC61	Mouse	Biolegend	102024
CD25	PE-Cy7	2A3	Human	BD Bioscience	335824
CD25	APC-Cy7	BC-96	Human	Biolegend	302613
CD27	PE-Cy7	LG7F9	Mouse	eBioscience	25-0271-80
CD27	PE-Cy7	M-T271	Human	Biolegend	356411
CD27	AF700	O323	Human	Biolegend	302814
CD27	PerCP-Cy5.5	LG.3A10	Mouse/human/rat	Biolegend	124213
CD279 (PD-1)	PE/Cy7	29F.1A12	Mouse	Biolegend	135216
CD279 (PD-1)	BV421	EH12.1	Human	BD Bioscience	562516
CD28	APC	CD28.2	Human	Biolegend	302911
CD3	PE-Cy7	17A2	Mouse	Biolegend	100220
CD3	APC	O323	Mouse	Biolegend	302822
CD3	PE/Dazzle 594	17A2	Mouse	Biolegend	100245
CD3	PE-Cy7	SK7	Human	BD Pharmingen	557851
CD3	APC-Cy7	SK7	Human	Biolegend	344817
CD3	AF700	HIT3a	Human	Biolegend	300323
CD3	APC-Cy7	HIT3a	Human	Biolegend	300317
CD38	Pacific Blue	90	Mouse	Biolegend	102719
CD4	Pacific Blue	GK1.5	Mouse	Biolegend	100428
CD4	PerCP-Cy5.5	RM4-4	Mouse	Biolegend	116012
CD4	BV605	GK1.5	Mouse	Biolegend	100451
CD4	APC	RPA-T4	Human	BD Pharmingen	555349
CD4	PE-Texas Red	RM4-5	Human	Life Technologies	MCD0417

Table 2.2. Antibodies and dyes used in flow cytometry					
Target	**Fluorophore**	**Clone**	**Reactivity**	**Company**	**Cat no**
CD4	PE-Cy5.5	S3.5	Human	eBioscience	MHCD0418
CD4	APC-Cy7	OKT4	Human	Biolegend	317417
CD40	PE	5C3	Human	Biolegend	334307
CD43	PE-Cy7	S7	Mouse	BD Bioscience	562866
CD44	PE-Cy7	IM7	Mouse/human	Biolegend	103030
CD44	AF700	IM7	Mouse/human	Biolegend	103025
CD44	AF700	IM7	Mouse	Biolegend	103025
CD4	PerCP-Cy5.5	IM7	Mouse	Life Technologies	45-0441-80
CD45.1	PE	A20	Mouse	Biolegend	110707
CD45.1	AF700	A20	Mouse	Biolegend	110724
CD45.2	BV650	104	Mouse	Biolegend	109835
CD45R/B220	Pacific Blue	RA3-6B2	Mouse/human	Biolegend	103227
CD45R/B220	BV785	RA3-6B2	Mouse/human	Biolegend	103245
CD45R/B220	AF700	RA3-6B2	Mouse/human	Biolegend	103231
CD45RA	BV785	HI100	Human	Biolegend	3041325
CD45RA	AF700	HI100	Human	Biolegend	304120
CD45RA	PE-Texas Red	MEM-56	Human	Life Technologies	MHCD45RA17
CD45RA	PE-Cy7	HI100	Human	Biolegend	304125
CD57	FITC	NK-1	Human	BD Pharmingen	555619
CD57	Pacific Blue	HCD57	Human	Biolegend	322315
CD62L	FITC	MEL-14	Mouse	Biolegend	104406
CD62L	APC	MEL-14	Mouse	Biolegend	104411
CD62L	APC/Fire750	MEL-14	Mouse	Biolegend	104449
CD69	FITC	H1.2F3	Mouse	Biolegend	104506
CD69	PE	H1.2F3	Mouse	Biolegend	104508
CD69	PE	FN50	Human	Biolegend	310903
CD69	AF700	FN50	Human	Biolegend	310922

Table 2.2. Antibodies and dyes used in flow cytometry					
Target	**Fluorophore**	**Clone**	**Reactivity**	**Company**	**Cat no**
CD69	FITC	FN50	Human	Biolegend	310903
CD69	AF700	FN50	Human	Biolegend	310922
CD69	PE-Cy7	FN50	Human	eBioscience	25-0699-71
CD86	APC-Cy7	GL-1	Mouse	Biolegend	105029
CD86	PE-Cy5	IT2.2	Human	Biolegend	305407
CD8a	APC-Cy7	53-6.7	Mouse	Biolegend	100714
CD8a	PE	GK1.5	Mouse	Biolegend	100432
CD8a	APC/Fire750	53-6.7	Mouse	Biolegend	100766
CD8a	AF700	53-6.7	Mouse	Biolegend	100730
CD8a	BV711	RPA-T8	Human	Biolegend	301044
CD8a	BV605	SK1	Human	Biolegend	344741
CD93	PE	AA4.1	Mouse	Biolegend	136503
CD93	PE	AA4.1	Mouse	Biolegend	136503
CXCR5	BV421	L138D7	Mouse	Biolegend	145511
FOXP3	AF647	MF-14	Mouse	Biolegend	126408
FOXP3	AF647	MF-14	Mouse	Biolegend	126408
HLA-DR	FITC	L243	Human	Biolegend	307603
HLA-DR	BV650	L243	Human	Biolegend	307649
IgD	APC-Cy7	11-26c.2a	Mouse	Biolegend	405716
IgD	AF700	11-26c.2a	Mouse	Biolegend	405729
IgG1	PE	RMG1-1	Mouse	Biolegend	406607
IgG1	APC	M1-14D12	Mouse	eBioscience	17-4015-82
IgG2B	PE	RMG2b-1	Mouse	Biolegend	406707
IgG3	Biotin	RMG3-1	Mouse	Biolegend	406803
IgM	FITC	RMM-1	Mouse	Biolegend	406506
IL-10	PercP-Cy5.5	JES3-9D7	Human	Biolegend	501417
IL-6	PE	MQ2-13A5	Human	Biolegend	501106
KLGR1	APC	2F1	Mouse	eBioscience	17-5893-81
LIVE/DEAD Fixable AQUA dead cell stain	N/A	N/A	N/A	Invitrogen	L34957
Ly-6C	PE-Dazzle 594	HK1.4	Mouse	Biolegend	128043
Ly-6G	APC	H1.2F3	Mouse	Biolegend	104505

Table 2.2. Antibodies and dyes used in flow cytometry					
Target	**Fluorophore**	**Clone**	**Reactivity**	**Company**	**Cat no**
MHC Class II (I-A/I-E)	FITC	M5/114.15.2	Mouse	eBioscience	11-5321-81
NK1.1	PE	PK136	Mouse	Biolegend	108708
NP[1]	PE	N/A	N/A	Biosearch Technologies	N-5070-1
Propidium Iodide	N/A	N/A	N/A	Insight Biotechnology, Ltd.	13-6990-T200
TCR-b	PE-Dazzle 594	H57-597	Mouse	Biolegend	109240
TNF-alpha	AF647	MAb11	Human	Biolegend	502916
Zombie Red	N/A	N/A	N/A	Biolegend	423109

[1]NP directly conjugated to PE

2.5 Microscopy

2.5.1 Confocal and STED microscopy

Glass coverslips were coated with 0.1 mg/mL of poly-D-lysine hydrobromide MW 70,000 (Sigma-Aldrich) for at least 20 min, washed three times in water, and allowed to air dry. Cells were resuspended in PBS. To look at LC3 puncta in GIMAP5^{Sphnx} mice, splenocytes were stained with 50 µl of anti-CD4 AF647 antibody for 15 min on ice before washing and resuspension in PBS. For Mitotracker staining, T cell blasts treated with mitotracker were incubated for 30 min at 37^{o}C with 6.25 nM of Mitotracker Red CMX-ROS in complete media with 100 U/mL IL-2 before being washed and resuspended in PBS.

200-300 µl of the cell suspension was incubated on the coverslip for 5 min at room temperature. An equal amount of 8% PFA was added to the cell suspension, and cells were allowed to fix for 15 min at room temperature. If using the conjugated LC3 antibody, cells were instead fixed with 250 µL of ice-cold methanol for 10 min at -20^{o}C. The mixture was aspirated, and the coverslips were washed twice with PBS. Coverslips were then directly used or stored at 4^{o}C until staining.

Cells were permeabilized with 0.1% Triton X-100 (Sigma-Aldrich) in PBS for 15 min at room temperature and then washed twice with PBS. 0.5% digitionin (Insight Biotechnology) was used when staining for LC3. For 5-methylcytosine staining, the cells were then denatured with 250 µL of 2 N HCl for 1 hour at 37^{o}C, followed by neutralization with 250 µL of 100 mM Tris-Cl buffer (pH 8). The acid/base mix was then removed, and the cells were incubated for another 10 min at room temperature with 100 mM Tris-Cl.

Cells were blocked with 5% BSA (Sigma-Aldrich) and 0.01% sodium azide (Sigma-Aldrich) or 5% goat serum in PBS for 30 min at room temperature or overnight at 4^{o}C. Staining was then done by first adding 50 µl of primary antibody (**Table 2.3)** diluted in dilution buffer (5% goat serum and 0.05% Tween-20 in PBS) in a humid chamber for 1 to 2 hours at room temperature. Coverslips were then washed twice with dilution buffer before secondary antibodies and nuclear counterstain (**Table 2.4)** diluted in the same buffer was added for 30 min at room temperature in the dark. After washing twice with PBS, the coverslips were mounted with 3 µl of either VECTASHIELD Antifade Mounting Media (Vector Laboratories) or ProLong Gold Antifade Mountant (Thermo Fisher Scientific). If VECTASHIELD was used, the coverslips were then sealed with clear nail polish. Slides were dried overnight at room temperature in the dark before imaging. Confocal images were acquired on a Leica SP5 X-WLL microscope and for STED, images were acquired using a Leica SP8 STED microscope. Analysis was performed using Imaris software.

2.5.2 Proximity Ligation Assay (PLA)

PLA was performed using Duolink In Situ Red reagents (Sigma Aldrich). First, dead cells were removed from T cell blast cultures using the Dead Cell Removal Kit (130-090-101, Miltenyi) according to manufacturer's instructions. Cells were them washed and allowed to

rest for two hours in cRPMI with 100 U/mL IL-2 at 37°C. Cells were then washed and resuspended at 5 x 10^6/mL in PBS. An equal volume of 8% PFA was added to the cell mixture for a final volume of 4% PFA, and the cells were fixed at RT for 30 min. They were then spun down at 300xg for 5 min and washed in PBS. 200 µL of suspended cells were added to wells of a 97 V-bottom plate, spun down, and then permeabilized with 0.1% Triton X-100 for 5 min. The cells were then spun down again and washed with PBS. They were blocked with 1 drop of Duolink blocking buffer (Sigma Aldrich) for 30 min at 37°C. They were then spun down, and stained with primary antibodies (**Table. 2.3)** diluted in 100 µL Duolink probe diluent per well overnight at 4°C. The next day, the samples were washed in 200 µL 1X Wash Buffer A (Sigma Aldrich) three times for 10 min each at RT with rocking. PLA probes (**Table 2.4)** diluted 1:5 in antibody diluent were added to the cells after washing for 1 hour at 37°C. The plates were the spun down and washed twice for 5 min in 1x Wash Buffer A. Ligase (Sigma Aldrich) was added to 1x Ligation Buffer (Sigma Aldrich), vortexed, and then 40 µL was added to each well for 30 min at 37°C. For the amplification step, the Ligation solution as removed, and the wells were then washed twice for 2 min each under gentle agitation in Wash Buffer A. After removing the wash buffer, 40 µL of Polymerase (Sigma Aldrich) diluted 1:80 in 1x Amplification buffer (Sigma Aldrich) was added to each well for 100 min at 37°C. The cells were then washed twice in 1X Wash Buffer B for 10 min, and then in 0.01X Wash Buffer B for 1 min. Samples were resuspended in 50 µL of PBS. 5 µL of suspension was added to one drop of Fluoromont-G with DAPI (Thermo Fisher Scientific) and gently mixed on a glass slide. A coverslip was then added and allowed to dry at room temperature (RT) overnight in the dark. 200 µL of PBS was added to the rest of the sample, which analyzed using an LSR-II flow cytometer (BD).

2.5.3 Mouse histology

Preparation of mouse histology slides was done by the Histology Service at the Kennedy Institute of Rheumatology (University of Oxford, Oxford, UK). After fixation in 4% PFA, samples were processed using the Tissue Tek VIP Sakura (GMI Inc) by incubated first in 70% ethanol, then five times in 100% ethanol, and lastly three times in Xylene for 90 min at 40^0C each. Afterwards, they were incubated in paraffin at 63^{o}C four times for 90 min before embedding in paraffin. Haemotoxylin and Eosin (H&E) staining was also done using the Tissue TEK VIP Sakura. Periodic Acid Schiff (PAS) staining was performed using the NovaUltra PAS Stain kit (IW-3009; IHC World Online) according to manufacturer's directions.

2.5.4 Transmission electron microscopy

After harvesting kidneys, tissue was fixed in 2.5% glutaraldehyde with 2-4% PFA in 0.1 M sodium cacodylate buffer (SC) (pH 7.2) for 3-4 hours at room temperature, and then stored at 4^{o}C until processing. Processing and transmission electron microscopy was performed by Dr. Errin Johnson (University of Oxford, Oxford, UK). Samples were washed in 0.1 M SC 3-5 times at 10-30 min each. They were then washed for 20 min with 50 mM glycine in 0.1M SC with rotation. Before washing for another 20 min with 0.1M SC. As a secondary fixation, samples were incubated for 2 hours at 4^{o}C in 1% osmium tetroxide and 1.5% potassium in 0.1M SC. They were then washed 5-6 times in milli-Q (MQ) water for 10 min at a time. Tertiary fixation was performed at 4^{o}C in the dark at 0.5% Uranyl acetate overnight before washing three times with MQ water for 5-10 min each. The samples were then dehydrated by incubation at 4^{o}C for 20 min with rotation in increasing concentrations of ice-cold ethanol (30%, 50%, 70%, 80%, 90%, 95%). Epoxy resin infiltration was then performed by incubating samples with 25% Agar Scientific Low Viscosity epoxy resin in pure ethanol for 2 hours and

then 50% resin in pure ethanol overnight. The next day, samples were incubated first with 75% resin in pure ethanol for 2 hours, then twice for two hours each time with 100% resin, before an overnight incubation in 100% resin. The resin was changed once more for several hours before embedding. All resin steps were done with rotation. To embed samples, individual tissue was placed in flat dish embedding molds filled with 100% resin and polymerized in a 60^{o}C oven for 48 hours. Blocks were sectioned using a Leica UC7 ultramicrotome. Semi-thin (500nm) sections were transferred to glass slides and stained with toluidine blue to check for the presence of glomeruli. Ultra-thin (90nm) sections were taken using a Diatome diamond knife and transferred to 50 mesh copper grids, then post-stained for 5 min with lead citrate. Sections were imaged on a FEI Technai12 TEM operated at 129kV using a Gatan OneView camera. The images were then analyzed by Dr. Avi Rosenberg (John Hopkins School of Medicine, Baltimore, MD, USA).

2.5.5 Kidney immunoglobulin staining

To prepare cryosections, snap frozen organs were embedded in OCT (Thermo Fisher Scientific) and 5 µm sections were cut using a Leica CM1900 Cryostat (Leica). Sections were dried and stored at -80^{o}C. Slides were fixed in ice cold acetone for 10 min before rinsing twice with PBS. They were then blocked with 5% goat serum (Sigma-Aldrich) with 1:200 TruStain fcX block (Biolegend) for 30 min at room temperature in a humid chamber. Primary antibody was then added for 1 hour at RT with 1:2000 Draq5 (Biolegend) as a nuclear counterstain. After washing, coverslips were mounted with Prolong Gold Antifade Mountant (Life Technologies) and allowed to dry in the dark at RT overnight. Samples were imaged using a Zeiss LSM 710 confocal microscope, and analyzed using Fiji (*325*, *326*).

Table 2. 3 Primary antibodies for microscopy			
Antibody	**Dilution**	**Company**	**Cat. No.**
5-methylcytosine (5-mC) (33D3)	1:100	Epigentek	A-1014-010
Calnexin Antibody #2433	1:50	Cell Signaling Technologies	2433S
Calnexin Monoclonal Antibody (AF18)	1:100	Thermo Fisher Scientific	MA3-027
Alexa Fluor 647 anti-mouse CD4 (GK1.5)	1:50	Biolegend	100426
GIMAP5 MAC 429	10 ug/mL (Confocal); 20 ug/mL (STED); 1:250 (PLA)	A kind gift from Geoff Butcher (*327*)	N/A
Goat anti-mouse IgA-FITC	1:200	Cambridge Bioscience	1040-02
Goat anti-mouse IgG-AF488	1:800	Thermo Fisher Scientific	A-11001
Goat anti-mouse IgM-FITC	1:800	Cambridge Bioscience	A90-101F
LAMP1 (D2D11) XP® Rabbit mAb #9091	1:1000 (1:200 for STED)	Cell Signaling Technologies	9091
LAMTOR4/C7orf59 (D4P6O) Rabbit mAb #13140	1:1600 (1:200 for PLA)	Cell Signaling Technologies	13140S
anti-LC3 pAB	1:750	MBL International	PM036
LC3A/B (D3U4C) XP® Rabbit mAb (Alexa Fluor® 647 Conjugate) #13394	1:25	Cell Signaling Technologies	13394
Mouse IgG1	As necessary	Santa Cruz	sc-3877
mTOR (7C10) Rabbit mAb #2983	1:200 (PLA)	Cell Signaling Technologies	2983S
anti-Rab7 (EPR7589)	1:50	Abcam	ab137029
Rabbit (DA1E) mAb IgG XP® Isotype Control #3900	As necessary	Cell Signaling Technologies	3900
RagC	1:200 (PLA)	Cell Signaling Technologies	3360S
Rat normal IgG	As necessary	Santa Cruz	Sc-2026
TCRalpha (H-1)	1:50 (PLA)	Santa Cruz	sc515719
TCRbeta (H-197)	1:50 (PLA)	Santa Cruz	sc9101

Table 2.4 Secondary antibodies and dyes for microscopy			
Antibody	**Dilution**	**Company**	**Cat. No.**
Secondary antibodies			
Goat anti-Rabbit IgG (H+L) Highly Cross-Adsorbed Secondary Antibody, Alexa Fluor 488	1:500	Thermo Fisher Scientific	A-11034
Goat anti-Rabbit IgG (H+L) Highly Cross-Adsorbed Secondary Antibody, Alexa Fluor 647	1:500	Thermo Fisher Scientific	A-21245
Goat anti-Rat IgG (H+L) Cross-Adsorbed Secondary Antibody, Alexa Fluor 488	1:500	Thermo Fisher Scientific	A-11006
Goat anti-mouse IgG (H+L) Cross-Adsorbed Secondary Antibody, Alexa Fluor 488	1:500	Thermo Fisher Scientific	A-11001
Donkey anti-mouse IgG (H+L) Cross-Adsorbed Secondary Antibody, Alexa Fluor 488	1:500	Thermo Fisher Scientific	A-21202
Goat anti-Rabbit IgG (H+L) Highly Cross-Adsorbed Secondary Antibody, Alexa Fluor 700	1:500	Thermo Fisher Scientific	A-21038
Goat anti-Rat IgG (H+L) Cross-Adsorbed Secondary Antibody, Alexa Fluor 568	1:500	Thermo Fisher Scientific	A-11077
Goat anti-Rat IgG (H+L) Cross-Adsorbed Secondary Antibody, Alexa Fluor 594	1:500	Thermo Fisher Scientific	A-11007
Rabbit IgG (H&L) Antibody ATTO 647N Conjugated Pre-Adsorbed	1:500	Rockland Antibodies and Assays	611-156-122
Dyes			
Mitotracker Red CXMRos	6.25 nM	Thermo Fischer Scientific	M7512
Hoescht 33342	1 ug/mL	Sigma Aldrich	B2261-25MG
Draq5	1:2000	Biolegend	424101
PLA secondary antibodies			
Duolink In Situ PLA Probe Anti-Mouse PLUS	1:5	Sigma Aldrich	DUO92001
Duolink In Situ PLA Probe Anti-Rabbit PLUS	1:5	Sigma Aldrich	DUO92002
Duolink In Situ PLA Probe Anti-Rabbit MINUS	1:5	Sigma-Aldrich	DUO92005
Goat anti-rat Duolink In Situ PLA Probe MINUS conjugated[1]	1:100	Thermo Fischer Scientific	31220

[1]PLA probe was made using the Duolink In Situ Probemaker MINUS kit (DUO92010; Sigma Aldrich) on goat anti-rat IgG (H+L) secondary antibody (31220; Thermo Fischer Scientific)

2.6 PCR

2.6.1 Transformations

Heat shock was used to transform competent bacteria. Bacteria were thawed on ice, and the plasmid to be transformed was added for 10 min on ice. The bacteria were then incubated at 42^{o}C for 45s before immediately being placed on ice for 2 min. SOC medium (15544034; Thermo Fisher Scientific) was added, and the bacteria were allowed to recover at 37^{o}C with shaking for 30 min. They were then plated on LB agarose plates with the selective antibiotic and incubated overnight at 37^{o}C. The next day, colonies were picked for minipreps.

2.6.2 RT-PCR

For RT-PCR, monocytes were enriched using an EasySep Human Monocyte enrichment kit (STEMCELL Technologies) according to manufacturer's instructions before activation with LPS. At the indicated time points, cells were spun down at 4^{o}C and 300xg for 5 min, washed in ice cold PBS, and then directly lysed in TRIzol reagent (15596026; Thermo Fisher Scientific). For snap frozen organs from perfused mice, organs were homogenized in 1 mL TRIzol and then incubated at RT for 5 min. 200 µL of chloroform (194002; MP Biomedical) per mL of TRIzol was added and mixed for 20s and the mixture was incubated at RT for 2-3 min. The sample was then centrifuged at 12,000xg for 12 min at 4^{o}C, and the aqueous phase was removed. An equal amount of 100% ethanol was then added before purification of the RNA using a RNeasy Mini kit (74104; Qiagen) according to manufacturer's instructions. RNA was eluted to water. RNA was reverse transcribed into cDNA using the Super Script III kit (Life Technologies) and stored at -20^{o}C until analysis.

For the mouse samples, Taqman probes (**Table 2.5)** (Thermo Fisher Scientific) and TaqMan Gene Expression Master Mix (4369016; Thermo Fisher Scientific) were used for real-

time PCR using the ViiA 7 Real-Time PCR System (Thermo Fisher). For human samples, probes listed in **Table 2.5** were used with PowerUp SYBR Green Master Mix (A25742; Life Technologies) on a 7500 Real Time PCR System (ABI). ΔΔCt method was used for the quantification of target mRNA expression using either *Hprt1* (mouse) or *GAPDH* (human) as reference genes. Relative expression was determined by arbitrarily setting one sample as 1 and normalizing expression levels.

Table. 2.5 RT-PCR Probes	
TaqMan Probes	
Target Gene	**Cat. No.**
Mouse *Gimap6*	Mm00462641_m1
Mouse *Hprt*	Mm01545399_m1
Mouse *Gapdh*	Mm99999915_g1
Sybr Green Probes	
Target gene	**Primers**
Human *IL1B*	Fw: 5'- ATGATGGCTTATTACAGTGGCAA -3' Rv: 5'- GTCGGAGATTCGTAGCTGGA -3'
Human *IFNB1*	Fw: 5'- AGTAGGCGACACTGTTCGTG -3' Rv: 5'- GGCAGTATTCAAGCCTCCCAT -3'
Human *GAPDH*	Hs.PT.39a.22214836 (IDT) Fw: 5'- ACATCGCTCAGACACCATG-3' Rv: 5'- TGTAGTTGAGGTCAATGAAGGG -3'
Human *TICAM1*	Fw: 5'- CCGGATCCCTGATCTGCTTGG -3' Rv: 5'- TGTCGAAGGCGCTAGGAAGT -3'
Human *TICAM2*	Fw: 5'- TTTCTTTTCAATCTGCAGGCGAG -3' Rv: 5'- CCCCAAACTCTCGACGCC -3'
Human *TNFA*	Fw: 5'- CCTCTCTCTAATCAGCCCTCTG -3' Rv: 5'- GAGGACCTGGGAGTAGATGAG -3'

2.7 ELISAs and other *in vitro* assays

2.7.1 Cytokine ELISAs

Monocytes were enriched as described in Section 2.6.3. Supernatants were collected and tested in triplicate using the human IL-6 ELISA MAX Deluxe (430504 Biolegend) and

Human TNF-alpha ELISA MAX Deluxe (430204, Biolegend) according to manufacturer's protocol.

2.7.2 Luciferase assay

2.7.2.1 Luciferase plasmids

IFN-β-pGL3 (Promega; (*328*)), a firefly luciferase plasmid controlled by the human IFN-β promoter, and the pRL-TK (Promega), a plasmid constitutively expressing *Renilla* luciferase, were gifts from Y. He (National Institute of Diabetes and Digestive and Kidney Diseases, Bethesda, MD). Firefly luciferase plasmid driven by NF-κB response element (pGL4.32-*luc3*P/NF-κB-RE/EGFP; (*329*)) was a gift from I. Lamborn (National Institute of Allergy and Infectious Disease, Bethesda, MD). Plasmid expressing TICAM2 (pEF-Bos TRAM Flag) was a gift from Kate Fitzgerald and Doug Golenbock (Addgene plasmid #41551), and plasmid expressing TRIF (pCDNA3-TRIF-CFP) was a gift from Doug Golenbock (Addgene plasmid #13644). pEF-Bos TRAM Flag was modified to create plasmids containing the $TICAM2^{G2A}$, $TICAM2^{C117H}$, and $TICAM2^{K166Q}$ constructs.

2.7.2.2 Luciferase assay

The luciferase assay was done as described previously (*329*). A 24-well plate was seeded the night before transfection with 293FT cells. Plasmids were transfected into ~70-80% confluent cells using TurboFect (ThermoFisher Scientific), according to manufacturer's instructions. In short, DNA was diluted in Opti-MEM reduced serum media (ThermoFisher Scientific) before the recommended amount of Turbofect was added. After a 15 min incubation at RT, the mixture was added drop-wise onto the cells. The cells were then incubated at 37°C for 24 hours. Transfected cells were tested for luciferase activity using the

Dual-Luciferase Reporter Assay System (Promega) according to manufacturer's directions. In summary, cells were harvested by washing with PBS and then adding Passive Lysis Buffer (Promega) to the cells for 15 min at RT with shaking. Lysates were either frozen at -20^{o}C or used directly. To measure luciferase activity, 20 ul of lysates diluted 1:3 in lysis buffer was added in triplicate to a 96-well white Costar polystyrene microplate (Corning). Plates were read using a FLUOstar Omega plate reader (BMG Labtech). The plate reader was set to inject 100 ul of room temperature LAR II (luciferase assay substrate) (Promega) to detect firefly luciferase activity, and subsequently add 100 ul of STOP & Glo reagent (Promega), which simultaneously quenches firefly luciferase activity and provides *Renilla* luciferase substrate, to measure *Renilla* luminescence. Firefly luciferase activity was normalized to *Renilla* luciferase activity.

2.7.3 NP-CGG ELISA

A microplate 96 PS half area high binding plate (Greiner Bio-one) was coated overnight at 4^{o}C in 5 µg/ml of NP_{20}-BSA (2B Scientific) in 100 mM bicarbonate/carbonate coating buffer (pH 9.6). The next day, plates were washed with PBS three times and blocked with 5% skimmed milk in PBS for 1-3 hours at 37^{o}C. Serum samples were thawed and diluted in 1% milk at 1:500 for the anti-NP_{20} IgM enzyme-linked immunosorbent assay (ELISA) and at 1:1000 (primary response) or 1:5000 (secondary response) for the anti-NP_{20} IgG1 ELISA. Pooled sera from day 7 after a secondary immunization from mice that had been previously been injected with NP-CGG in a previous experiment was serially diluted and used as standard curve for all ELISA plates, starting with a 1:400 or 1:4000 dilution for the IgM or IgG1 ELISA, respectively. After blocking, the plates were further washed, and diluted sera was added to the plates for one hour at 37^{o}C. Plates were then washed with 0.05% Tween-20 in PBS before detection.

Anti-NP_{20} IgM was detected with 1:1000 AP-conjugated goat anti-mouse IgM, human adsorbed (1020-04; Southern Biotech); anti-NP_{20} IgG1 was detected with 1:2000 AP-conjugated goat anti-mouse IgG1, human adsorbed (1070-04; Southern Biotech). These antibodies were diluted in 1% milk and incubated for 1 hour at 37°C. Following further washing, plates were developed by incubating phosphatase substrate (S0942; Sigma-Aldrich) in pNPP buffer for 10-15 min at room temperature in the dark. Absorbance was then measured at 405 nM by ELISA plate reader (FLUOstar Omega, BMG Labtech).

2.7.4 NP-CGG ELISpot

MultiScreenHTS-HA filter plates (MSHAS4510; Merck Millipore) were rinsed with 35% ethanol for 30 s before washing with PBS. They were then coated with 20 µg/mL NP_{20}-BSA (2B Scientific) in PBS overnight at 4°C. After washing three times with PBS, plates were blocked with cRPMI at 37°C for 30 min. Splenocytes and bone marrow cells were counted using Precision Count Beads (424902; Biolegend) and propidium iodide (13-6990-T200; Insight Biotechnologies) on a CyAn ADP (DakoCytomation) and resuspended in cRPMI. Cells were plated in duplicate in 100 µL per well and incubated overnight at 37°C. Two dilutions were used per condition: 2×10^5 and 4×10^5 cells/well. The next day, cells were removed from the plates. Plates were washed three times with PBS, three times with PBS-0.05% Tween-20, and then once more with PBS. 50 µL of 1:2000 AP-conjugated anti-mouse IgG1 detection antibody diluted in 1% FBS in PBS was added to each plate for 1 hour at 37°C. Plates were then washed five times with PBS-0.05% Tween-20 and once with PBS. To develop the plate, 50 µL of alkaline phosphatase (AP) ELISpot substrate (170-6432, Bio-Rad) was added per well and incubated for about 8 min until clear spots were visible on a clean background.

Development was stopped by washing plates with water. The plates were then dried and counted with an AID ELISpot Reader (Autoimmun Diagnostika GmbH).

2.7.5 Serum antibody ELISAs

Serum was tested for total IgM and IgG levels using the IgG (Total) Mouse (88-50400-22, Thermo Fisher Scientific) and IgM Mouse (88-50470-22, Thermo Fisher Scientific) ELISA kits. ACA antibodies were tested from mouse plasma using the mouse anti-cardiolipin antibody-IgG ELISA kit (EM0274, Universal Biologicals). All kits were used according to manufacturer's instructions.

2.7.6 Anti-nuclear antibody (ANA) assay

Mouse serum was tested for anti-nuclear antibodies by Eleanor Cawthorne (Richard Cornall laboratory, University of Oxford, Oxford, UK) using HEp-2000 substrate slides (ImmunoConcepts, UK) according to the manufacturer's protocol.

2.8 Western blot

Lysates were prepared by washing cells in PBS and then lysing in either RIPA (150 mM NaCl, 5 mM EDTA [pH 8.0], 50 mM Tris [pH 8.0], 1.0% NP-40, 0.5% sodium deoxycholate, 0.1% SDS) or NP-40 buffer (1% NP-40, 50 mM Tris [pH 7.5], 100 mM NaCl) and Complete mini protease inhibitor cocktail (11836153001; Roche) and Halt phosphatase inhibitor cocktail (1861277; Thermo Fisher) for 15 min on ice. For experiments with multiple time points, cell pellets were flash frozen on dry ice and stored at -80^{o}C for simultaneous processing. Frozen pellets were thawed in lysis buffer on ice for 30 min with trituration pipetting. Samples were then centrifuged for 10 min at 15,000xg at 4^{o}C, and the supernatant was collected. Lysates were heated at 95^{o}C for min with reducing Laemmli Sample Buffer (1610747; Bio-Rad) and

100 mM DL-Dithioreitol (DTT) solution (43816; Sigma-Aldrich). 10-35 µg of protein were loaded for SDS-PAGE analysis. Samples were run on either a NuPAGE Novex 10% or 4-12% Bis-Tris protein gel (Life Technologies) with either NuPAGE MOPS SDS Running Buffer (Thermo Fisher Scientific) or with MES SDS Running Buffer (Thermo Fisher Scientific) if blotting for LC3. Proteins were transferred to a polyvinylidene difluoride (PVDF) membrane (IPFL00010; Millipore) for 50-60 min at 15 V constant. The membrane was then blocked with 5% non-fat milk in PBS + 0.1% Tween-20 (PBST) for 1 hr at RT with shaking. Membranes were then incubated with primary antibodies (**Table 2.6)** diluted in 1% milk in PBST either overnight at 4^{o}C or for 2 hours at RT with shaking followed by washing for three times with PBST for 10-20 min before incubation with secondary antibodies (**Table 2.7)** for 1 hr at RT in the dark. The membrane was then washed three times with PBST and once with PBS. Fluorescent secondary antibodies were imaged using the Odyssey CLx Imaging System (LI-COR Biosciences). When using HRP-conjugated secondary antibodies (**Table 2.7)**, SuperSignal West Dura Extended Duration Substrate (34075; Life Technologies) was added to the membrane for 1 min before imaging on a PXi imager (Syngene). Data were analyzed using Image Studio Lite.

Table 2.6 Primary antibodies for westerns

Antibody	Dilution	Company	Cat no.
beta Tubulin Loading Control Monoclonal Antibody (BT7R), DyLight 680	1:5000	Life Technologies	MA5-16308-D680
beta Actin Loading Control Monoclonal Antibody (BA3R), DyLight 680	1:5000	Life Technologies	MA5-15739-D680
THE beta Actin Antibody, mouse mAb (2D1D10)	1:5000	GenScript	A00702
anti-mouse GIMAP6 (MAC436)	1:10 (supernatant)	A kind gift from Geoff Butcher (*331*)	N/A
anti-human GIMAP6 (MAC445)	1:1000	A kind gift from Geoff Butcher (*332*)	N/A
anti-human GIMAP5 (MAC429)	1:1000	A kind gift from Geoff Butcher (*327*)	N/A
Ha-Tag (6E2) mouse mab	1:1000	Cell Signaling Technologies	2367S
anti-LC3 rabbit polyconal	1:1000	Sigma-Aldrich	L8918

Table 2.7 Secondary antibodies for westerns

Antibody	Dilution	Company	Cat no
IRDye® 800CW Goat anti-Rat IgG (H + L)	1:15000	Li-COR	925-32219
Donkey anti-Mouse (Murine) IgG (Heavy & Light Chain) Antibody (IRDye800CW)	1:15000	antibodies-online.com	ABIN2169610
Donkey anti-Rabbit IgG (Heavy & Light Chain) Antibody (IRDye800CW)	1:15000	antibodies-online.com	ABIN2169612
Goat anti-Mouse (Murine) IgG (Heavy & Light Chain) Antibody (IRDye680RD)	1:15000	antibodies-online.com	ABIN2169639
Goat anti-Rabbit IgG (Heavy & Light Chain) Antibody (IRDye680RD)	1:15000	antibodies-online.com	ABIN2169643
Goat Anti-Mouse IgG H&L (HRP) preadsorbed (ab97040)	1:15000	Abcam	ab97040
Goat Anti-Rabbit IgG H&L (HRP) preadsorbed (ab97080)	1:15000	Abcam	ab97080
Goat Anti-Rat IgG H&L (HRP) preadsorbed (ab7097)	1:15000	Abcam	ab7097

2.9 Statistics

All statistical analysis was performed using Graphpad Prism 7.0. Data is shown as mean +/- standard deviation (SD) unless otherwise stated. Statistical tests (two-tailed

Student's T-test, Mann-Whitney U test, two-way ANOVA with Tukey's multiple comparison test, repeat measures two-way ANOVA with Sidak's multiple comparison test, or log-rank Mantel-Cox test) were used as appropriate. A difference was considered statistically significant when *$p<0.05$.

Chapter 3. Investigation of causative mutations in novel Mendelian immune diseases

3.1 Introduction

In this chapter, I aimed to determine the causal genes and affected molecular pathways underlying disease in patients with congenital or primary immunodeficiencies (PID) of unknown cause. As discussed in Chapter 1, NGS has been pivotal role in the identification of new PIDs and PID-associated genes. These genes were largely identified by utilizing NGS in either whole exome sequencing (WES), in which genomic DNA for the protein-coding or exonic regions (~1% of the genome) is captured by hybridization, or in whole genome sequencing (WGS), which uses the entire DNA content of the nucleus (*6*). In this thesis, we used WES to identify potential candidate genes in four sets of patients with PID of unknown etiology.

3.1.1 Whole exome sequencing

After the identification of potential PID patients, WES is followed by bioinformatic analysis, prioritization and validation of candidate genes, and exploration of gene function to determine novel PID causal genes and their role in the normal immune system (**Fig. 3.1A).** While there are several different protocols for WES, in most protocols (and the one used in this thesis), DNA is first extracted and then fragmented. Adaptors are added to the ends of the strands to prepare a DNA library. The library is then hybridized with labelled nucleotide "baits" that correspond to exonic or exon flanking sequences. The targeted sequences are

then captured, amplified, and sequenced using primers complementary to the adaptor sequences (*333–335*).

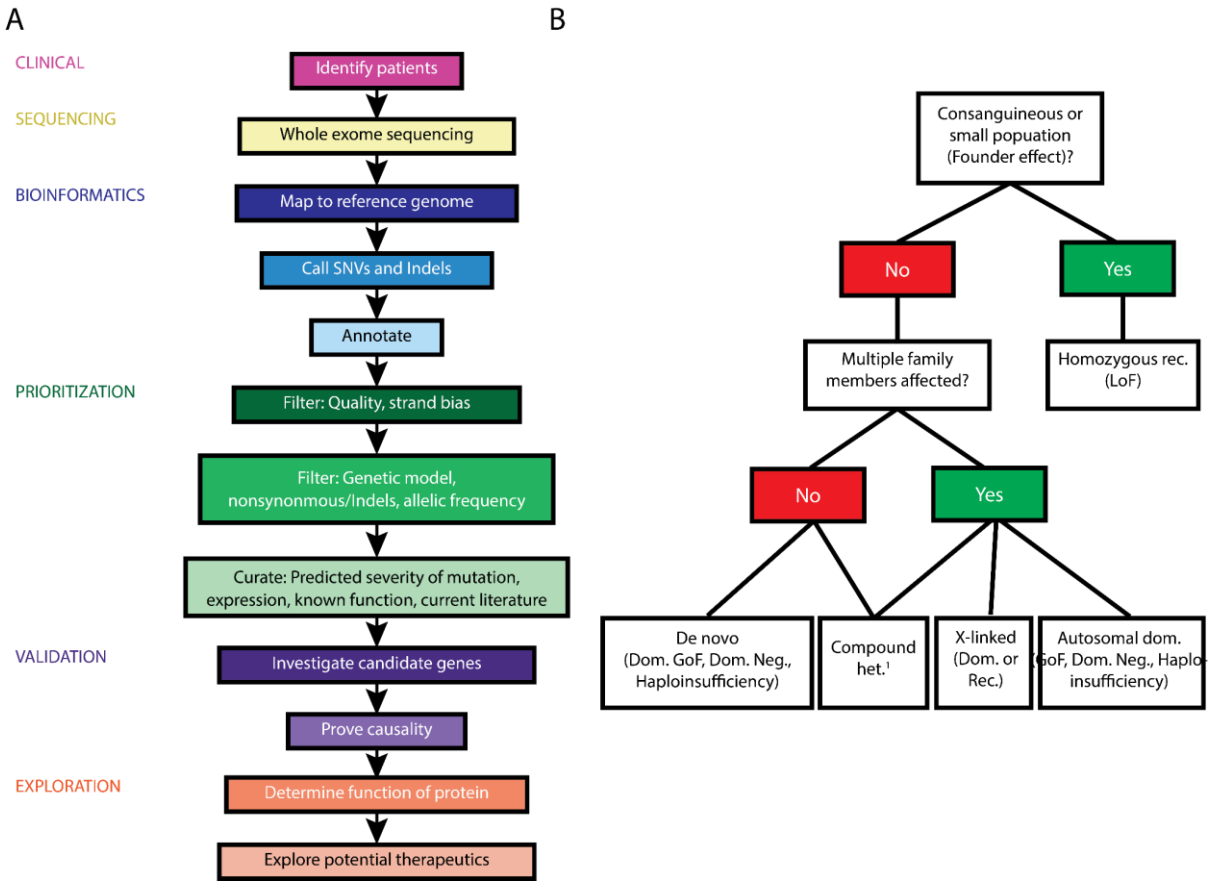


Fig. 3.1. **Identification of novel primary immunodeficiencies. A)** Summary of the workflow used in the study of PIDs. Patients are clinically identified and their genomic DNA is whole exome sequenced. Bioinformatic analysis is used to align DNA reads and map them to a reference genome. Single nucleotide variants (SNVs) and insertion/deletions (indels) are then called using algorithms such as the Genome Analysis Toolkit, before annotation and prediction of the mutation's severity. Candidates genes are then investigate for causality and relationship to the patient's phenotype. **B**) Decision tree for prioritization of inheritance models. SNV= single nucleotide variants; Indels= insertions/deletions; LoF= loss of function; GoF= gain of function; rec= recessive; dom= dominant; het= heterozygous.
[1]If family members affected are siblings.

From there, candidate genes are determined using various filtering criteria based on a specific lab's pipeline. In general, and in our lab specifically, filtering begins either at this step or prior to annotation by looking at call quality parameters such as read quality, coverage (the average number of reads that align to the region) of a specific locus, and allele balance (the ratio of reads supporting the alternate allele) (*336*, *337*). Variants expected to affect

protein sequence (indels and mutations predicted to cause nonsense mutations or frameshifts, missense mutations, or changes to splice sites) are then selected. As polymorphisms are unlikely to cause Mendelian diseases due to negative selection, variants can then be filtered on allelic frequency in the population (*338*, *339*). Next, tools such PolyPhen and Combined Annotation Dependent Depletion (CADD) score, can be utilized to predict the likelihood that protein function will be affected(*340*–*342*). Polyphen estimates the probability of a single nucleotide variants (SNV) to affect protein function by looking at protein sequence, structure, and conservation, generating a score of "benign", "possibly damaging", or "probably damaging" (*341*). CADD works by integrating multiple functional annotations and compares genetic alleles present in the human population to simulated variants, with the thought that deleterious variants will be selected against. It then gives a score for "deleteriousness", called a C-score, that should correlate with pathogenicity, with a score of ≥ 15 meaning that the variant was among the 5% variants predicted to be most damaging and ≥ 20 among the 1% most deleterious (*340*). Programs like CADD and Polyphen are helpful in determining the variants mostly likely to be pathogenic, but due to the complexity involved, there is often a discrepancy between the real impact of mutations on proteins and that predicted by computational tools: one study has shown that approximately half of variants predicted to be deleterious had little impact on phenotype (*343*). Therefore, further experimental verification is required to verify the actual consequences of the genetic change on protein structure and function.

Along with deleteriousness predictor, genetic inheritance modelling is particularly invaluable in filtering down the list of potential candidate genes (**Fig.3.1B)**. If, for example, a patient is from a family with a high level of consanguinity or a member of a small community (e.g. a minority ethnic group or isolated area), a homozygous recessive LOF inheritance is the

most likely model. Therefore, variants that are homozygous exclusively in all of the affected family members would comprise the most likely candidates. Otherwise, families with multiple affected members would likely fit a compound heterozygous (if the members affected are siblings), X-linked, or autosomal dominant model. Lastly, if a patient is the only person affected in a family with no history of disease, then variants might be filtered using a compound heterozygous or de novo model. Once a list of candidate genes is determined using the mentioned criteria, prioritization of specific genes can be made using manual curation. This includes looking at a gene's expression profile, known functions, and already known associations with any diseases.

Three types of patients have been most utilized in PID discovery: 1) patients with multiple family members affected or from consanguineous unions or small populations; 2) unrelated patients who have very unique and rare clinical presentations; and 3) patients from families with no family history of disease but who present with very unusual phenotypes (*344*). Of all these types, diseases following a homozygous recessive mode of inheritance are the easiest to identify, and comprise the largest percentage of verified PIDs (*3*). I present three sets of patients in this chapter, and four in total throughout this thesis, who are thought to have novel PIDs following a homozygous recessive model. Each patient was whole exome sequenced and potential pathogenic variants identified and investigated for causality and protein function.

3.2 Results

3.2.1 Identification of patient with a homozygous mutation in DNA methyltransferase 3 beta (DNMT3B) resulting in Immunodeficiency, Centromeric instability, and Facial anomalies (ICF) syndrome

3.2.1.1 Immunophenotyping of patient 1294

Patient 1294, hence forth referred to as PID1294, was born into a consanguineous Turkish family (**Fig. 3.2)**. He presented at 1 month old with a CVID marked by agammaglobulinemia, leukopenia, thrombocytopenia, and recurrent otitis and pneumonia, as well as other symptoms including dysmorphic features, motor and mental retardation, and failure to thrive (**Table 3.1)**. After collaborators at Marmara University in Istanbul, Turkey referred PID1294 to the NIH, genomic DNA from him and his immediate family was whole exome sequenced.

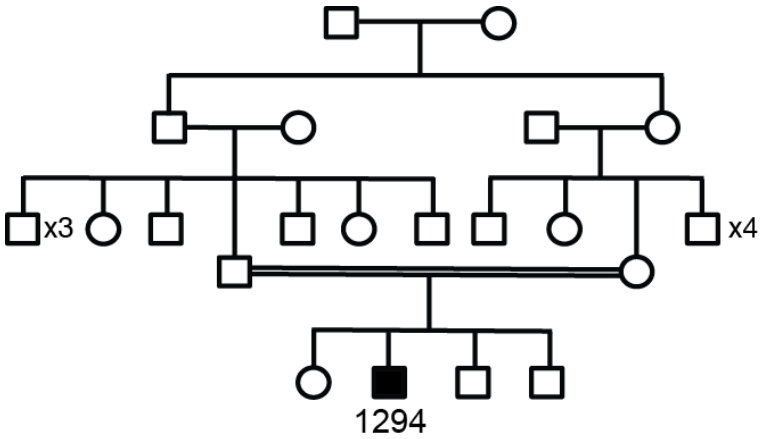


Fig. 3.2 Pedigree of PID1294. The proband is shaded in black. A double line represents a consanguineous relationship. Circles= females; squares= males.

Table 3.1. Clinical presentation of patient 1294.	
Lymphadenopathy?	No
Splenomegaly?	Yes
Hematologic abnormalities?	Leukopenia and thrombocytopenia CD4 ↓, CD8↑, CD19↓, NK↓
Autoimmunity or autoinflammatory disease?	No
Immunodeficiency or susceptibility to infection?	• CVID • Recurrent otitis • Recurrent pneumonia • Bronchiectasis • Diarrhea • Agammaglobulinemia (IgG 110 mg/dL before IVIG; IgA undetectable; IgM <16 mg/dL)
Dysmorphic features?	• Hyperpigmentation of skin • Hypertelorism • Antevert ears • High palate • Long facies • Down slanted palpebral fissures • Asthenic feature
Other	• Osteoporosis • Deafness • Mental retardation • Failure to thrive

CVID= common variable immune deficiency; IVIG= intravenous immunoglobulin treatment

While the samples were being processed, I began immunophenotyping the patient. Patient's T cells had a reduction in naïve T cells, with a corresponding skew toward an effector memory phenotype (**Fig. 3.3)**. Due to the observed abnormalities, I examined whether these cells had normal function in response to stimulation with anti-CD3/28 antibodies (**Fig. 3.4**). As an indicator of T cell responsiveness, I stained cells for activation markers. One such marker was CD69, a C-type lectin protein that has potential roles in lymphocyte migration, differentiation, and metabolism and is upregulated soon after T cell activation (*345*). The other marker used was CD25, the IL-2 receptor alpha chain; while it has slightly slower kinetics than CD69, it is also upregulated after TCR stimulation (*346*). At 20 hours post-activation, the

patient's T cells had markedly reduced expression of both markers, particularly in the CD8 T cell population (**Fig. 3.4)**. This suggests the patient's cells have defective responses to TCR activation, though a further time course is necessary to confirm this. Further analysis showed that ~65% of the patient's CD8 T cells were $CD57^+$, indicating a senescent phenotype (**Fig. 3.5**) (*347*). Senescent T cells are known to have impaired functionality, which could explain the patient's dampened T cell response. As the patient has lymphopenia and an increased susceptibility to infection, the higher percentage of $CD57^+$ T cells and skew towards effector memory phenotype may be consistent with chronic antigenic stimulation or a virtual memory phenotype due to lymphopenia-induced proliferation.

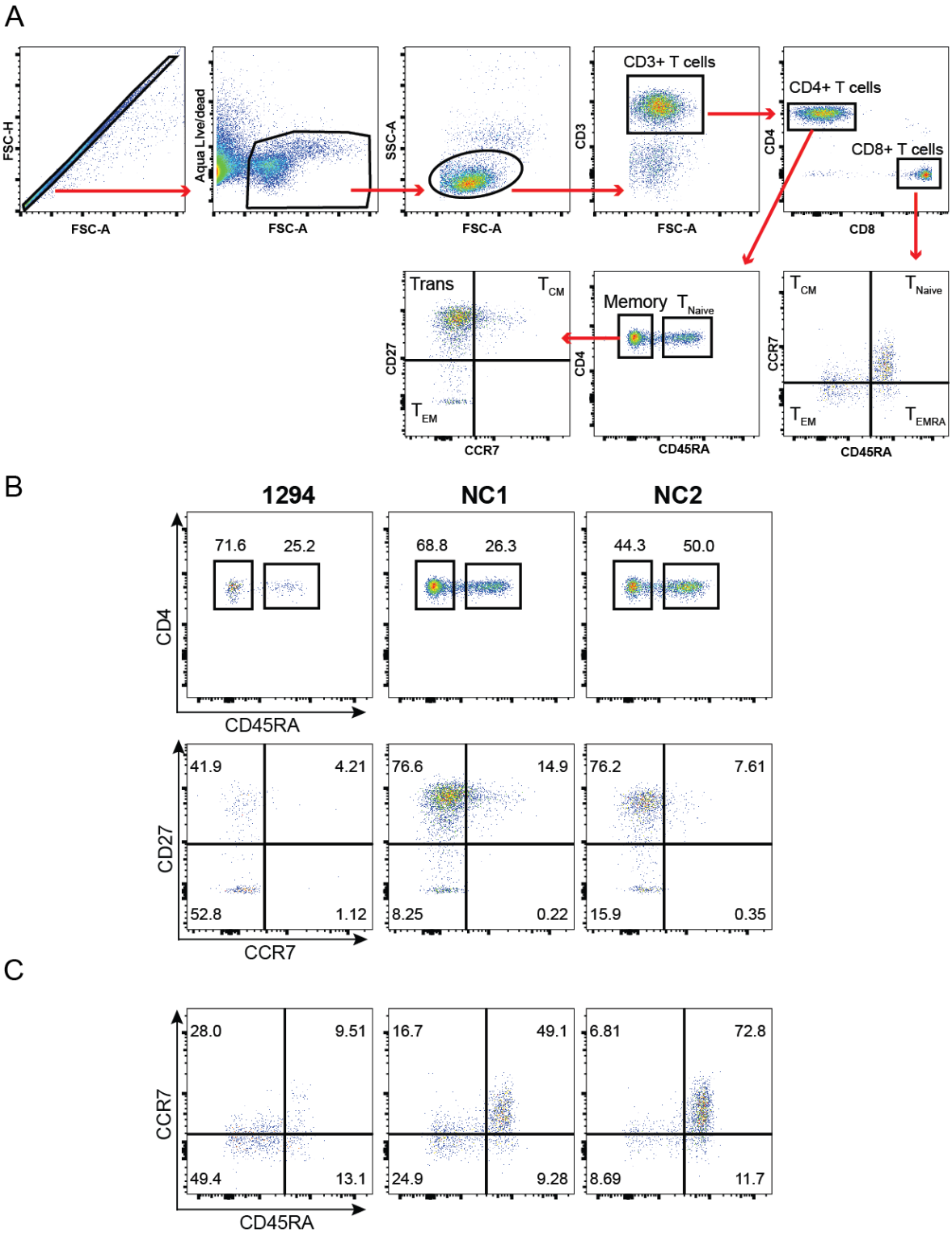


Fig. 3.3 Skew towards memory phenotype in patient T cells. PBMCs were stained with anti-CD3, -CD4, -CD8, -CCR7, -CD45RA, and -CD27 antibodies, and cell populations were analyzed after flow cytometry. **A**) Gating strategy for T cell populations **B)** Naïve and memory subsets in CD4 T cells. **C)** Naïve and memory subsets in CD8 cells. NC=normal control; T_{EM}= T effector memory; T_{CM}= T central memory; Trans=transition; T_{EMRA}= T effector memory expressing CD45RA

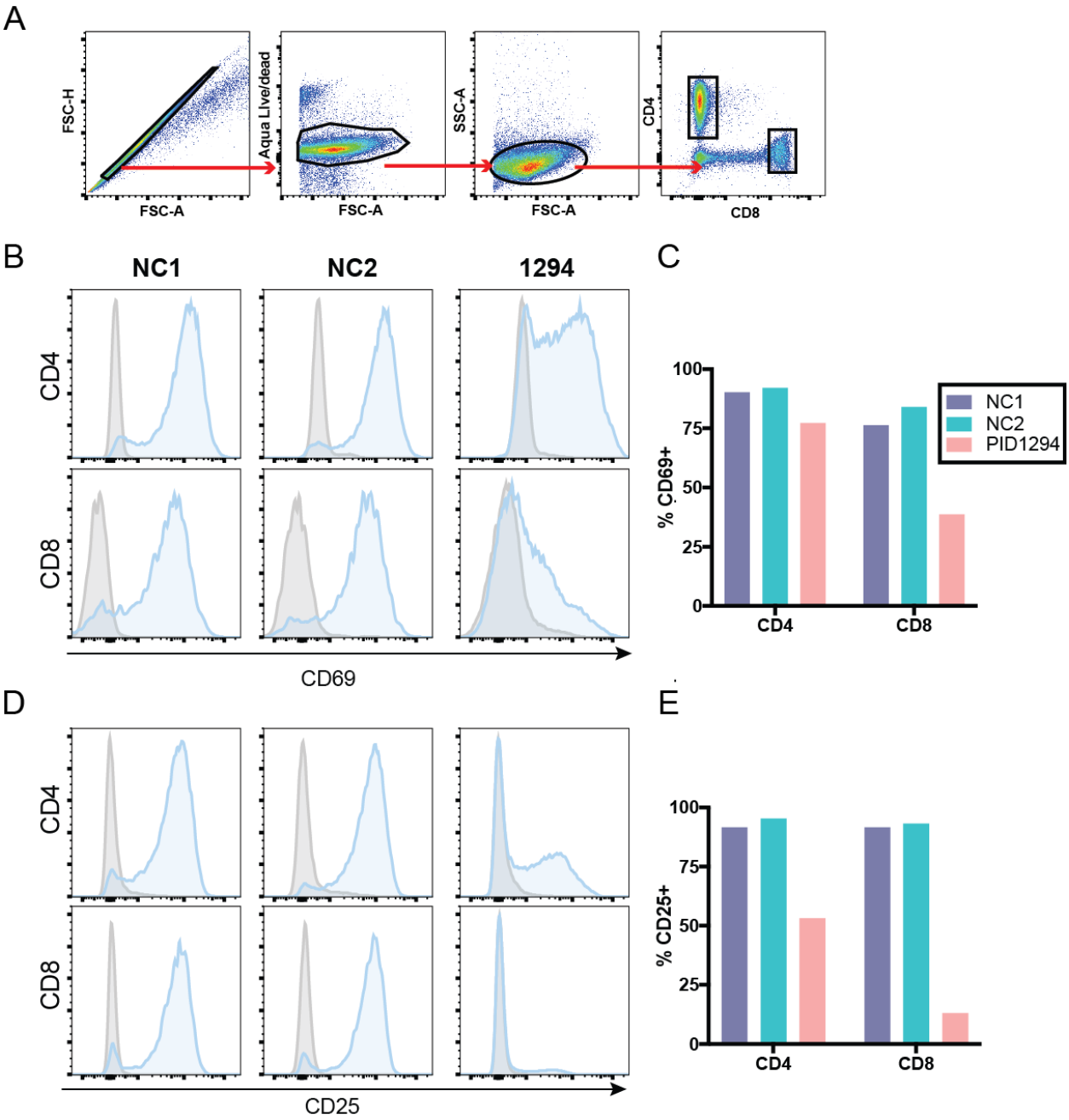


Fig. 3.4 Patient CD4 and CD8 cells have reduced response to TCR activation. PBMCs were stimulated with anti-CD3/28 antibodies for 20 hours and then stained for activation markers. **A)** Gating strategy for CD4 and CD8 T cells. **B-E)** Flow plot showing CD69 (**B**) and CD25 (**D)** expression in unstimulated (grey) and stimulated (blue) T cells. Quantification of the percent of CD4 or CD8 T cells after stimulation is shown for CD69 (**C**) and CD25 (**E**). NC= normal control; FSC-A= forward scatter-area; FSC-H= forward scatter-height; SSC-A= side scatter-area

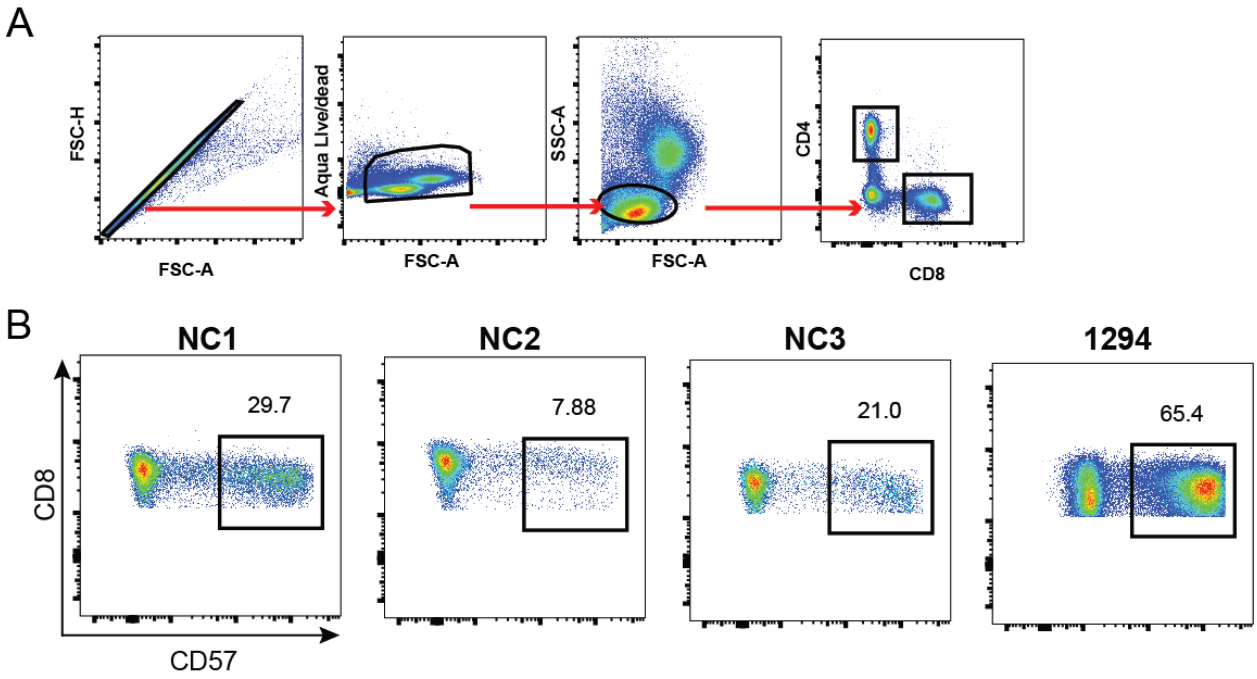


Fig. 3.5 PID1294 has an increase in senescent-like CD8 T cells. PBMCs were stained *ex vivo* with Aqua Live/dead, anti-CD4, -CD8, -CD45RA, and -CD57 antibodies and analyzed by flow cytometry. **A**) Gating strategy for CD8 T cells. **B)** Frequency of senescent $CD57^{+}$ CD8 T cells. NC=normal control; FSC-A= forward scatter-area; FSC-H= forward scatter-height; SSC-A= side scatter-area

Because the patient has agammaglobulinemia and B cell lymphopenia, I examined whether his B cells could activate normally. Whole PBMCs were stimulated with either CpG and IL-4 or anti-IgM/CD40 to activate B cells (**Fig. 3.6**). The patient's B cells had relatively normal upregulation of multiple activation markers (CD25, CD69, CD40, and CD86) after 20 hours, suggesting that they can respond normally to stimulation. This indicates that the patient's agammaglobulinemia may be due to his B cell lymphopenia, another B cell defect, or secondary to a T cell defect rather than a failure to react to challenge.

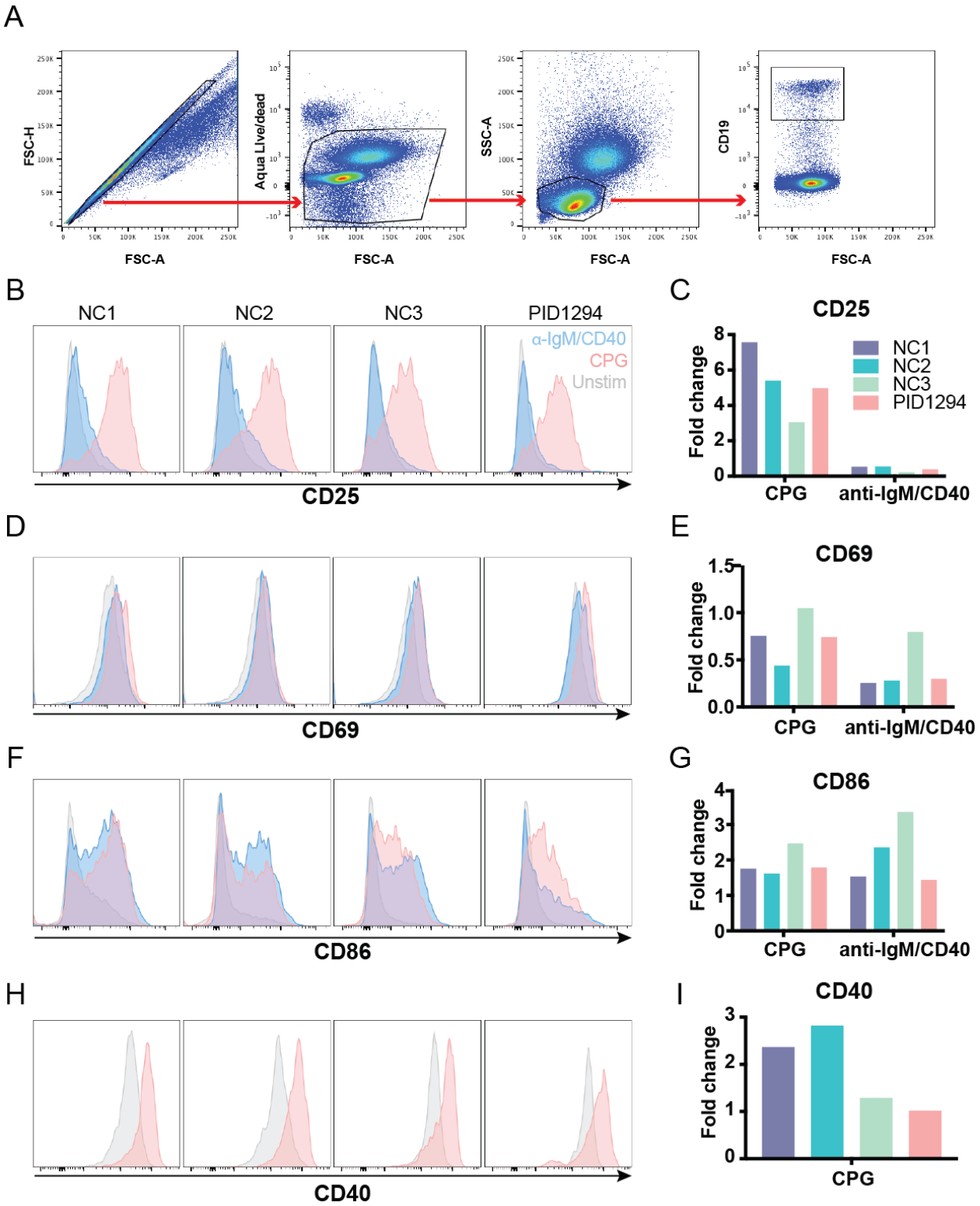


Fig. 3.6 B cells from PID1294 react normally to activation. Ficolled PBMCs were stimulated with either 25 µg/mL of anti-IgM and 1 µg/mL anti-CD40 antibodies or CpG and IL-4, or left unstimulated for 20 hours. They were then stained with Aqua live/dead, anti-CD20, -CD19, -CD86, -CD25, and -CD69 antibodies as well as for Annexin V before flow cytometric analysis. **A)** Gating strategy showing the selection of CD19+ B cells used for analysis. Upregulation of CD25 (**B)**, CD69 (**D**), CD86 (**F)**, and CD40 (**H**) were determined. Changes in activation marker

expression was quantified and is reported in **C** (CD25), **E** (CD69), **G** (CD86)**,** and **I** (CD40) as fold change ([$gMFI_{Stim}$ – $gMFI_{Unstim}$]/ [$gMFI_{Unstim}$]). NC=normal control; FSC-A= forward scatter-area; FSC-H= forward scatter-height; SSC-A= side scatter-area

3.2.1.2 Identification of homozygous missense mutation in DNMT3B causing immunodeficiency, centromeric instability, and facial anomalies 1 (ICF1) syndrome in patient 1294

After receiving the WES data, we screened the patient's variants to determine which was most likely to underly the patient's disease. Based on the inheritance pattern and level of consanguinity between the patient's parents, we hypothesized that a homozygous recessive mutation likely accounted for his disease and thus screened for variants homozygous in only the patient and not in any of his healthy family members. Synonymous variants were further filtered out, as were poor quality reads and common variants (<0.001 in queried databases), resulting in a list of twenty-seven candidate variants. The top candidates are shown in **Table 3.2** and a complete table is shown in **Appendix Table A.1**.

Table 3.2 1294 Selected Top Candidate Genes												
Genetics			Allele Frequency		Severity Prediction		Genotypes					
Gene	Position	Mutation	ExAC	gnomAD	Polyphen	CADD	P	M	F	S	B	YB
PLXNA4	Chr 7: 131878934	ENST00000359827.7: c.2743G>T, p.Val915Leu	1.52E-05	0	PoD	34	A/A	C/A	C/A	C/C	C/A	C/C
DNMT3B	Chr 20: 31387129	ENST00000328111: c.1754C>T, p.Ala585Val	0	0	PrD	34	T/T	C/T	C/T	C/T	C/C	C/T
TULP4	Chr 6: 158927641	ENST00000367097: c.4547C>T, p.Ala1516Val	4.32E-04	2.19E-04	PrD	33	T/T	C/T	C/T	T/T	C/T	C/C
TMEM232	Chr 5: 109976595	ENST00000455884: c.340G>A, p.Asp114Asn	0	7.13E-06	PoD	32	T/T	C/T	C/T	C/T	C/T	C/C
ALDH3A1	Chr 17:19641649	ENST00000457500: c.1334C>T, p.Pro445Leu	9.65E-05	4.07E-06	PrD	26.7	A/A	G/A	G/A	A/A	G/A	G/A
GNL2	Chr 1: 38048467	ENST00000373062: c.707A>G, p.His236Arg	0	0	B	16.03	C/C	T/C	T/C	T/T	T/C	C/C
ASB16	Chr 17: 42248374	ENST00000293414: c.217G>A, p.Val73Ile	0	0	B	15.76	A/A	G/A	G/A	A/A	G/A	G/A
NKAIN2	Chr 6: 125112527	ENST00000368417: c.517A>G, p.Thr173Ala	0	0	B	14.83	G/G	A/G	A/G	A/A	A/G	A/A

P= Patient; M=Mother; F=Father; S=Sister;
B=Brother; YB= Younger brother
PrD=Probably damaging; PoD= Possibly damaging;B= Benign

Reviewing the literature about these 27 candidate variants led me to conclude that the patient's variant in *DNMT3B* was most likely the cause of his disease. DNMT3B (DNA methyltransferase 3 beta) is a DNA methyltransferase important in epigenetic modification by functioning in *de novo* methylation (*348*). Mutations in *DNMT3B* are known to cause immunodeficiency, centromeric instability, and facial anomalies syndrome 1 (ICF1 syndrome), which is characterized by agammaglobulinemia with facial dysmorphism and hypomethylation of genomic DNA (*349*). While germline deletion of murine *Dnmt3b* is embryonic lethal, mice with missense mutations corresponding to those seen in ICF patients have hypomorphic DNMT3B activity and survive to term (*348*, *350*). These mice have similar morphological and immunological abnormalities as ICF patients, though they lack the characteristic agammaglobulinemia. Instead, these mice have T cells defects, which occur more rarely in human ICF patients(*350*, *351*). The proband's mutation is a C to T conversion that results in an alanine to valine substitution in the highly conserved methyltransferase motif I region (**Fig. 3.7**). This domain binds to the cofactor S-adenosylmethionine (SAM), and structural modeling reveals that the patient's mutated residue is indeed located directly in the SAM binding pocket (**Fig. 3.7B**)(*352*). Furthermore, 1294's variant has been previously been identified in verified ICF patient (*349*, *353*). Similar to PID1294, the reported patient was born from a consanguineous marriage and had agammaglobulinemia, typical ICF facial features, and growth and mental retardation (*353*). Thus, the variant appears to be pathogenic.

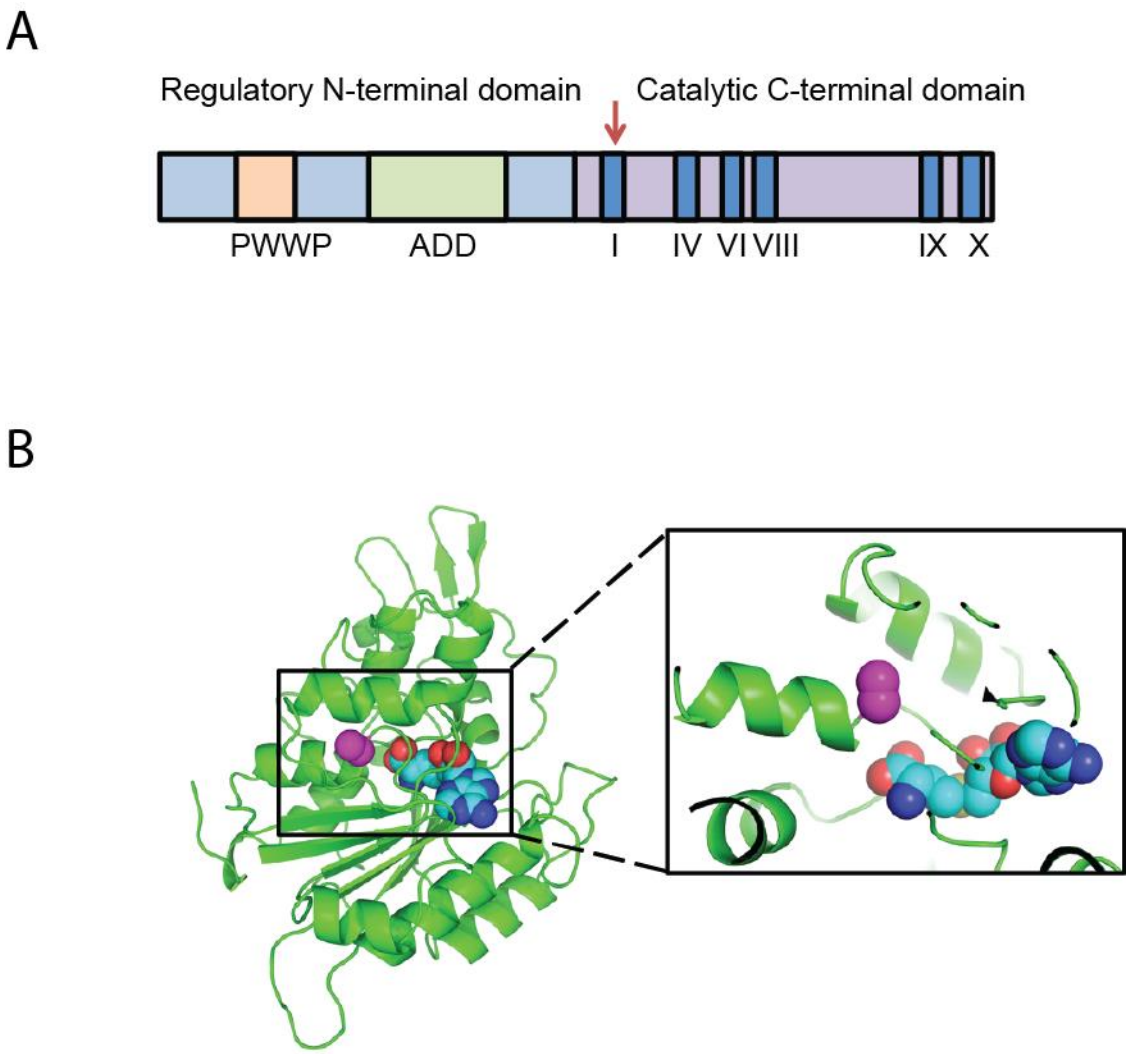


Fig. 3.7. Patient 1294 has a homozygous missense mutation within the substrate binding pocket of DNMT3B. A) Cartoon representation of DNMT3B's functional domains. The red arrow points to the site of the patient's mutation. (PWWP= PWWP domain; ADD= ATRX, DNMT3, DNMT3L domain; roman numerals= motifs I - X) **B)** Homology modeling of the catalytic SAM-dependent MTase C5-type domain of DNMT3B using PyMOL. Insert contains a zoomed in, cleaved image of the mutation site. Pink= mutation site. Blue and red spheres= S-adenosylmethionine.

Two tests were done to further verify the diagnosis of ICF syndrome: 5-methylcytosine (5-mC) staining and karyotyping. Murine embryonic stem cells (ES) with DNMT3B mutations have diminished levels of 5-mC (*348*, *354*). DNMT3B mutations in ICF syndrome patients are thought to cause hypomorphic isoforms, resulting in minimal 5-mC in satellite regions of chromosomes (*355*). PID1294's T cells similarly showed greatly reduced C-5 methylation,

supporting an ICF diagnosis (**Fig. 3.8A**). Likely due to the role of DNMT3B in methylation of centromeric minor satellites, another defining characteristic of ICF patients is structural aberrations of chromosomes 1, 16, and 9 in lymphocytes, including chromosomal branching, deletion, and stretching (*356*–*359*). Giemsa banding and spectral karyotyping (SKY) confirmed the presence of various cytogenic abnormalities in PHA-activated patient cells, especially in chromosome 1 (**Fig. 3.8B,C; Appendix Table A.2).** The patient's clinical symptoms together with the cytogenic features demonstrated are all characteristic of ICF syndrome, thus making it highly likely that the homozygous missense mutation in *DNMT3B* is the root cause of PID1294's disease.

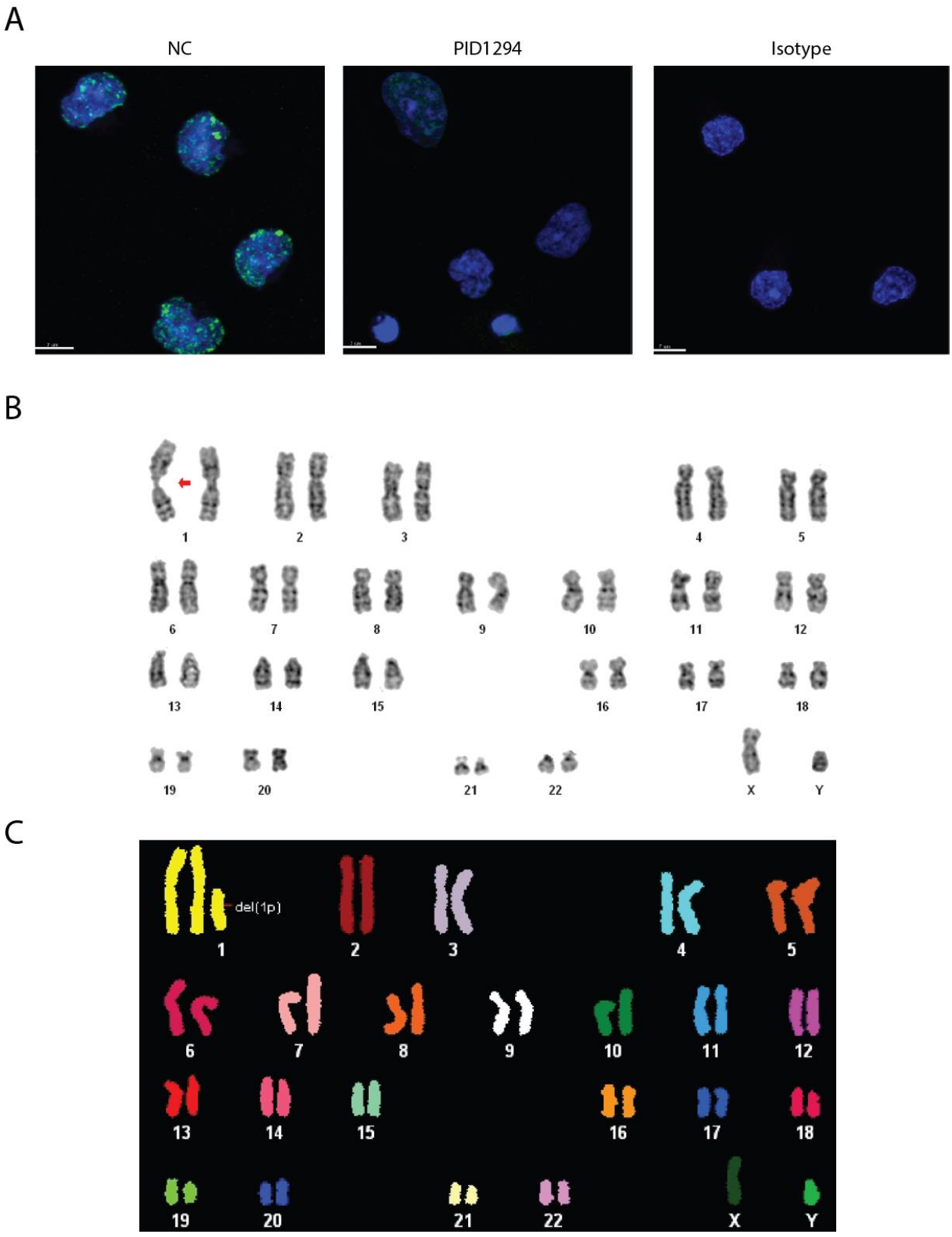


Fig. 3.8. 5-mC staining and karyotyping of activated lymphocytes from PID1294 reveal hypomethylation and aberrant cytogenic features characteristic of ICF syndrome. A) Representative images showing immunofluorescent staining of 5-mC (green) or an isotype control with DAPI as a nuclear counterstain (blue) in activated T cells. Scale bar= 7 μm. NC= normal control. **B,C)** Giemsa banding (**B)** and spectral karyotyping analysis (**C)** of metaphase-

arrested PBMCs stimulated for 4 days with phytohemagglutinin-P. Red arrow points to a stretched arm. Shown in **C** is a gain of the p arm of chromosome 1. Karyotyping shown in **B** and **C** was performed by Sandra Burkett (NCI, USA).

3.2.3 Investigation of novel TICAM2 variant as causal mutation underlying patient 1414's disease

3.2.3.1 Identification of missense mutation in TICAM2 as top candidate gene for patient 1414

After confirming ICF syndrome in PID1294, I then worked to identify the causative gene underlying the disease of another PID patient in our cohort. PID1414 was born from consanguineous Turkish parents (**Fig. 3.9A**) and presented at 4 months of age with recurrent pneumonia (**Table 3.3)**. The patient has also had transient proteinuria and lymphopenia, mild hypogammaglobulinemia, and a congenital heart defect. After his referral to the NIH from Marmara University, we sent genomic DNA from PID1414 and his immediate family (excluding his infant brother, 1418) for WES.

Table 3.3. Clinical presentation of PID1414	
Lymphadenopathy?	No
Splenomegaly?	No
Hematologic abnormalities?	• Transient lymphopenia (CD3+) (resolved) • Hypogammaglobulinemia (IgG)
Autoimmunity or autoinflammatory disease?	No
Immunodeficiency or susceptibility to infection?	Recurrent pneumonia
Other	• Proteinuria (transient) • Congenital heart disease • Interstitial pattern of lung

Because the high level of consanguinity between the patient's parents, we focused on variants that fit a homozygous recessive model while screening for candidates. Variants were

further filtered for quality and rarity (<0.001 in all tested genomic databases), leading to a group of 36 genes (**Appendix Table A.3)**, with an abbreviated list shown in **Table 3.4.** Though there were several strong candidates, I chose to focus on the patient's *TICAM2*/*TMED7-TICAM2* variant for multiple reasons. First, out of the patient's eleven homozygous variants that have a CADD score over 20, literature searches suggest that nine are not involved in the immune system. *GRM2* (Glutamate metabotropic receptor 2*)*, *SCN11A* (Sodium channel, voltage-gated, type XI, alpha subunit), and *PPP1R9A* (Protein phosphatase 1, regulatory subunit 9A), for example, are expressed mostly in the nervous system, and *PLEKHH2* (Pleckstrin homology domain-containing protein, family H, member 2) is expressed in kidneys (*360–363*). Several of these genes are also already associated with monogenic diseases. For example, homozygous recessive LOF mutations in the tooth-restricted gene *ENAM* (Enamelin) cause local hypoplastic amelogenesis imperfecta and class II anterior open bite malocclusion (*364*); patients with homozygous missense mutations in *AK7* [Adenylate kinase 7] have infertility and no reported lung issues (*365*). Knockout mouse models of *GRM2, AK7, SCN11A,* and *ENAM* do not display immune defects (*366–370*).

TICAM2 and *EOMES* (Eomesodermin), on the other hand, do have known immunological functions. I chose to focus on *TICAM2* instead of *EOMES* for two reasons. First, *EOMES* is known to be important in T cell activity, particularly in effector functions and memory development in CD8 T cells (*371–373*). However, PID1414 primarily has respiratory infections and not the increased susceptibility to intracellular and viral pathogens that one would expect to accompany defective CD8 T cell activity (**Table 3.3**). Additionally, the patient has shown clinical improvement as he ages: his lymphocyte subsets and serum immunoglobulins have normalized, and he has had no significant infections in the past few years at the time of writing. This is similar to other diseases caused by genetic lesions in PRR

signaling, which typically result in vulnerability to a very narrow set of pathogens at only certain periods of life, as discussed in **Chapter 1**. Mutations in TLR3, for example, cause susceptibility primarily to herpes simplex virus infections in the brain during childhood (*374*). Additionally, while homozygous knockout of *Eomes* in mice is embryonic lethal, conditional deletion in the brain results in microcephaly and behavioral defects (*375*, *376*). An autosomal recessive microcephaly has also been attributed to a translocation resulting in *EOMES* silencing in human patients, supporting the role of EOMES in brain development (*377*). *Ticam2* knockout mice, on the other hand, have no reported defects except for increased susceptibility to Severe Acute Respiratory Syndrome coronavirus (SARS-CoV) and defective TLR signaling *in vitro* (*51*, *378*). Thus, a TICAM2 deficiency seems to be more consistent with the patient's clinical presentation than loss of EOMES based on known literature.

Table 3.4 Abbreviated homozygous recessive candidates for patient 1414										
Genetics			**Allele Frequency**		**Severity Prediction**		**Genotypes**			
Gene	Position	Mutation	ExAC	gnomAD	Polyphen	CADD	1414	1415	1416	1417
GRM2	Chr 3: 185155301	ENST00000395052: c.1103G>A, p.Arg368Gln	1.16E-04	1.63E-05	B	34	T/T	C/T	C/T	C/T
AK7	Chr 14: 96864440	ENST00000267584: c.134C>T, p.Ser45Leu	4.50E-05	1.63E-05	PrD	34	T/T	C/T	C/T	C/T
KCNK10	Chr 14: 88652306	ENST00000319231: c1205G>A., p.Arg402His	6.06E-05	8.13E-06	PrD	33	T/T	C/T	C/T	C/T
SCN11A	Chr 3: 38936100	ENST00000302328: c.2759C>T, p.Ala920Val	1.73E-04	6.50E-05	PoD	31	A/A	G/A	G/A	G/A
ENTPD3	Chr 3: 40456270	ENST00000301825: c.536G>A , p.Gly179Glu	1.50E-05	8.13E-06	PrD	28.2	A/A	G/A	G/A	G/A
TMED7-TICAM2, TICAM2	Chr 5: 114916458	ENST00000282382: c.1003A>C, p.Lys335Gln	0.00E+00	0.00E+00	PrD	28.2	G/G	T/G	T/G	T/G
MCF2L2	Chr 3: 183027551	ENST00000328913: c.1066G>A, p.Val356Met	1.05E-04	4.47E-05	PrD	26.2	T/T	C/T	C/T	C/T
ENAM	Chr 4: 71503556	ENST00000396073: c.584G>C, p.Gly195Ala	9.61E-05	3.66E-05	PrD	23.7	C/C	G/C	G/C	G/C
PPP1R9A	Chr 7: 94827760	ENST00000433360: c.1854A>C, p.Glu618Asp	0.00E+00	0.00E+00	PrD	23.5	C/C	A/C	A/C	A/A
PLEKHH2	Chr 2: 43934658	ENST00000282406: c.1940C>T, p.Pro647Leu	3.63E-04	4.88E-05	PoD	22.7	T/T	C/T	C/T	C/T
EOMES	Chr 3: 27758892	ENST00000295743: c.1730G>A, p.Gly577Asp	0.00E+00	0.00E+00	B	20.5	T/T	C/T	C/T	C/T

PrD=Probably damaging; PoD= Possibly damaging; B=Benign

PID1414's *TICAM2* variant has an adenosine to cytosine conversion that results in a lysine to glutamine missense mutation (K166 in TICAM2 and K335 in TMED7-TICAM2) in the TIR domain (**Fig. 3.9B,C**). While this mutation is not located in the known TICAM1-binding sites (the "TS" site [Thr155 and Ser156] and the "EDD" site [Glu87, Asp88, and Asp89]), it is predicted to be damaging from most tested protein prediction software, with a CADD score of 28.2 (**Table 3.4**)(*379*). TMED7-TICAM2 is a read-though of *TMED7* (transmembrane emp24 protein transport domain containing 7) into *TICAM2.* The resulting fusion protein, referred to as TAG (TRAM adaptor with GOLD [Golgi dynamics] domain), is thought to negatively regulate TICAM2 (*380*, *381*). TICAM2 itself is a scaffold protein that serves as an essential adaptor between TLR4 and TICAM1 that allows for propagation of the TICAM1 signaling cascade (*382*–*384*). As TICAM2 is more highly expressed than TAG and is an important component of TLR signaling, I investigated whether the patient's TICAM2 variant underlies his disease (*381*).

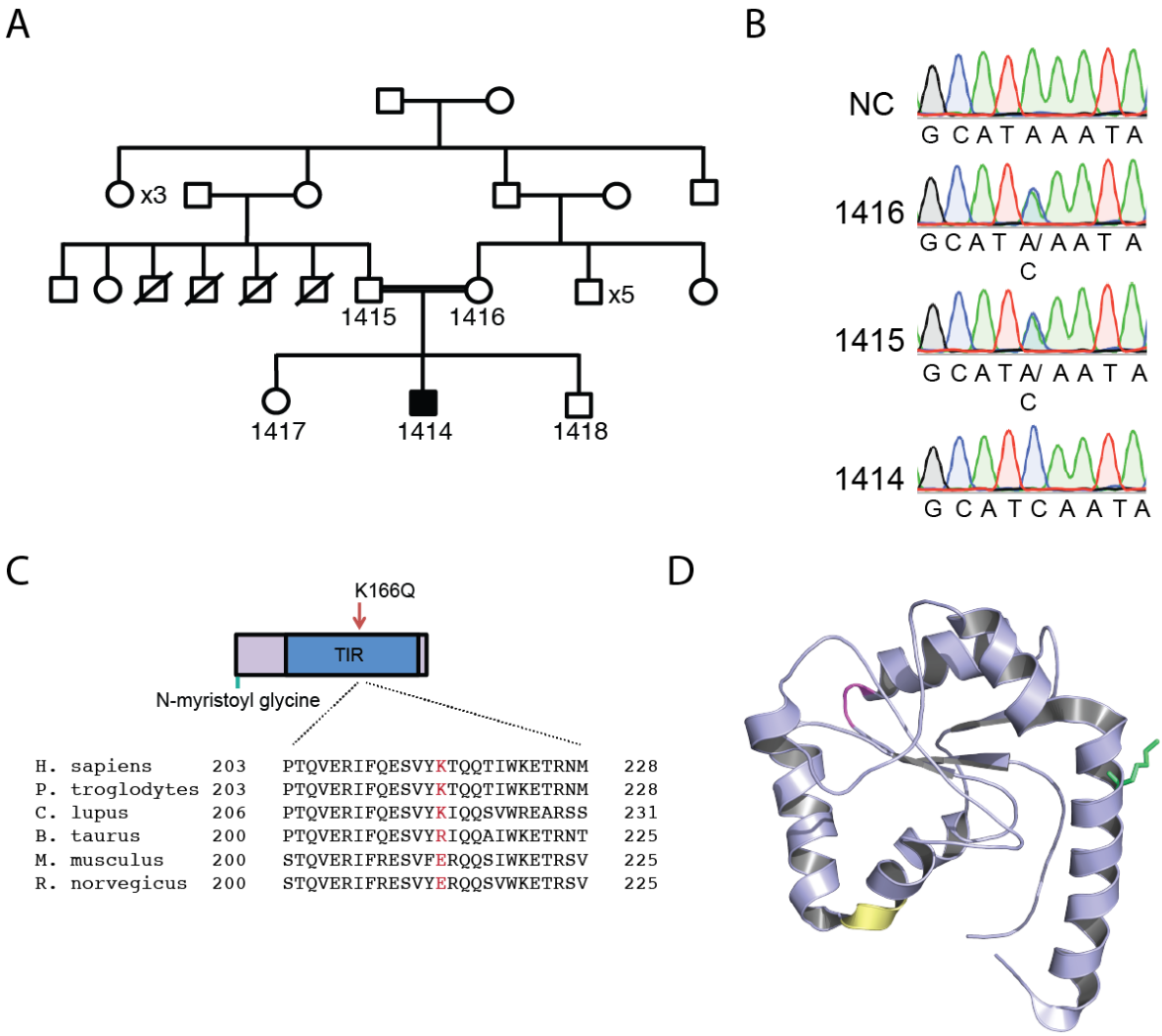


Fig. 3.9. Patient 1414 has a homozygous missense mutation in the TIR domain of TICAM2. **A)** Pedigree of PID1414**.** The proband is shaded in black. A double line represents a consanguineous relationship. Circles= females; squares= males. **B)** Sanger sequencing of PCR product amplified from genomic DNA of the patient, his parents, and a normal control. **C)** Diagram of TICAM2's structure with an arrow showing the location of the patient's missense mutation (K166Q) and sequence alignment from HomoloGene of TICAM2 from several species showing conservation of sequence. **D**) A PyMOL visualization of the TIR domain of TICAM2 (PDB accession code TM1W(*379*)) with K166 in green, the TS site [Thr155 and Ser156] shown in magneta, and the EDD site [Glu87, Asp88, and Asp89][TS and EDD sites described in (*379*)]. NC= normal control; TIR= Toll/Interleukin-1 receptor domain

3.2.2.2 Investigation of the functional activity of TICAM2^{K166Q}

To verify which PBMC cell type has the highest levels of TICAM2, I determined the relative expression of *TICAM2* in different cell population using RT-PCR. *TICAM2* was most

greatly expressed in monocytes and pan-dendritic cells (mixed myeloid and plasmacytoid). (**Fig. 3.10)**. Because monocytes constitute a larger fraction of cells in blood than dendritic cells, I used patient monocytes to investigate TICAM2 function *ex vivo*.

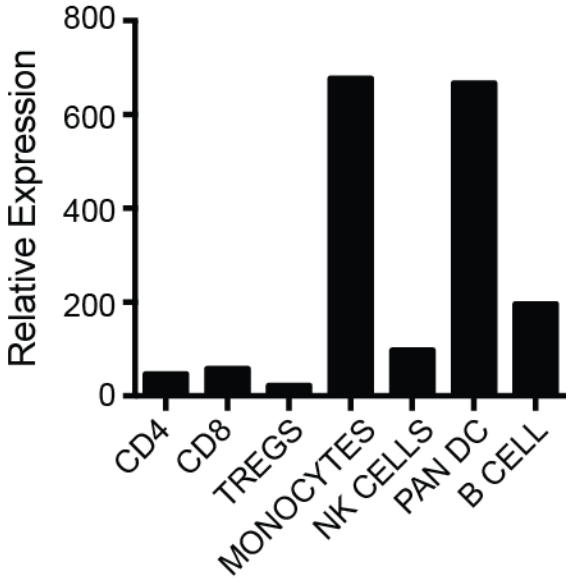


Fig. 3.10. Monocytes and dendritic cells express high transcriptional levels of *TICAM2*. Transcript levels of *TICAM2* in cell populations enriched from a normal control buffy coat using Miltenyi kits. ΔΔCT was determined using GAPDH as a housekeeping gene. Relative expression was determined by normalizing to Tregs, which were set at 1. Treg= regulatory T cell; NK= natural killer cell; DC= dendritic cell

Similar to MyD88, TICAM1 signaling results in pro-inflammatory cytokine secretion; however, the TICAM1 pathway also induces expression of type I IFNs and associated IFN-inducible genes (*385*). Demonstrating the importance of TICAM2 in TLR4 signaling, macrophages from *Ticam2* knockout mice showed reduced production of pro-inflammatory cytokines after LPS stimulation(*51*). Because I hypothesized that the patient's missense mutation results in a LOF TICAM2 variant, I enriched PBMCs for $CD14^+$ monocytes (**Fig. 3.11A,B)** and stimulated them with LPS to examine cytokine production as a readout for TICAM2 function. Purity of the enriched populations was low and highly variable (**Fig. 3.11B**).

However, though PID1414's cultures had the second highest amount of monocytes, his cells produced the lowest levels of IL-6 and TNF-α in the 24 hours following stimulation (**Fig. 3.11C,D)**. This result is consistent with defective TLR4 responses. However, results from RT-PCR of the enriched cells were less clear. Transcription levels of TNF-α, IL-1β, and IFN-β three hours after LPS stimulation varied greatly between controls, and patient cells upregulated these genes at levels consistent with controls (**Fig. 3.11E-G**). Patient monocytes had normal levels of TLR4 (**Fig. 3.11H)**, suggesting that differences in TLR4 expression do not account for the observed variability between responses.

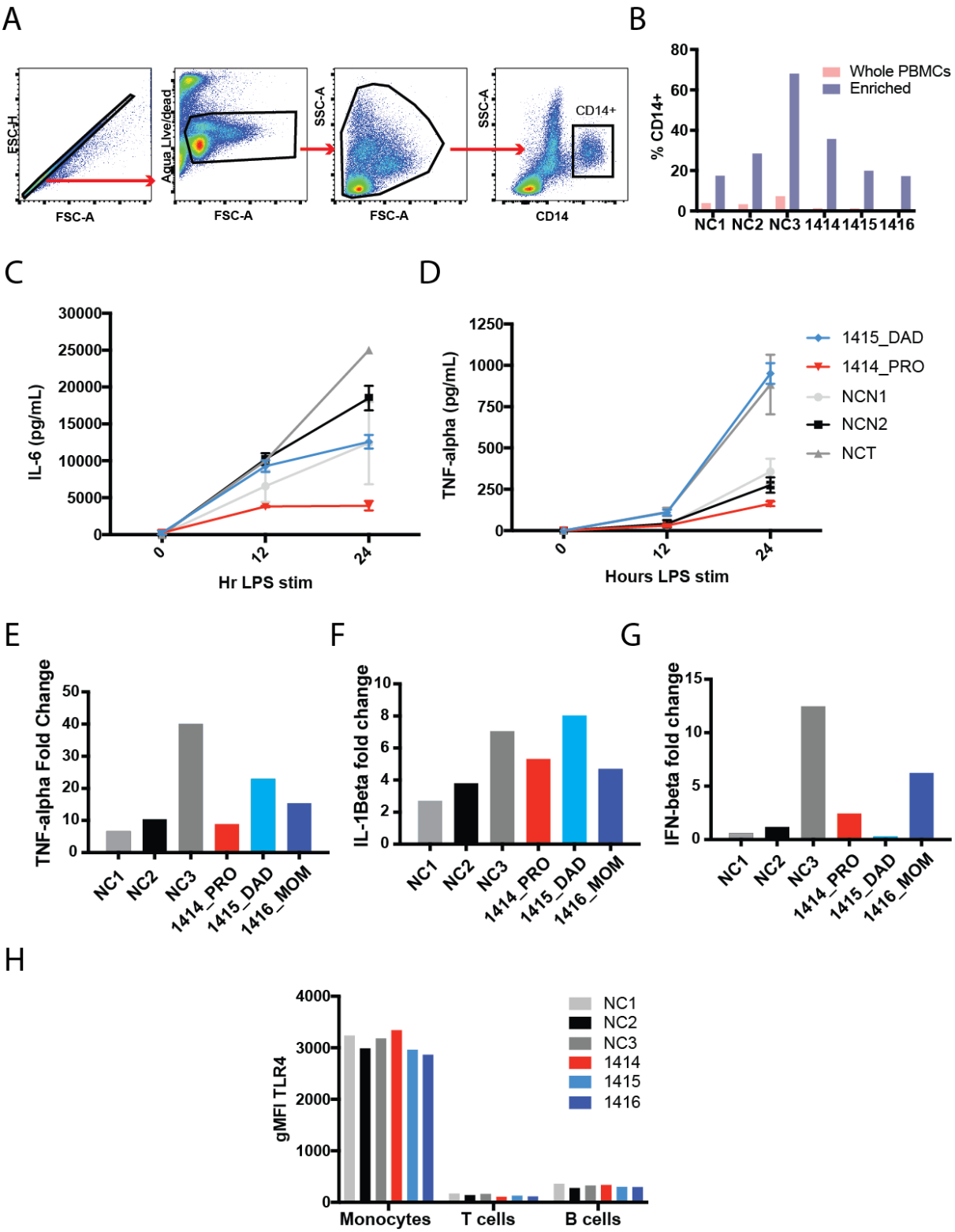


Fig. 3.11. Patient 1414 has reduced secretion of inflammatory cytokines following LPS stimulation. Whole PBMCs were enriched for CD14⁺ monocytes using the EasySep Human Monocyte Enrichment kit. **A, B)** Purity of the monocyte enrichment was assessed by staining for cell populations according to the gating strategy in **A** and quantified in **B** as percent of CD14⁺ cells in the total live cells. **C, D)** Enrichment monocytes were stimulated with 1 µg/mL of LPS, and supernatants were taken after 12 and 24 hours of stimulation and IL-6 **(C)** and

TNF-α (**D)** secretion was determined by ELISA. Shown are technical triplicates. **E-G**) mRNA levels of TNF-α (**E**), IL-1β (**F**), and IFN-β (**G**) were determined by RT-PCR from enriched monocytes stimulated with 1 ug/mL of LPS for 3 hours. Fold change was calculated as $2^{-\Delta\Delta CT}$ using *GAPDH* as a reference gene. **H)** Surface TLR4 levels were measured by flow cytometry as gated upon in **A**.

To further investigate the response of patient cells to LPS, I also analyzed cytokine production using intracellular cytokine staining (ICS). After 9 hours of LPS stimulation (**Fig. 3.12)**, the patient had only slightly fewer TNF-α^+ monocytes than controls (**Fig. 3.12B,C).** More striking was the reduction in IL-6 producing cells: less than 30% of patient monocytes were IL-6^+, compared to an average of 70% in controls (**Fig. 3.12B,D).** Similarly, patient monocytes upregulated IL-10 more poorly than controls (**Fig. 3.12E)**. Together, these results further support a potential defect in TLR4 signaling.

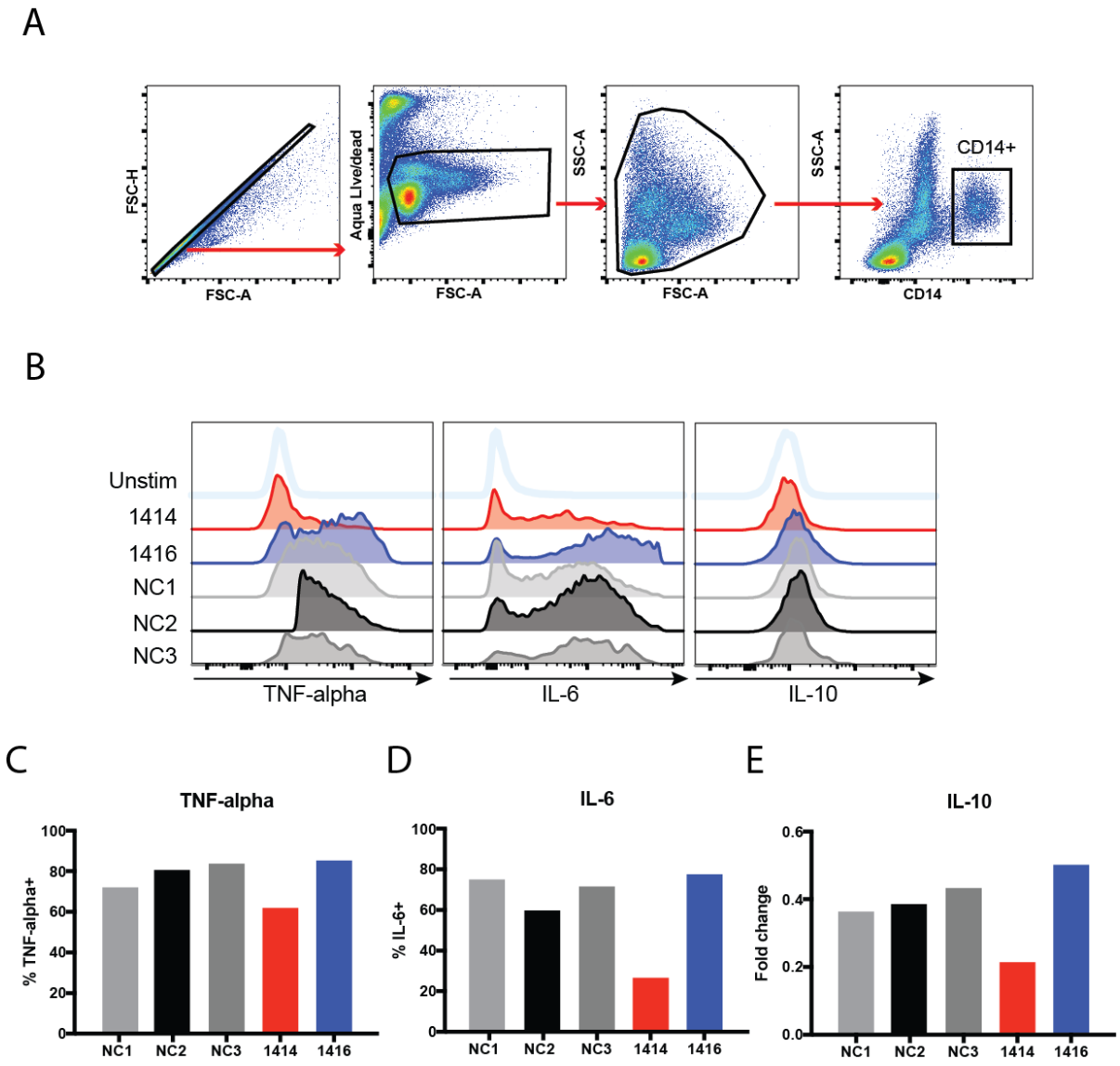


Fig. 3.12. Patient 1414 has reduced cytokine production following LPS stimulation. Whole PBMCs were stimulated for 9 hours with 1 μg/mL of LPS before brefeldin A treatment, intracellular cytokine staining, and flow cytometric analysis. **A)** Gating strategy showing the staining of $CD14^{+}$ monocytes. **B)** Flow diagrams showing levels of the indicated cytokines in $CD14^{+}$ monocytes. **C, D**) Quantification of the percent of monocytes that were TNF-α^{+} or IL-6^{+}. **E**) IL-10 levels were expressed as fold change, which was quantified as ([$gMFI_{Unstim}$-$gMFI_{stim}$]/$gMFI_{Unstim}$.

Due to the inconclusive results from the above assays as well as difficulties receiving patient samples, I utilized an *in vitro* technique to assess the functionality of the patient's TICAM2 variant ($TICAM2^{K166Q}$) in a cleaner system. Luciferase assays are a commonly employed tool to quantitatively measure gene expression. The assay works by placing the

firefly luciferase gene downstream of the gene of interest's regulatory region; binding of the target's promoter region will thus lead to transcription of luciferase. When the luciferin substrate is added to cell lysates, quantifiable bioluminescence is produced at levels correlating to the amount of luciferase transcribed (*328*). The ability of TICAM2^{K166Q} to propagate downstream signaling can thus be assessed by co-expression of a TICAM2 overexpression vector and a vector containing luciferase under the control of either the *IFNB1* promoter or NF-κB responsive elements.

Previously published *in vitro* experiments demonstrated that mutagenesis of key residues of TICAM2 results in a loss of protein function. TICAM2 is myristoylated at its position 2 glycine; TICAM2 becomes mislocalized and does not propagate the TICAM1 signaling cascade without this myristoylation (*386*). On the other hand, TICAM2^{C117H} is properly localized but is unable to form the homodimers or TICAM1 heterodimers necessary for its function (*387*). TICAM2^{G2A} and TICAM2^{C117H} were thus used as LOF controls (**Fig. 3.13A**). 293T cells express little to no *TICAM2* (**Fig. 3.13B**), and thus were used in the *in vitro* assay. As reported in the literature, transfection of TICAM2 alone resulted in negligible levels of IFN-β expression(*387*). Conversely, expression of TICAM1 alone was capable of promoting IFN-β production, and this was amplified upon addition of TICAM2 (**Fig. 3.13C**). As expected, NF-κB and IFN-β activity were highly induced upon co-expression of TICAM1 with WT TICAM2 and largely suppressed by expression with the negative controls (**Fig. 3.13D,E**). Strikingly, the patient's variant, TICAM2^{K166Q}, showed a level of NF-κB and IFN-β activity similar, if not even further reduced, than that of the null isoforms. Lysine is a positively charged amino acid that is often used to make salt bridges, whereas glutamine is polar and uncharged, leading us to hypothesize that the K166Q mutation may affect TICAM2 stability or its binding to another protein. This potential binding partner is unlikely to be TICAM1 since the mutation is on the

opposite side of TICAM2 as the known TICAM1 binding domains (*379*) (**Fig. 3.9).** Alternatively, while the acetylation state of K166 is unknown, lysines are often post-translationally modified. Glutamine can both neutralize electric charge and act as a mimic for lysine acetylation, which could also affect binding to interacting partners. I thus suggest that TICAM2^{K166Q} is indeed a deleterious variant of TICAM2 with reduced capability to propagate proper downstream signaling cascades.

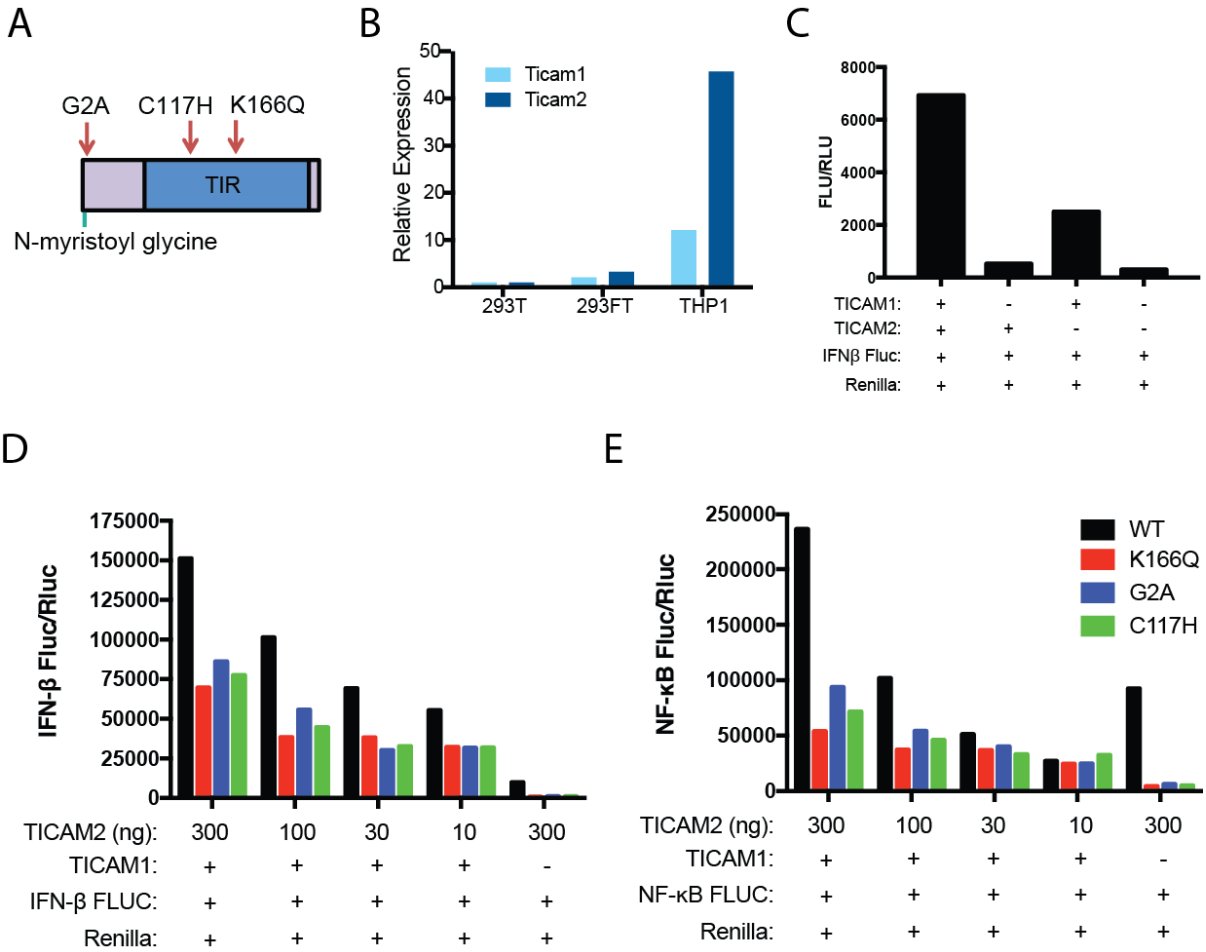


Fig. 3.13. TICAM2^{K166Q} has reduced ability to promote NF-κB and IFN-β signaling. A) Diagram showing the location of the cloned TICAM2 constructs. **B)** RT-PCR of transcripts of *TICAM1* and *TICAM2* in cell lines. GAPDH was used as a housekeeping gene to determine DDCT, and relative expression was determined by normalizing to transcript levels in 293T cells, which were set at 1. **C)** Normalized luciferase activity driven by the *IFNB1* promoter. 293T cells were transfected with 300 ng of expression plasmids containing TICAM1 (pCDNA3-TRIF-CFP) and/or WT TICAM2 (pEF-Bos TRAM Flag), as well as 300 ng of firefly luciferase reporter plasmid under the control of the human IFN-β promoter (IFNB-pGL3), and 30 ng of a

constitutively expressing *Renilla* luciferase plasmid (pRL-TK). **D, E**) Normalized luciferase activity driven by the *IFNB1* promoter (**D)** or NF-κb response element (**E)** when 293T cells were transfected with the luciferase reporter plasmids, 300 ng of pCDNA3-TRIF-CFP, and the indicated amounts of overexpression plasmid containing $TICAM2^{WT}$, $TICAM2^{K166Q}$, $TICAM2^{G2A}$, or $TICAM2^{C117H}$. Data shown in D, E is representative of two independent experiments. Fluc= firefly luciferase; Rluc= *Renilla* luciferase

At the time of PID1414's referral to the NIH, his younger brother (PID1418) was a newborn and thus was not included in genomic sequencing. However, within a year, he had a severe respiratory infection requiring hospitalization. While still too young to be definitively categorized as a PID patient, we suspect him of having a similar disease as his older brother. As such, we checked whether PID1418 had the *TICAM2* variant as PID1414. However, PID1418 was actually homozygous for the wildtype allele (**Fig. 3.14**). While PID1414 does have some reduced cytokine production after LPS stimulation, some of his responses also seemed to be within the normal range. Conversely, *Ticam2* knockout mice have very clearly abrogated TLR signaling(*51*). While preliminary *in vitro* experiments suggested that $TICAM2^{K166Q}$ does have reduced function compared to wildtype protein, it is uncertain whether this defect is sufficient to have caused the patient's disease. As the potentially affected brother does not share PID1414's *TICAM2* allele, I believe it unlikely that the patient's *TICAM2* variant is the primary driver of his disease. Therefore, sequencing the brother will be important to identify shared genotypes that might be responsible for the brothers' phenotypes. Because the other candidate genes were of specific interest to other members of the Lenardo lab, I decided to focus my work instead on a newly identified cohort of PID patients with mutations in *GIMAP5.*

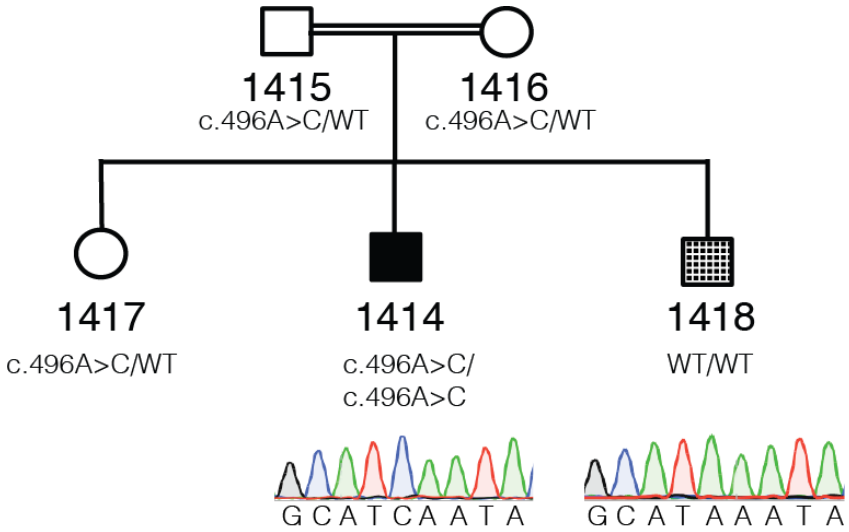


Fig. 3.14. 1418, the brother of PID1414, is suspected of having a primary immunodeficiency and is wildtype for *TICAM2*. Pedigree of PID1414's family. Genotypes of at position 496 of the *TICAM2* coding sequence is displayed below each family member. Chromatograms from Sanger sequencing of 1414 and 1418 are displayed below the representation of each respective brother. A double line represents a consanguineous relationship. Circles= females; squares= males. Black= clinical phenotype; Checkered= suspected of displaying clinical phenotype.

3.2.3 Inherited disease caused by mutations in GIMAP5, a lysosomal protein with a possible role in metabolism

3.2.3.1 GIMAP5 is localized to lysosomes, endosomes, and autophagosomes

Michael Leney-Greene, a doctoral student in Dr. Michael Lenardo's group, discovered affected members of a large consanguineous Turkish family (Family 1 in **Fig. 3.15A)** shared a homozygous mutation in GTPase of the immunity-associated protein 5 (GIMAP5) that resulted in a loss of protein. Later, he confirmed that affected individuals in three other families had similar homozygous or compound heterozygous missense mutations in GIMAP5 that clustered in the conserved GTPase and alpha-6-helix domains (**Fig. 3.15A,B)**. No unaffected family members had a loss of both wildtype *GIMAP5* alleles, providing strong genetic evidence that GIMAP5 deficiency is a novel PID. While there was some variation in

clinical symptoms, all patients presented with splenomegaly and lymphopenia (**Table 3.5)**. Interestingly, several patients also presented with severe liver disease, which was the ultimate cause of mortality for three patients.

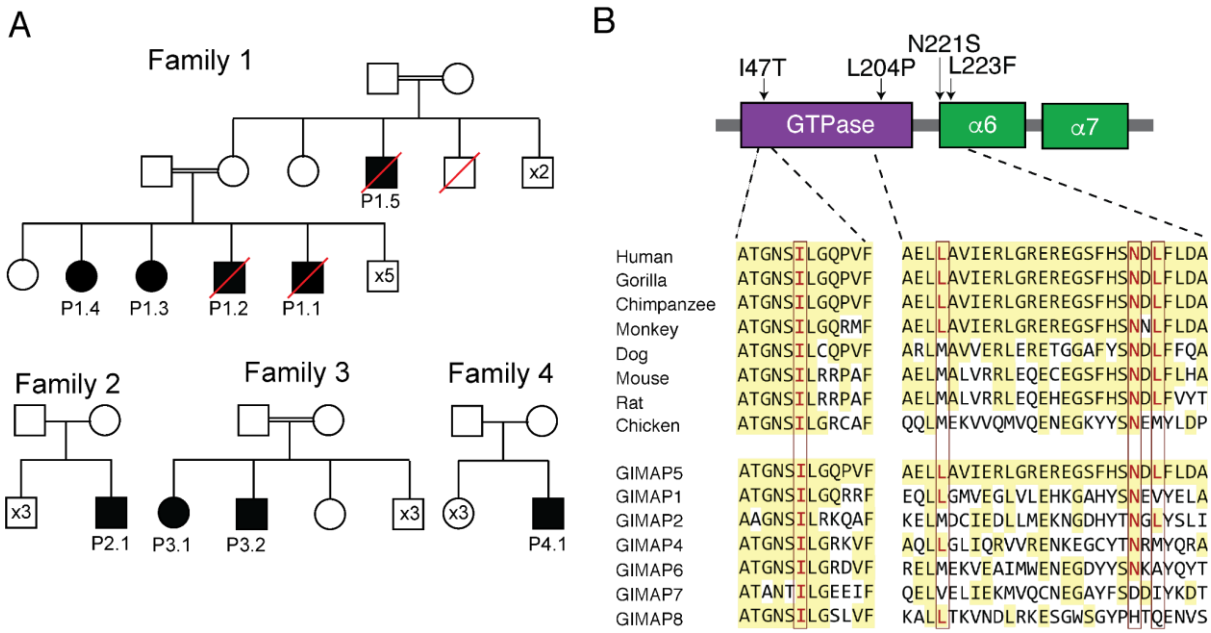


Fig. 3.15 Patients from multiple pedigrees have homozygous or compound heterozygous missense mutations in conserved regions of GIMAP5. A) Pedigrees of families with GIMAP5 mutations. Affected patients are shaded in black. A double line represents a consanguineous relationship. A red slash represents a deceased family member. Circles= females; squares= males. **B)** Schematic diagram of GIMAP5, showing the GTPase, alpha helix 6, and alpha helix 7 domains. Locations of missense mutations identified in patients are identified by arrows. Sequence alignment of GIMAP5 in multiple species (above) and between members of the human GIMAP family members (below) are shown, with yellow highlights showing amino acids conserved between human GIMAP5 and the other sequences. Boxes show the site of the patients' missense mutations, with red letters showing conservation of amino acids.

Table 3.5 Clinical presentation of patient cohort									
Patient	P1.1	P1.2	P1.3	P1.4	P1.5	P2.1	P3.1	P3.2	P4.1
Demographics	Died at 17 yo, Male	Died at 22 yo, Male	27 yo Female	29 yo female	Died at 44 yo, Male	16 yo Male	20 yo Female	22 yo Male	5 yo Male
IMMUNODYSREGULATION									
Splenomegaly	Y	Y	Y	Y	Y	Y	Y	Y	Y
Lympadenopathy	Y	Y		Y	Y	Y	Y		
Lung infections	Y, diffuse bronchiectasis	Y, focal bronchiectasis, atelectasis, ground glass opacities & infiltration	Y, Focal bronchiectasis, peribronchial thickening	Y, consolidation at left lung	Y, focal bronchiectasis	Y, ground glass changes & nodular pulmonary infiltrates	Y, chronic fibrotic changes	Not tested	Not tested
IMMUNOLOGY LABS									
Lymphopenia	↓T, B, Neutrophil	↓T, B, Neutrophils	↓Lymphocyte count	↓T, B cells	↓T, Neutrophils	↓Lymphocyte count	↓Lymphocytes	↓Lymphocytes	
Dysgammaglobul-inemia	IgG-, IgA-, IGM: N	IgG:N, IgA:N, IgM: N	IgG-, IgA:N, IgM:N	IgG:N, IgA:N, IgM:N	IgG:N, IgA:N, IgM:N	IgG-, IgA-, IgM-	IgG-, IgA:N, IgM:N	IgG:N, IgA:N, IgM:N	IgG:N, IgA-, IgM-
Autoantibodies	Anti-thrombocyte antibodies	-	-	-	ANA(+)	Anti-thrombocyte, neutrophil antibodies	-	-	-
OTHER									
Liver Disease	↑Transaminases, Esophageal varices	↑Transaminases, Esophageal varices, ascites	ND	ND	↑Transaminases, Esophageal varices, hepatocellular carcinoma	↑Transaminases	↑Transaminases, Esophageal varices	↑Transaminases, Esophageal varices	Yes

Y=Yes; ND= not determined; N=Normal. Modified from Leney-Greene et al. (manuscript in preparation); ANA= anti-nuclear antibodies; yo= year old

Since the discovery that a *Gimap5* mutation caused lymphopenia in the Bio-Breeding rat, GIMAP5 has been the most-well studied member of the GIMAP family and has been linked to immune deficiencies in both rats and mice (*388–391*). However, the cellular localization of GIMAP5 has been widely disputed in the past, with some purporting it to be in the mitochondria, ER, Golgi complex, centrosomes, or, more recently, lysosomes (*327*, *392–395*). Therefore, I verified the localization of endogenous human GIMAP5 in primary T cells by using microscopy to determine its colocalization with markers for lysosomes (LAMP1) or mitochondria (Mitotracker) (**Fig. 3.16)**. The mean Pearson's coefficient (PC) for GIMAP5 and LAMP1 was 0.716, indicating strong colocalization; conversely, the PC for GIMAP5 and Mitotracker was 0.055, suggesting no colocalization (**Fig. 3.16B).** Thus, the majority of GIMAP5 in human T cells is located in LAMP1^{+} lysosomes.

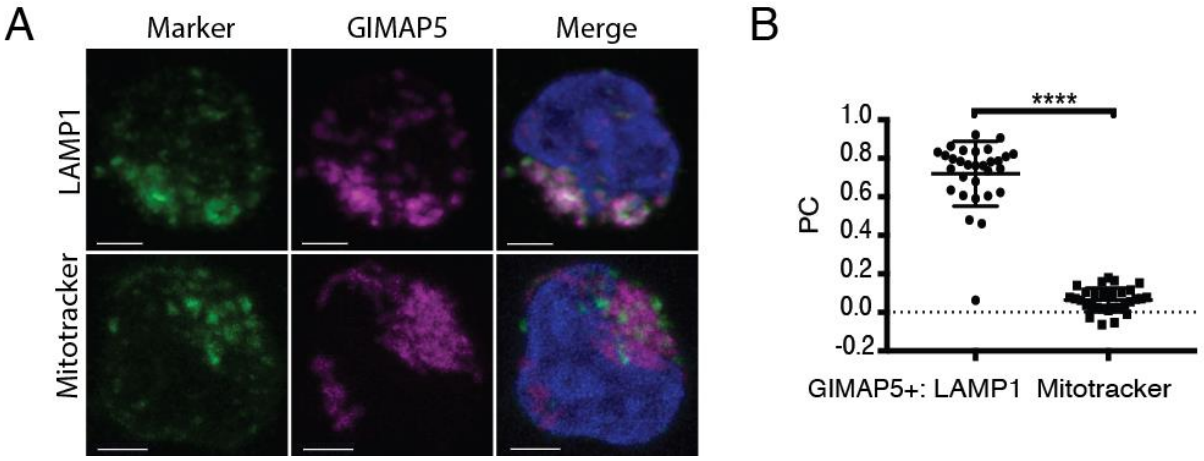


Fig. 3.16 GIMAP5 colocalizes with LAMP1 and not with Mitotracker in human T cell blasts. A) Representative images showing Z-stacks of immunofluorescent staining of GIMAP5 with markers for the mitochondria (Mitotracker) or lysosome (LAMP1) in human T cells that were activated from whole PBMCs with anti-CD3/CD28 and cultured in IL-2. DAPI (blue) was used as a nuclear counterstain in the merged image. Quantification of the colocalization of GIMAP5 with the two markers in **A** are shown in **B.** Data are representative of three independent experiments showing mean ± SD of Pearson's correlation coefficient in 10-30 cells. ****p < 0.001 (Mann-Whitney). Scale bar=2 μm. PC=Pearson's coefficient of colocalized volume

GIMAP5's localization suggests to us that it might be involved in lysosomal function. One potential binding partner identified from co-immunoprecipation/mass spectrometry of overexpressed GIMAP5 in Jurkat cells (Leney-Greene, data not shown) was RAB7, a small GTPase involved in lysosomal trafficking and fusion (*396*). RAB7's interaction with GIMAP5 was verified by co-immunoprecipitation in an overexpression model by Ann Park (data not shown). As such, we looked at whether GIMAP5 is expressed in $RAB7^{+}$ vesicles, which include late endosomes, mature autophagosomes, and endolysosomes (*396*). Confocal microscopy of human T cell blasts confirmed that GIMAP5 does indeed colocalize with RAB7 (**Fig. 3.17A; PC=0.399)**. GIMAP5 colocalized equally as strongly with LC3 as with RAB7 (**Fig. 3.17C,D**), suggesting that GIMAP5 may also be localized to autophagosomes and/or autophagolysosomes. However, PC scores indicate that GIMAP5 colocalize more strongly with LAMP1 than RAB7 or LC3 **(Fig. 3.17)**, confirming that GIMAP5 is present primarily on lysosomes.

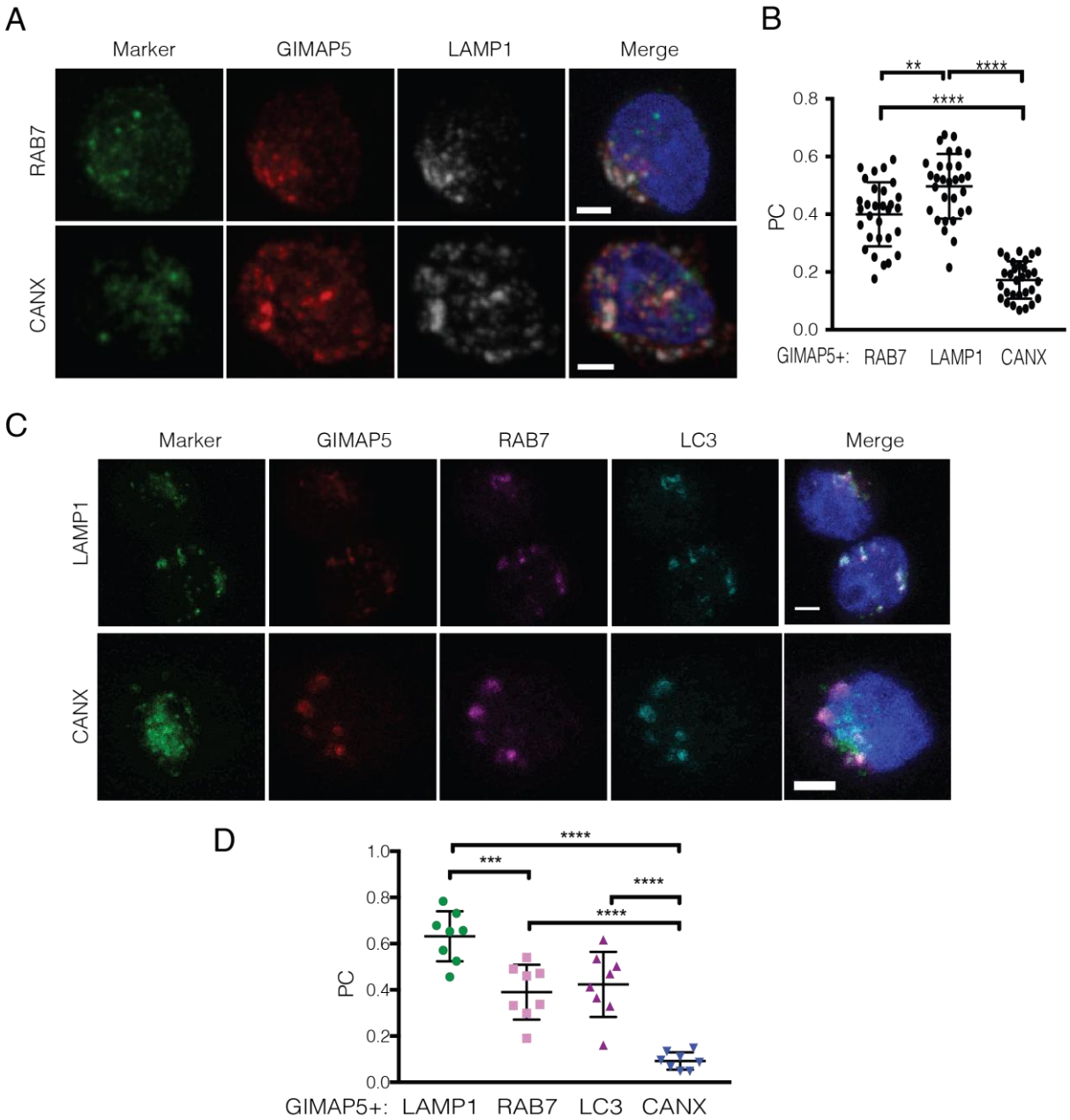


Fig.3.17 GIMAP5 colocalizes in RAB7$^+$ and LC3$^+$ vesicles. A) Representative images of Z-stacks showing immunofluorescent staining of GIMAP5 with markers for lysosome (LAMP1, white) and the ER (calnexin [CANX], green in bottom panel) or for RAB7 (green, upper panel) in blasting human T cells. DAPI (blue) was used as a nuclear counterstain in the merged image. **B)** Quantification of the colocalization of GIMAP5 with the markers in **A.** Data is pooled from three independent experiments showing mean ± SD of Pearson's correlation coefficient in a total of 30 cells. **C)** Representative images showing Z-stacks of immunofluorescent staining of GIMAP5 with markers for lysosome (LAMP1, green, top panel) or the ER (calnexin [CANX], green in bottom panel) and GIMAP5 (red), RAB7 (magenta), and LC3 (cyan). **D)** Quantification of the colocalization of GIMAP5 with the markers in **D.** Data shown is representative of three independent experiments showing mean ± SD of Pearson's correlation coefficient in 8 fields of view. **P<0.01; ***P<0.005;****P< 0.001 (Mann-Whitney). Scale bar=2.5 μm. PC=Pearson's coefficient of colocalized volume.

3.2.3.2 Investigation of the role of GIMAP5 in lysosomal function

Colocalization of GIMAP5 with RAB7^{+} and LC3^{+} vesicles suggests that GIMAP5 may be involved in the endocytic or autophagic pathways. RAB7 is known to have an important role in autophagy, and knockout of *Rab7* in murine T cells results in defective autophagosome degradation as well as lymphopenia (*194*, *397*). As *Gimap5* knockout mice are also severely lymphopenic, we examined autophagy in T cells in *Gimap5*^{Sphinx} (sphinx) mice, which have a N-ethyl-N-nitrosourea (ENU)-induced missense mutation in *Gimap5* (*390*, *391*). Because sphinx mice have very few circulating CD8 T cells, we instead looked at basal autophagy in CD4 T cells(**Fig. 3.18)**. To determine the rate of autophagy, cells were treated with the autophagy inhibitor Bafilomycin A1, a lysosomal inhibitor that prevents lysosomal acidification and autophagosome-lysosome fusion (*398*, *399*). Comparison of cells treated with vehicle to those treated with bafilomycin allows for determination of autophagic flux. Using confocal microscopy, I identified LC3^{+} puncta, which are indicative of autophagosomes, and observed a greater number of puncta on average in both treated and untreated sphinx cells compared to controls (**Fig. 3.18B)**. However, sphinx cells had normal autophagic flux (**Fig. 3.18C**), suggesting while there may be an increase in autophagosome number, there is no difference autophagic rate.

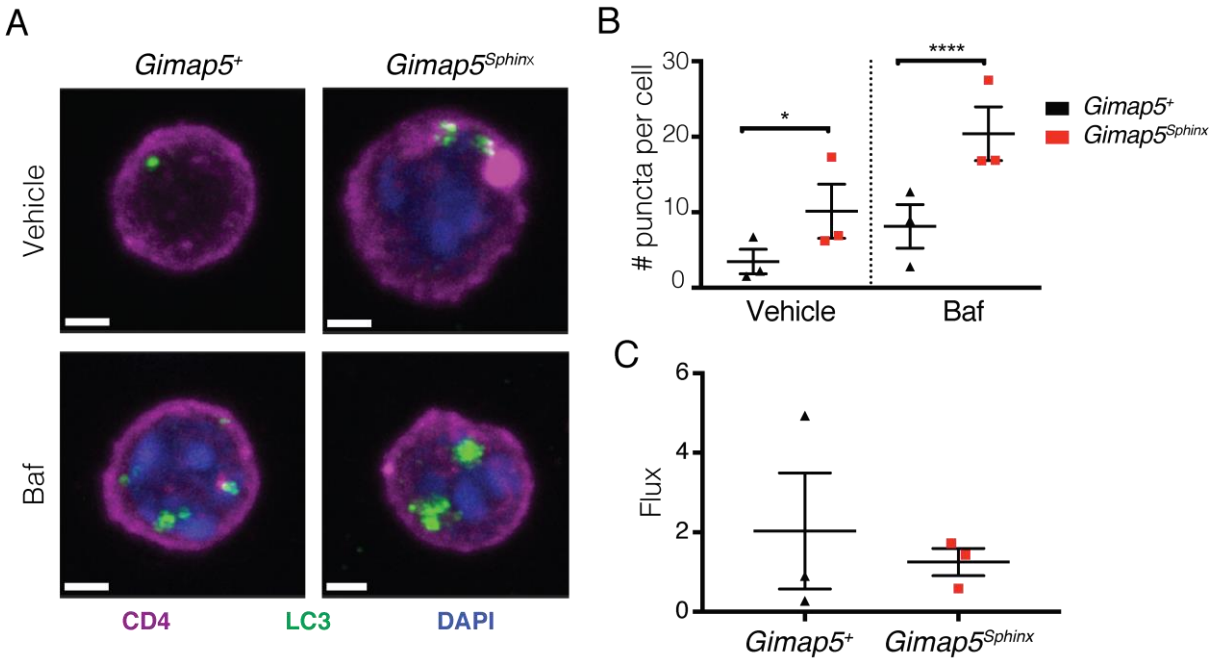


Fig. 3.18 CD4+ T cells from *Gimap5*^{Sphnx} mice have increased numbers of autophagosomes. Splenocytes were treated with 100 μM Bafilomycin A1 (Baf) or DMSO (vehicle) for 2 hours at 37°C, stained with anti-CD4 antibody, and then placed on a poly-lysine coated coverslip. Cells were then fixed and permeabilized before staining for LC3, followed by incubation with secondary antibody and DAPI as a nuclear counterstain. Representative confocal z-stack images from sphinx and control mice are shown in **A**, with quantification of the number of LC3+ puncta per cell shown in **B. C)** Quantification of autophagic flux by normalizing the number of LC3+ puncta with and without bafilomycin (([number of puncta$_{Baf}$] – [number of puncta$_{vehicle}$])/ [number of puncta$_{Vehicle}$]). Scale bar= 2 μm. Three independent experiments on one mouse each were pooled in **B** and **C**, with ten cells quantified for each condition. Mean + SEM is shown for each bar graph. *P<0.05; ****P<0.001 (Two-way ANOVA with a Tukey's comparison test)

To further investigate the role of GIMAP5 in autophagy and other lysosomal pathways, I generated *GIMAP5* knockout Jurkat lines using the CRISPR (Clustered Regularly Interspaced Short Palindromic Repeats)/Cas9 (CRISPR-associated protein 9) system. M. Leney-Greene screened and designed a suitable guide RNA (gRNA) targeting exon 3 of *GIMAP5* (data not shown). I then cloned the chosen gRNA into a suitable plasmid and transfected it into Jurkat cells along with a Cas9 expression vector (**Fig. 3.19A)**. Clonal lines were made through serial dilution and then screened for GIMAP5 expression by western blot. The presence of frameshifts mutations was verified using TIDE analysis, which detects indels from Sanger

sequencing traces of PCR products from the targeted region (**Table. A. 4)**(*324*). Clones from cells transfected with an empty gRNA vector were used as experimental controls.

I used both a flow cytometric assay and Western blotting to examine autophagy in *GIMAP5* KO CRISPR lines. The flow-based assay relies on the permeabilization of cells to release cytosolic LC3-I, leaving behind only autophagosomal membrane bound LC3-II, which can then be used as a marker for autophagosomes (**Fig.3.19B)**. The autophagy inhibitor Bafilomycin A1 allows for accumulation of autophagosomes for a measurement of autophagic flux. Because different clonal lines had highly variable levels of autophagy, at least three lines were used per assay. At basal conditions, KO and control lines had similar levels of LC3-II with and without bafilomycin as well as normal autophagic flux (**Fig. 3.19C,D**). Western blotting of cell lysates allows both detection of both LC3-I (the cytosolic form) and LC3-II (the membrane-bound form); lysates from KO lines similarly showed no autophagic defect (**Fig. 3.19E,F**). In agreement with these results, preliminary studies showed no changes in autophagy levels in GIMAP5 patients after T cell activation (M. Leney-Greene, correspondence, data not shown). Therefore, the defects seen in the *Gimap5*^{Sphinx} T cells may be due to secondary effects.

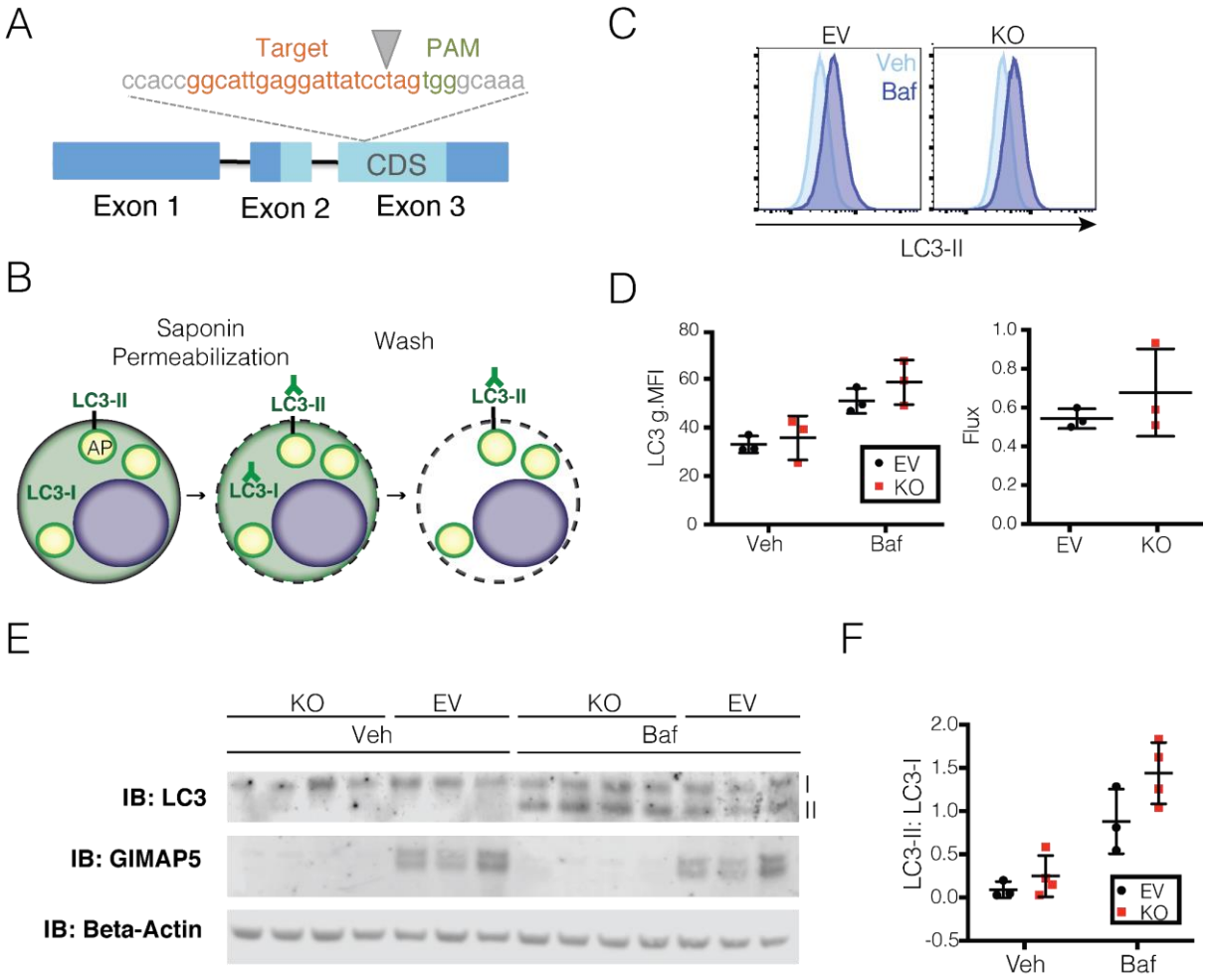


Fig. 3.19 *GIMAP5*$^{-/-}$ Jurkat CRISPR lines have normal basal autophagy. A) Diagram showing the *GIMAP5* genomic sequence targeted for CRISPR cloning. The light blue shows the coding sequence (CDS). The orange sequence above shows the DNA sequence targeted by the CRISPR guide RNA (gRNA) and green shows the protospacer adjacent motif (PAM). An arrow shows the Cas9 cleavage site **B)** Diagram showing the steps used in flow cytometric staining for LC3-II on autophagosomes (AP). Cells are permeabilized with saponin before addition of an anti-LC3 antibody. The permeabilized cells are then washed, which removes cytosolic LC3-I while retaining membrane-bound LC3-II. **C,D)** Jurkat lines were treated with either 10 nM bafilomycin A1 (Baf) or DMSO (Veh) for 2 hours at 37°C. They were then stained for LC3-II using the FlowCellect Autophagy LC3 Antibody-based Assay Kit (Merck Millipore) and assessed by flow cytometry. Cells were gated for singlets and live cells. Representative flow plots of one GIMAP5^{+} (EV) and one GIMAP5$^{-/-}$ (KO) CRISPR line is shown in **C.** Quantification of the geometric MFI of LC3 and autophagic flux (([g.MFI $LC3_{Baf}$] – [g.MFI $LC3_{Veh}$])/[g.MFI $LC3_{Veh}$]) is shown in **D.** n=3 **E,F)** Western blot of Jurkat lines. Cells were treated as in A before being lysed. Lysates were run on an 4-12% Bis-Tris SDS Page gel and transferred onto a PVDF membrane. The membrane was immunoblotted (IB) with antibodies against MAP1A/1BLC3 (LC3), GIMAP5, and beta-actin. Bands for LC3-I and LC3-II are marked on the right of the both. The ratio of LC3-II to LC3-I for each sample is quantified by densitometry in **E.** n_{EV}=3; n_{KO}=4. One representative experiment of two shown is for both A-B and C-D.

Along with its role in autophagy, the lysosome has a prominent role in metabolism. mTORC1 is recruited to the lysosome by the Rag-Ragulator complex where it can be activated through interaction with lysosomal Rheb (*205*, *206*, *209–211*, *400*). We therefore wondered whether GIMAP5 might be associated with this complex. Stimulated emission depletion microscopy (STED), a type of super-resolution imaging, showed strong colocalization of GIMAP5 and LAMTOR4, a member of the Ragulator complex (**Fig. 3.20A,B**). To determine whether GIMAP5 is associated with the Ragulator complex, we performed a proximity ligation assay (PLA) in T cell blasts (**Fig. 3.20C**). PLA works through conjugation of positive and negative sense probes to two antibodies (in this case, two secondary antibodies). If the antibodies (and thus, the targeted proteins) are in close proximity to each other, the probes will be able to amplify DNA by rolling circle DNA synthesis. Fluorescent probes can then bind to the amplified DNA, giving a positive signal (*401*). For example, most TCR complexes contain a TCRα and TCRβ heterodimer; thus, a positive PLA signal is seen when probing for both proteins (**Fig. 3.20C).** In our assay, patient cells were used as negative controls for PLA signal. However, some background signal could be detected, possibly due to either non-specific binding of antibodies or some residual GIMAP5 protein in the patient's cells. Quantification of PLA signal by flow cytometry showed a strong positive signal above this background when GIMAP5 was probed together with LAMTOR4 (**Fig. 3.20C)**. Antibodies against LAMTOR1, RagC, and mTOR itself also gave a weakly positive PLA signal when probed with GIMAP5**.** This data suggests that GIMAP5 is indeed associated with the Ragulator complex. To further support the observed interaction with the Ragulator, A. Park has shown that endogenous GIMAP5 can be detected after immunoprecipitation of components of the Ragulator complex, including

LAMTOR1, LAMTOR4, RagA, and RagC (data not shown [Leney Greene et al., manuscript in progress]).

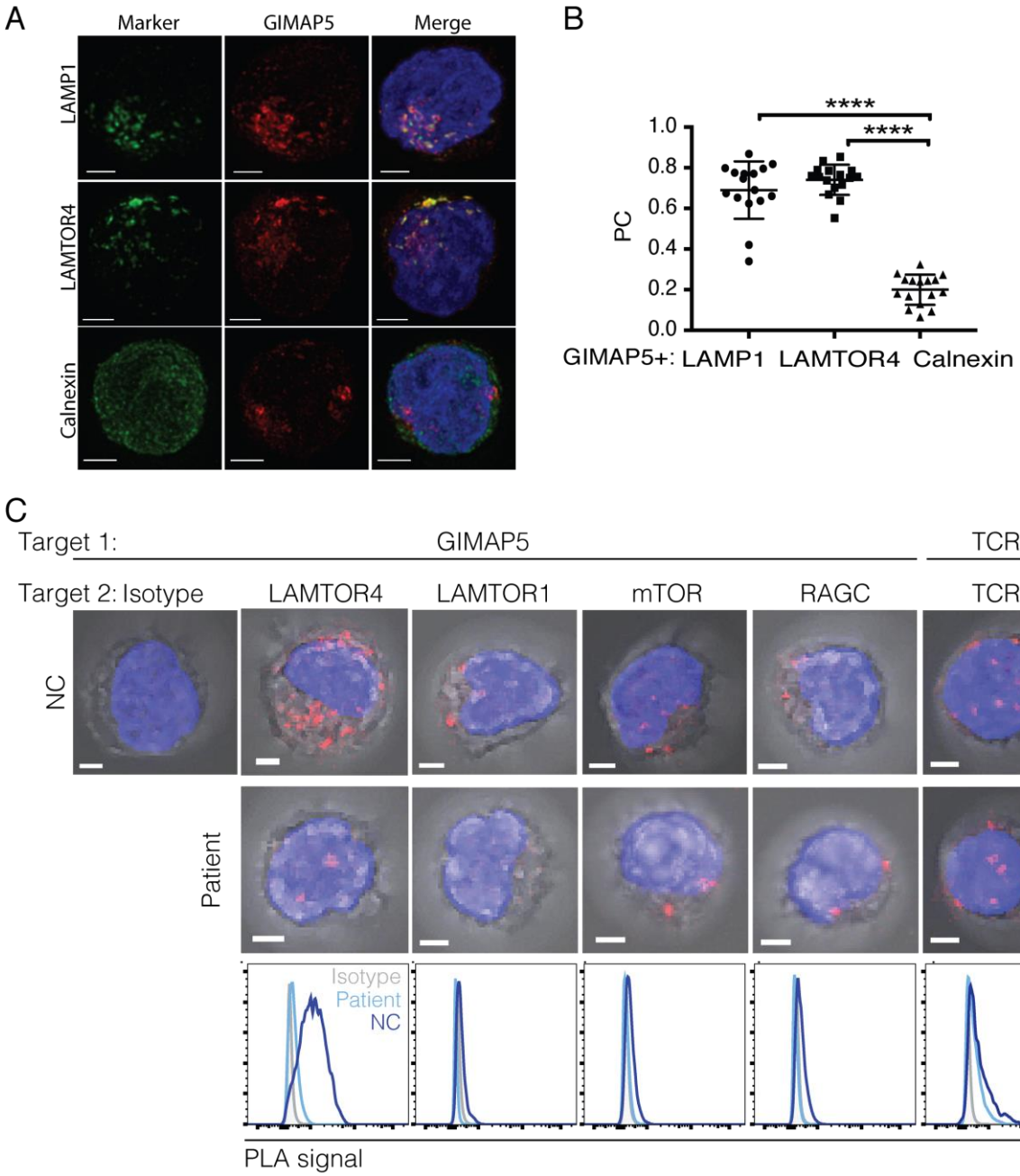


Fig. 3.20 GIMAP5 is closely localized to components of the Ragulator-Rag complex. A,B) Primary human T cell blasts were imaged by STED microscopy and stained for GIMAP5 (red) and the indicated organelle markers (green), while the rightmost column is the merge. Representative z-stack images are shown in **A**. Data shown in **B** is representative of three independent experiments showing mean ± SD of Pearson's correlation coefficient in 10-30 cells. ****$p < 0.0001$ as calculated by Tukey's t test. **C)** Proximity Ligation Assay (PLA) is shown via microscopy (upper two panels) or flow cytometry (lower panel). Representative images of

primary T cell blasts from either healthy controls or GIMAP5$^{L223F/L223F}$ patients are shown stained with the indicated antibodies overlaid on top of differential interference contrast (DIC) to show bounds of cell. Blue=DAPI; Red=PLA puncta. Scale bar= 2 μm. Shown is one representative experiment of three (two repeats done by Juan Ravell). NC=normal control

Due to the identification of GIMAP5 as a PID causing gene, we screened the NIH cohort for patients with mutations in any of the other GIMAP proteins and identified a patient with a homozygous missense mutation in *GIMAP6*. As several members of the Lenardo lab were working on the GIMAP5 project, I switched focus to this patient (PID1467) and GIMAP6 for my primary project. Thus, the following chapters will concentrate on exploring the function of GIMAP6 and the consequences of its loss.

3.3 Discussion

In this chapter, I investigated three sets of patients with the aim of identifying genes and molecular pathways associated with novel PIDs. Causative genes were determined for two sets of patients: PID1294 who has a known pathogenic mutation in *DNMT3B*, and patients identified by M. Leney-Greene who have a novel PID caused by GIMAP5 deficiency. Though I investigated a variant of *TICAM2* as a strong candidate for PID1414's phenotype, it ultimately seemed unlikely to be the driver of his disease.

3.3.1 Identification of ICF patient

DNA methylation, in which a methyl (-CH3) group is added to nucleotides (typically CpG dinucleotides) to form of 5-methylcytosine, is the most well-characterized epigenetic modification (*402*, *403*). DNA can become methylated *de novo*, have methylation patterns maintained, or become unmethylated via DNA methyltransferases and DNA demethylases, respectively. Of the three DNA methyltransferases in humans, *DNMT3A* and *DNMT3B* largely

function in *de novo* methylation, whereas *DNMT1* is primarily responsible for maintenance of patterns on hemimethylated DNA (*404*). All are essential for development, and deletion of any of the three is embryonic lethal in mice (*348*, *354*).

In humans, mutations in each of the three methyltransferases have been associated with Mendelian diseases. De novo or heterozygous mutations in *DNMT3A* are associated with Tatton-Brown-Rahman syndrome, an overgrowth syndrome where patients present with facial abnormalities, intellectual disabilities, and faster than normal growth (*405*, *406*). Heterozygous mutations in *DNMT1*, on the other hand, have been identified in two syndromes involving hearing loss and mental disabilities: hereditary sensory neuropathy type IE (*407*) and autosomal dominant cerebellar ataxia, deafness, and narcolepsy syndrome (*408*). While *DNMT3A* and *DNMT1* mutations have been linked with autosomal dominant diseases, only autosomal recessive inheritance has been observed with *DNMT3B* mutations, which cause the majority of cases of ICF syndrome (*409*). Interestingly, while diseases caused by these methyltransferases present with mental, growth, and facial abnormalities, ICF syndrome also results in immunodeficiency. This discrepancy suggests a specific role of DNMT3B in the immune system. Here, I have identified a patient who has a mutation which likely results in a hypomorph of DNMT3B leading to ICF syndrome.

Before the WES was completed, I began immunophenotyping T and B cells of the patient because I suspected a functional defect in these cell types due to the patient's lymphopenia, agammaglobulinemia, and CVID phenotype. Preliminary studies revealed that the patient's T cells poorly responded to TCR stimulus, likely in part due to an increase in senescent cells. This agrees with current literature on ICF1 patients: while there is a heterogeneous T cell phenotype, several patients have reduced T cell proliferation in response to stimuli, potentially due to an increased susceptibility to apoptosis (*349*, *410*).

Both intrinsic causes, such as the characteristic DNA damage in proliferating ICF lymphoblasts or potential changes in gene expression or DNA replication due to reduced methylation, and environmental factors, such as persistent viral infections or homeostatic induced proliferation, have been suggested as causes of this T cell defect (*356*, *411–415*).

Unlike the patient's T cells, his B cells responded normally to *in vitro* stimuli. Due to the low number of B cells in the patient's shipped blood, I did not further characterize his B cell population. However, previous literature has reported that only naïve B cells are found in ICF patients, suggesting defective memory and plasma cell formation or survival (*416*). In agreement with the B cell assay I performed using cells from PID1294, B cells from patients in this study were capable of normal activation, suggesting that it is instead defects in differentiation and negative selection that cause the characteristic agammaglobulinemia in ICF1 patients (*416*).

The function of DNA methylation and the specific role of DNMT3B has been widely studied, but much remains unknown. Hypomethylation and chromosomal instability are characteristic of ICF, and indeed, key in the diagnosis of ICF1 syndrome. Hypomethylation of pericentromeric DNA and the associated stretching and breakage of chromosomes in ICF syndrome has provided evidence that DNA methylation is important in chromosome stability; further support comes from similar phenotypes in certain cancers (*417–420*). Other known functions of DNA methylation include silencing of transposable elements and transcriptional start sites, such as in imprinting or X-inactivation (*421–425*). However, its role in gene bodies, where it is not associated with decreased transcription, and regulatory elements has been less clear (reviewed in Moore et al., 2013). ICF cells show significant changes in expression of genes involved in neurogenesis, development, and immunity, as well as alterations in other epigenetic features, including histone modifications and polycomb binding, DNA replication,

and transcription (*412*, *413*, *427*). The study of ICF patients will be useful in further elucidating how DNMT3B and DNA methylation specifically affect these functions, and especially its seemingly pivotal role in specific tissues (i.e. the nervous and immune system). However, there are several groups dedicated to the study of ICF syndrome, and treatment standards have been established for affected patients (*428*). These guidelines have been followed for patient 1294. Since I am interested in identifying novel PIDs in the hopes of furthering understanding of the immune system and informing clinical practice for our patients, I therefore chose to focus on the study of other patients in our cohort.

3.3.2 Mutation in TICAM2 identified as possibly inactivating but not pathogenic

As reviewed in Chapter 1, the TLR family are a group of PRR that require adaptors to transmit signaling (*429*). One of these adaptors, TICAM2, recruits TICAM1 to endosomal TLR4 and possibly TLR2 (*51*, *430*). In this chapter, I identified a potentially deleterious variant of *TICAM2* that was homozygous in patient 1414, but ultimately rejected it as the underlying cause of his disease.

Ticam2 deletion in mice results in a significant reduction in cytokine production and a lack of type I interferon responses after LPS stimulation (*51*). Therefore, I tested PID1414's monocytes to determine whether they had a similar phenotype. While the patient's monocytes generally appeared to have reduced responses to LPS when measured by ICS or ELISA, upregulation of transcription levels of pro-inflammatory cytokines was within range of the controls. Due to technical issues resulting in impure monocyte populations, the possibility of extrinsic factors affecting the monocytes in culture cannot be ignored, and single-cell RNA-seq in sorted populations might yield clearer results. When tested in an *in vitro* system in the absence of receptor signaling, TICAM2^{K166Q} did, however, appear to affect protein function.

However, the patient's brother presented as a probable second patient and did not have the *TICAM2* variant, suggesting that though the variant may affect protein function, it does not cause their PID.

The innate immune system has been positively selected for, resulting in a high level of redundancy in these pathways (*431–433*). Only 3.8% of genes involved in the innate immune system are known to cause monogenic susceptibility to disease, compared to 40% of those in the adaptive system (*57*). Furthermore, perturbations of genes involved in innate immunity tend to cause very narrow phenotypes, with susceptibility to few, specific pathogens in a tissue-dependent manner often only when young (*57*). This initially supported the idea of *TICAM2* as a possible PID causing gene, as the patient was vulnerable primarily to pneumonia and seems to be losing this susceptibility as he aged. However, patients with TICAM1 deficiencies have a similar phenotype to those with TLR3 LOF mutations (increased susceptibility to herpes simplex encephalitis), and are not reported to have increased pneumonia (*434*). As TICAM2 is an adaptor protein for TICAM1 in TLR4 and possibly TLR2 and TLR7 signaling, we would expect TICAM1 deficient patients to have a partially shared clinical phenotype with our patient if their TICAM2 deficiency was the root of their disease(*383*, *435*).

As such, though the patient appears to have a potential LOF TICAM2 variant, it seems unlikely to cause his PID. While this seems surprising, it is actually predicted that each person has about 100 loss of function genotypes, with about 20 of those homozygous (*436*). Indeed, complete knockouts have been identified in several reportedly healthy people (*437–439*), with several adults identified who have mutations in genes known to cause Mendelian disorders yet have no apparent clinical phenotype (*438*, *439*). As discussed in Chapter 1, the innate immune system has a high level of redundancy. Indeed, though the patient's cells have reduced responses to LPS *in vitro*, this is not a good model for a true infection setting, where

a whole pathogen would be present and stimulate multiple PRRs. While TLR4 is involved in responses to pneumonias, so are TLR2, TLR5, TLR9, NOD1, and NOD2 (*440*). Therefore, while TICAM2 signaling may be affected in the patient, its effects might be masked through redundant and/or compensatory mechanisms. Owing to limited sample availability, we did not run additional tests on patient cells, but a repeat of the experiments shown in this chapter using whole heat-killed bacteria rather than purified LPS might have confirmed this hypothesis.

In summary, we conclude that the patient's *TICAM2* mutation is unlikely to cause his PID and homozygous variants shared between him and his brother should be further screened to determine the causal gene in their disease. As the brother had not yet been whole exome sequenced, which would be invaluable in narrowing down candidate genes, I concentrated instead on patients thought to have novel PIDs caused by mutations in *GIMAP5* and *GIMAP6*.

3.3.3 GIMAP5 as a protein involved in lysosomal function

Unlike the other patients presented in this chapter, there were several family members affected in our original GIMAP5 pedigree and we were then able to identify multiple other patients with mutations in *GIMAP5*. The identification of these patients highly enhanced our confidence that *GIMAP5* was causal of their disease. The similar disease phenotype in mice and rats with mutated *Gimap5* and the publication of another patient with a *GIMAP5* LOF mutation earlier this year by the Hoebe group further supports *GIMAP5* deficiency as a novel PID (*389*–*391*, *441*). However, its cellular and molecular mechanisms are still unclear. Elucidating GIMAP5 function is of great interest both scientifically and clinically, as it could reveal much about the human immune system as well as help inform therapeutics for our patients.

GIMAP5 has previously been reported in several cellular locations, such as the mitochondria and ER; however, many of these studies used overexpression constructs that may have induced artifacts (*327*, *392–395*). I confirmed that endogenous GIMAP5 is largely located on LAMP1$^+$ lysosomes rather than mitochondria in primary human T cells, supporting earlier results in primary rat T cells and various cell lines (*327*, *442*). I also demonstrated that GIMAP5 partially localizes to RAB7$^+$ and LC3$^+$ vesicles (endosomes or autophagosomes), though the colocalization studies here do not rule out the possibility that some GIMAP5 may localize to other structures under certain conditions. A study published after I completed this work verified my findings; using overexpression constructs, Serrano et al. (2017) demonstrated that GIMAP5 localizes on lysosomes as well as on late-, early-, and recycling-endosomes, including RAB7+ vesicles. These localization studies have provided hints about possible GIMAP5 function. Several previous studies have hypothesized possible mechanisms for GIMAP5 based on localization, including a potential role in ER stress, interactions with the mitochondrial anti-apoptotic proteins Bcl-2 and Bcl-xL, or a possible function in mitochondrial integrity(*393*, *444*, *445*). While GIMAP5 may affect these processes, its localization to lysosomes and endosomes makes it more likely that these are secondary effects. For example, loss of GIMAP5 causes mitochondrial dysfunction, possibly due to impaired calcium uptake (*442*, *445*, *446*). However, it was later shown that rather than directly influencing mitochondrial calcium content, GIMAP5 may regulate lysosomal calcium storage, which has an unknown function in T cell signaling but might indirectly affect mitochondrial integrity (*443*, *446*).

We also observed interaction of RAB7, an important protein in both autophagy and endocytosis, in co-immunoprecipitation of overexpressed GIMAP5 (*194*, *396*, *447*, *448*). As lysosomes are critical for autophagy and autophagy can affect ER and mitochondrial

homeostasis as well as survival, I measured LC3-II levels in GIMAP5 deficient models. In the CD4 T cells of sphinx mice, I observed an increased in $LC3^{+}$ puncta both with and without bafilomycin A1 treatment, but no change in autophagic flux. While a larger number of samples and additional measurements of autophagy (e.g. measurement using western blot or flow cytometry) would be important to confirm this observation, this data suggests that sphinx T cells have an increased autophagosome pool, but no change in autophagic rate. Conversely, studies of *GIMAP5* KO CRISPR lines and patient T cells showed no changes in autophagy by flow and/or western blotting. Additionally, the interaction between RAB7 and GIMAP5 was not observed with endogenous protein, which might indicate spurious binding due to an overexpression artifact. Together, these pieces of evidence suggest to us that GIMAP5 likely does not have a direct role in autophagy.

Because *Gimap5* knockout mice have hyperactive mTORC1 signaling and the lysosome plays a major role in metabolism, we therefore next looked at whether GIMAP5 might be involved in this pathway (*449*). We determined that GIMAP5 is closely localized to components of the Rag-Ragulator complex through confocal and PLA. While both these techniques simply show that GIMAP5 is near the complex, co-immunoprecipitations have confirmed a direct interaction between the endogenous proteins, suggesting a potential role of GIMAP5 in the negative regulation of mTORC1 signaling in lymphocytes. Since these studies, other members of the Lenardo lab have pursued this line of work and seen evidence that both does and does not support this hypothesis (data not shown, but see M. Leney-Greene's thesis for full results).

3.3.4 Use of single patients in studying Mendelian Disease

As with all work on single-patient PIDs, a certain level of caution must be taken in my work. With only one patient, it is always difficult to definitively determine causality of a specific variant or the exact phenotype associated with the disease. Without another patient, there is low statistical power, thus making it easier to make a false positive. Additionally, there can be problems with heterogeneity in clinical presentation and different environmental and genetic backgrounds that can affect the patient's clinical and cellular phenotype. For example, every patient is on different medications that will have various effects. Adding to the statistical problems inherent in single patient studies, in this particular thesis, due to various issues around receiving patient samples, including logistical and human problems, most experiments reported were only done once on blood samples that often took 2-3 days before they could be processed. Furthermore, due to limitations in collecting control samples, the normal controls used frequently were not fully matched for age, sex, or ethnicity.

While it is ideal to find other patients, our searches through colleagues, collaborators, and databases such as Geno2MP were unsuccessful in the case of the *TICAM2* patient and the *GIMAP6* patient (discussed in Chapter 4). As such, we rely heavily on work with genetic models, such as knockout mice and cell lines, to inform and confirm our patient studies. Therefore, in the future chapters of this thesis, I will use mouse and cell line models for the study of *GIMAP6*, alongside more limited studies on patient samples.

Chapter 4. Characterization of a patient with a homozygous missense mutation in GIMAP6 and of a mouse model for GIMAP6 deficiency

4.1 Introduction

GIMAP5 is one of seven functional GIMAP proteins in humans. After determining that mutations in *GIMAP5* can result in human disease, the NIH PID cohort was then screened for patients with variants in any of the *GIMAP* genes. Through this screen, we identified a patient with a homozygous missense mutation in *GIMAP6*. In this chapter, I characterize this patient and her disease, as well as describe a mouse model for GIMAP6 deficiency.

4.1.1 The GIMAP family of proteins

As discussed in Chapter 3, the GIMAP proteins are a family of G proteins conserved amongst vertebrates and some plant species that are thought to be involved in immune function due to their high and fairly specific expression in lymphoid tissue (*450–453*). Previously referred to as the immune-associated nucleotide binding proteins (IAN) family, the *GIMAP* genes are clustered in a single locus on chromosome 7 in humans and chromosome 6 in mice (*452*, *454*). Each GIMAP protein contains a characteristic guanine-nucleotide binding AIG1 domain, except GIMAP8 which contains three consecutive domains (*452*, *453*, *455*). Here I will summarize the known roles of the seven human and eight mouse GIMAP proteins in the immune system.

4.1.2 GIMAP1

GIMAP1 is a membrane-anchored protein expressed in all murine lymphocyte lineages (NK, NKT, T, and B), as well as some F4/80^{+} macrophages and bone marrow-derived dendritic cells (*456*). *Gimap1* mRNA is upregulated as thymocytes transition from the double negative (DN) to double positive (DP) stage in mice and rats, indicating a potential role in thymocyte development (*451*, *457*). Mice with a conditional knockout of *Gimap1* in CD2^{+} cells have a severe loss of mature T and B lymphocytes, confirming its importance in these lineages (*458*). In human CD4 T cells, *GIMAP1* expression is induced by IL-12 but downregulated by IL-4 during Th1/Th2 differentiation (*459*).

4.1.3 GIMAP2

GIMAP2 is expressed in human T cells, but has no mouse or rat ortholog (*460*). It is expressed on lipid droplets, which are fat storage organelles, and thus may have a role in lipid metabolism (*461*). Dimerization with GIMAP7 stimulates GIMAP2's GTP hydrolase activity (*460*).

4.1.4 GIMAP3

GIMAP3 is a pseudogene in humans and has no ortholog in rats, but is functional in mice (*451*, *452*). *Gimap3* mRNA expression is induced in thymocytes during the transition from the DP to single positive (SP) phase (*457*). Co-immunoprecipitation experiments have identified Bcl-2 family proteins as potential interaction partners of GIMAP3, and it may also play a role in mitochondrial DNA segregation (*451*, *462*). Germline deletion of *Gimap3* in mice gave no obvious phenotype, though a double knockout of *Gimap3* and *Gimap5* resulted in a

defect in T cell cellularity more severe than a loss of *Gimap5* alone (*463*). GIMAP3 may play a complementary role to GIMAP5 in mice.

4.1.5 GIMAP4

Unlike the other GIMAPs, GIMAP4 is thought to be pro-apoptotic rather than pro-survival. Expressed in B and T cells, it has a potential role during thymocyte development in mice, where it is expressed in both the DN4 and the SP stages and thus may be involved positive selection (*450*, *454*, *464–466*). GIMAP4 has recently been identified as a novel target of miR-146a, a feedback suppressor of NF-kB signaling, supporting a potential role in positive selection (*467*). However, GIMAP4 is not necessary for T cell development as *Gimap4* knockout mice have normal T cell maturation (*465*). Rather, T cells from these mice, as well as from a strain of Brown Norway rat with a hypomorphic variant of GIMAP4, are resistant to apoptotic death (*464*, *465*). Co-immunoprecipitation of GIMAP4 shows a potential interaction with the pro-apoptotic protein Bax (*451*). IL-7 induces *Gimap4* expression, but activation of B and T cells downregulates GIMAP4 protein levels, indicating a role in T and B cell activation (*468*, *469*). GIMAP4 is widely implicated in Th1/Th2 differentiation, particularly in regulation of cytokines (*459*, *469*, *470*).

4.1.6 GIMAP5

GIMAP5 was largely discussed in **Chapter 3**. As a brief summary, GIMAP5 is involved in T cell survival in mice and rats, as well as in B cells in mice (*389–391*). SNPs in human *GIMAP5* has been associated with autoantibodies in type I diabetes, systemic lupus erythematosus, and asthma, though a subsequent study showed no association with diabetes (*471–475*).

4.1.7 GIMAP6

At the start of my studies, it was known that GIMAP6 is expressed in rat and murine B and T cells, with high expression in all thymocyte populations except CD8 SP in rats and DN cells in mice (*451*, *457*, *476*). Downregulation of *GIMAP6* has been observed in hepatocellular and non-small cell lung cancers (*477*, *478*). GIMAP6 has also been associated with head and neck squamous cell carcinoma and Paroxysmal Nocturnal Hemoglobinuria (PNH) in humans, as well as Johne's Disease caused by chronic mycobacterial infection in ruminants (*479–481*). GIMAP6 has been linked to autophagy, which will be further discussed in Chapter 5.

4.1.8 GIMAP7

Human *GIMAP7* is detected in spleen, lymph nodes, and fetal kidney, with lower expression in the heart and small intestine (*452*). In mice, *Gimap7* is expressed in T and B cells, with low expression prior to the SP stages in thymocytes (*451*). GIMAP7 forms homodimers that have GTP hydrolytic activity, as well as heterodimers with GIMAP2 that stimulate GIMAP2's catalytic activity (*482*).

4.1.9 GIMAP8

GIMAP8 is unique amongst the GIMAPs in that it contains three G-domains (*457*). Early double negative (DN1 and DN2) and SP thymocytes highly express murine *Gimap8*, as do mature CD4 and CD8 T cells. Mouse B cells begin to express GIMAP8 during the transitional phase of maturation (T2), with highest levels in mature B cells (*331*). However, *Gimap8* knockout mice have normal T cell development, though a delay in death after apoptotic conditions (*10*). Knockout mice also have a mild decrease in mature recirculating B cell numbers, suggesting a role in maintenance of that population in bone marrow (*331*).

4.1.10 GIMAP9

GIMAP9 is expressed in mice and rats, but not in humans (*452*). Its function has not been studied, though it appears to be expressed lowly in thymocytes and in a non-B or T cell hematopoietic lineage in rats (*476*, *483*).

4.2 Results

4.2.1 Identification of a novel GIMAP6 variant in a primary immunodeficiency patient

Patient 1467 (PID1467) is a 31 years old female belonging to a Turkish family from a village in Anatolia (**Fig. 4.1)**. She presented at 6 months old with hepatosplenomegaly and thrombocytopenia, which persisted until she eventually received a splenectomy at 18 years old (**Table 4.1)**. Patient 1467 has a systemic lupus erythematosus (SLE)-like disease, with Direct Coombs + autoimmune hemolytic anemia (AIHA), immune thrombocytopenia (ITP), and anti-phospholipid syndrome (APS) with the presence of anti-cardiolipin and -phospholipid antibodies. She has developed hyper-IgM with hypo-IgA and borderline low IgG and has had several infections over her life, including a severe infection with *Acinetobacter baumannii* (a gram-negative bacterium that causes opportunistic infections in immunosuppressed individuals), recurrent pneumonia, and shingles. All of these indicate that she has a chronic immunopathology. Currently, she is also undergoing treatment for pulmonary hypertension, which may be secondary to her recurrent lung infections and vasculitis. Patient 1467 was referred to the NIH from Hacettepe University in Istanbul, and genomic samples from her and her family members were whole-exome DNA sequenced.

Table 4.1. Clinical presentation of Patient 1467	
Lymphadenopathy?	Yes (left axillary lymphadenopathy) (resolved)
Splenomegaly?	Yes [hepatosplenomegaly] (received splenectomy)

Autoimmunity or autoinflammatory disease?	• SLE-like
	• AIHA (Direct Coombs test +)
	• ITP
	• Anti-phospholipid syndrome with + Anti-Cardiolipin (IgM) and + anti-phospholipid
	  ○ Vasculitis of lungs
	  ○ Livedoid vasculitis
	  ○ Femoral artery pseudoaneurysm

Immunodeficiency or susceptibility to infection?	• Hyper-IgM (3000-4000 mg/dL) • Hypo-IgA (<6.67 mg/dL) • Meningitis, pneumonia, and sepsis (*Acinetobacter baumannii*) • Recurrent pneumonia • Herpes zoster • Gram-positive diplococcus
Other	• Pulmonary hypertension

SLE= Systemic lupus erythematosus; AIHA= autoimmune hemolytic anemia; ITP= immune thrombocytopenia

Though no consanguinity was reported in the patient's family, we hypothesized that she is most likely affected by a recessive LOF mutation because she is from a small village in rural Turkey, thus increasing the likelihood of consanguinity, and is the only member of her family affected. WES results gave a list of potential candidate genes, but due to the prior identification of the GIMAP5 patients, we prioritized the patient's homozygous variant of *GIMAP6* as the top candidate gene. However, we also screened for other homozygous recessive, compound heterozygous, and de novo variants unique to her amongst her family members (abbreviated list in **Table 4.2;** full list in **Table A.5**). On this list, *GIMAP6* remained the top candidate for several reasons. First, it is a novel variant that is not present in any of

our screened genomic databases, which means it is unlikely to be found in healthy individuals and fits with it being a rare genetic disease (**Table 4.2)**. GIMAP6 is also known to be expressed in lymphocytes, which fits the model of a primary immunodeficiency with a strong humoral component. Additionally, the patient's variant results in a missense mutation in a fairly conserved residue of GIMAP6 (**Fig. 4.1B)** that is predicted to be highly deleterious, with a CADD score of 22.9.

However, because there is only a single patient, we cannot exclude the possibility that there may be other genetic variants at play that may contribute to the patient's disease. Of the other rare, nonsynyonymous homozygous variants with high CADD scores (**Table 4.2)**, C4orf45 is an uncharacterized protein that seems to be exclusively expressed in sperm and testes, making it unlikely to be contributing to the patient's phenotype (biogps.org; *38*). FLYWCH1 is also a candidate with a scant literature, but a recent paper suggests it is a novel suppressor of beta-catenin involved in cell motility (*485*). Autosomal recessive mutations in heparan sulfate proteoglycan 2 (HSPG2), a basement membrane protein involved in growth-promotion and angiogenesis, are known to cause Schwartz-Jampel syndrome and Silverman-Handmaker disease, which affect muscular, skeletal, and cartilage function (*486–488*). Argonaute-1 (AGO1) is a part of the RNA-induced silencing complex (RISC) essential for RNA interference; because it has fairly ubiquitous expression, mutations affecting *AGO1* would be expected to have effects on multiple organ systems rather than primarily the lymphoid system as in the patient (*489*, *490*). Of the gene candidates listed in **Table 4.2**, the second strongest is acid mammalian chitinase (CHIA), which hydrolyzes chitin, a component of the cell walls of fungi and the exoskeleton of anthropods(*491*). CHIA has been associated with Th2-mediated inflammation, allergy, and asthma in respiratory innate cells (*492*, *493*). However, the patient does not have allergies, asthma, or an increased susceptibility to fungal

or helminth diseases. Therefore, while we cannot exclude the possibility that other genetic variants may affect the patient's phenotype, a homozygous loss of function of *GIMAP6* remains the strongest candidate for the patient's disease.

Table 4.2 Abbreviated homozygous recessive candidates for patient 1467

Genetics			Allele Frequency		Severity Prediction		Genotypes				
Gene	**Position**	**Mutation**	**ExAC**	**gnomAD**	**Polyphen**	**CADD**	**1467**	**1468**	**1469**	**1470**	**1471**
C4orf45	Chr 4: 159894373	ENST00000434826: c.155A>T, p.Asp52Val	0.00E+00	0.00E+00	PrD	28.5	A/A	T/A	T/A	T/T	T/A
CHIA	Chr 1: 111854818	ENST00000369740: c.62C>T, p.Ala21Val	0.00E+00	0.00E+00	PoD	27.2	T/T	C/T	C/T	C/C	C/C
AGO1	Chr 1: 36354076	ENST00000373204: c.74G>A, p.Arg25His	0.00E+00	0.00E+00	PoD	26.3	A/A	G/A	G/A	G/A	G/A
FLYWCH1	Chr 16: 2988407	ENST00000416288: c.1997C>G, p.Ala666Gly	4.29E-04	1.65E-04	PrD	25.4	G/G	C/G	C/G	C/G	C/C
HSPG2	Chr 1: 22169930	ENST00000374695: c.8618T>G, p.Val2873Gly	2.07E-04	2.49E-05	PrD	23.3	C/C	A/C	A/C	A/C	A/C
GIMAP6	Chr 7: 150325228	ENST00000328902: c.458G>T, p.Gly153Val	0.00E+00	0.00E+00	PoD	22.9	A/A	C/A	C/A	C/A	C/A

PrD=Probably damaging; PoD= Possibly damaging; B= Benign

1467= Patient; 1468= Father; 1469= Mother; 1471= Sister; 1470= Brother (See Fig. 4.1A)

Almost all mutations of *GIMAP5* identified in affected patients result in a loss of protein in patient cells. Western blot of T cell blasts from patient 1467 similarly showed a reduced level of GIMAP6 in her cells compared to normal controls (**Fig. 4.1C,D**). Interestingly, the residual GIMAP6 protein present appeared to migrate faster through the gel. Overexpression of plasmids containing HA-tagged GIMAP6 similarly showed reduced levels of GIMAP6^{G153V} compared to wildtype (WT) (**Fig. 4.1E,F)**. The presence of the faster migrating species in the overexpressed construct indicates that the G153V missense mutation may result in a significant structural change in the protein that affects its gel migration. Together, this evidence supports our hypothesis that the patient's mutation results in an abnormality in the GIMAP6 protein that may contribute to her disease.

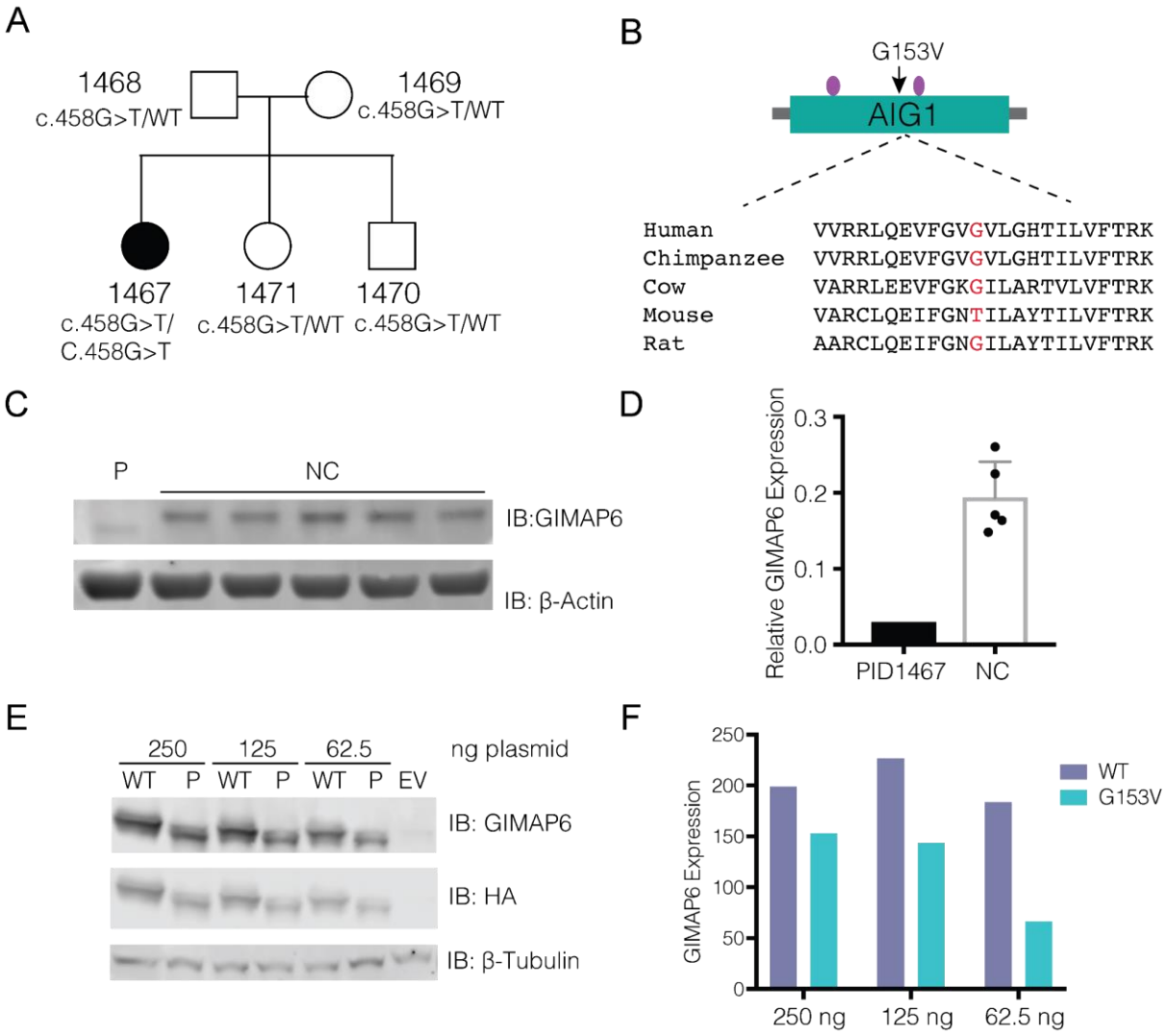


Fig. 4.1 Patient 1467 has a homozygous missense mutation in *GIMAP6* leading to decreased protein expression. A) Patient pedigree. The proband is shaded in black. Genotypes of each family member are located below their subject ID numbers. Circles= females; squares= males. **B**) Schematic of GIMAP6 showing the AIG1-type G domain with arrow at location of patient mutation. Purple ovals represent putative GTP binding sites. Below is a sequence alignment of GIMAP6 in multiple species. Red highlights the site of the patient's mutation. **C, D)** Western blot of lysates from T cell blasts of patient (P) and normal controls (NC) that were activated from whole PBMCs with anti-CD3/28 for three days and then cycled in 100 U/mL IL-2. Lysates were prepared and run on a 4-12% Bis-Tris gel before transferring to a PVDF membrane. Blots were immunoblotted (IB) with antibody against GIMAP6 and beta-actin. Quantification of **C** by densitometry is shown in **D.** Relative GIMAP6 expression was determined by dividing the signal of the GIMAP6 band by the signal of the actin band for each subject. The mean and standard deviation of the five normal controls is shown for NC, with individual values shown as dots. Blot is representative of two independent repeats. **E, F)** Western blot of overexpressed HA-tagged GIMAP6. 250, 125, or 62.5 ng of plasmid expressing WT GIMAP6 (WT) or GIMAP6^{G153V} (P) was transfected into 293T cells with GeneJuice. Empty vector (pCDNA3.1) was added to keep the amounts of DNA transfected equal for all samples. Cells

were incubated for 24 hours before lysates were made and run on a 10% Bis-Tris gel. Blots were then probed with antibodies against GIMAP6, HA, and beta-tubulin. Quantification by densitometry is shown in **F.** GIMAP6 expression was determined by dividing the signal of the GIMAP6 bands of sample by that of the corresponding beta-tubulin band. Shown is one representative experiment of three. AIG1= avrRpt2 induced gene 1

4.2.2 Immunophenotyping of patient T cells

Because GIMAP6 is highly expressed in T cells, I looked at whether the patient's T cells respond normally to stimuli (**Fig. 4.2**). As in **Fig. 3.4**, the activation markers CD69 and CD25 served as indicators for T cell responsiveness. Because hyper-IgM syndrome is usually caused by defects in class-switching, especially in the CD40-CD40L signaling pathway, I also examined upregulation of CD154, also known as CD40 ligand (CD40L) (*494*). Compared to five normal controls, all three markers for activation were poorly induced in the patient's T cells after TCR stimulation by anti-CD3 and -CD28 antibodies(**Fig. 4.2B,C**). The one exception was the patient's CD4 T cells, which had fairly normal levels of CD25 expression after 20 hours. CellTrace Violet (CTV) is a fluorescent dye that covalently binds to free amines in and on cells, allowing identification of multiple generations of dividing cells through sequential dilution of the dye (*495*). I therefore utilized CTV to examine T cell expansion in patient cells (**Fig. 4.2D-H**). Proliferation index, a measurement of the average number of divisions each cell in the total population has undergone, and division index, an indicator for the average number of divisions each cell in the proliferating population has undergone, were used to quantify cell proliferation (**Fig. 4.2E,F**)(*496*). While the patient's CD8 T cells expanded similarly to control cells after stimulation, her CD4 T cells had a lower proliferation index, indicating fewer responding cells. Interestingly, while patient T cells were capable of proliferating, CD25 upregulation remained poor, especially amongst CD8 T cells (**Fig. 4.2G,H**). Cells that have diluted more CTV and thus undergone more divisions express increasingly high levels of CD25

in normal controls; however, in the patient, even highly proliferative populations had low levels of CD25 (**Fig. 4.2H),** indicating a physiological difference even in proliferating patient cells.

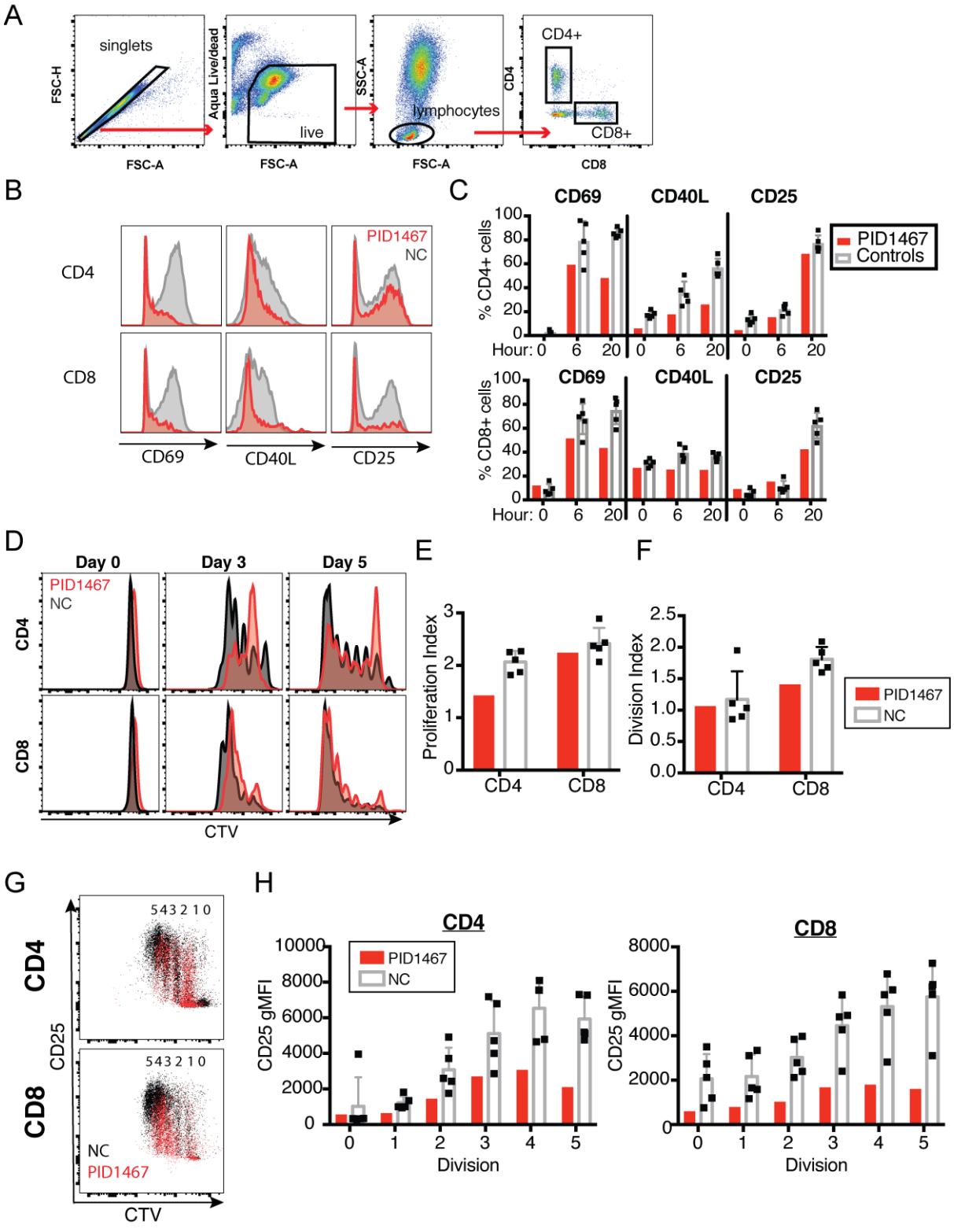


Fig. 4.2. Patient 1467 CD4 and CD8 cells have reduced response to TCR activation. A) Gating strategy for CD4 and CD8 T cells. **B, C)** PBMCs were stimulated with 1 μg/mL of anti-CD3/28 for the indicated numbers of hours and then stained for the activation markers CD69, CD40L, and CD25. Flow plots of activation marker upregulation at 20 hours of T cells from the patient and a representative normal control are shown in **B.** Quantification of the percent of CD4 or CD8 cells that upregulated the indicated marker in **B** is shown in **C. D-H)** PBMCs were stained with CellTrace Violet (CTV) and stimulated with 1 μg/mL of anti-CD3/28 for the indicated numbers of days before flow analysis. **D**) Flow plots of CTV dilution in T cells from the patient and a representative normal control. **E)** Quantification of **D** showing the proliferation index and division index of each sample. **G)** Representative flow plot showing anti-CD25 staining in proliferating T cells activated for 3 days. The number of divisions each population has undergone is shown above, as indicated by dilution of CTV. **H**) Quantification of **G.** Graphs shown mean + SD of normal controls. Each black square represents the values of each individual normal control. n_{NC}= 5. NC = normal control; FSC-A = forward scatter-area; FSC-H = forward scatter-height; SSC-A = side scatter-area.

PBMCs contain a heterogenous mixture of T cell populations, including naïve and memory subsets. Several intrinsic and extrinsic factors, such as autoimmunity, infections, lymphopenia, or ageing, can affect the frequency of these subsets in the periphery. The patient had a dramatic loss in the proportion of CD4 and CD8 T cells with a naïve-phenotype, with a corresponding increase in those with T_{EM}-phenotype (**Fig. 4.3B,C**). To further dissect the likely properties of patient T cells, I examined markers for T cell activation (Human leukocyte antigen-antigen D related [HLA-DR]), exhaustion (programmed cell death protein 1 [PD-1]), and senescence (CD57, CD27, and CD28) (**Fig. 4.3D-F**). HLA-DR, an MHCII protein that is a late activation marker for human T cells, was highly expressed on patient T cells, similar to what is seen in SLE (*497*, *498*) (**Fig. 4.3D, F**). Strikingly, over 70% of CD4 and 40% of CD8 T cells were PD-1+, suggesting an exhausted phenotype, though PD-1 expression can also indicate recently activated T cells (*499*). Additionally, both the patient's CD4 and CD8 T cells had comparatively high levels of CD57+ cells, which is indicative of senescence (*347*, *500*). This is consistent with an increase in T cells lacking both of the co-stimulatory molecules CD27 and CD28 (**Fig. 4.3E,F)**, which is associated with impaired telomerase activity and replicative

senescence (*501–503*). In general, the patient's T cell phenotype fits that of chronic antigenic stimulation, resulting in an increased proportion of cells with activated, exhausted, and/or senescent phenotypes. This could contribute to the defective activation and proliferation seen in **Fig. 4.2**.

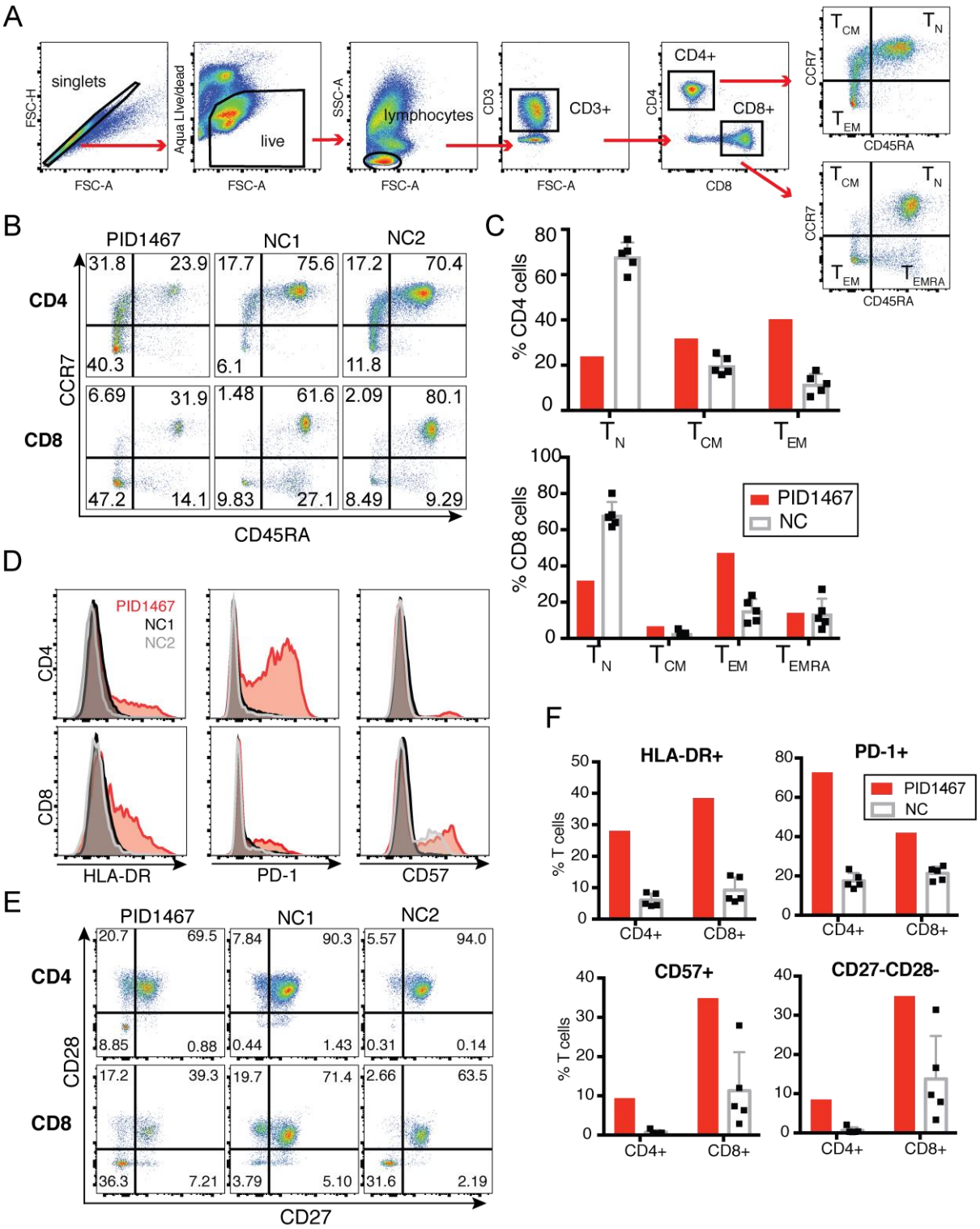


Fig. 4.3. Patient 1467 has an increase in T cells with activated, senescent, and exhausted phenotypes and a loss of naïve T cells. PBMCs were stained with anti-CD3, -CD4, -CD8, -CD45RA, -CCR7, -HLA-DR, -PD-1, -CD27, -CD28, and -CD57 antibodies and analyzed on flow cytometry. **A)** Gating strategy for T cell subsets. **B)** Flow plots showing two naïve and memory populations of CD4 and CD8 T cells in the patient and two representative normal controls (NC1 and NC2). **C)** Quantification of naïve and memory populations shown in **B**. **D)** Flow plots showing HLA-DR, PD-1, and CD57 staining in CD4 and CD8 T cells in the patient and two

representative normal controls. **E)** Flow plots showing CD27 and CD28 staining in CD4 and CD8 T cells in the patient and two representative normal controls. **F**) Quantification of **D** and **E**. Graphs shown mean + SD of normal controls. Each black square represents the values of each individual normal control. n_{NC}= 5.T_{CM}= Central memory T cells; T_{EM}= Effector memory T cells; T_N= Naïve T cells; T_{EMRA}= CD45RA+ effector memory T cells; NC= normal control; FSC-A= forward scatter-area; FSC-H= forward scatter-height; SSC-A= side scatter-area.

4.2.3 Immunophenotyping of T cells in Gimap6$^{-/-}$ mice

Because of limited access to patient samples, I used a *Gimap6* knockout (KO) mouse strain as a model for the patient's loss of function mutation. This also gave me the opportunity to experimentally explore the consequences of GIMAP6 deficiency. Created by the Knock Out Mouse Project (KOMP^2), an initiative aimed at creating and analyzing knockout strains of every mouse gene, *Gimap6* KO mice have a germline excision of *Gimap6* exons 2 and 3, which contain its coding sequence (CDS) (*316*, *317*). Though the International Mouse Phenotyping Consortium (IMPC) has since done extensive phenotyping on the B6N(Cg)-*Gimap6$^{tm1b(KOMP)Wtsi}$*/J strain (henceforth referred to as "KO mice"), these mice were newly available and uncharacterized at the beginning of this study. Therefore, I began immunophenotyping the strain to determine how similar its phenotype is to that of PID1467 (**Fig.4.4)**. KO mice have increased splenocyte counts compared to WT and heterozygous controls (**Fig. 4.4B**). Because murine GIMAP6 is expressed in T and B cells, I examined splenic lymphocytes to determine if the increased cellularity was due to changes in these populations (*458*). Indeed, the frequency of both B and T cell populations was altered in KO mice, with an increase in B cells and a corresponding moderate decrease in CD4 and CD8 T cells (**Fig. 4.4C**). However, determination of total cell counts revealed that the increase in splenocyte number was largely due to an expansion in the number of splenic B cells **(Fig. 4.4D,E**). Interestingly, while T and NK cell numbers were normal, the NKT population was diminished in KO mice

(**Fig. 4.4D,E**). Further work is needed to determine if NKT cells express GIMAP6 or whether this is a secondary effect.

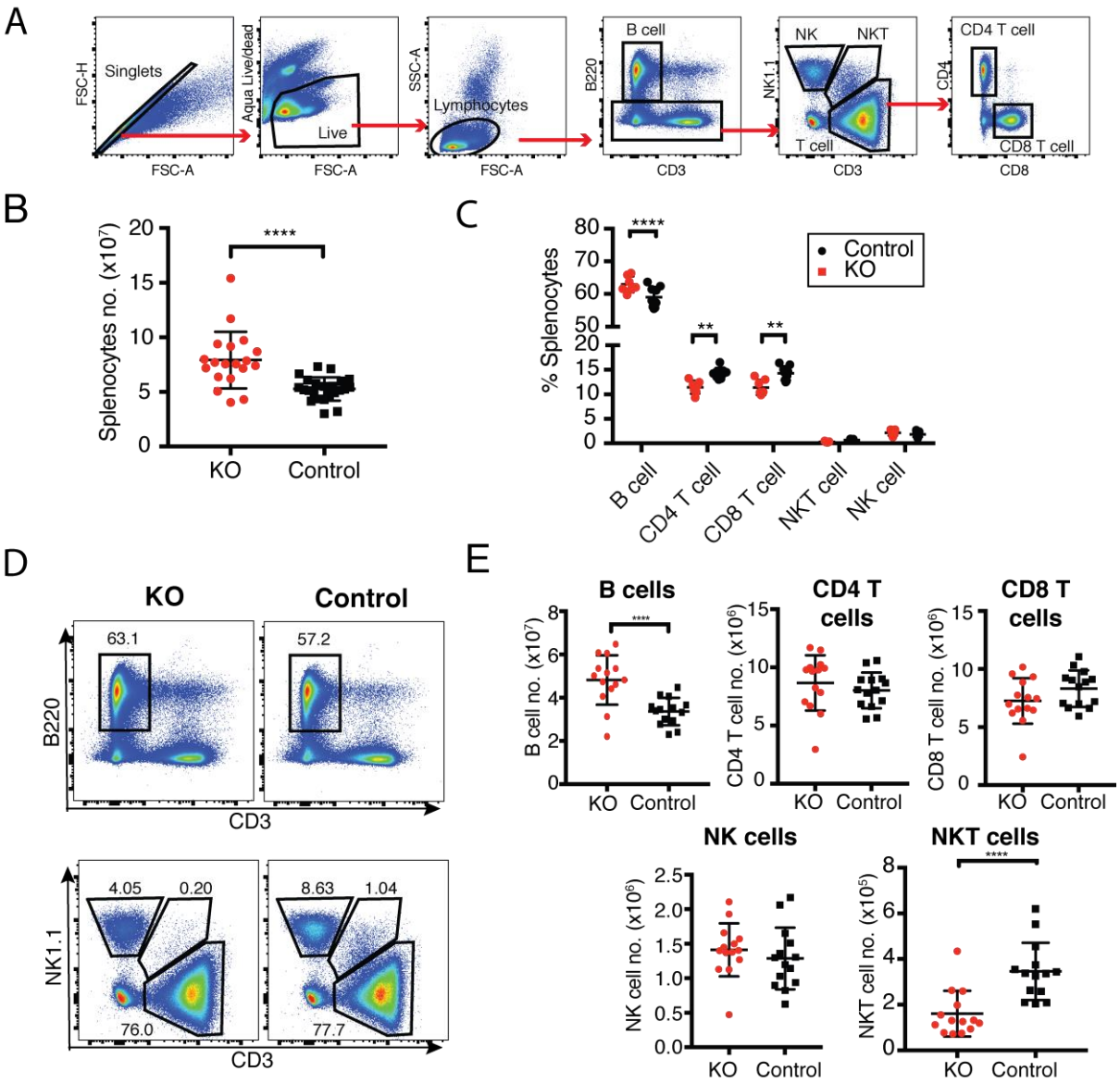


Fig. 4.4 *Gimap6*$^{-/-}$ mice have an increase in B cells and decrease in NKT cells. Splenocytes were stained and analyzed for cell populations using flow cytometric analysis. **A)** Gating strategy for splenocyte populations. **B**) Total splenocyte numbers counted with flow cytometry-counting beads **C**) Frequency of B220^{+} B cells, CD4 T cells, CD8 T cells, NK1.1^{+}CD3^{-} NK cells, and NK1.1^{+}CD3^{+} NKT cells in splenocytes populations as determined by flow cytometric analysis. **D**) Representative flow plots showing B, T, NK, and NKT populations in KO and control mice. **E**) Cell counts for each population was determined by multiplying the total amount of splenocytes by the frequency of the population determined in **C**. Three experiments were pooled in **B**, with n_{KO}=19, $n_{control}$=23. For **C, D,** one of three independent experiments is shown, with n_{KO}=7, $n_{control}$=9. For **E,** two experiments were pooled together,

with n_{KO}=14, $n_{control}$=14. *P<0.05, **P<0.01; ****P<0.001 Mann-Whitney U test. FSC-A= forward scatter-area; FSC-H= forward scatter-height; SSC-A= side scatter-area.

Both Treg and Tfh cells have been implicated in autoimmunity (*504*, *505*). The surface markers CD25 and PD-1 with CXCR5 served as indicators for the Treg and Tfh populations, respectively (**Fig. 4.5)**. KO mice had an increased percentage of $CD25^+$ CD4 T cells, signaling a potential increase in Tregs (**Fig. 4.5B,C**). However, as CD25 can also indicate activated T cells, a subsequent analysis utilized staining of the key transcription factor for Tregs, FOXP3 (forkhead box P3) to distinguish Tregs from activated T cells (**Fig. 4.5H-J)** (*125*, *127*, *506*). While both the frequency of $CD25^+FOXP3^+$ Tregs and $CD25^+FOXP3^-$ were generally higher in KOs than controls, neither reached statistical significance, thus suggesting that the increase in $CD25^+$ CD4 T cells may be due to a slight increase in both populations. Similarly, KO mice displayed slightly higher levels of CD4 T cells with a $PD\text{-}1^+CXCR5^+$ Tfh-like phenotype (**Fig. 4.5D,E)** (*507*). Interestingly, there was also a significant increase in $CXCR5^-PD\text{-}1^+$ CD4 T cells as well as a more modest increase in $PD\text{-}1^+$ CD8 T cells (**Fig. 4.5D-G**). As with the patient (**Fig. 4.3)**, the increases in CD25 and PD-1 expression could be indicative of T cells with an activated phenotype, potentially due to increased antigenic stimulation. Additional exhaustion and activation markers could be used to further delineate these populations.

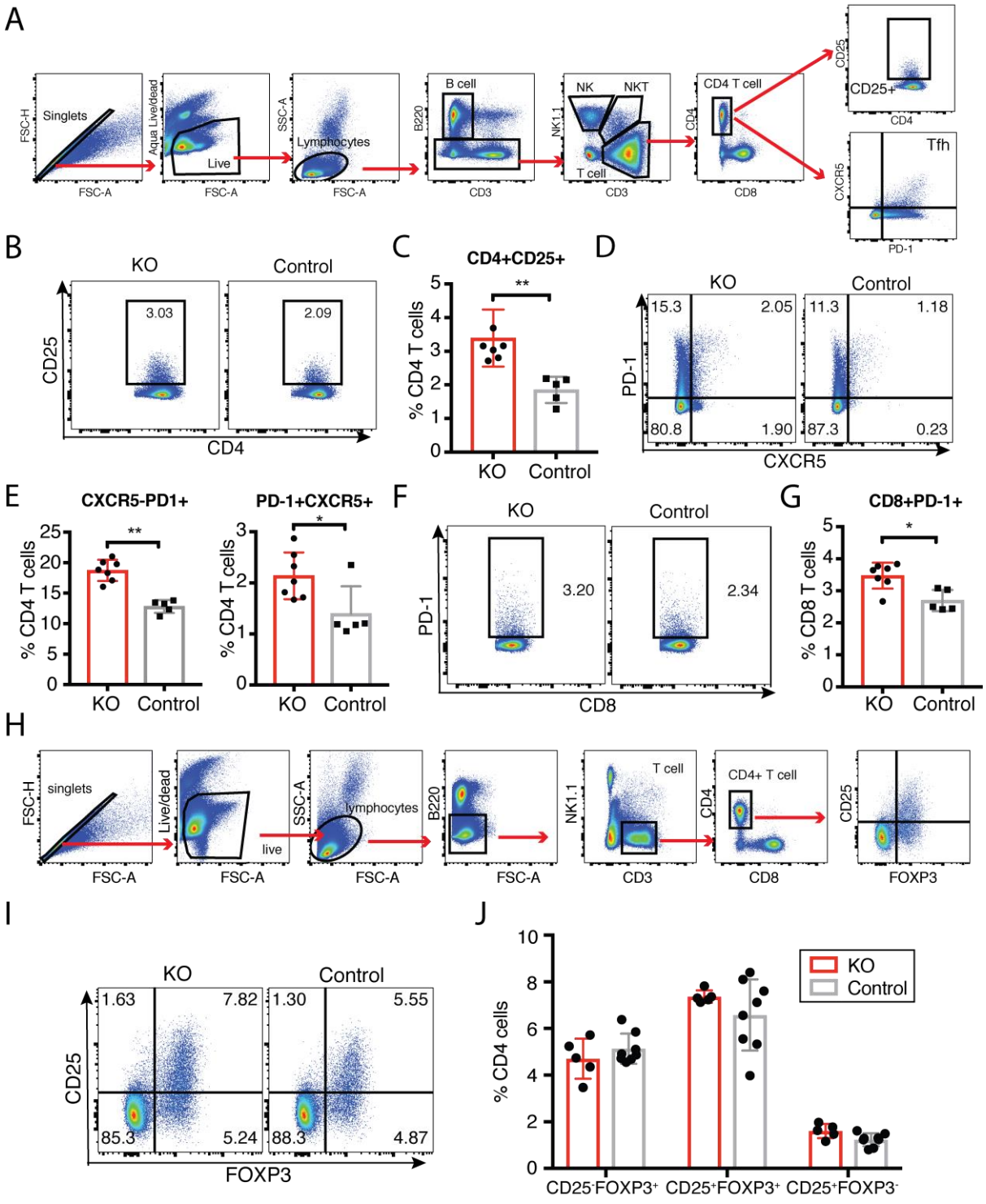


Fig. 4.5 *Gimap6*$^{-/-}$ mice have an increase in CD25^{+} CD4 T cells and PD-1^{+} T cells. Splenocytes were stained and analyzed for cell populations using flow cytometric analysis. **A)** Gating strategy for T cell populations. **B**) Representative flow plot showing CD25 expression in CD4 T cells. **C**) Quantification of **B. D**) Representative flow plot showing CXCR5 and PD-1 expression in CD4 T cells. **E**) Quantification of **D. F**) Representative flow plot showing PD-1 expression in CD8 T cells. **G**) Quantification of **F**. **H-J**) Splenocytes were fixed, permeabilized, and intracellularly stained for the transcription factor FOXP3. **H** shows the gating strategy used. A representative flow plot of FoxP3 and CD25 staining in CD4 T cells is shown in **I**, with

quantification in **J**. **A-G** were done in conjunction with **Fig. 4.4**, with one of three independent experiments shown. n_{KO}=7, $n_{control}$=9. For **H-J**, n_{KO}=5, $n_{control}$=7. *P<0.05, **P<0.01; ****P<0.001 Mann-Whitney U test. FSC-A= forward scatter-area; FSC-H= forward scatter-height; SSC-A= side scatter-area.

Because the patient has skewing towards memory and effector T cells and an increase in senescent cells, I was interested in whether that might also be true of knockout mice. Murine T_N, T_{CM}, T_{EM}, and effector T cell (T_{EFF}) populations are identified using differential staining for the adhesion molecules CD44 and CD62L, with T_N staining as $CD62L^+CD44^-$, T_{CM} as $CD44^+CD62L^+$, T_{EM} as $CD44^+CD62L^-$, and T_{EFF} as $CD44^-CD62L^-$(**Fig.4.6)**. Unlike PID1467, CD4 T cells in the KO mice showed no significant difference in memory subsets (**Fig. 4.6 B,C**). Interestingly, KO CD8 T cells showed a minor but consistent decrease in T_{CM} with a corresponding increase in T_N (**Fig. 4.6B,C**). This is contrary to the memory-skewed phenotype in the patient, though peripheral blood and not splenocytes were examined. Additionally, while patient T cells had high levels of both CD4 and CD8 T cells with a senescent phenotype, only KO CD4 T cells had a slightly elevated expression of KLRG1 (Killer lectin inhibitory receptor 1), an inhibitory receptor associated with senescence (*501*, *508*, *509*) (**Fig. 4.6D-F**).

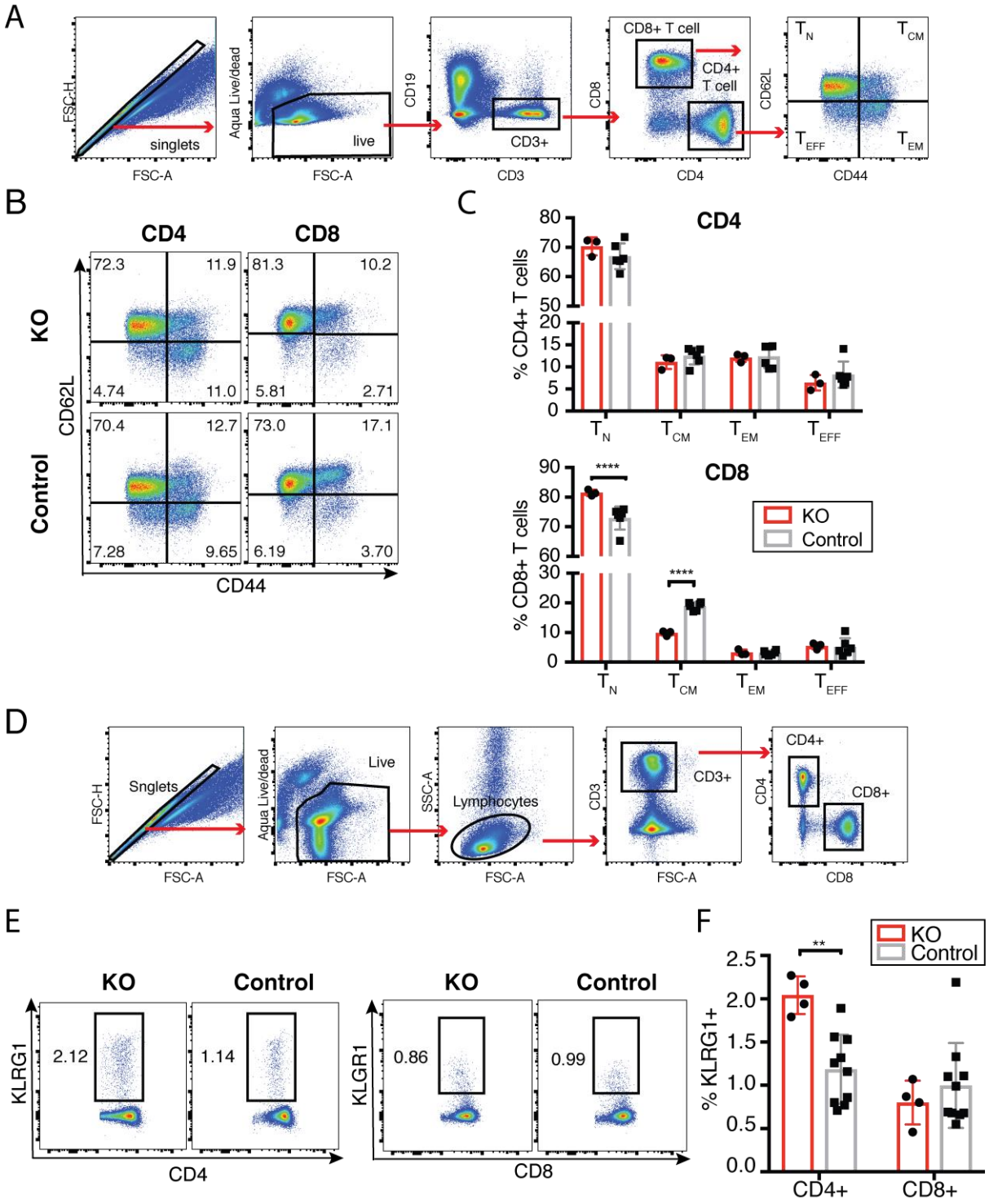


Fig. 4.6. *Gimap6*$^{-/-}$ mice have a decrease in central memory CD8 T cells and an increase in KLGR1^{+} CD4 T cells. Splenocytes were stained and analyzed for T cell populations using flow cytometric analysis. **A)** Gating strategy for naïve and memory T cell populations. **B**) Representative flow plots showing two naïve and memory populations of CD4 and CD8 T cells in KO and control mice. **C)** Quantification of naïve and memory populations shown in **B**. **D)** Gating strategy for KLGR1 staining. **E)** Representative flow plots showing KLGR1 staining in CD4 and CD8 T cells in KO and control mice. **F**) Quantification of **E**. Graphs shown mean + SD. Shown in **A-C** is one repeat of two experiments. n_{KO}=3; $n_{Control}$=6. In **D-F**, n_{KO}=4; $n_{Control}$= 10. **P<0.01; ****P<0.001 Two-way ANOVA with Sidak's multiple comparison. T_{CM}= Central

memory T cells; T_{EM}= Effector memory T cells; T_N= Naïve T cells; T_{EFF}= effector T cells; FSC-A= forward scatter-area; FSC-H= forward scatter-height; SSC-A= side scatter-area.

To detect early T cell responses to CD3/28 stimulation, I again measured CD154, CD69, and CD25 upregulation (**Fig. 4.7A-E**). Unlike the patient, KO T cells expressed normal levels of all three activation markers at the time points examined, with the exception of a slight decrease in CD154 upregulation after 24 hours (**Fig. 4.7B-E**). Similarly, KO T cells were capable of proliferating normally after three (**Fig. 4.7F,G)** and five (data not shown) days of stimulation, as quantified by division and proliferation indices. This would suggest that the defective T cell responses seen in the patient are due to the increase in T cells with exhausted or senescent phenotypes rather than a direct consequence of GIMAP6 loss. However, this discrepancy may also result from a difference between human and mouse GIMAP6 function or additional genetic modifiers in the patient. Alternatively, the patient could potentially have a digenic Mendelian disease, for which the *Gimap6* KO mice would be an incomplete model.

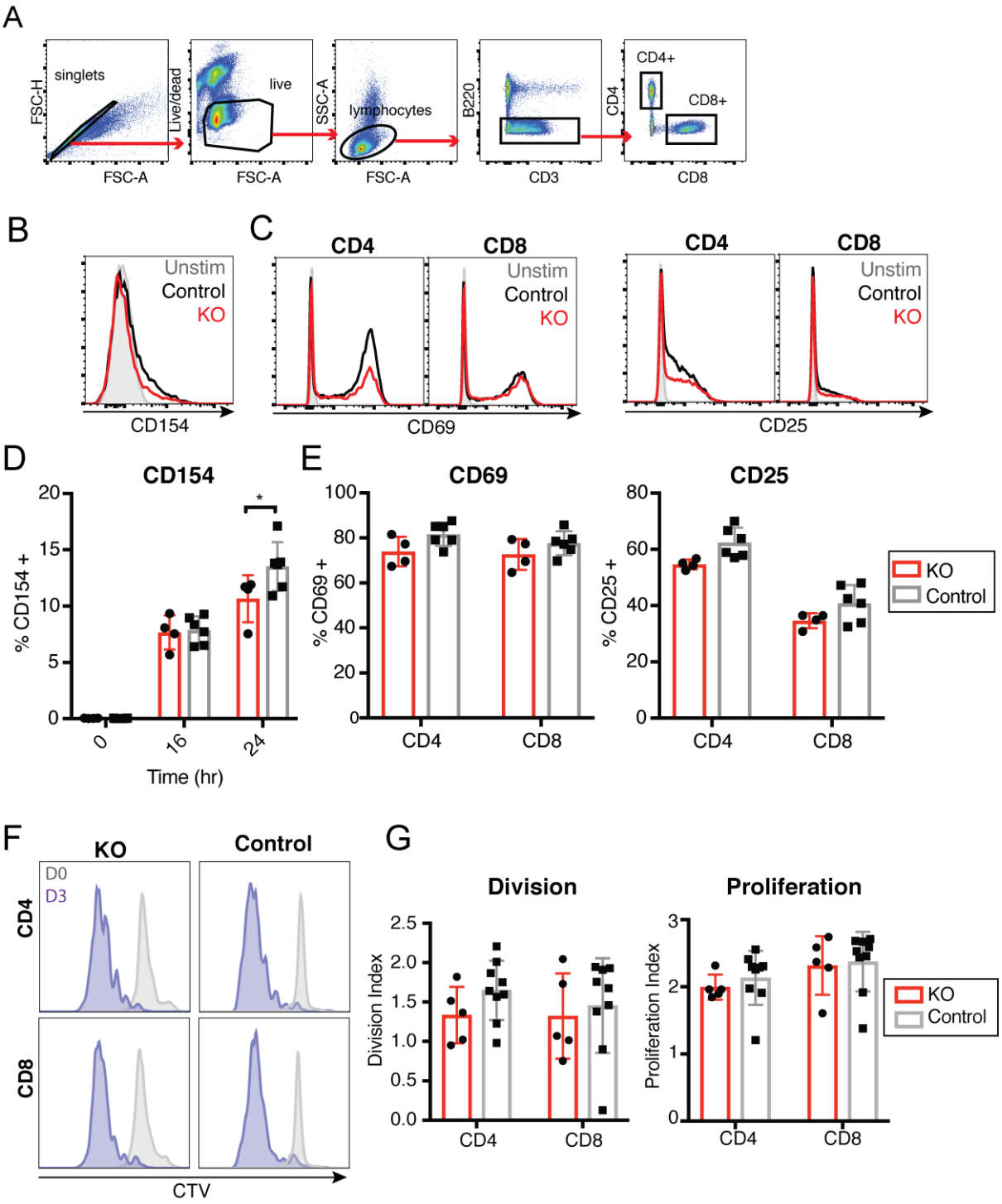


Fig. 4.7. *Gimap6*$^{-/-}$ mice have normal T cell activation and proliferation. Whole splenocytes from *Gimap6*$^{-/-}$ or *Gimap6*$^{+}$ mice were stimulated with 1 μg/mL of plate bound anti-CD3 and 1 μg/mL of soluble anti-CD28 antibody for the indicated amount of time before flow cytometric analysis. **A)** Gating strategy for CD4 and CD8 T cells. **B, C)** Representative flow plots showing CD154 upregulation in CD4 T cells (**B**) or CD69 and CD25 (**C)** upregulation in unstimulated (unstim) CD4 and CD8 T cells or after 24 hours of stimulation. **D**) Quantification of **B**. **E**) Quantification of **C**. **F)** Representative flow plots showing CellTrace Violet (CTV) dilution in T cells stimulated for 0 or 3 days (D0 or D3 respectively). **G**) Quantification of Quantification of **F.** Graphs shown mean + SD. For **A-E**, n_{KO}=4; $n_{control}$=6. For **F, G,** n_{KO}=5;

$n_{control}$=9. Shown in **F,G** is one of two independent repeats. *P<0.01; **p<0.01; ***P<0.005; ****P<0.001 Two-way ANOVA with Tukey's multiple comparison test. FSC-A= forward scatter-area; FSC-H= forward scatter-height; SSC-A= side scatter-area; d=day.

4.2.4 Immunophenotyping of Gimap6$^{-/-}$ competitive bone marrow chimeras

Alterations in cellular phenotypes can be due to either cell intrinsic factors, meaning those caused by changes in the affected cells themselves, or extrinsic factors, meaning those caused by changes in other cells that influence the behavior of the altered cells, such as secretion of cytokines. To determine whether the alterations in the KO mice were due to intrinsic or extrinsic factors, I analyzed cell populations in mixed bone marrow chimeras. CD45, a protein tyrosine phosphatase, is expressed on all nucleated cells of hematopoietic origin (*510*). Because CD45 exists in two allelic variants (CD45.1 and CD45.2), cells arising from different progenitors can be tracked in chimeras as long as the donors had different CD45 isoforms. *Gimap6* KO mice are CD45.2$^+$, so I combined bone marrow from a KO or CD45.2$^+$ WT mouse with that of a B6.SJL mouse that is CD45.1$^+$ in a one to one mixture before transferring it to a lethally irradiated CD45.1$^+$ host (**Fig. 4.8A).** Staining of peripheral blood revealed that KO haemopoietic stem cells (HSC) were capable of normal levels of reconstitution (**Fig. 4.8B).** A closer examination of the lymphocyte populations showed KO bone marrow gave rise to similar levels of B, T, and NK cells as WT (**Fig.4.8C-F**). Levels of follicular (FO) B cells, which comprise of the majority of mature lymphoid tissue B cells, and marginal zone (MZ) B cells, specialized B cells in the marginal zone of the spleen, were also comparable between the two CD45.2$^+$ groups (**Fig. 4.8F**). Though not statistically significant, CD45.2^{KO} NKT cells comprised a smaller percentage of the total NKT population than CD45.2^{WT} cells **(Fig.4.8E**), which is consistent with the reduced NKT population seen in *Gimap6* KO mice. A repeat of this experiment displayed variation in the reconstitution of CD45.2$^+$ cells, but

showed similar results as shown here. Intrinsic factors therefore do not seem to cause the B cell lymphocytosis present in KO mice, suggesting extrinsic factors must be involved.

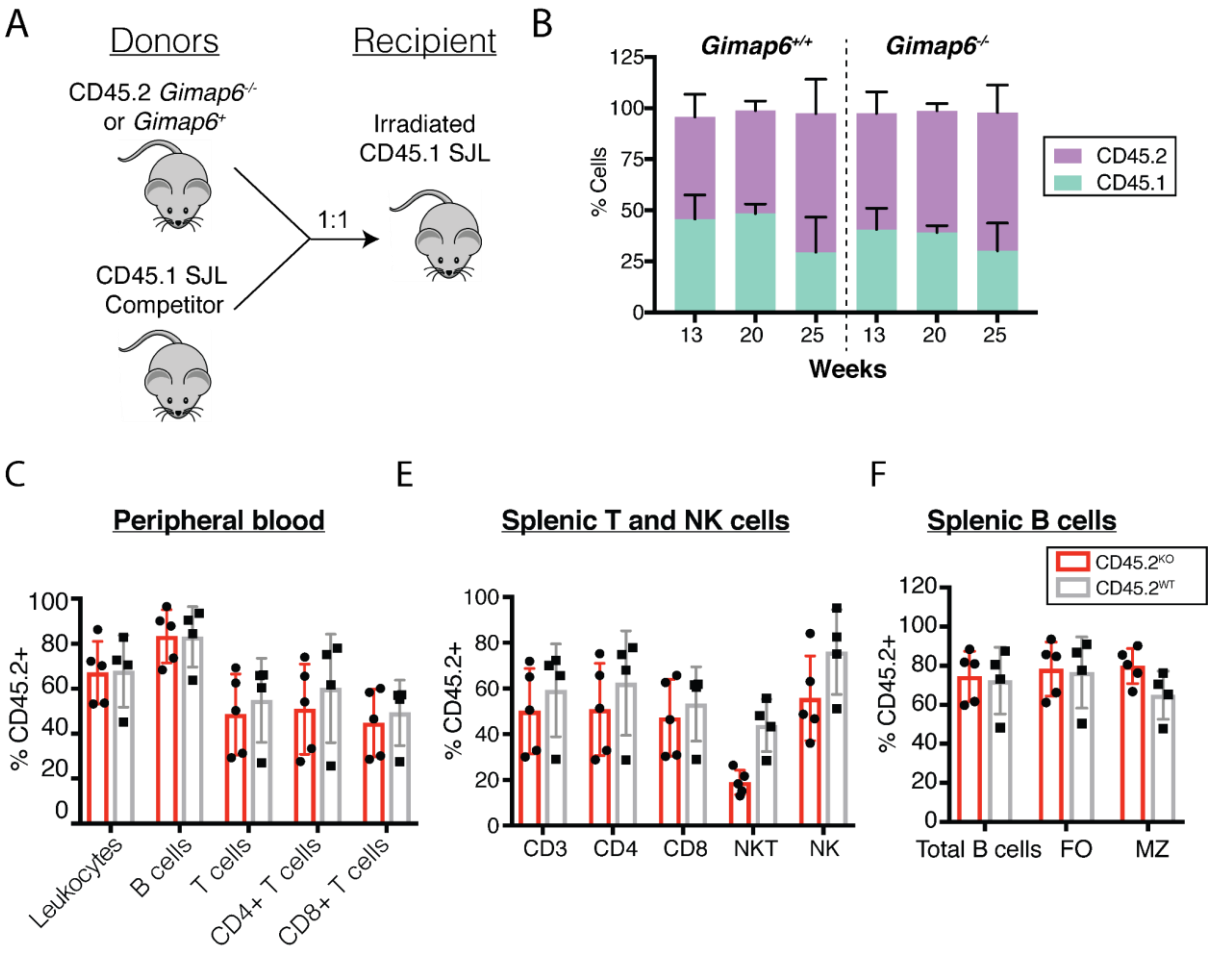


Fig. 4.8. *Gimap6*$^{-/-}$ lymphocyte populations are normally reconstituted in mixed bone marrow chimeras. Either CD45.2^{+} knockout (CD45.2^{KO}) or CD45.2^{+} control (CD45.2^{WT}) bone marrow was mixed with an equal amount of CD45.1^{+} B6.SJL bone marrow and used to reconstitute lethally irradiated B6.SJL hosts, as shown in **A**. **B)** Reconstitution of leukocytes was assessed at the indicated weeks after the transfer **C-F)** At 25 weeks post transfer, mice were harvested for further assays. The percent of CD45.2^{+} B and T cells in peripheral blood is shown in **C**. Splenocytes from chimeras were stained and analyzed by flow cytometry for T and NK populations (**E**) and total, follicular (FO), and marginal zone (MZ) B cells (**F**). Gating strategies for **B,C** are shown in **Fig. A.1A**, in **Fig. A.1B** for **E,** and **Fig. A.1C** for **F.** Shown in is one of two independent repeats. $n_{KO:SJL}$=5; $n_{WT:SJL}$=4. ns= not significant by Two-way ANOVA with Tukey's multiple comparison test. FSC-A= forward scatter-area; FSC-H= forward scatter-height; SSC-A= side scatter-area.

T cells in KO mice have a decrease in CD8 central memory cells and a slight increase in cells with an exhausted and senescent phenotype. I stained T cells from the chimeras to determine if these phenotypes were due to intrinsic factors in *Gimap6*$^{-/-}$ T cells (**Fig. 4.9**). As in the KO mice, CD8 T cells originating from KO progenitors had reduced T_{CM} with a shift towards a naïve-phenotype (**Fig. 4.9A,B**). Contrary to KO mice, CD4 T cells in the chimeras also showed this same skewing. Therefore, the GIMAP6 deficiency appears to cause intrinsic alterations that favor a naïve phenotype over central memory. On the other hand, the increase in PD-1^{+} and KLGR1^{+} cells in KO mice appears to be due to environmental factors, as CD45.2^{KO} CD4 and CD8 T cells had normal levels of both markers (**Fig.4.9C-F,K,L**). Interestingly, while KO mice had a slight increase in Tfh cells, CD45.2^{KO} Tfh cells made up less than 30% of the total subset in chimeras (**Fig. 4.9G,H**). In comparison, over 50% of Tfh cells in chimeras with CD45.2^{WT} bone marrow were CD45.2^{+}, suggesting that *Gimap6*$^{-/-}$ Tfh cells have a competitive disadvantage in chimeras. Though FOXP3 staining is necessary for confirmation, it does not appear that *Gimap6*$^{-/-}$ Tregs have any disadvantage as there was no significant difference between the frequency of CD45.2 CD4^{+}CD25^{+} cells (**Fig. 4.9I,J**).

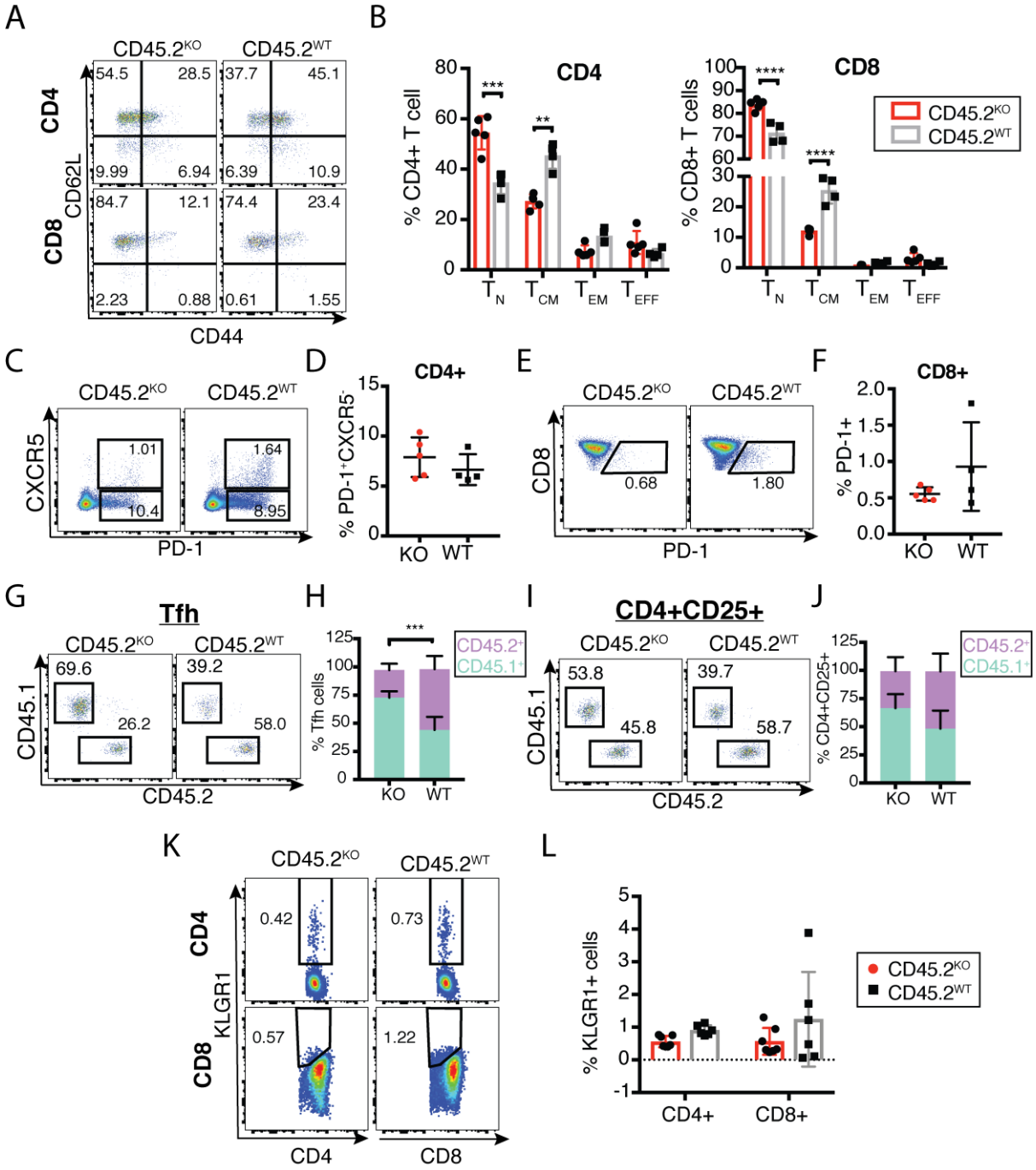


Fig. 4.9 *Gimap6*$^{-/-}$ T cells have skewed subsets in mixed bone marrow chimeras. Splenocytes from mice shown in **Fig. 4.8** were stained to assess T cell subsets. **A)** Representative flow plots showing naïve and memory populations of CD45.2+ CD4 and CD8 T cells. **B)** Quantification of **A**. showing mean, standard deviation, and values of individual samples. **C, E)** Representative flow plot showing CXCR5 and PD-1 expression in CD45.2+ CD4 (**C)** or CD8+ (**E**) T cells. **D,F**) Quantification of **C** and **E** respectively**. G,I**) Flow plot showing CD45.1+ and CD45+ populations in CXCR5+PD-1+ Tfh cells (**G**) or CD4+CD25+ (**I**) cells. **H,J**) Quantification of **G** and **I**, respectively. **K)** Flow plots showing KLGR1 staining in CD45.2+ CD4 and CD8 T cells. **L**) Quantification of **K.** Gating strategies for **A-J** are shown in **Fig. A.1B** and in **Fig. A.1D** for **K,L.** Shown in is one of two independent repeats. $n_{KO:SJL}$=5; $n_{WT:SJL}$=4. *P<0.05,

P<0.01;*P<0.005, ****P<0.001 by Two-way ANOVA with Tukey's multiple comparison test. FSC-A= forward scatter-area; FSC-H= forward scatter-height; SSC-A= side scatter-area; Tfh= T follicular helper; T_N= naïve T cell; T_{CM}= T central memory; T_{EM}= T effector memory; T_{EFF}= T effector.

To verify the results seen in the KO mice, I also stimulated splenocytes from the mixed bone marrow chimeras with anti-CD3/28 antibodies to examine T cell activation (**Fig. 4.10)**. As expected, CD45.2^{KO} CD4 and CD8 T cells upregulated CD69 to similar levels as both CD45.2^{WT} and control CD45.1^{+} cells at the time points examined (**Fig. 4.10B,C**). Quantification of division and proliferation index in CTV stained cells also showed normal proliferation after three days (**Fig. 4.10D,E**). These data are consistent with the results seen after TCR activation in germline *Gimap6* KO mice and indicates that GIMAP6 deficiency in mouse cells does not impair TCR-induced responses.

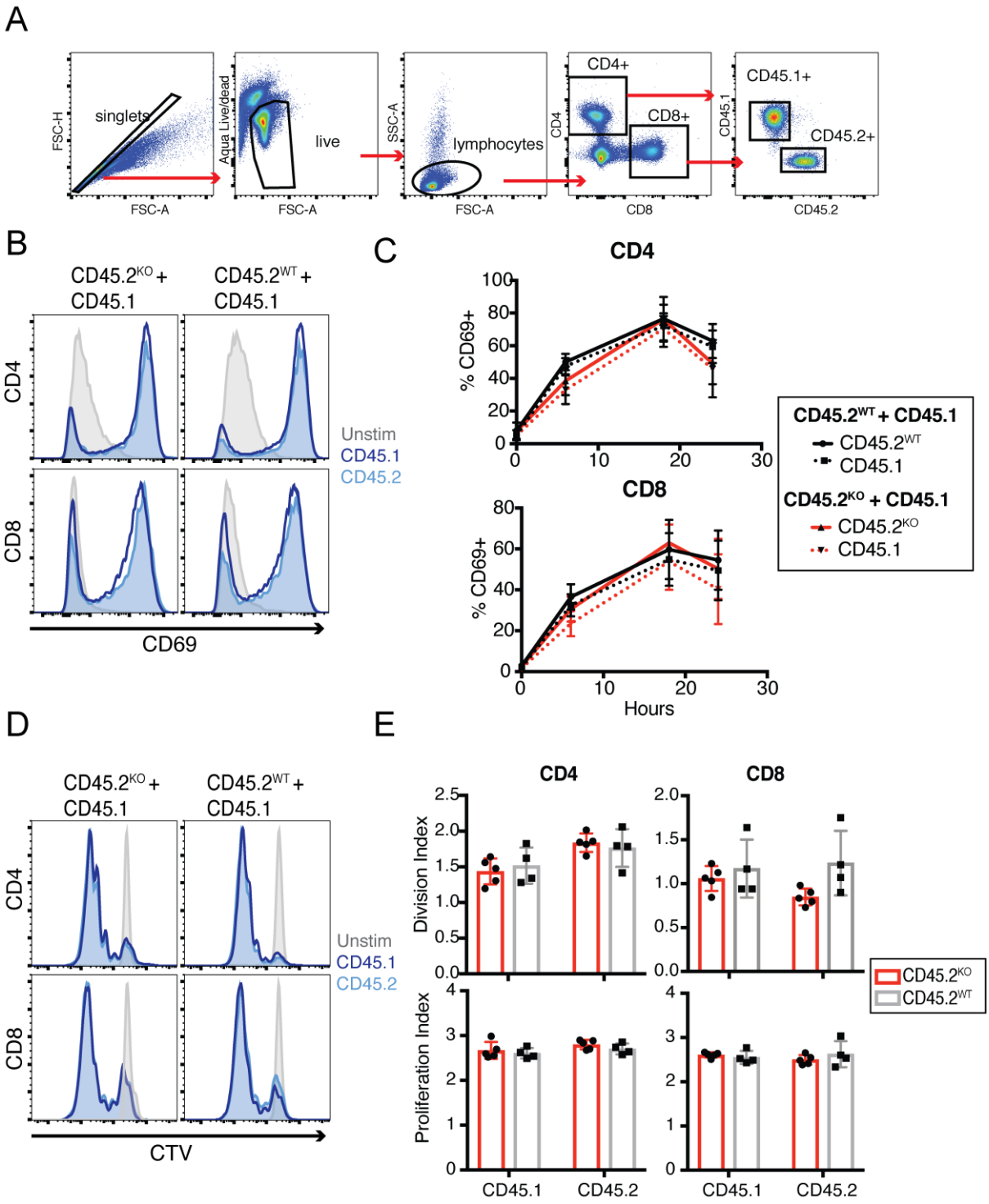


Fig. 4.10 T cell proliferation in bone marrow chimeras. Either CD45.2 knockout (CD45.2^{KO}) or CD45.2 control (CD45.2^{WT}) bone marrow was mixed with an equal amount of CD45.1 B6.SJL bone marrow and used to reconstitute irradiated SJL hosts. Splenocytes were activated with 1 μg/mL of plate bound anti-CD3 and 1 μg/mL of soluble anti-CD28 antibody, analyzed by flow cytometry at the times indicated, and gated for CD4 and CD8 CD45.1^{+} or CD45.2^{+} T cells. **A)** Gating strategy **B)** Representative flow plots showing CD69 upregulation in unstimulated (unstim) CD4 and CD8 T cells or after 24 hours of stimulation. **C)** Quantification of **B. D**) Representative flow plots showing CellTrace Violet (CTV) dilution in T cells stimulated for 3

days **E**) Quantification of **D.** Graphs shown mean + SD. $n_{KO:SJL}$=5; $n_{WT:SJL}$=4. Shown is one of two independent repeats. FSC-A= forward scatter-area; FSC-H= forward scatter-height; SSC-A= side scatter-area.

4.2.5 Investigating B cell responses in Gimap6$^{-/-}$ mice

PID1467's disease appears to be largely antibody-mediated. As murine GIMAP6 is expressed in B cells, I examined whether its loss affected B cell function in KO mice. ELISAs for total serum IgG and IgM revealed normal levels of both antibody subclasses (**Fig. 4.11A,B).** I then assessed humoral responses by immunizing mice with the T-cell dependent (TD) antigen NP-CGG along with alum as an adjuvant (**Fig. 4.11C-J).** ELISAs showed rapid induction of antigen-specific IgM soon after the primary immunization (**Fig. 4.11D**), as well as a gradual increase in class-switched NP-specific IgG1 in KO and control mice (**Fig. 4.11E**). To assess memory responses, a secondary immunization (boost) was given to mice after five weeks, resulting in a strong, rapid production of NP-specific IgG1 in both sets of mice (**Fig.4. 11E**). Measurement of NP-specific IgG1+ B cells in splenocytes by flow cytometric analysis showed similar levels of these memory B cells in KO mice (**Fig. 4.11F-H**). Additionally, I measured the amount of NP-specific IgG1 secreting cells in both spleen and bone marrow using an enzyme-linked immunospot (ELISpot) assay one month post boost (**Fig. 4.11I,J**). KO splenocytes and bone marrow cells produced similar numbers of spots as controls, indicating comparable level of antibody secreting cells. While there was a large amount of variance between mice in each group, possibly due to technical issues, there is no indication that murine GIMAP6 deficiency impairs TD antibody responses.

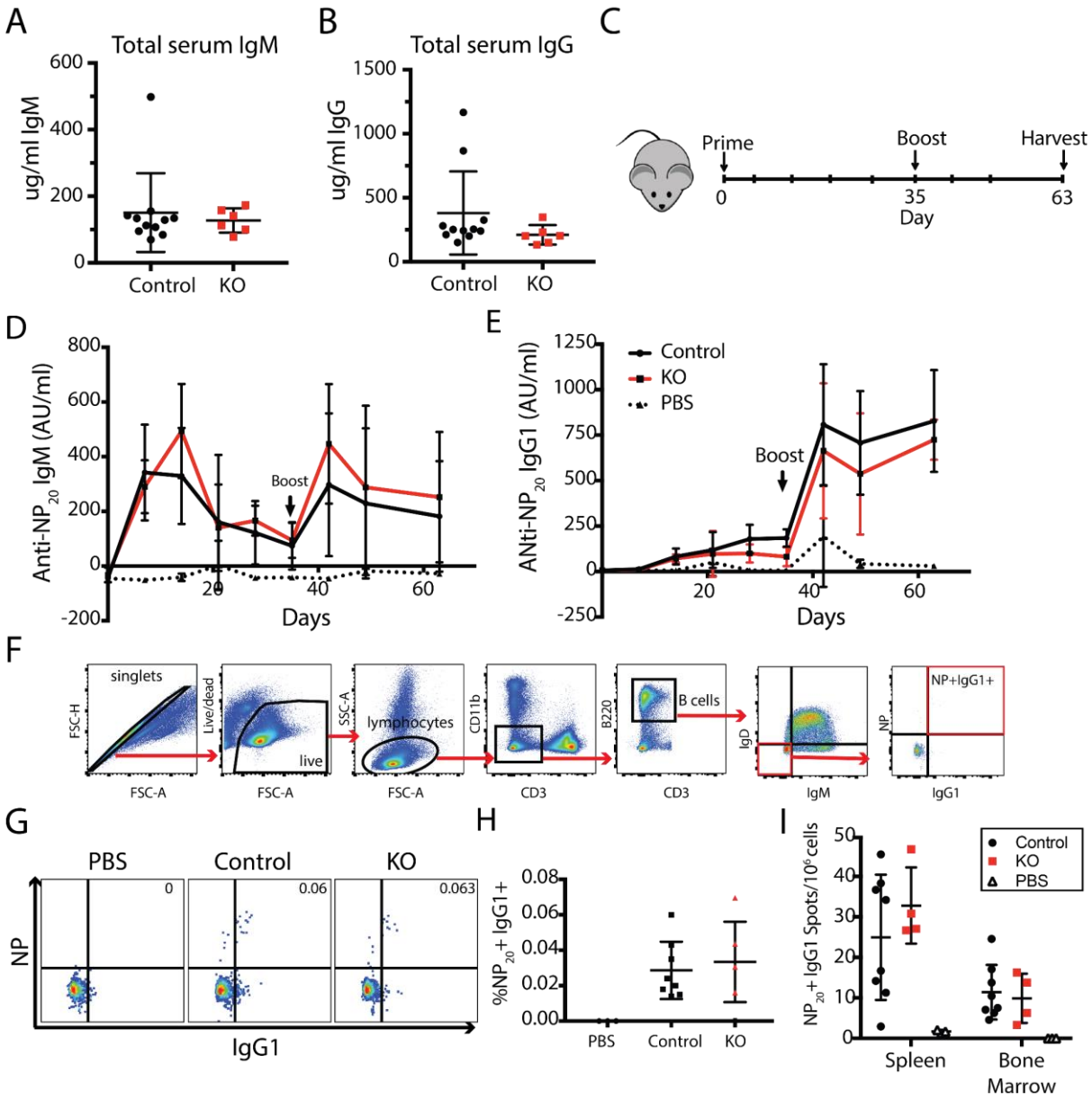


Fig. 4.11 *Gimap6*$^{-/-}$ mice have normal antibody responses. A,B) Total serum IgM (A) and total serum IgG (B) were analyzed by ELISA. **C-I)** Mice were given an i.p. injection of 50 μg NP-CGG in PBS with a 1:1 ratio of Imject alum adjuvant and then boosted 35 days later. PBS with alum was injected in some mice as a negative control. Serum was collected and analyzed for NP-specific IgM (**D**) and IgG1 (**E**) antibodies using an ELISA. **C)** Diagram showing experimental regimen. **D,E**) Anti-NP_{20} IgM (**D)** and IgG (**E)** in collected samples were analyzed by ELISA **F-H)** Spleens of immunized mice were harvested on day 63 and splenocytes were stained and analyzed by flow cytometry to determine levels of NP-specific $IgG1^+$ B cells. **F)** Gating strategy of NP-specific $IgG1^+$ B cells. **G)** Representative flow plots showing percent of NP^+IgG1^+ B cells in PBS controls or NP-CGG immunized control and KO mice. **H)** Quantification of **G**. **I)** ELISPOTs were used to quantify the number of NP-specific IgG1 secreting cells from the spleen and bone marrow of NP-CGG injected mice. Shown is one representative experiment of three for **A, B**. Shown is one representative experiment of two for **D-I**. $n_{control}$=11, n_{KO}=6 for **A,B**. n_{PBS}= 3, $n_{control}$= 8, n_{KO}=4 for **D-I**. Graphs show mean +/- SD. FSC-A= forward scatter-area; FSC-H=

forward scatter-height; SSC-A= side scatter-area; AU=arbitrary units; NP= 4-Hydroxy-3-nitrophenylacetyl; NP-CGG= NP-chicken gamma globulin.

Given that I observed no impairment in TD antibody responses, I wondered whether T cell-independent (TI) responses might be affected. I stimulated enriched B cells *in vitro* with LPS, a TI stimulus, and measured upregulation of the activation markers CD69, CD86, and MHC II **(Fig. 4.12A-C**). MHC II levels in response to stimulus were comparable between KO and control mice, but KO B cells showed significantly higher expression of CD86 and CD69 by 18 hours post-activation (**Fig. 4.12B,C**). KO B cells also had an increase in proliferation as quantified by division index, but not proliferation index, by day three; this indicates that a greater percentage of KO B cells than controls underwent proliferation, but that cells that entered the cell cycle divided a similar number of times in both groups **(Fig. 4.12D,E**). LPS induces class switching from IgM and IgD to IgG3 and IgG2b in mice, and both could be detected by flow cytometry by day 3 (**Fig. 4.12F,G)** (*511*, *512*). Interestingly, while they had a similar frequency of class switching to IgG3, KO B cells had a greater percentage of $IgG2b^+$ cells than controls by day five. Although this data is preliminary, it suggests that loss of GIMAP6 may cause differences in murine TI B cell responses, including potential hyperactivation and skewing towards certain antibody subclasses.

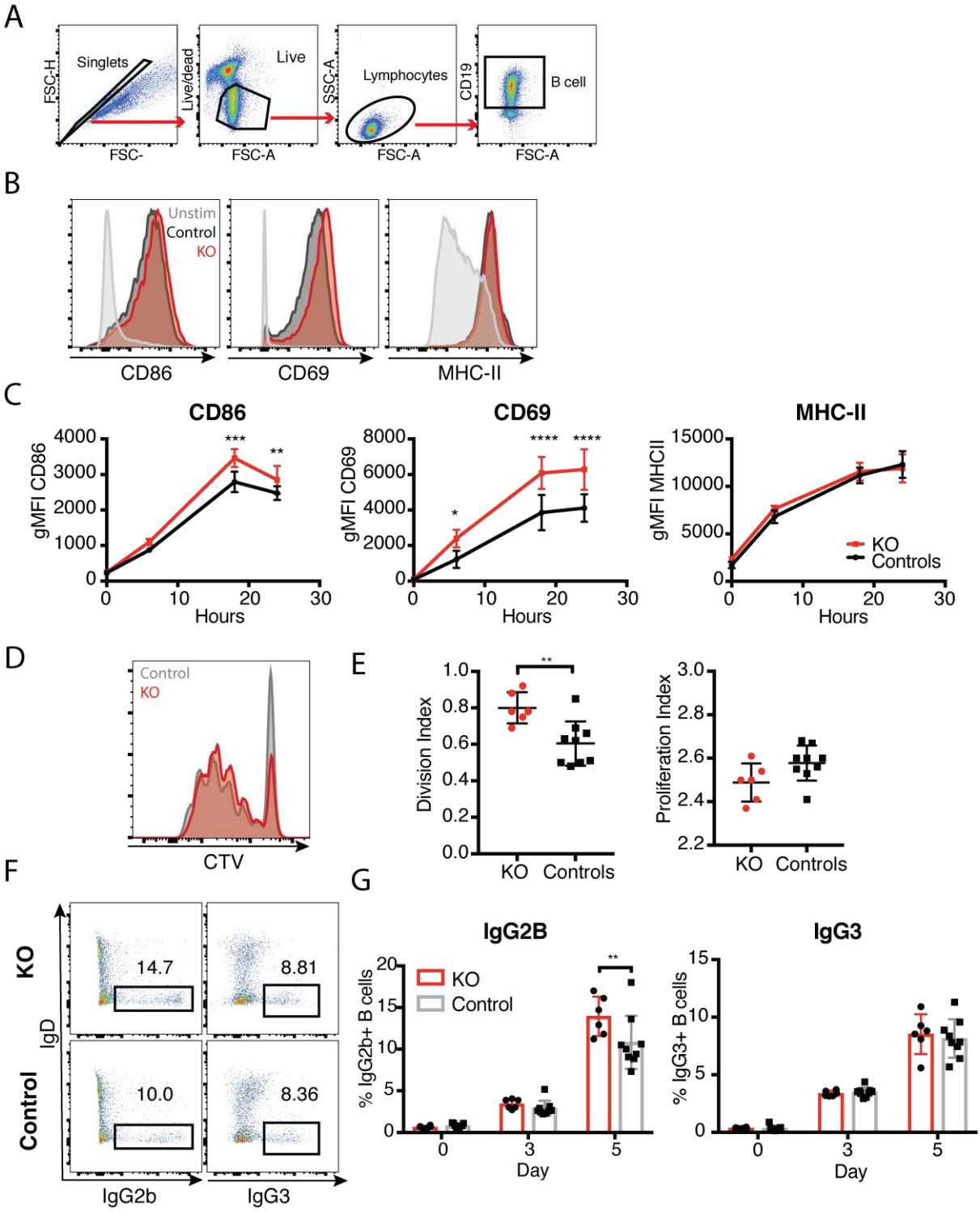


Fig. 4.12 *Gimap6*$^{-/-}$ B cells have potential hyperactivation. B cells were enriched from splenocytes and activated for the indicated amount of time using 10 μg/mL LPS before staining for flow cytometric analysis. **A**) Gating strategy used. **B**) Representative flow plots showing upregulation of the activation markers CD86, CD69, and MHC-II in B cells stimulated for 18 hours or an unstimulated control. **C)** Quantification of **B**. **D)** Representative flow plot showing CTV dilution in proliferating B cell after three days of stimulation. **E)** Quantification of cell proliferation in **D** showing division index and proliferation index**. F)** Representative flow plot showing the percent of IgG2B^{+} or IgG3^{+} B cells after five days of LPS stimulation. **G**)

Quantification of **F**. n_{KO}=6; $n_{Control}$=9. *P<0.05; **P<0.01; ***P<0.005; ****P<0.001 Repeat measures two-way ANOVA with Sidak's multiple comparison. . Graphs show mean +/- SD. FSC-A= forward scatter-area; FSC-H= forward scatter-height; SSC-A= side scatter-area; gMFI= geometric mean fluorescence intensity; CTV= cell trace violet.

4.3 Discussion

In this chapter, I discuss the identification of a novel missense mutation in *GIMAP6* in a Turkish PID patient and work done to immunophenotype both the patient and a mouse model of her disease.

4.3.1 Identification of mutation in GIMAP6 as a potential disease-causing variant

In **Chapter 3**, I described a cohort of patients with homozygous or compound heterozygous missense mutations in *GIMAP5* that resulted in a novel PID. Because of that finding, we screened our patient cohort for patients with mutations in other GIMAP proteins, leading to the identification of the patient described in this chapter. The clinical presentation of the GIMAP6 patient was similar to patients with GIMAP5 deficiency, including splenomegaly, lymphadenopathy, and lung infections. However, she did not share the lymphopenia or liver disease characteristic of the GIMAP5 patients; instead, her major symptoms seemed to be due to autoimmunity with some vascular complications, whereas only one third of GIMAP5 patients had detectable autoantibodies. Additionally, PID1467 has hyper-IgM and hypo-IgA and IgG, whereas GIMAP5 patients presented only with reduced antibody levels. While difficult to reach firm conclusions based on one patient, this difference suggests that GIMAP6 and GIMAP5 influence different aspects of immunity, with GIMAP5 more involved in peripheral lymphocyte survival and homeostasis and GIMAP6 in humoral immunity. However, GIMAP5 is associated with several autoimmune diseases, including SLE,

diabetes, and asthma in humans as well as diabetes and colitis in rodents (*471–475*, *513–515*). Other GIMAPs are also implicated in autoimmunity: GIMAPs 1, 2, and 4 with Behçet's disease, a chronic inflammatory disorder, in Asians but not Europeans, and GIMAP4 with allergic sensitization (*70*, *475*, *516*). Therefore, a role for GIMAP6 in autoimmunity is consistent with current GIMAP literature.

All identified mutations in the GIMAP5 cohort are missense mutations that seem to result in a loss of protein. The identified mutation in PID1467 is also a missense mutation. Western blotting of patient T cells and an overexpressed construct of the patient's variant showed both a decrease in GIMAP6 levels and a faster migrating form of the protein. Therefore, the glycine to valine mutation may affect GIMAP6 structure or possibly an unidentified post-translational modification, resulting in protein instability. The G153V mutation therefore likely causes a LOF disease similar to those in the GIMAP5 cohort.

4.3.2 The role of GIMAP6 in T cell activation

Because GIMAP6 is highly expressed in T cells, I examined T cell function in response to TCR stimulation in patient and mouse cells. Though patient T cells had poor upregulation of several activation markers, CD8 T cells were capable of normal proliferation while CD4 T cells had reduced capabilities. Mouse T cells lacking GIMAP6, on the other hand, had no such aberrations. Consistent with these results, a paper published after the start of this study also saw no differences in T cell activation in mice with a conditional ablation of GIMAP6 in B and T cells (*517*). Another paper published during this study, however, observed an increase in activation markers and IL-2 secretion following PMA/ionomycin stimulation in Jurkat and primary human T cells lacking GIMAP6, suggested GIMAP6 deficiency may cause

hyperactivation (*518*). However, the study tested only two clonal Jurkat lines and had poor knockdown efficiency in primary cells (an average of ~26% and 6%).

Species differences or possibly other mitigating factors may explain these discrepancies. While similar, mouse and human immune systems have several differences, including variations in expression of some genes (reviewed in (*519*)). This, however, does not fully explain discrepancy between the defective activation observed here in the patient and hyperactivation resulting from GIMAP6 knockdown observed by Ho et al. (*518*). An equally plausible explanation is that the patient's T cell defect may be due to extrinsic factors affecting her T cell function. Staining of patient T cells showed a skewing towards cells with a memory-phenotype, as well as an expansion of cells with markers for activation, exhaustion, and senescence. This phenotype is consistent with a state of continuous immune activation common in people with chronic infection, CVID, or autoimmunity like the patient (*498*, *520*–*522*). Therefore, the abnormalities in the patient's T cell responses could be due to functional changes resulting from constant antigenic stimulation and inflammation rather than inherently from a loss of GIMAP6. Lastly, it is possible that the patient's unique genetic background, such as the variants discussed in Section 4.2.1, may contribute to her T cell phenotype. GIMAP6 knockdown in healthy human T cells as well as transduction of wildtype GIMAP6 into naïve patient T cells for rescue experiments should be done to verify which of the proposed explanations is correct.

4.3.3 Changes in T cell populations in Gimap6 KO mice

Though there was a decreased T cell frequency in KO mice, there was no observed decrease in splenic T cell numbers. By contrast, mice with CD2-Cre driven ablation of *Gimap6* were reported to have significant lymphopenia due to increased apoptosis (*517*). This

discrepancy is not easily explained, but it is possible that a non-lymphocyte lineage cell affecting T cell homeostasis also expresses GIMAP6 and thus be affected in the germline, but not conditional, knockouts. However, as mixed bone marrow chimeras had no obvious difference in T cell reconstitution, this potential extrinsic factor is likely of hematopoietic origin.

While the patient's T cells skewed towards a memory phenotype, there was instead a loss of T_{CM} with a corresponding gain in T_N in KO CD8 T cells. A similar shift was also evident in both CD45.2^{KO} CD4 and CD8 T cells in mixed bone marrow chimeras, suggesting an intrinsic factor at work. This is an interesting phenotype as T_{EM} do not appear to be affected and an inclination for naïve cells is an uncommon phenotype in knockout strains. One possibility may be that GIMAP6 affects metabolism; while naïve cells utilize oxidative phosphorylation and effector cells use aerobic glycolysis, memory T cells rely on fatty acid oxidation (FAO) (*371*, *523–526*). In particular, T_{CM} seem to have specific metabolic requirements not yet clearly understood, with the need for excess mitochondrial spare respiratory capacity and uptake of glycerol and glucose to generate triacylglycerides that they then internally break down into fatty acids for FAO rather than take up external free fatty acids as T_{EM} do (*270*, *271*, *527*). GIMAP6 may perhaps alters metabolism in a way that disfavors survival or differentiation into the T_{CM} but not T_{EM}.

Though not as dramatic as in patient T cells, KO mice also had an increase in the frequency of cells expressing the senescence marker KLRG1 and the exhaustion marker PD-1, especially in the CD4 T cell population. There also was an expansion of CXCR5$^+$PD-1$^+$ CD4 T cells, which are typically Tfh cells; however, staining for the lineage marker Bcl-6 would be needed to confirm their status as true Tfh cells since both CXCR5 and PD-1 can also be upregulated shortly after activation. CD25 expression was slightly elevated in CD4 T cells,

though this appeared to be due to mild increases in both the $CD25^{+}FOXP3^{+}$ Treg compartment and the $CD25^{+}FOXP3^{-}$ activated T cell population. These changes were not seen in mixed bone marrow chimeras, indicating they are likely due to extrinsic factors in KO mice, possibly a different cytokine environment. It would thus be interesting to measure cytokine levels in KO mice to see if perhaps there is a pro-inflammatory environment resulting in upregulation of these markers. One other interesting observation was that though $CXCR5^{+}PD\text{-}1^{+}$ Tfh-like cells were elevated in KO mice, *Gimap6*$^{-/-}$ cells reconstituted a lower percentage of that subset in mixed bone marrow chimeras, suggesting that *Gimap6* KO cells can differentiate into Tfh cells, but may have a competitive disadvantage filling that niche.

While several GIMAPs are important in lymphocyte survival, the data presented in this thesis suggests GIMAP6 is less critical for this function. However, apoptosis studies will be needed to verify whether GIMAP6 has any anti-apoptotic function as has been suggested in recent papers (*517*, *518*). While KO T cells had no obvious issues in responding to TCR stimulus, it would be interesting to determine whether GIMAP6 has a role in differentiation or cytokine release. GIMAP1 and GIMAP4, after all, are differentially regulated during Th1/Th2 differentiation, with GIMAP4 playing a particular role in cytokine production (*459*, *469*, *470*). A skewing towards a pro-inflammatory subset could explain both the autoimmunity in the patient and the phenotypic alterations in KO T cells.

4.3.4 Role of GIMAP6 in B cells

Unlike mice, human B cells do not appear to express GIMAP6, though that does not exclude the possibility that GIMAP6 may be upregulated under specific conditions (*518*). As the patient has antibody-mediated autoimmunity, I immunized mice with a TD antigen to determine whether *Gimap6* KO mice had impaired antibody responses. Though there was

large inter-mouse variation, no obvious defect was observed. This finding was supported by experiments in the CD2-Cre conditional *Gimap6* knockout mice, which had comparable results using a similar antigen (*517*). Interestingly, the increased cellularity in KO spleens was due to an increase in B cells that did not seem to be reproduced in mixed bone marrow chimeras, again suggesting an extrinsic factor. It would be interesting to see if the increased upregulation of activation markers or increased class-switching to IgG2b in response to LPS are also observed in chimeras as both of these effects could potentially be explained by changes in cytokines. Further work is needed to elucidate the role of GIMAP6 in murine B cells and its relevance to its human counterparts.

Chapter 5. Loss of GIMAP6 results in defective autophagy in T cells

5.1 Introduction

5.1.1 Potential role of GIMAP6 in autophagy

In this chapter, I investigate the potential role of GIMAP6 in autophagy in lymphocytes. The GIMAP family of proteins are small GTPases in the TRAFAC (Translation Factors) family of G proteins (*528*). They are closely related to Toc (translocon on the outer chloroplast membrane) proteins, which are chloroplast transport proteins, and septins, which are scaffolding proteins involved in cytoskeletal organization (*461*, *529*, *530*). Structurally, GIMAPs also have similar features as the dynamin vesicular trafficking proteins (*461*). Though all seven human and eight murine GIMAP proteins contain guanine nucleotide-binding domains (G domains), only GIMAP1, GIMAP2, GIMAP3 (a pseudogene in humans), and GIMAP5 have transmembrane domains involved in membrane association(*327*, *461*, *513*). Overexpressed GIMAP6 was originally reported to be cytosolic (*460*). However, the Butcher group later showed that both overexpressed and endogenous GIMAP6 are recruited to autophagosomes following autophagy induction through starvation or mTORC1 inhibition, thus indicating a potential link between GIMAP6 and autophagy (*332*).

Supporting this potential connection, the Butcher group identified GABARAPL2 (GABA [gamma-aminobutyric acid] type A receptor associated protein like 2) as a strong binding partner of human GIMAP6 in cross-linking studies (*332*). This interaction was later independently verified by the Daumke group (*531*). GABARAPL2, also called GATE-16 (Golgi-associated ATPase enhancer of 16 kDa), is one of the seven human homologues of the

autophagy protein Atg8, which consists of the LC3 (LC3A, LC3B, and LC3C) and GABARAP subfamilies (GABARAP, GABARAPL1, GABARAPL2, and GABARAPL3) (*532*). As discussed in **Chapter 1**, Atg8 proteins are involved in autophagosomal maturation and closure, as well as autophagosome-lysosome fusion (*533–536*). Additionally, Atg8 proteins confer cargo specificity by targeted binding to receptors containing Atg8 interacting motifs (AIM) (*537*, *538*). Interestingly, though GIMAP6 has a putative N-terminal AIM, it does not mediate its interaction with GABARAPL2; instead, the terminal ten amino acids (283-292) are necessary for binding (*332*). Deletion of these residues prevents autophagosomal localization after starvation, and both full length GIMAP6 and GABARAPL2 levels drop within 12 hours of starvation, suggesting that GABARAPL2 may recruit GIMAP6 to the autophagosome for degradation (*332*). However, mouse GIMAP6 binds only weakly to GABARAPL2, and GIMAP6 expression seems to modulate GABARAPL2 level (*332*). Therefore, GIMAP6 may play a functional role in autophagy rather than simply being a target for autophagic degradation.

Due to the importance of autophagy in immune cells (discussed in **Chapter 1**) and the potential connection between autophagy and GIMAP6 demonstrated in mice by the Butcher lab, I investigated whether loss of GIMAP6 affects autophagy in primary human or murine lymphocytes or in cultured cell lines.

5.2 Results

5.2.1 Gimap6$^{-/-}$ mice have an autophagic defect in lymphocytes

To determine the role of GIMAP6 in autophagy, I first looked at whether this pathway was affected in *Gimap6* KO mice. Because GIMAP6 is expressed in murine T and B cells, I measured basal autophagy levels in splenic lymphocytes using the flow cytometric assay described in **Chapter 3** (**Fig. 5.1)**. Other than B cells, all KO populations observed had higher

LC3-II levels than normal controls (vehicle samples in **Fig. 5.1A, B**). Accumulated autophagosomes could signal either an increase in autophagic flux or a block somewhere in the autophagic process. To distinguish between the two, I used bafilomycin A1 (baf), a lysosomal inhibitor that prevents lysosomal acidification and autophagosome-lysosome fusion (*398*, *399*), to block autophagosome degradation. Only KO NK and NKT cells had higher LC3-II levels than controls after bafilomycin treatment; treated *Gimap6*$^{-/-}$ CD8 T cells had lower levels than controls **(**bafilomycin samples in **Fig. 5.1A,B**). When autophagic flux, or the rate of autophagy, was determined by normalizing LC3-II levels in bafilomycin-treated cells to those in vehicle treated cells, it revealed a diminished flux in several KO cell populations (**Fig.5.1C**). While KO B cells had only a very minor, though statistically significant, reduction in flux, KO T cells had a comparatively large defect, particularly in CD4 T cells (**Fig. 5.1C)**. Surprisingly, though NK cells were not previously thought to express *Gimap6*, they also exhibited a significantly reduced flux in KO mice, suggesting NK cells may indeed express *Gimap*6 as detected in a recent RNA-seq study (*457*, *539*). The accumulation of autophagosomes prior to bafilomycin treatment along with the decrease in autophagic flux suggests that GIMAP6 deficiency results in a block during the late stages of autophagy, potentially in autophagosome maturation or in autophagosome-lysosome fusion.

Memory and naïve T cells have different autophagic requirements, and autophagy is particularly critical for the development of memory T cells (*256*, *267*). Therefore, I investigated whether autophagy was equally affected in naïve and memory T cell populations. Indeed, LC3-II levels in both CD44^{-} naïve and CD44^{+} memory CD4 and CD8 T cells were higher in KO cells; these levels were either not significantly changed or were slightly decreased when cells were treated with bafilomycin, similar to what was seen in the bulk T cell populations

(**Fig. 5.1D,E).** All subsets showed a decrease in autophagic flux (**Fig. 5.1F)**, suggesting that GIMAP6 deficiency affects autophagy in both naïve and memory T cells.

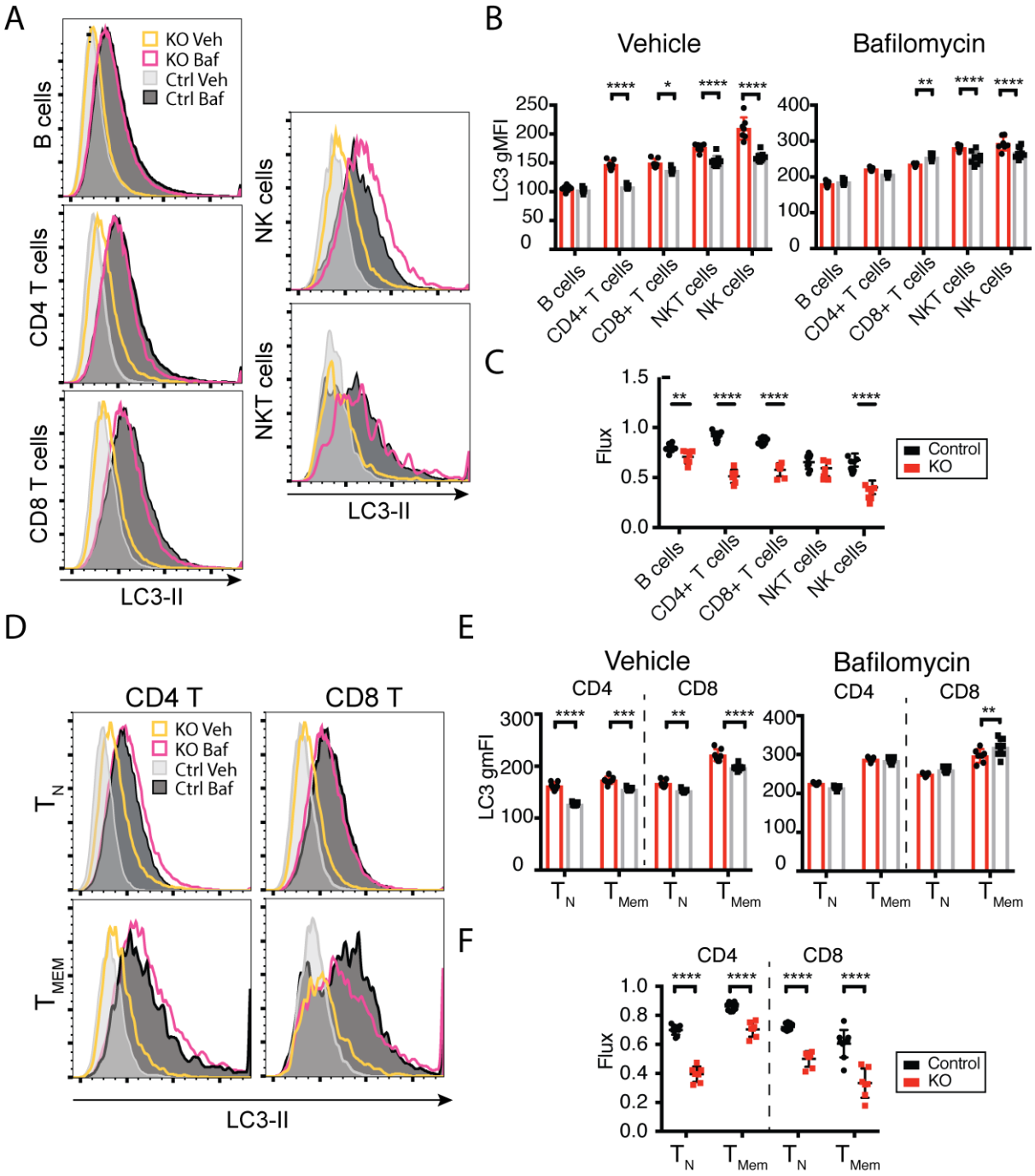


Fig. 5.1. ***Gimap6*$^{-/-}$ mice have reduced basal autophagic flux in lymphocytes**. Whole splenocytes from *Gimap6*$^{-/-}$ or *Gimap6*$^{+}$ mice were treated with 100 nM Bafilomycin A1 or an equal volume of vehicle (100% ethanol) for 2 hours and then stained with antibody against LC3. **A)** Representative flow plots of splenocytes gating on B cells (B220^{+}), CD4 T cells (CD3^{+}CD4^{+}), CD8 T cells (CD3^{+}CD8^{+}), NK cells (NK.1.$^{+}$CD3^{-}), or NKT cells (NK1.1^{+}CD3^{+}). Gating was done as in **Fig 4.4A. B**) Quantification of A, showing geometric MFI of LC3-II. **C)** Quantification of autophagic flux ([g.MFI LC3$_{Baf}$] – [g.MFI LC3$_{Veh}$])/[g.MFI LC3$_{Veh}$]). **D**) Representative flow plots showing LC3-II levels in naïve (T_N)(CD44^{-}) or memory (T_{MEM})(CD44^{+})

T cells. **E**) Quantification of D, showing geometric MFI of LC3-II. **F**) Autophagic flux of D as calculated in C. n_{KO}=7; $n_{control}$=9. Shown is one of three independent repeats. Veh=vehicle, Baf=bafilomycin A1. *P<0.01; **p<0.01; ***P<0.005; ****P<0.001 Two-way ANOVA with Tukey's multiple comparison test.

Resting T cells have low levels of basal autophagy; TCR and common gamma-chain cytokine signaling lead to autophagy upregulation (*263–265*). To determine whether the autophagy defect seen in *ex vivo* KO T cells was maintained or perhaps even exacerbated after activation, I quantified LC3-II levels in TCR-stimulated T cells. Activated *Gimap6*$^{-/-}$ T cells showed greatly reduced levels of autophagy compared to controls, especially CD4 T cells **(Fig. 5.2)**. Similar to *ex vivo* lymphocytes, activated KO T cells had an accumulation of LC3-II which did not increase proportionally upon bafilomycin treatment, supporting the hypothesis that GIMAP6 deficiency results in a block during the late stages of autophagy. This appeared to be a cumulative effect, with the greatest difference in flux in both CD4 and CD8 T cells occurring five days after stimulation. Of note, unstimulated KO T cells had no significant difference in autophagic flux as they did in **Fig. 5.1**; we hypothesize that this discrepancy may be due to the CTV staining used in **Fig. 5.2** and not in **Fig. 5.1,** though further testing would be needed to verify this. Interestingly, activation seemed to upregulate protein levels of GIMAP6 in CD4 T cells, with high levels at three days post-activation which then declined by day five (**Fig.5.2D)**. A paper published after the start of this project demonstrated that Jurkat T cells stimulated with PMA/ionomycin also upregulated transcriptional and protein levels of GIMAP6 (*518*). Together, these findings hint at a potential role of GIMAP6 specifically in TCR-induced autophagy regulation.

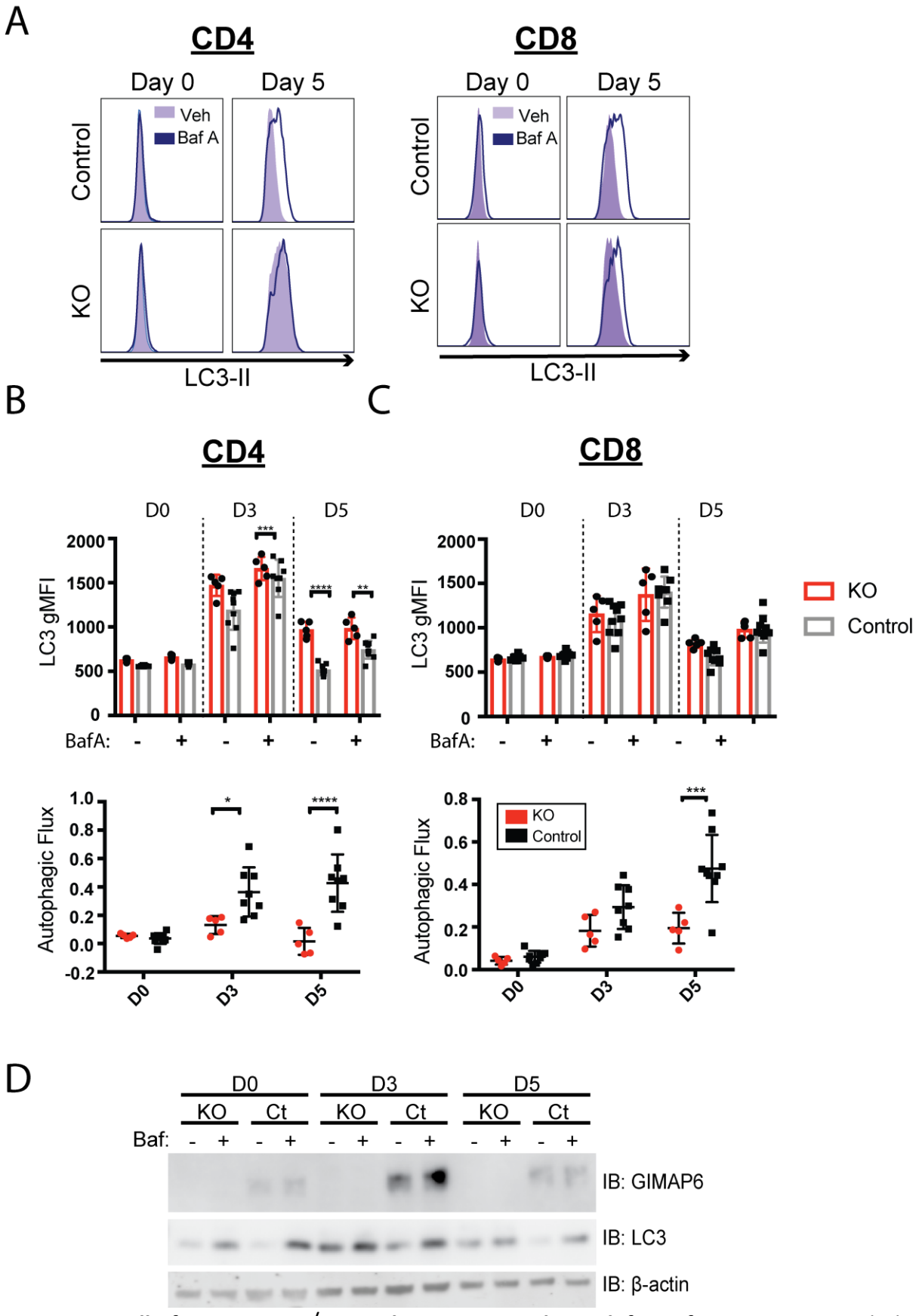


Fig. 5.2. T cells from *Gimap6*$^{-/-}$ mice have an autophagy defect after activation. Whole splenocytes from *Gimap6*$^{-/-}$ (KO) or *Gimap6*$^{+}$ (control) mice were stimulated with 1 μg/mL of

plate-bound anti-CD3 and 1 μg/mL of soluble anti-CD28 antibody for the indicated number of days. They were then treated with 10 nM Bafilomycin A1 (baf) or vehicle (veh)(100% ethanol) for 2 hours and then stained with antibodies and analyzed by flow cytometry. **A)** Representative flow plots showing LC3-II staining in CD4 and CD8 T cells. Experiment was done as part of **Fig 4.7**, with gating as shown in **Fig. 4.7A**. **B,C**) Quantification of A, showing geometric MFI of LC3-II. and autophagic flux ([g.MFI $LC3_{Baf}$] – [g.MFI $LC3_{Veh}$])/[g.MFI $LC3_{Veh}$]) of CD4 (**B)** or CD8 (**C)** T cells. n_{KO}=5; $n_{control}$=9. Shown is one of two independent repeats. Veh=vehicle, Baf=bafilomycin A1. *P<0.01; **p<0.01; ***P<0.005; ****P<0.001 Two-way ANOVA with Tukey's multiple comparison test. **D**) Western blot of enriched CD4 T cells activated for the indicated number of days with 1 μg/mL of plate-bound anti-CD3 and -CD28. On the day of harvest, cells were incubated for 2 hours with vehicle (100% ethanol) or 10 nM bafilomycin A1 and then lysed in RIPA buffer. Lysates were run on Bis-Tris gels and transferred onto PVDF membranes before immunoblotting with antibodies against mouse GIMAP6, LC3, and β-actin. Cells from 1-3 mice were pooled for each experiment. Shown is one representative experiment of three.

To confirm that the defect in autophagy in activated T cells is cell intrinsic, I created mixed bone marrow chimeras using *Gimap6*$^{-/-}$ and control bone marrow. To do this, I reconstituted irradiated CD45.1^{+} B6.SJL mice with an equal amount of CD45.2^{KO} or CD45.2^{WT} and CD45.1^{+} B6.SJL bone marrow (**Fig. 4.8**). Because I saw the most dramatic effects after TCR stimulation in nonchimeric mice, I examined autophagy after activation in the chimeras. LC3-II levels after activation were generally higher in CD45.2^{KO} cells than in CD45.2^{WT} and CD45.1^{+} cells, though this was statistically significant only between CD4 T cells after five days of activation (**Fig.5.3A,B)**. Bafilomycin-treated cells, on the other hand, had similar amounts of autophagosomes in all groups. Similar to nonchimeric KO mice (**Fig 5.2**), reduced flux was observable by three days after TCR activation in *Gimap6*$^{-/-}$ CD4 T cells, and by five days in CD8 T cells (**Fig.5.3C**). Taken together, the observed mild but statistically significant effects on T cell autophagy were observed across several *ex vivo* settings, thus supporting the hypothesis that loss of *Gimap6* causes an intrinsic defect in autophagy in murine T cells. Whether this a

direct consequence of stress due to GIMAP6 deficiency or a direct link between GIMAP6 and the autophagy pathway remains unclear at this point.

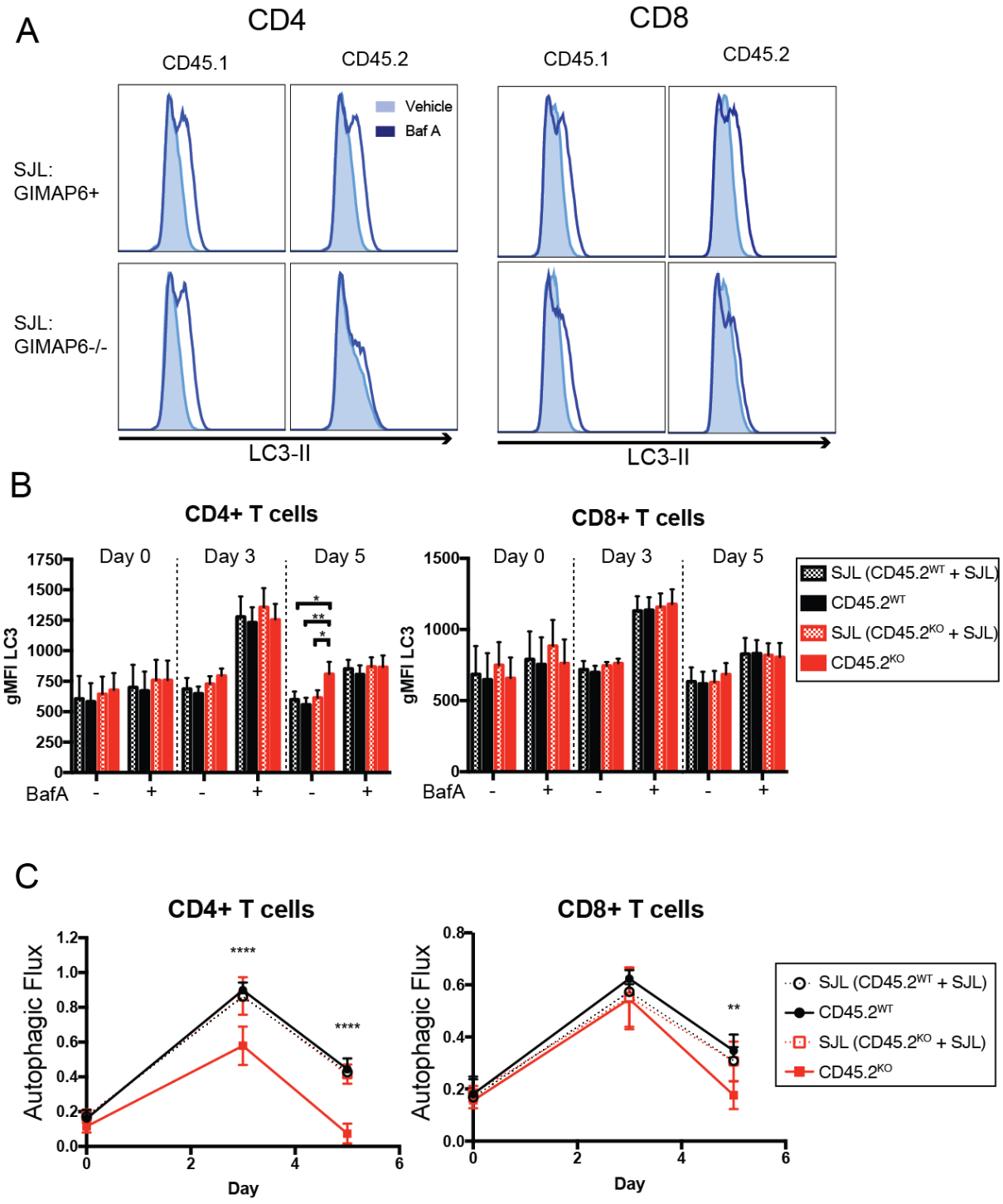


Fig. 5.3. Autophagy defect in *Gimap6*$^{-/-}$ T cells in mixed bone marrow chimeras. A) Bone marrow from either a *Gimap6*$^{-/-}$ mouse (CD45.2^{KO}) or control (CD45.2^{WT}) was mixed with an equal amount of CD45.1 B6.SJL bone marrow and used to reconstitute irradiated CD45.1 B6.SJL hosts. Splenocytes were activated with anti-CD3/28 antibody, stained for LC3-II after 2 hours incubation with 10 nM Bafilomycin or vehicle, and gated for CD4 and CD8 CD45.1^{+} or

CD45.2^{+} T cells. Done in conjunction with **Fig 4.10** and gating done as in **Fig. 4.10A.** Shown are representative flow plots of T cells 5 days after activation. **B,C)** Quantification of A. Autophagic flux (C) was quantified by normalizing LC3-II gMFI (B) with and without bafilomycin A1 (([LC3-II gMFI]$_{Baf}$ – [LC3-II gMFI]$_{Veh}$)/ [LC3-II gMFI]$_{Veh}$). Data is pooled from two experiments. $n_{CD45.2\ [GIMAP6+]:\ CD45.1\ [SJL]}$=6; $n_{CD45.2\ [GIMAP6-/-]:\ CD45.1\ [SJL]}$= 7. *P<0.05 **P<0.01 ***P<0.005 ****P<0.001 Repeated measures 2-way ANOVA and Sidak multiple comparison test.

Autophagy maintains organelle homeostasis and quality control by clearance of damaged proteins and organelles. One example is mitophagy, the selective degradation of mitochondria; deletion of the autophagy proteins Atg7 or Vps34 in T cells results in an increase in mitochondrial content (*256*, *259*, *540*). To determine whether this is true in *Gimap6* KO T cells, I used the MitoTracker Green, a fluorescent dye that selectively accumulates in mitochondria independently of membrane potential, to look at mitochondrial load (**Fig. 5.4)**(*541*). KO B cells and unstimulated T cells showed no difference in MitoTracker staining (**Fig. 5.4A-F).** Proliferating T cells, on the other hand, increased their mitochondrial load, presumably to cope with increased ATP demands, or for mitochondrial biogenesis to pass on to the daughter cells. However, though only statistically significant in CD8 cells, both activated *Gimap6*$^{-/-}$ CD4 and CD8 T cells had higher levels of MitoTracker staining than controls (**Fig. 5.4F)**. In particular, dividing CD8 T cells (i.e. those diluting CTV) had significantly higher amounts of mitochondria in KO cells compared to controls (**Fig. 5.4G,H)**. The increased MitoTracker staining in KO cells supports the hypothesis that *Gimap6* KO T cells have defective clearance of mitochondria due to decreased mitophagy.

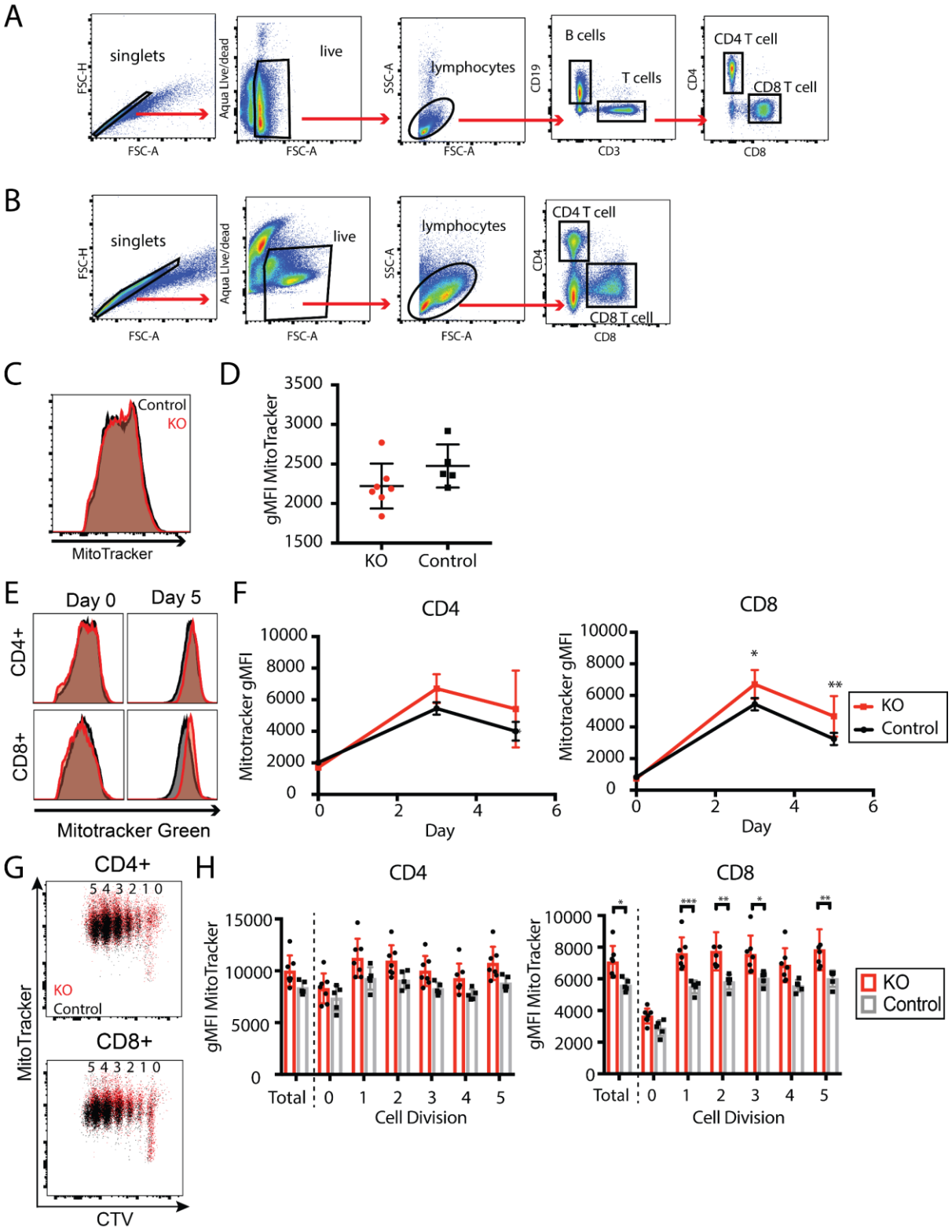


Fig. 5.4. *Gimap6*$^{-/-}$ activated CD8 T cells have Mitotracker staining. **A)** Gating strategy for d0 (unstimulated) whole splenocytes labeled with CellTrace Violet (CTV) and stained with MitoTracker Green for 25 min. **B)** Gating strategy for whole splenocytes labeled with CellTrace Violet (CTV) and activated for 3 or 5 days with 1 μg/mL plate-bound anti-CD3 and soluble anti-CD28 before staining with MitoTracker green for 25 min. **C)** Representative flow plot of MitoTracker Green staining in B220^{+} B cells. **D**) Quantification of C**. E)** Representative flow

plots showing MitoTracker Green staining of unstimulated (d0) and stimulated CD4 and CD8 T cells, gated on as shown in A and B, respectively. **F)** Quantification of E. *P<0.05; **P<0.01; ***P<0.005 Repeated measures Two-Way ANOVA with a Sidak's multiple comparison test. **G)** Representative flow plot showing MitoTracker Green staining in proliferating T cells activated for 3 days. The number of divisions each population has undergone is shown above, as indicated by dilution of CTV. **H**) Quantification of G. Total refers to the bulk CD4 or CD8 population. n_{KO}= 4; $n_{Control}$=11. Shown is one experiment of two independent repeats. *P<0.05; **P<0.01; ***P<0.005; ****P<0.001 Two-way ANOVA with Sidak's multiple comparison test. FSC-H= forward scatter-height; FSC-A=forward scatter-area; SSC-area= side scatter-area; CTV= CellTrace Violet; gMFI= geometric mean fluorescence intensity.

Depolarized mitochondria accumulate PTEN [phosphatase and tensin homolog]-induced kinase 1 (PINK1), which recruits the E3 ubiquitin ligase Parkin and leads to the ubiquitination of outer membrane proteins, initiating mitophagy (*542–545*). Alternatively, mitophagy can be mediated by BCL2/adenovirus E1B-interacting protein 3-like (BNIP3L), likely through an interaction with the LC3 proteins through its LIR domain (*546*). Autophagy defects can cause oxidative stress and ensuing apoptosis due to accumulation of damaged mitochondria and increased reactive oxygen species (ROS) (*259*, *260*, *547*). Therefore, I checked ROS levels in T and B lymphocytes in KO mice using the dye MitoSOX Red, a superoxide indicator (*548*) (**Fig. 5.5)**. Though unstimulated T and B cells had no change in ROS, both CD4 and CD8 T cells had significantly more ROS after activation **(Fig. 5.5E, F)**. A closer examination of proliferating cells three days post-activation showed that KO cells that have undergone more than one round of division, as determined through the dilution of CTV, seemed to have higher levels of ROS than corresponding control cells (**Fig. 5.5G, H)**. Together with the MitoTracker data, this suggests an increased accumulation of damaged mitochondria.

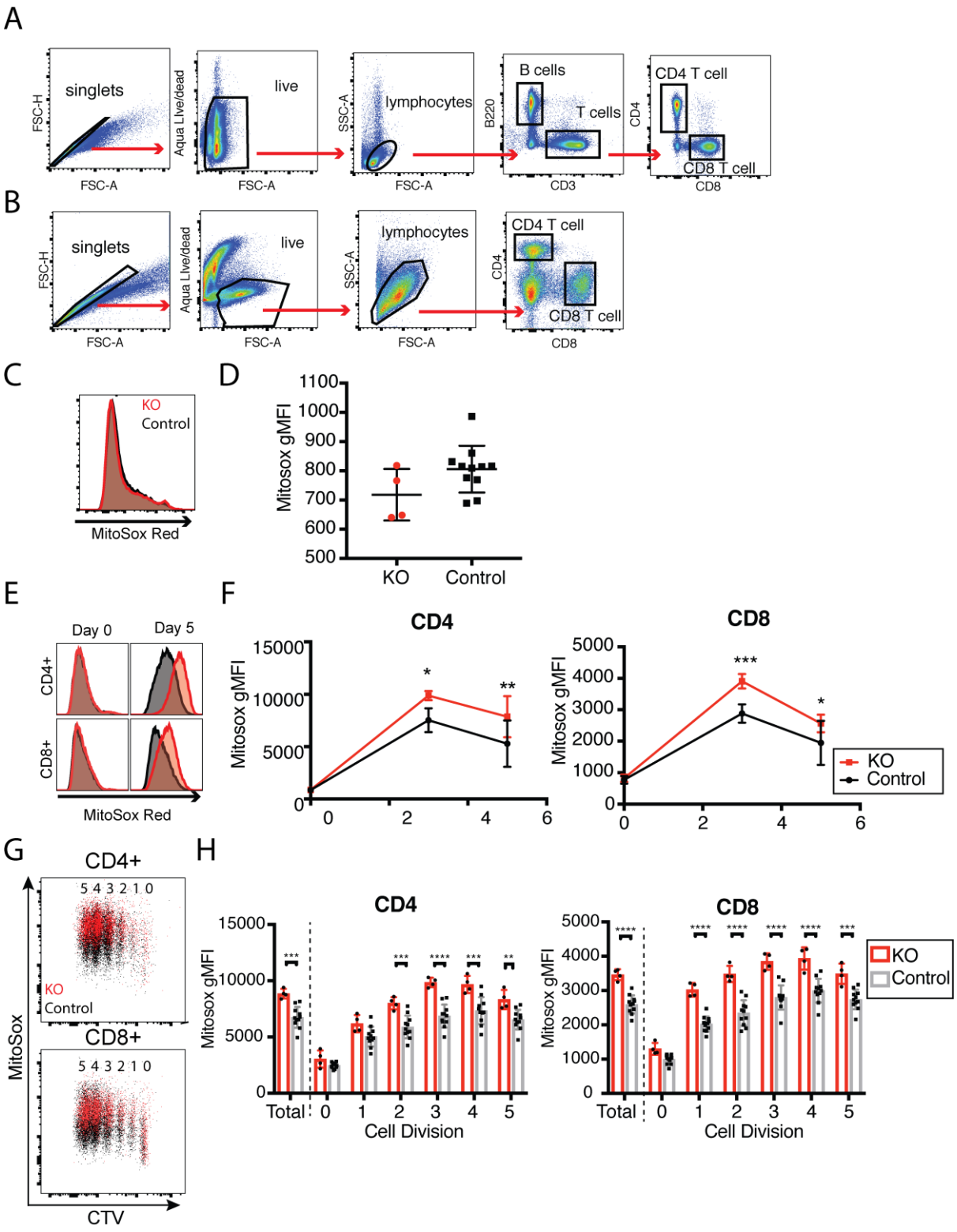


Fig. 5.5. *Gimap6*$^{-/-}$ activated T cells have increased reactive oxygen species. **A)** Gating strategy for day 0 (unstimulated) whole splenocytes labeled with CellTrace Violet (CTV) and stained with MitoSox Red for 15 min. **B)** Gating strategy for whole splenocytes labeled with CellTrace Violet (CTV) and activated for 3 or 5 days with 1 μg/mL plate-bound anti-CD3 and soluble anti-CD28 before staining with MitoSox Red for 15 min. **C)** Representative flow plot of MitoSox Red staining in B220+ B cells. **D**) Quantification of C**. E)** Representative flow plots

showing MitoSox Red staining of unstimulated (d0) and stimulated CD4 and CD8 T cells, gated on as shown in A and B, respectively. **F)** Quantification of E. *P<0.05; **P<0.01; ***P<0.005 Repeated measures Two-Way ANOVA with a Sidak's multiple comparison test. **G)** Representative flow plot showing MitoSox Red staining in proliferating T cells activated for 3 days. The number of divisions each population has undergone is shown above, as indicated by dilution of CTV. **H**) Quantification of G. Total refers to the bulk CD4 or CD8 population. n_{KO}= 4; $n_{Control}$=11. Shown is one experiment of two independent repeats. **P<0.01; ***P<0.005; ****P<0.001 Two-way ANOVA with Sidak's multiple comparison test. ROS= reactive oxygen species; FSC-H= forward scatter-height; FSC-A=forward scatter-area; SSC-area= side scatter-area; CTV= CellTrace Violet; gMFI= geometric mean fluorescence intensity.

Like T cells, B cells upregulate autophagy after activation (*280*, *549*). Because *ex vivo* B cells had a small decrease in autophagy (**Fig. 5.1)**, I wondered whether this would be exacerbated upon B cell activation. As expected, B cells stimulated with LPS or anti-CD40 and IL-4 did have increased levels of autophagy; however, *Gimap6* KO B cells had similar levels of both LC3-II and autophagic flux as controls (**Fig. 5.6**). Though further studies are needed, this indicates that GIMAP6 may not be as contribute to autophagy as much in B cells as in T cells.

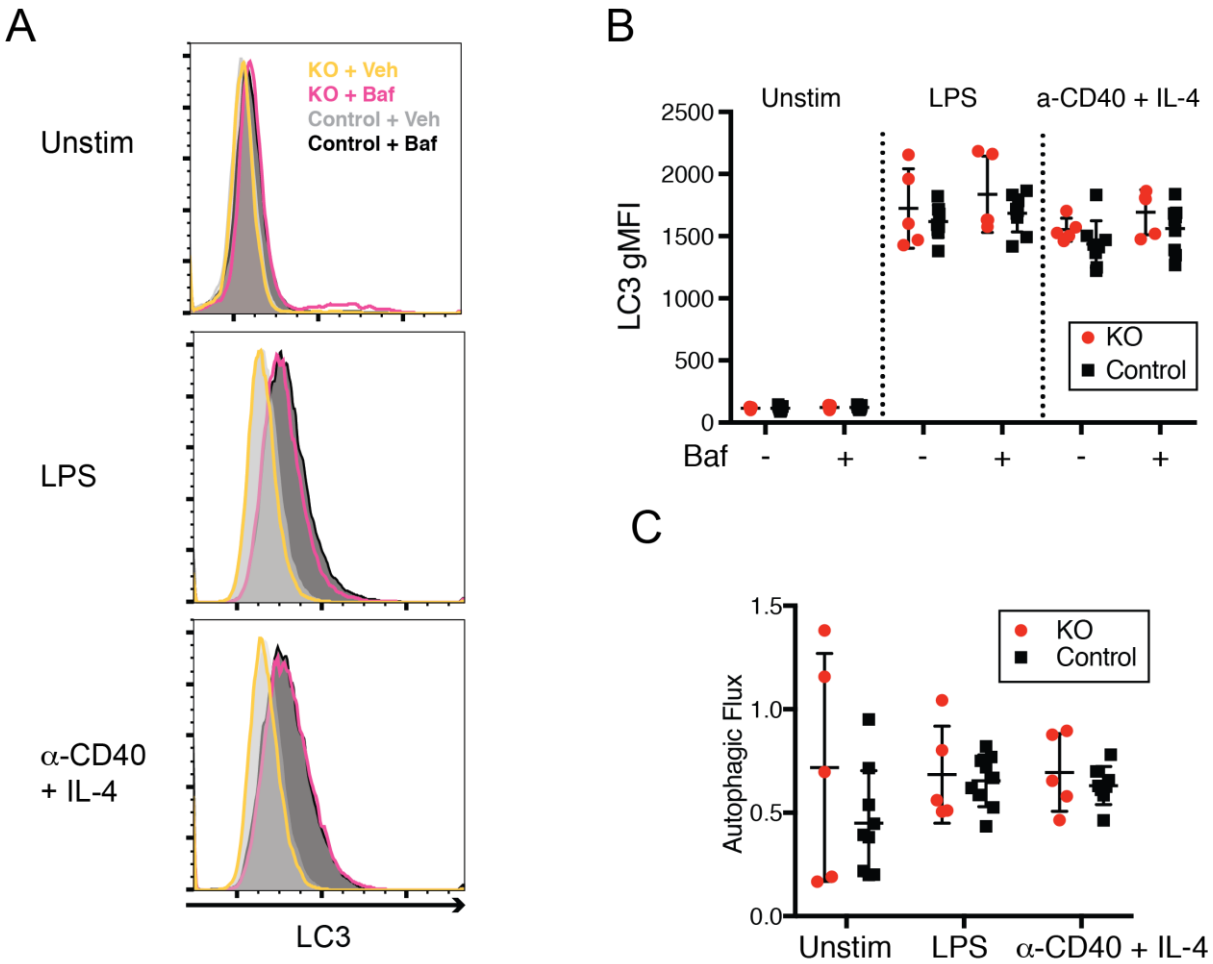


Fig. 5.6. **B cells from *Gimap6*$^{-/-}$ mice do not have an autophagy defect after activation**. B cells enriched from whole splenocytes from *Gimap6*$^{-/-}$ (KO) or *Gimap6*$^{+}$ (control) mice were stimulated with either 10 μg/mL of LPS or 20 ng/mL of IL-4 and 10 μg/mL of anti-CD40 for two days. They were then treated with 10 nM Bafilomycin A1 (baf) or vehicle (veh) for 2 hours, and stained with antibodies and analyzed by flow cytometry. **A)** Representative flow plots showing LC3-II staining in CD19^{+} B cells. **B**) Quantification of A, showing geometric MFI of LC3-II C) Quantification of autophagic flux ([g.MFI $LC3_{Baf}$] – [g.MFI $LC3_{Veh}$])/[g.MFI $LC3_{Veh}$]) of cells from A. n_{KO}=5; $n_{control}$=9. Experiment done once. No significance difference found by two-way ANOVA.

5.2.2 T cells from patient 1467 have reduced autophagy after activation

Because I observed an autophagy block in murine T cells, I examined whether T cells from patient 1467, which have decreased GIMAP6 protein levels, might also have an similar defect. Similar to KO mice, no difference in autophagy was seen in unstimulated T cells (**Fig. 5.7 A-C)**. Because the patient's T cells do not activate and proliferate as well as normal

controls (**Fig. 4.2)** and activated T cells have higher levels of autophagy than resting cells (*23–25)*, I compared autophagy levels only in proliferating cells, as indicated by the dilution of CTV. Proliferating patient T cells had higher levels of LC3-II with and without bafilomycin treatment compared to most normal controls, though one control did have similar levels as the patient on day 3 (**Fig. 5.7B)**. The patient's CD4 T cells also had the lowest levels of autophagic flux out of all samples on days 3 and 5 post-activation, and her CD8 T cells had the lowest flux on days 2 and 3 (**Fig. 5.7C)**. Comparison of cells that had undergone the same number of divisions on day 5 showed a striking autophagic defect in the patient's prolifrating CD4 cells (**Fig. 5.7D-F).** The observed defect seemed to be due to an autophagic block similar to that in KO mice, in which LC3-II levels were high in vehicle but not bafilomycin-treated T cells**.** The patient's proliferating CD8 T cells, on the other hand, had high levels of LC3-II both with and without treatment, and their autophagic flux was within the range of controls (**Fig. 5.7D-F**). This data agrees with the stronger autophagic defect observed in GIMAP6-deficient murine CD4 T cells compared to CD8 T cells. However, caution must be taken when interpreting these results as the patient has been taking Plaquenil (hydroxychloroquine), which is a chloroquine derivative used to treat SLE (*550*). Like bafilomycin, chloroquine and hydroxychloroquine are autophagy inhibitors that raise lysosomal pH, preventing autophagosome-lysosome fusion as well as inhibiting the function of lysosomal hydrolyases (*551*, *552*). As hydroxychloroquine has a long half-life of about 40 days (*553*), it cannot be certain that the block in autophagy seen here is cell intrinsic rather than secondary to the Plaquenil treatment. However, bafilomycin, which is also a lysosomal inhibitor, retains some effect as seen in the increase of LC3-II. This effect is comparable to mouse T cells treated with bafilomycin, indicating that Plaquenil cannot be the full explanation for this blocked autophagic flux in the patient. As there is only one patient,

no statistical tests were possible. However, altogether, this data indicates that the decrease in autophagic flux is reproducible between the *Gimap6* KO mouse and the patient,

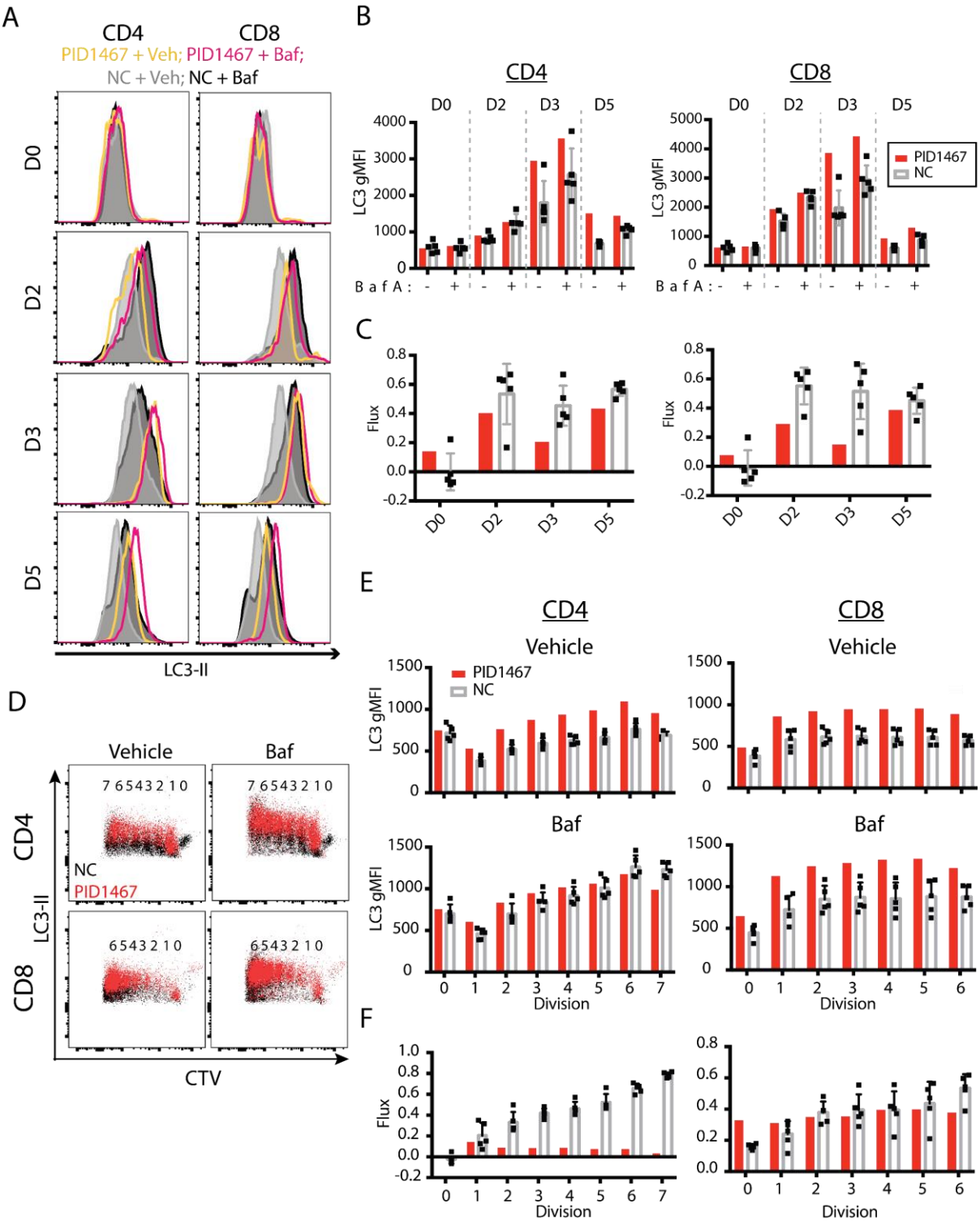


Fig. 5.7. Activated T cells from patient 1467 have an autophagy defect. PBMCs were stimulated with 1 μg/mL of soluble anti-CD3 and -CD28 antibody for the indicated number of days. They were then treated with 10 nM bafilomycin A1 (Baf) or vehicle (Veh) for 2 hours

before staining and running on a flow cytometer. **A)** Representative flow plots showing LC3-II staining in CD4 or CD8 T cells. For days 2, 3, and 5 (d2-5), cells were gated on proliferating cells only. Experiment was done in conjunction with **Fig4.2** and gating done as in **Fig. 4.2A. B**) Quantification of gMFI of LC3-II in A. Bafilomycin '+' refers to treatment with 10 nM bafilomycin and bafilomycin '-' refers to treatment with an equivalent amount of vehicle (DMSO) **C)** Quantification of A showing autophagic flux ([g.MFI $LC3_{Baf}$] – [g.MFI $LC3_{Veh}$])/[g.MFI $LC3_{Veh}$]). **D**) Representative flow plot showing LC3-II staining in proliferating T cells activated for 5 days. The number of divisions each population has undergone is shown above, as indicated by dilution of CTV. **E**) Quantification of gMFI of LC3-II in D. **F)** Quantification of D showing autophagic flux ([g.MFI $LC3_{Baf}$] – [g.MFI $LC3_{Veh}$])/[g.MFI $LC3_{Veh}$]). Experiment was done once. n_{NC}= 5; individual values for each NC is represented by a black box in each graph. $_{Veh}$= vehicle; Baf= bafilomycin; NC= normal control; CTV= CellTrace Violet

5.2.3 GIMAP6$^{-/-}$ Jurkat lines have no detectable difference in autophagy

Due to the limitations in obtaining patient sample, I generated *GIMAP6* knockout Jurkat T cell lines to investigate the role of GIMAP6 in human T cells. To do this, I again utilized the CRISPR/Cas9 system as discussed in Chapter 3. Originally, I chose exon 2, where the GIMAP6 coding sequence (CDS) begins, as a CRISPR target. However, GIMAP6 contains a polyT site upstream of the ATG start codon; as polyT sites are RNA polyermase III termination sequences, this limited the number of useable gRNAs and none tested showed potential cutting (*554*) (data not shown). Therefore, I instead designed gRNAs targeting the 5' end of exon 3 using the MIT CRISPR design tool (http://crispr.mit.edu)(*322*) (**Fig. 5.8, Appendix Table A.6)**. The tool ranks gRNAs based on various criteria, including the number of predicted off-target cutting sites, the favorability of the sequence of the PAM motif, the GC content of the gRNA, and the gRNA's predicted Cas9 binding ability (Cas9 Loading Score) (*322*). I cloned three of the top gRNAs into the pSPgRNA expression vector and transfected them into 293T cells with a Cas9 expressing plasmid (pCas9_GFP) to test their cutting efficiency with a T7 endonuclease I (T7EI) assay (**Fig. 5.8)**. In this assay, T7E1 is added to denatured and reannealed PCR products that cover the targeted locus; T7EI cleaves mismatched DNA

structures, so the presence of digested DNA on an electrophoresis gel indicates CRISPR activity (*555*). gRNA 3 appeared to cut most efficiently, so it was co-transfected into Jurkats with pCas9_GFP to create the *GIMAP6*$^{-/-}$ clonal lines. Empty pSPgRNA (EV) transfected clones were used as controls. I confirmed deletion of *GIMAP6* by testing lysates for GIMAP6 protein by western and by using TIDE analysis on genomic DNA to identify indels causing frameshifts (**Fig. 5.8**, **Table A.7)**(*324*).

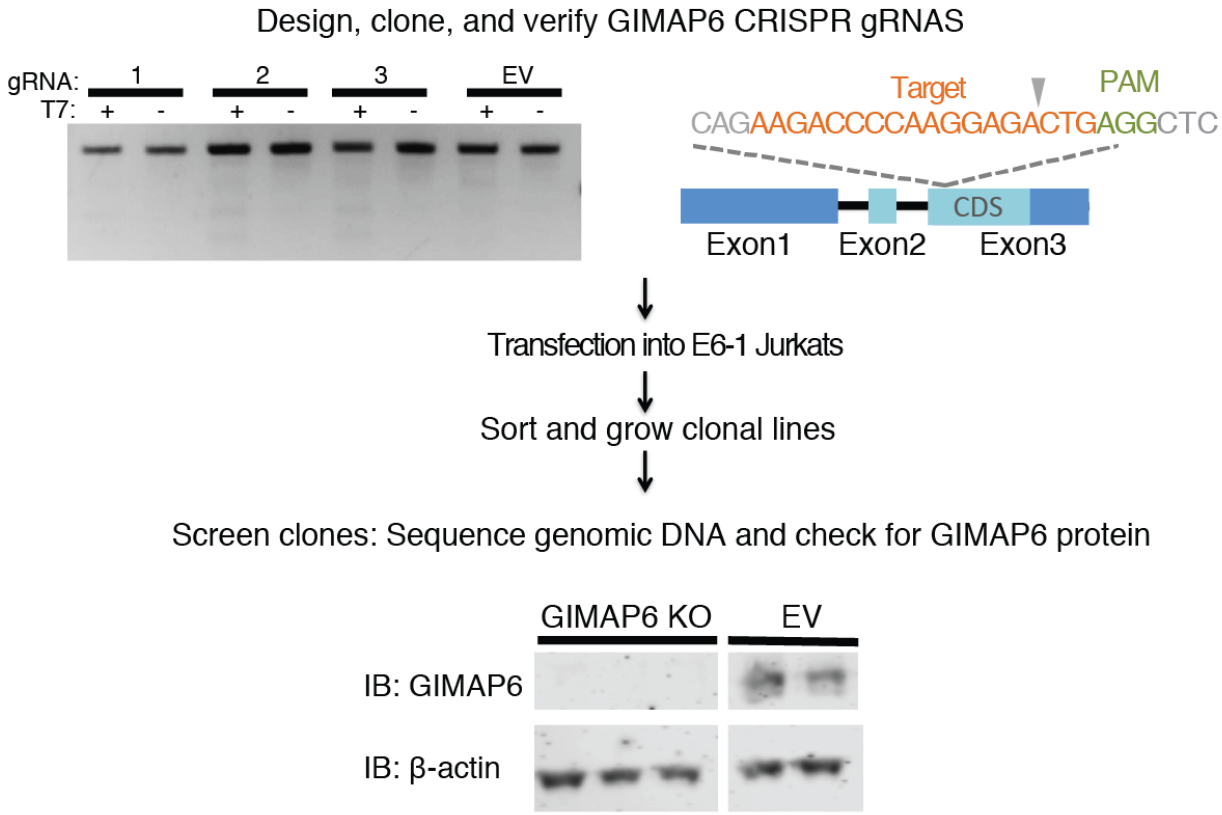


Fig. 5.8. Creation of *GIMAP6*$^{-/-}$ Jurkat lines using CRISPR-Cas9 system. Three guide RNAs (gRNA 1-3) targeting the 5' end of exon 2 of *GIMAP6* were cloned into an expression plasmid (pSPgRNA) and transfected into 293T cells along with a Cas9 overexpression plasmid expressing GFP (pCas9_GFP). After 36 hours, genomic DNA was extracted from the cells, and the target region of *GIMAP6* was amplified by PCR. T7 endonuclease I (T7) was added after denaturation and reannealing of the PCR products, and the DNA was run on an electrophoresis gel to look for cleavage. gRNA 3 was chosen, and it or empty pSPgRNA vector (EV) was transfected into E6-1 Jurkats with pCas9_GFP. After two days, GFP^{+} cells were sorted and cloned by limiting dilution. Lysates of clones that grew out were tested for GIMAP6 protein levels by western. Deleterious mutations were verified by sequencing and TIDE analysis of extracted genomic DNA.

To determine if *GIMAP6* KO lines had abnormal autophagy, I first looked at LC3 levels under basal conditions. Though there was a wide variability in autophagy levels between individual clones even at baseline, KO lines generally had normal levels of LC3-II both with and without bafilomycin treatment when analyzed by western blotting or a flow-based assay (**Fig. 5.9**). Autophagic flux was also comparable to that in control lines. As such, I induced autophagy through starvation and treatment with rapamycin, an mTORC1 inhibitor, to determine whether a difference in autophagy that perhaps was too small to detect at baseline might become more evident during stress conditions. Though these treatments did increase autophagic flux (**Fig. 5.9D)**, KO lines had a similar LC3-II levels when treated with vehicle or bafilomycin as well as a rate of autophagic flux within the range of EV lines (**Fig. 5.9)**.

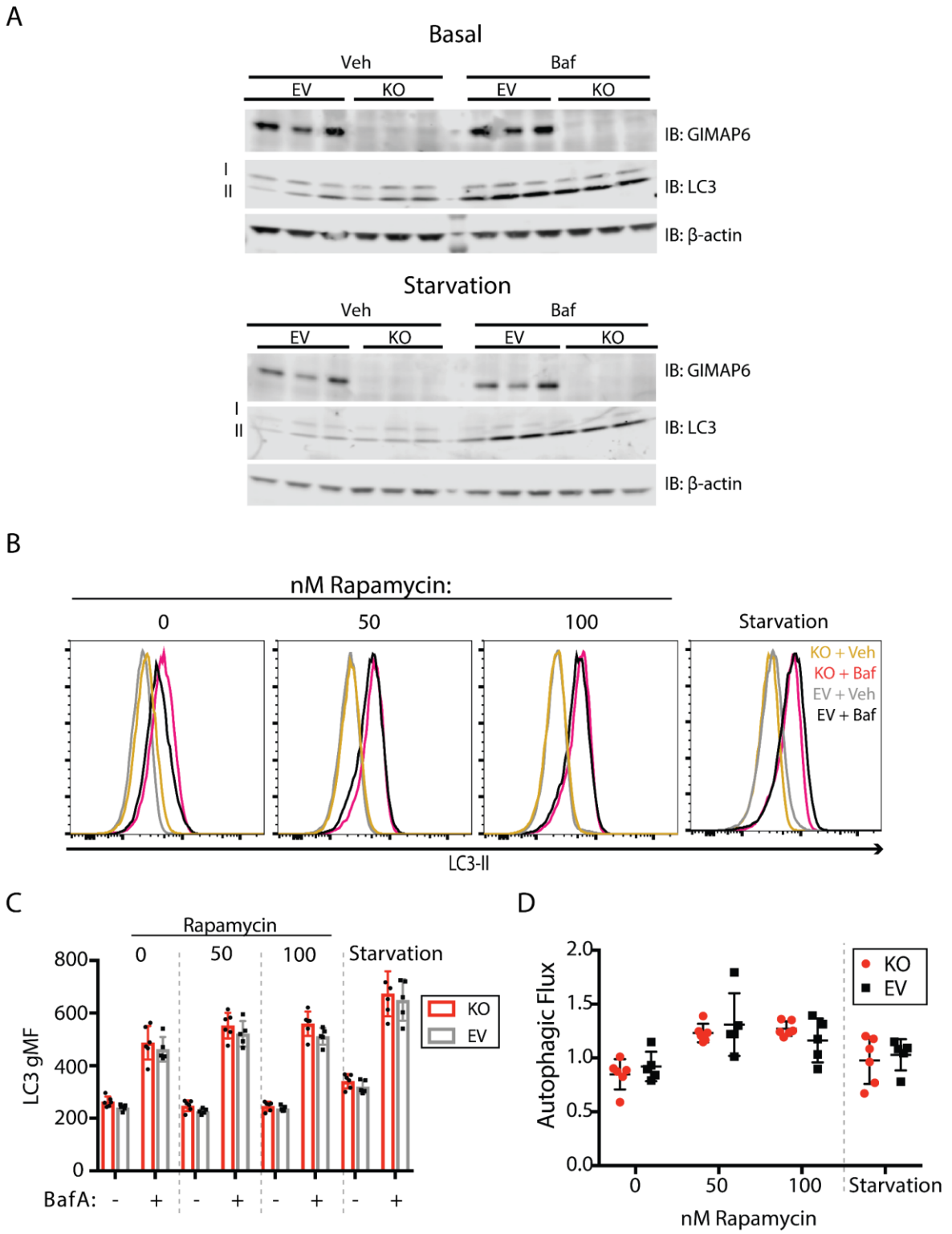


Fig. 5.9. *GIMAP6*$^{-/-}$ Jurkat lines have normal autophagy at basal and starved conditions, as well as after rapamycin treatment. A) *GIMAP6*$^{-/-}$ (KO) or *GIMAP6*$^{+}$ (EV) Jurkats were cultured in cRPMI (basal) or HBSS with either 10 nM bafilomycin A1 (Baf) or vehicle (Veh) for 2 hours. Cells were then lysed in RIPA buffer, and western blots of lysates were immunoblotted with antibodies against GIMAP6, LC3, and beta-actin. The LC3-I and LC3-II bands are indicated to the left of each blot. n=3. Shown is one representative experiment of two. **B-D)** KO or EV

Jurkats were treated with DMSO or the indicated amount of rapamycin, or were starved in amino acid deprivation buffer (*179*) with either 10 nM bafilomycin A1 (Baf) or vehicle (Veh) for 2 hours. Cells were then stained for LC3-II and analyzed by flow cytometry. **B)** Representative flow plots showing LC3-II staining in stimulated Jurkats. **C**) Quantification of gMFI of LC3-II in B. **D)** Quantification of B showing autophagic flux ([g.MFI $LC3_{Baf}$] – [g.MFI $LC3_{Veh}$])/[g.MFI $LC3_{Veh}$]). n_{KO}=6; n_{EV}=5. The rapamycin experiment was repeated three times; starvation was repeated twice. Veh= vehicle; Baf= bafilomycin.

Because I detected no consistent difference in autophagy in the Jurkat CRISPR lines at basal, starved, or rapamycin-treated conditions, I tested whether there might be one after TCR stimulation as was seen in mouse T cells. Cross-linking of anti-CD3 and anti-CD28 antibodies activates Jurkats, resulting in upregulation of the activation marker CD69 **(Fig. 5.10A,B)**. Jurkats have a high level of basal autophagy, which increases further after TCR stimulation (**Fig. 5.10C-H)**. Though CD69 remains upregulated two days after activation, LC3-II staining by flow cytometry and western blotting shows that autophagic flux peaks at one day post-activation and then falls by day two (**Fig. 5.10E-H)**. While autophagy levels appear to still be elevated at day two, I chose to use day one to look at autophagy in the KO lines.

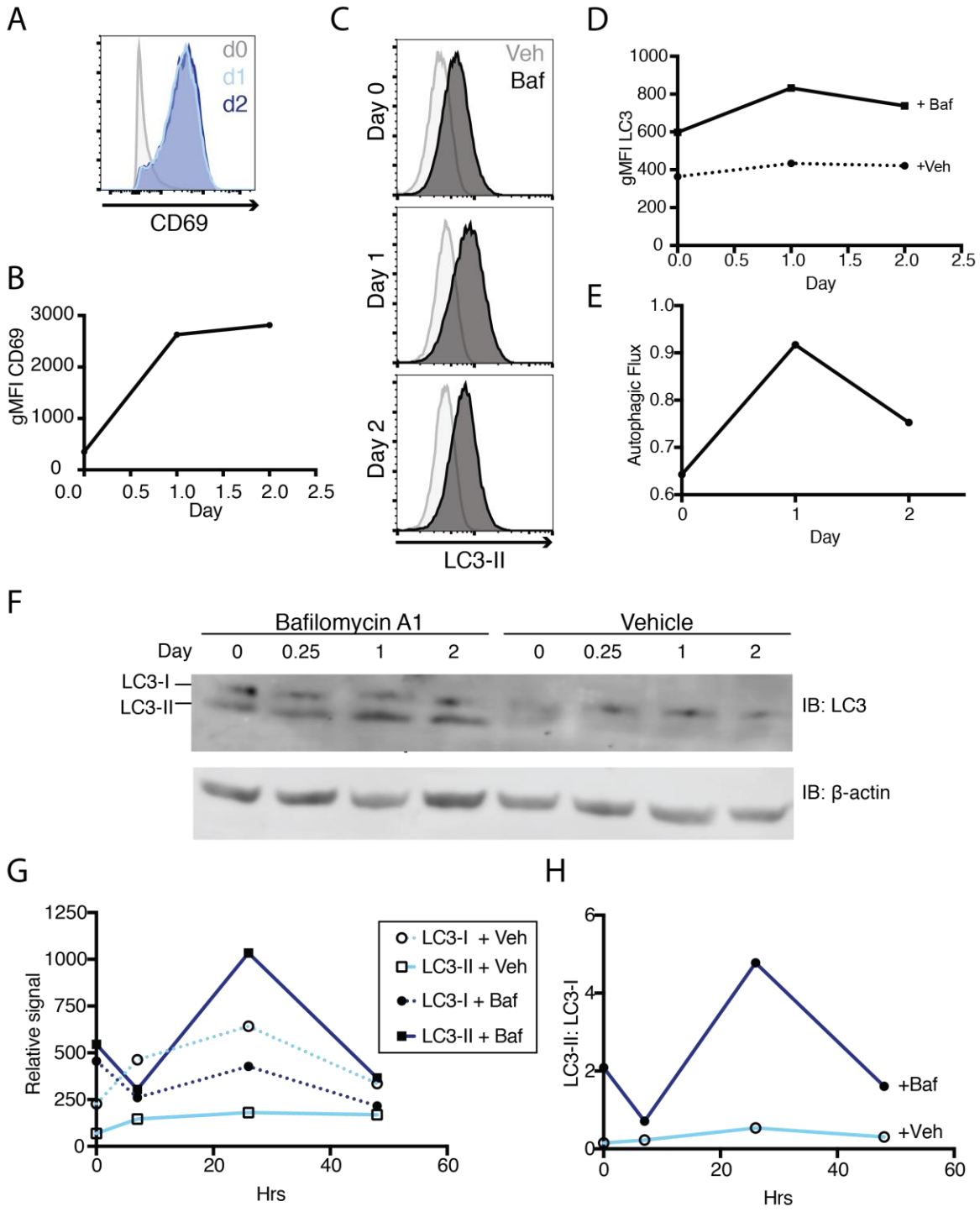


Fig. 5.10. Autophagy after TCR stimulation in Jurkats. Jurkats were stimulated with 1 μg/mL of anti-CD3, 0.05 μg/mL anti-CD28 antibody, and 3 μg/mL goat anti-mouse Fab for the indicated number of days. They were then treated with 10 nM bafilomycin A1 (Baf) or vehicle (Veh) for 2 hours before harvesting. **A)** Representative flow plots showing CD69 staining in stimulated Jurkats. **B)** Quantification of gMFI of CD69 in A.**C)** Representative flow plots showing LC3-II staining in stimulated Jurkats. **D)** Quantification of gMFI of LC3-II in C. **E)** Quantification of C showing autophagic flux ([g.MFI $LC3_{Baf}$] – [g.MFI $LC3_{Veh}$])/[g.MFI $LC3_{Veh}$]). **F**)Western showing lysates from stimulated Jurkats were lysed after treatment with Bafilomycin or vehicle immunoblotted with antibodies against LC3 and beta-actin. **G)**

Densitometry of F, showing signal of the LC3-I or LC3-II band divided by the signal of the corresponding actin band for each sample. **H**) The relative LC3-II to LC3-I signal of each sample as calculated in G. Each experiment was done once.

Though a recent paper has reported hyperactivation in Jurkat lines in which GIMAP6 has been knocked down (*518*), the *GIMAP6* KO CRISPR lines had no significant difference in CD69 upregulation compared to control lines after 24 hours of stimulation (**Fig. 5.11A, B)**. While unstimulated cells sometimes showed a decrease in autophagic flux, this was inconsistent (**Fig. 5.11E)**. While the KO lines generally had higher levels of LC3-II and reduced flux after stimulation compared to controls, this failed to reach significance when tested (**Fig. 5.11C-H)**. Unlike in murine *Gimap6*$^{-/-}$ T cells, loss of GIMAP6 did not seem to cause a consistent autophagic defect in Jurkat cells.

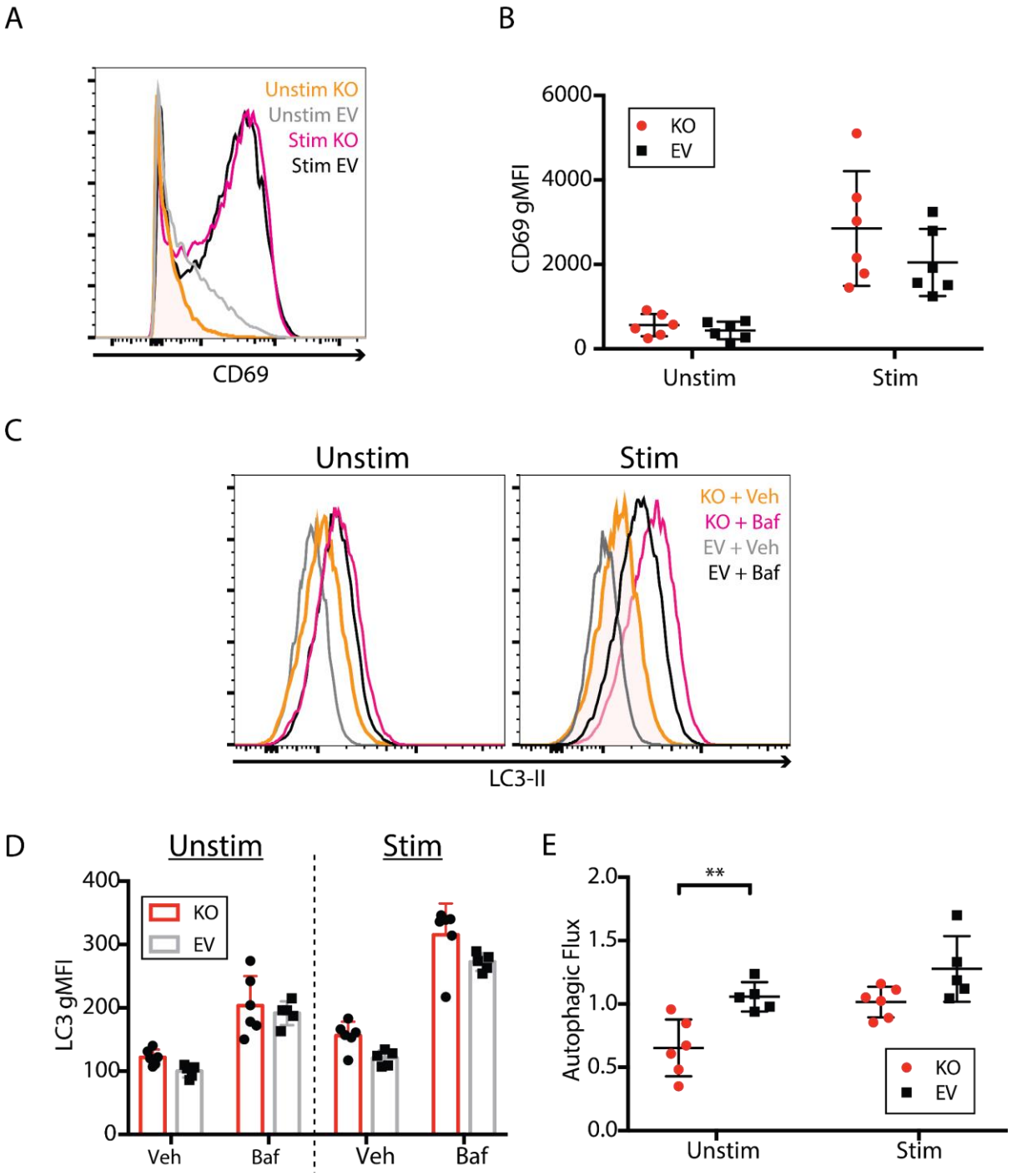


Fig. 5.11. Autophagy after TCR stimulation in *GIMAP6*$^{-/-}$ Jurkats. *GIMAP6*$^{-/-}$ (KO) or *GIMAP6*$^{+}$ (EV) Jurkats were either left unstimated (unstim) or stimulated with 1 μg/mL of anti-CD3, 0.05 μg/mL anti-CD28 antibody, and 3 μg/mL goat anti-mouse Fab (stim) for 24 hours. They were treated with 10 nM bafilomycin A1 (Baf) or vehicle (Veh) for the last 2 hours before harvesting. **A)** Representative flow plots showing CD69 staining in stimulated Jurkats. **B)** Quantification of gMFI of CD69 in A. **C)** Representative flow plots showing LC3-II staining in Jurkats. **D**) Quantification of gMFI of LC3-II in C. **E)** Quantification of C showing autophagic flux ([g.MFI $LC3_{Baf}$] – [g.MFI $LC3_{Veh}$])/[g.MFI $LC3_{Veh}$]).n_{KO}=6; n_{EV}=5. Shown is one experiment of three independent experiments. Veh= vehicle; Baf= bafilomycin.

5.3 Discussion

In this chapter, I examined autophagy levels in mouse and Jurkat models of GIMAP6 deficiency, as well as in patient samples. I demonstrated that loss of GIMAP6 in mouse and patient lymphocytes results in a partial block in autophagy leading to accumulation of autophagosomes in affected cells.

5.3.1 The role of GIMAP6 in autophagy in murine lymphocytes

I showed in this chapter that germline deletion of murine *Gimap6* results in reduced autophagy in B, T, and NK cell populations that is characterized by an accumulation of the LC3-II protein consistent with a block in the late stages of autophagy. Mixed bone marrow chimeras demonstrate that the autophagy defect seen in GIMAP6 deficient cells is cell intrinsic in activated T cells, though basal autophagy levels in *ex vivo* lymphocytes were not tested in chimeras. Furthermore, stimulated T cells had increased ROS and mitochondrial loads consistent with deregulated mitophagy. Together, the data presented here suggests that GIMAP6 deficiency in murine T cells does result in an autophagic block, likely at the late stages of autophagy. Other experiments will be useful in further understanding this defect. For example, electron microscopy (EM) would allow observation of autophagosome structure and, to some degree, contents, which could be valuable in understanding the nature of this autophagic defect; for example, if GIMAP6 deficiency results in a block in autophagosome maturation, an increased amount of immature autophagosomes should be detectable through EM (*556*). It will also be important to further determine what functional consequences the autophagy phenotype has on cells. Loss of mitophagy can affect cell survival due to oxidative stress (*259*, *260*); however, preliminary studies using annexin V have shown no survival defect in activated GIMAP6-deficient T cells (data not shown), though the

reduced frequency of splenic T cells in KO mice may indicate a slight T cell lymphopenia *in vivo*. As NK and NKT cells showed a similar autophagy phenotype as T cells at basal conditions, if they also express GIMAP6, it will be interesting to examine whether any cellular affects observed in T cells are true in these cells as well.

Interestingly, activated KO T cells had a striking defect in autophagy, but activated B cells did not. It is possible that culturing the B cells for a longer period of time might reveal an autophagy abnormality similar to CD8 T cells. However, a recent paper has shown the importance of noncanonical autophagy in germinal center and naïve B cells after stimulation (*280*). Therefore, another intriguing possibility is the involvement of noncanonical autophagy, or autophagy that occurs through a different mechanism as canonical autophagy, and does not require the same proteins essential for canonical autophagy (*557*, *558*). In the studies presented in this thesis, I used only bafilomycin A1, which detects canonical autophagy, rather than chloroquine, which blocks both canonical and noncanonical autophagy (*559*). It would therefore be interesting to compare levels of canonical and noncanonical autophagy flux in *Gimap6*$^{-/-}$ B cells to determine if there might be an autophagic defect in these cells that was not captured in this study.

Supporting the findings in this thesis, a paper published earlier this year by the Butcher laboratory demonstrated defects in autophagy and mitophagy in a *Gimap*$^{fl/fl}$ CD2Cre mouse model, which lack *Gimap6* specifically in T and B lymphocytes (*517*). While they did not check autophagy after activation, the Butcher group saw accumulation of LC3-II in *ex vivo* lymphocytes by western blot, as well as increased phosphorylation of the autophagy receptor p62 (also called SQSTM1) at S403, which is consistent with defective autophagy (*517*, *560*). Interestingly, when *Gimap6* was ablated *in vitro* using an inducible tamoxifen Cre model, accumulated p-p62 but not LC3-II was observed, though the authors suggested the timescale

used may have been too brief to see a gradual accumulation of LC3-II (*517*). It would thus be interesting to investigate p-p62 levels in the models presented in this thesis as well as the patient's T cells, though it is unclear whether GIMAP6 directly affects phosphorylation of the protein or if it solely a consequence of the autophagy defect. Regardless, the studies by the Butcher lab and in this thesis together provide strong evidence that GIMAP6 ablation in mice results in LC3-II accumulation consistent with a block in autophagic degradation, suggesting a role for GIMAP6 in cell-type specific autophagy.

5.3.2 Germline deletion of GIMAP6 in Jurkat T cells does not result in an autophagy defect

Due to the limitations in receiving and using patient samples, I generated *GIMAP6*$^{-/-}$ Jurkat clonal lines to use as a model for the patient's cells. Jurkats cells are a human leukemic CD4^{+} T cell line, and are arguably the most popular T cell line currently used for biomedical experimentation (*561–563*). I chose to use Jurkats because immortalized cell lines have several advantages over primary cells: they are simple to obtain, grow, and maintain in large quantities, and are more easily manipulated than primary cells, which can often be very difficult to genetically modify. Additionally, unlike T cell populations from mice or humans, which have heterogeneous phenotypes (e.g. naïve, memory, exhausted, senescent, etc), cell lines provide more or less homogeneous populations that help with reproducibility and consistency between experiments. Cell lines can be incredibly useful for elucidating molecular pathways; Jurkats, for example, have been pivotal in the study of TCR signaling (*564*). However, cell lines also have several disadvantages. Along with potential issues with contamination, immortalized lines are either derived from cancer cells or have been manipulated to continuously proliferate (*565*). As such, they typically have abnormal characteristics, especially in pathways such as survival, proliferation, and metabolism, and

thus may not accurately represent primary cell populations (*566–568*). Jurkats, for example, are enriched for mutations in TCR signaling, genome stability, and O-linked glycosylation (*569*). Continuous passaging of cell lines can exacerbate the cellular abnormalities due to selection and genetic drift (*570*, *571*).

Unlike murine and patient's T cells, I could not demonstrate a definitive autophagic defect in *GIMAP6* KO Jurkat lines at basal or starved conditions, nor when cells were TCR stimulated or treated with rapamycin. While KO cells generally had higher levels of LC3-II than EV controls and sometimes showed decreased autophagic flux, these results were not consistent amongst experiments. This variation is likely due in part to differences in cell lines due to genetic drift. To generate the CRISPR lines, I serially diluted transfected Jurkats and grew out clones; as such, each CRISPR line was derived from a single cell that then proliferated exponentially. This method inherently selects for cells that grow well under culture conditions, and Jurkats have several mutations leading to genome instability and resistance to apoptosis, so advantageous mutations may have been unintentionally selected (*569*, *572*). Adding to potential variations between cell lines, CRISPR cloning can have off-target effects due to partial or complete matching of the gRNA sequence (*573*, *574*). Furthermore, Jurkats already have aberrant metabolism, with known mutations in two PI3K inhibitors, PTEN and SHIP1 (SH-containing inositol 5' phosphatase 1), that result in hyperactive PI3K activity (*569*, *575–577*). PI3K phosphorylates AKT (also known as protein kinase B), leading to the activation of the mTORC1 pathway, which negatively regulates autophagy (*578*); therefore, it is possible that any autophagy defects in Jurkats might be masked due to the constitutively active PI3K/AKT/mTORC1 pathway.

In the future, a few options exist to deal with the potential issues mentioned here. First, rather than using clonal knockout lines, knockdown of bulk populations of primary or

cultured cells using siRNA, shRNA, or CRISPR-Ribonucleoproteins might be prevent problems with genetic drift (*579*). Alternatively, knockout lines could serve as their own controls to reduce problems with variability between lines if transduced or transfected with wildtype GIMAP6.Lastly, though many T cell leukemic lines have PTEN or SHIP1 mutations similar to Jurkats, Hut-78 cells have intact SHIP1 and PTEN expression similar to primary T cells and thus may be a better cell line in which to investigate autophagy (*576*).

5.3.3 Autophagy in patient T cells

While activated patient T cells did show reduced autophagic flux, there are several caveats. First, as has been previously discussed, because of limited availability of patient blood samples, this experiment was done once and with only five normal controls. Additionally, while both the CRISPR lines and the mice have a complete loss of GIMAP6 protein, the patient has residual GIMAP6 which might affect the severity of the phenotype observed. Her clinical background may also affect the results of these experiments; to treat her autoimmunity and other clinical symptoms, she is on multiple medications, the most relevant of which in these experiments is Planquenil, or hydroxychloroquine. As a chloroquine derivative with a long half-life, hydroxychloroquine could possibly cause the block in autophagosomal degradation observed in this thesis (*550–553*). However, autophagic flux in the patient's T cells appeared low only after activation and not in unstimulated cells on day 0, perhaps supporting a cell intrinsic defect rather than one caused by the medication.

To determine whether loss of GIMAP6 directly impacts the autophagy machinery or whether the defects in autophagy observed in the mice and patient are secondary effects, future work could be done using by knocking down GIMAP6 in primary lymphocytes to see whether this phenocopies the patient's T cells. Additionally, rescue of the autophagic block

by WT GIMAP6 but not the patient's variant in either the patient's or knocked down cells would provide strong support that aberrant GIMAP6 function in the patient results in her autophagy phenotype. Overall, it is very encouraging that both the patient and the *Gimap6* KO mice show a similar block in autophagic flux, indicating that the patient's GIMAP6 deficiency may be associated with her disease.

Chapter 6. Loss of germline *Gimap6* in mice results in early mortality due to progressive kidney disease

6.1 Introduction

In this chapter, I report the unexpected and previously unreported finding of impaired survival in *Gimap6* KO mice and my investigation of its etiology.

6.2 Results

6.2.1 Gimap6 KO mice have early mortality

Gimap5$^{-/-}$ mice have extramedullary hematopoiesis and colitis, resulting in mortality between 10 and 20 weeks of age (*390*, *391*). In contrast, *Gimap6* KO mice were not reported to have early mortality by the early phenotyping by the IMPC (http://www.mousephenotype.org); however, I observed a stark survival defect in the KO mice compared to wildtype and heterozygous littermates after several months (**Fig. 6.1).** This was not reported in mice with a conditional *Gimap6* ablation in only lymphocytes (*517*).Though a large portion of knockout mice were culled for experimental purposes before 4 months of age and thus considered censored in the Kaplan-Meier survival curve, about 80% of females (10 mice) and 60% of males (8 mice) were either found dead or had to be culled due to sickness by 23 and 35 weeks of age, respectively. It is not known whether 100% of KO mice exhibit this early mortality as females older than 16 weeks and males older than 23 weeks old need to be culled after discovery of the survival defect under Home Office advisement. In general, though, females appeared to be affected to a greater degree than

males, with a precipitous drop in survival in the span of a few weeks, whereas survival in males dropped at a slightly more gradual pace. Interestingly, the majority of females did not display obvious symptoms before death, whereas half of the males were culled because of signs of sickness, including a rough coat, hunched posture, occasional weight loss, and slow movement, possibly suggesting some sex differences in phenotype.

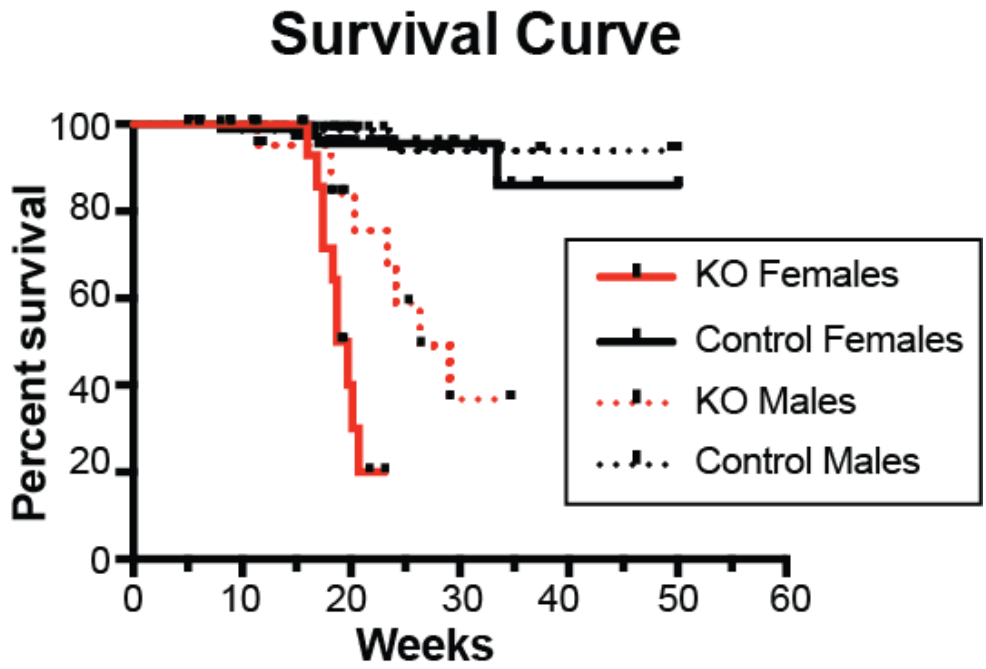


Fig.6.1. *Gimap6*$^{-/-}$ mice have early mortality. Kaplan-Meier curve showing survival in KO and control (pooled WT and het) mice. Mice who were culled for experiments were censored at the time of death. $n_{KO\ females}$= 33, $n_{KO\ males}$= 35, $n_{Control\ females}$= 99, $n_{Control\ males}$= 80. Females: $p<0.0001$; Males: $p<0.0005$ (log-rank Mantel-Cox test).

6.2.3 Renal disease in KO mice

We used gross morphological and histological examination of tissues to determine the cause of mortality in KO mice. Enlarged hearts and spleens were evident upon necropsy, as were pale, scarred kidneys (**Fig. 6.2A).** KO female and male mice had larger hearts than age- and sex- matched controls when compared to their body weight (**Fig. 6.2B,C**). KO mice

also had larger spleens than controls, but this was not statistically significant (**Fig. 6.2D,E**). I also harvested bone marrow, thymi, spleens, lymph nodes, intestines, lungs, kidneys, and hearts from knockout and control mice for histological analysis. Hematoxylin and eosin (H&E) stained slides prepared by the Kennedy Institute Histology Service were then analyzed by Elizabeth Soilleux (University of Cambridge, Cambridge, UK), a consultant clinical pathologist (**Fig. 6.2F,G**; detailed results listed in **Table. A.7**). As expected, slides from control organs showed normal histology (**Fig.6.2G).** On the other hand, there were histological abnormalities in multiple tissues from knockout mice, with the kidneys affected the most consistently and severely. In the kidneys, there was damage to the renal tubules thought to be secondary to the damage in the glomeruli, most of which showed a focal segmental glomerulosclerosis with some features of microangiopathy, or damage to the small blood vessels resulting in blood clots (**Fig. 6.2H**). Additionally, some vessels had indications of vasculitis. Though KO mice have cardiomegaly, most slides examined had normal histology although some showed signs of dilation. Heart and kidney diseases are linked comorbidities, and injury to one can result in damage in the other; hypertension secondary to renal disease, for example, often results in enlarged hearts (*580–583*). However, while kidney disease was almost completely penetrant, heart damage was histologically evident only in about a third of samples examined, so could have been a more variable secondary pathology. Therefore, we focused on the kidneys, hypothesizing that loss of GIMAP6 either directly or indirectly affects the kidneys causing severe renal damage that then affects the heart. It is much less likely that the inverse is true or that a third undetected factor results in both phenotypes.

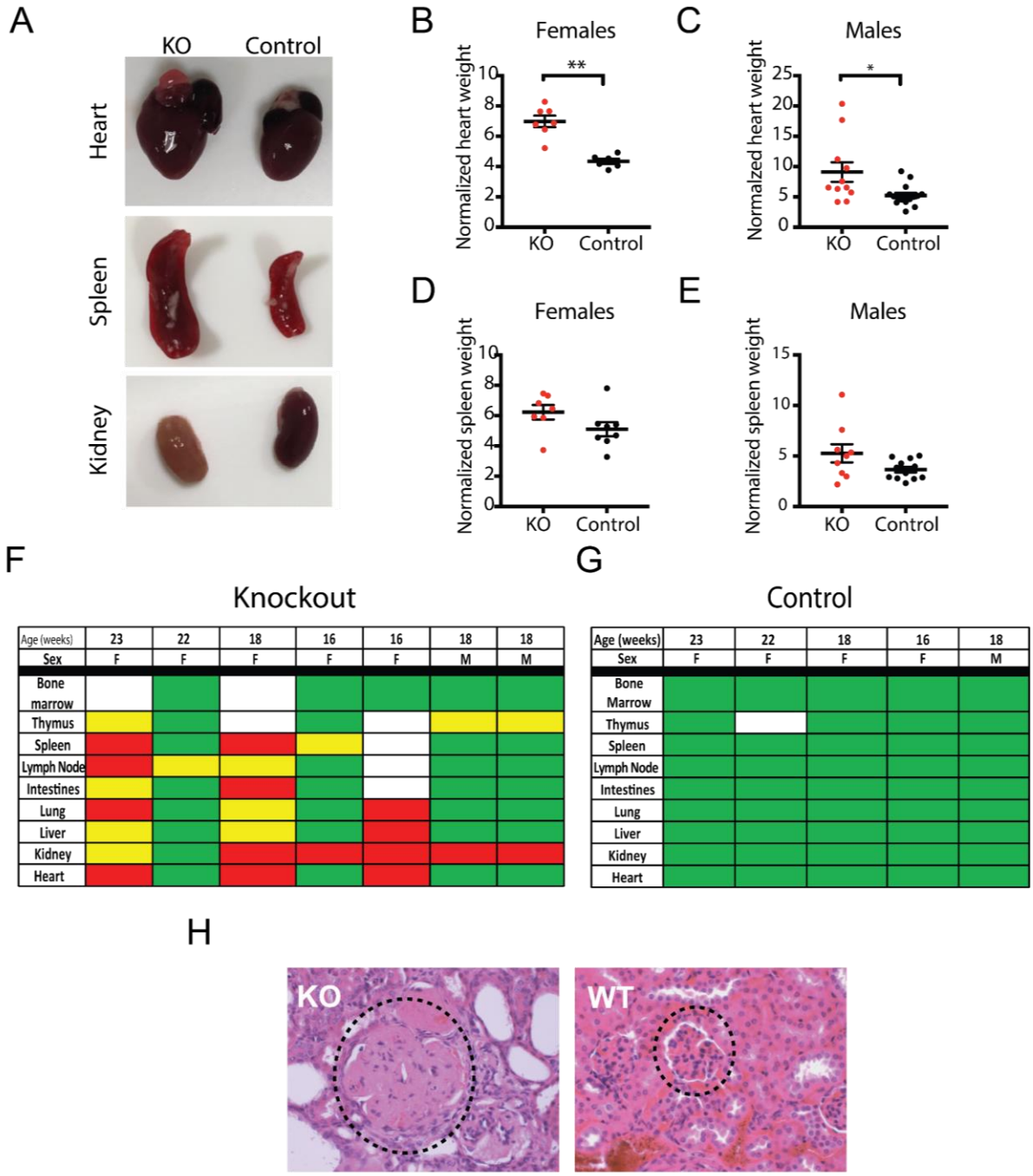


Fig.6.2. *Gimap6*$^{-/-}$ mice have cardiomegaly, splenomegaly, and glomerulosclerosis. A) Representative images of heart, spleen, and kidney of a knockout (KO) mouse and age- and sex- matched control. **B,C**) Normalized heart weight (mg heart/g body weight) in females (**B**, n_{KO}=7, $n_{Control}$=6) and males (**C**, n_{KO}=11, $n_{Control}$=15). **D,E**) Normalized spleen weight (mg spleen/g body weight) in females **(D**, n_{KO}=7, $n_{Control}$=8**)** and males (**E,** n_{KO}=9, $n_{Control}$=12). **F,G**) Female (F) and male (M) mice were sacrificed, and the indicated organs were harvested before fixation in 4% PFA for 24-48 hours. Paraffin sections were cut and stained with hematoxylin and eosin (H&E) by the Kennedy Institute Histology Service, and then analyzed by Elizabeth Soilleux for histological abnormalities. Each column represents one mouse. Rectangles represent the severity of the histological findings (green=normal; yellow= mild; red= severe; white= no sample). **H**) Representative images (400x) of H&E stain from control

and KO mouse kidneys. Dotted circle encircles a glomerulus. *P<0.05; **P<0.01 Mann-Whitney U test. wt= wildtype

Kidneys filter blood and excrete waste into urine while maintaining blood composition through reabsorption and regulation of electrolytes, glucose, and amino acids. To get an indication of KO mouse kidney function, I collected plasma that was then analyzed by the MRC Harwell Clinical Chemistry Laboratory (**Fig. 6.3**). Sodium, potassium, and chloride osmolarities in KO plasma were normal (**Fig. 6.3A-C**). However, levels of blood urea nitrogen and creatinine were elevated in plasma of 9-10 week old KO mice, indicative of compromised renal function (**Fig. 6.3D,E**). While healthy kidneys filter waste products like urea and creatinine, they retain protein in the plasma. However, both plasma albumin and total protein levels in 4 months old mice were reduced, with a corresponding increase in relative protein levels in urine (**Fig. 6.3F-H**). This proteinuria suggests that KO mice have damaged kidneys that leak protein indicating a glomerular defect in filtration. Due to difficulties in collecting large enough quantities of urine, however, male mice were not tested. However, some preliminary tests using urine dipsticks, which are colorimetric tests for a variety of urine parameters, showed normal ketone and glucose levels indicating that the kidney disease is not likely due to diabetes (data not shown).

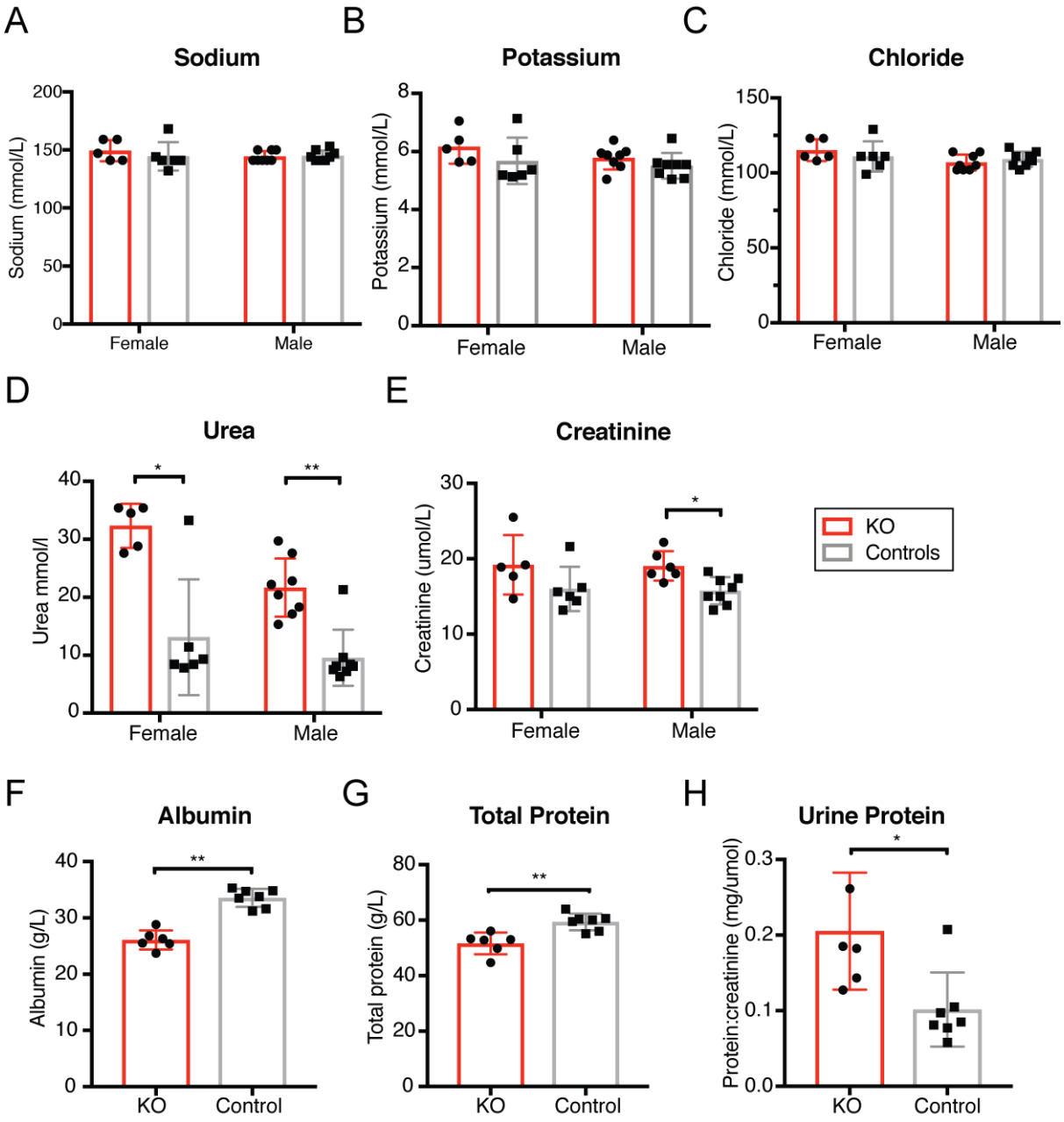


Fig.6.3 Poor renal function in *Gimap6*$^{-/-}$ mice. A,B) Urea **(A)** and creatinine **(B)** levels in plasma from 9-10 week old male and female mice **C,D**) Albumin **(C)** and total protein **(D)** levels in 16 week old female mice. **E)** Protein levels in 9-10 week old female mice expressed as a ratio between total urinary protein and urine creatinine levels. All samples were analyzed on an AU680 Analyser (Beckman-Coulter). For **A,B**, $n_{KO\ Female}$=5, $n_{Control\ Female}$= 6, $n_{Control\ Male}$=8. $n_{KO\ male}$=8 (**A**) and 7 (**B**). For **C-E**, n_{KO}=6, $n_{Control}$=7. *P<0.05; **P<0.01 (Mann-Whitney U-test).

Anemia is commonly associated with chronic renal disease, largely due to a diminished ability of the damaged kidney to synthesize erythropoietin, a hormone that promotes RBC production in bone marrow, though other factors may contribute (*584*). KO mice were therefore checked for anemia (**Fig. 6.4**). While white blood cell (WBC) and platelet counts

were normal (**Fig. 6.4A-B**), KO blood had a relatively low hematocrit and reduced concentration of RBCs than controls, though this was only significant for 4 mo females and not males (**Fig. 6.4C-D).** Together with diminished levels of hemoglobin (**Fig. 6.4E**), these findings indicate KO mice do have anemia. Types of anemia can be differentiated by RBC indices, including mean corpuscular volume (MCV), mean corpuscular hemoglobin (MCH), mean corpuscular hemoglobin concentration (MCHC), and red cell distribution width (RDW) (*585*). The slightly but significantly reduced MCV and MCH (**Fig. 6.4F,G)** suggests the mice have a microcytic anemia with smaller RBCs that have less hemoglobin on a per cell basis than normal. However, MCHC was normal, meaning that the hemoglobin content per volume of RBC was unaffected (**Fig. 6.4H**). On the other hand, RDW was elevated in female but not male mice (**Fig. 6.4I**), indicating anisocytosis, or an increase variability in RBC size. Microcytic anemia with anisocytosis is most commonly caused by iron deficiency, anemia of chronic disease, or thalassemia (a genetic disease causing abnormal hemoglobin synthesis) (*586*, *587*). Microcytic anemia with normal RDW, as seen in the 4 mo males, can also be caused by anemia of chronic disease or thalassemia (*586*–*588*). Though males have not yet been tested, female KO indeed had diminished plasma iron levels (**Fig. 6.4J)**. These indices thus agree with an anemia due to chronic renal failure, partially due to dimished iron levels and likely also due to an erythropoietin deficiency.

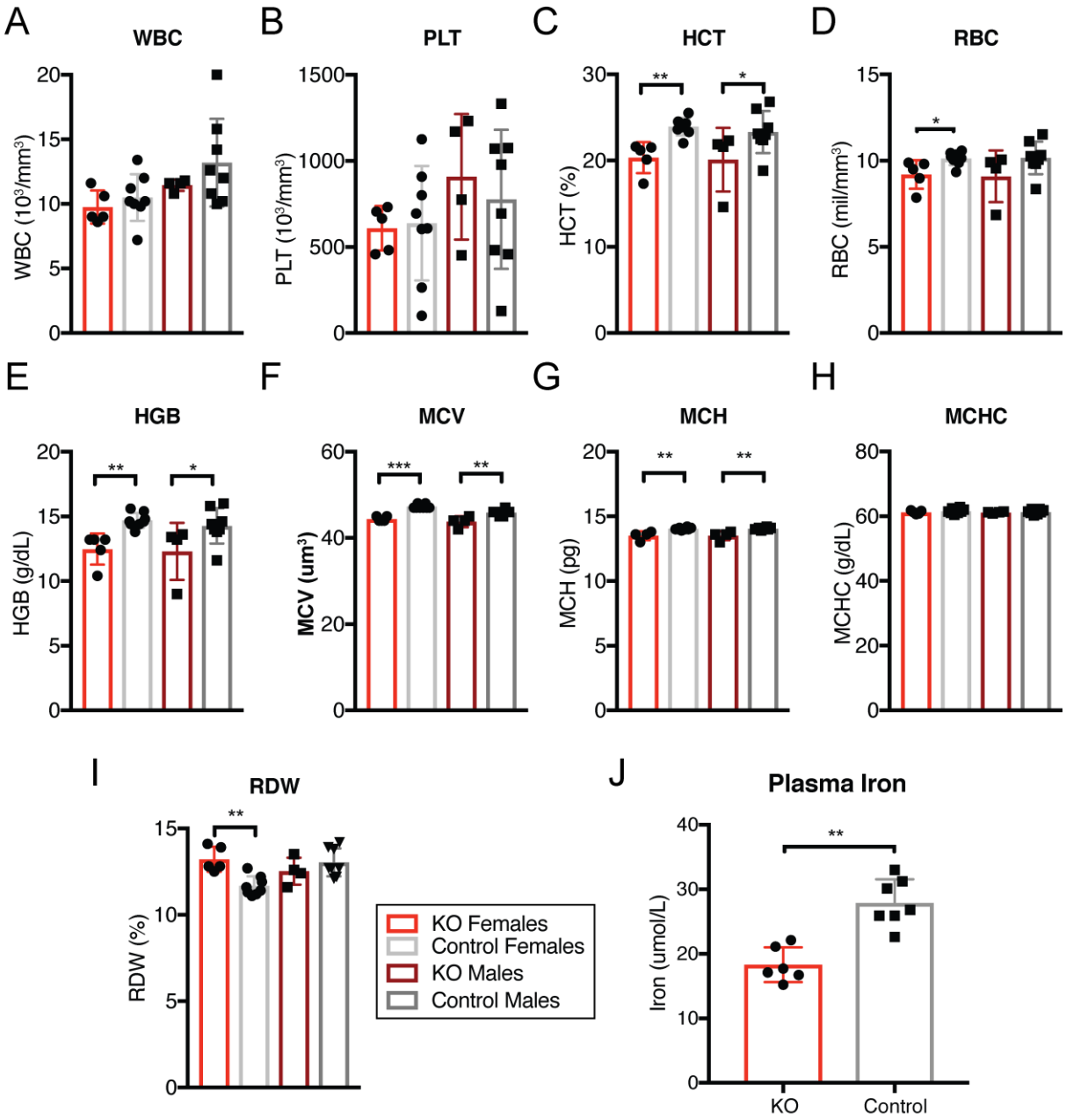


Fig.6.4 Anemia in *Gimap6*$^{-/-}$ mice. **A-J)** Whole blood was analyzed from 4 month old males and females using either the Pentraes 60 or Sysmex and analyzed for: white blood cell counts (WBC**, A**); platelet counts (PLT, **B**);hematocrit (HCT; **C**); red blood cell counts (RBC, **D**); hemoglobin content (HGB, **E**); mean corpuscular volume (MCV, **F**); mean cell hemoglobin (MCH, **G**); mean cell hemoglobin concentration (MCHC, **H**); and red cell distribution width (RDW, **I**). **J**) Plasma from 4 month old females was tested for iron levels using an AU680 Analyser**.** For **A-I**, $n_{KO\ Female}$=5; $n_{Control\ Female}$= 8, $n_{KO\ Male}$=4, and $n_{Control\ Male}$=8. For **J,** n_{KO}=6, $n_{Control}$=7. *P<0.05; **P<0.01; ***P<0.005; ****P<0.001 (Mann-Whitney U-test).

To help in the diagnosis of the kidney disease, we employed immunoglobulin and Periodic acid-Schiff (PAS) staining (**Fig. 6.5)**. Staining frozen kidneys sections with anti-

immunoglobulins revealed that KO glomeruli were strongly positive for IgG, IgA, and IgM, (**Fig. 6.5A**). However, the immunoglobulin staining was not granular as would be expected in an immune-complex-mediated disease, suggesting that the immunoglobulin staining is non-specific, possibly resulting from glomerular leaking of plasma proteins. To further analyze the glomerulus, I utilized PAS staining, which detects polysaccharides such as glycogen and mucopolysaccharides and provides details of glomerular cells, the mesangial matrix, and the basement membrane (*589*). Consultation with Dr. Avi Rosenberg (John Hopkins University School of Medicine, Baltimore, Maryland, USA), a renal pathologist, revealed that KO glomeruli had capillary wall thickening and duplication, mesangiolysis, and hyaline droplet in PAS stained sections, but no observable fibrin thrombi (**Fig. 6.5B).** These results are consistent with a microangiopathy, similar to the H&E staining result. The non-specific immunoglobulin staining can be explained as hyaline staining with mesangiolysis consistent with leakage of serum proteins into the glomeruli.

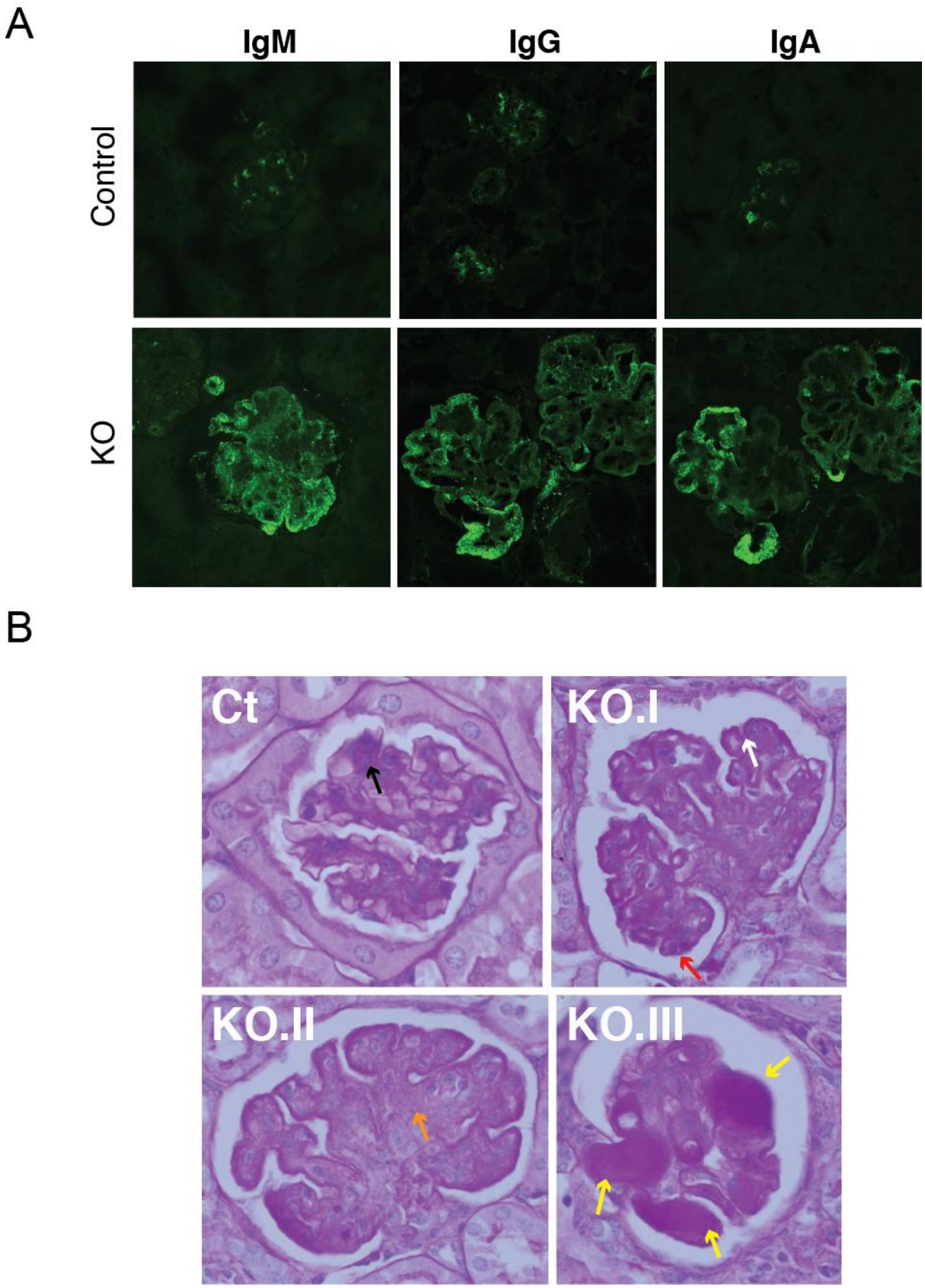


Fig.6.5 Histological findings in *Gimap6*$^{-/-}$ mouse kidneys. A) Representative images of glomeruli from cryosections of kidneys stained with anti-IgA, -IgG, and –IgM antibodies (Green). N_{KO}=3, $n_{Control}$=2 **B**) Representative images of glomeruli stained with periodic acid-Schiff (PAS) from control (Ct) and KO mice. Black arrow shows normal mesangium. KO.I shows

glomerular capillary wall thickening (white arrow) and duplication (red arrow). KO.II shows mesangiolysis (orange arrow). KO.III shows glomerular hyaline deposits (yellow arrows). N_{KO}=7, $n_{Control}$=5**.** KO=knockout.

Transmission electron microscopy (TEM) is a valuable technique to further diagnose glomerular disease (*590*). In collaboration with Dr. Errin Johnson (University of Oxford, Oxford, UK) and Avi Rosenberg, TEM of KO glomeruli were analyzed (**Fig. 6.6).** Cellular interposition between duplicated basement membrane, blockage of capillary vessels, and the presence of hyaline droplets indicated endothelial damage. As with the PAS staining, there was no evidence of fibrin thromboses. The TEM images further support microangiopathy as the cause of renal disease in KO mice.

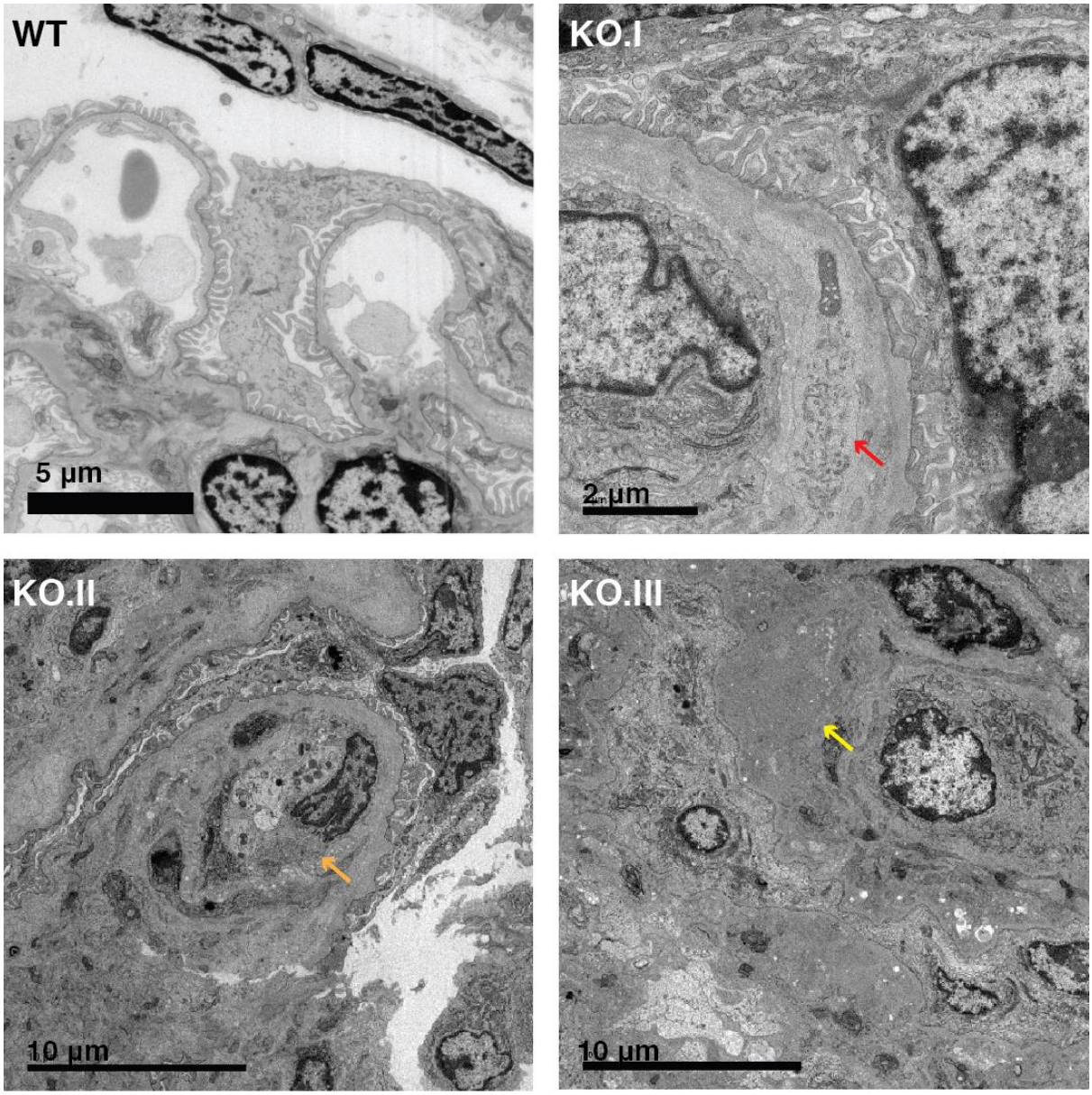


Fig.6.6 Transmission electron microscopy of *Gimap6*$^{-/-}$ mouse kidneys. Representative images of glomeruli from wildtype (WT) or knockout (KO) mice imaged with transmission electron microscopy. WT shows a normal glomeruli. KO.I shows cellular interposition (red arrow) between the glomerular basement membranes. KO.II shows capillary lumen occlusion (orange arrow). KO.III shows glomerular hyaline droplets (yellow arrows). N_{KO}=2, $n_{Control}$=1**.**

6.2.3 Renal disease in Gimap6$^{-/-}$ *mice appears to be non-hematopoietic in origin*

Because microangiopathy is a pathology associated with many diverse conditions, it can be difficult to determine its direct etiology. Microangiopathies, often referred to as "thrombotic microangiopathies"can be caused by a wide variety of conditions, including

infection, genetic defects typically in clotting- or complement-associated proteins, autoimmunity, glomerular diseases, or hypertension (reviewed in *11*). The microangiopathy in KO mice does not appear to be immune-complex mediated, but that does not exclude the possibility it being immune-mediated; APS, for example, can result in microangiopathy. Because GIMAP6 is expressed in lymphocytes and the patient's disease is largely autoimmune, we hypothesized that the microangiopathy in KO mice might be antibody-mediated. KO mice did not have any detectable anti-nuclear antibodies (**Fig. A6.1A**), and although some animals were positive for anti-cardiolipin antibodies, these were at comparable levels to control mice (**Fig. A6.1B).** However, we cannot exclude the possibility of other autoantibodies that could lead to kidney disease in mice, or possibly non-specific contributions such as immune-complexes or improperly glycosylated antibody. Therefore, on the basis that GIMAP6 is primarily expressed in lymphocytes we argued that they could be mediating the kidney disease in mice. We therefore made a preliminary test of a potential therapy that could be utilized in PID1467 or future patients, depleting B cells with an anti-CD20 antibody.

We depleted B cells in KO mice with anti-CD20 antibody (**Fig. 6.7)** to determine whether such therapy could improve KO mouse phenotype. Two anti-CD20 clones were used. The first was a rat monoclonal antibody from Biolegend (clone SA271G2), which did efficiently deplete B cells; however, mice given a rat isotype control lost significant weight after the injection (data not shown), potentially due to an inflammatory response. Therefore, for all further injections, a mouse monoclonal antibody kindly gifted by Prof Mark Cragg (University of Southampton, Southampton, UK) and a corresponding isotype control were used to limit immune responses against the therapy. Though depletion was variable amongst mice, B cells in the treatment group were generally maintained at levels less than half that of controls (**Fig.**

6.7B,C). However, kidney function as measured by bimonthly plasma urea and creatinine testing was not improved by treatment (**Fig. 6.7D,E)**. Additionally, although the experiment is still ongoing, B cell depletion has had no significant impact on KO mouse survival (**Fig. 6.7F**). These preliminary experiments indicated therefore that anti-CD20 therapy is not an effective therapy, at least under the conditions tested.

As a further test of the hypothesis that the kidney disease in KO mice is immune-mediated, we asked whether transfer of wildtype bone marrow might improve survival of KO mice. Therefore, we transferred either KO or CD45.1+ WT bone marrow into irradiated KO mice (**Fig. A6.1A)**. However, within two months of the transfer, all KO mice had to be culled as they had rapidly lost weight and exceeded the protocol's 15% weight loss cutoff (**Fig. A6.1B)**. None of the control mice (three CD45.1+ WT and one CD45.2+ heterozygous littermate) that received CD45.1+ bone marrow had significant weight loss, suggesting that it was not due to procedural complications or graft-versus-host disease but rather due to intrinsic differences between control and KO mouse phenotype. Irradiation damages several organ systems, including the hematopoietic system, intestines, and kidneys; microvascular endothelial cells are particularly sensitive to irradiation and are thought to be the main mediators of tissue damage (*592–594*). The KO mice used were males and females between 7-13 wo. Most, if not all, likely already had damage to the kidneys and possibly other organs as seen in **Fig. 6.2 and 6.3** which might have been exacerbated upon irradiation resulting in weight loss. Therefore, we could not conclusively determine whether transfer of WT bone marrow might rescue KO mouse survival. However the findings do imply that the KO mice were already chronically sick by week 7-13 and the provision of normal bone marrow cells does not ameliorate the disease.

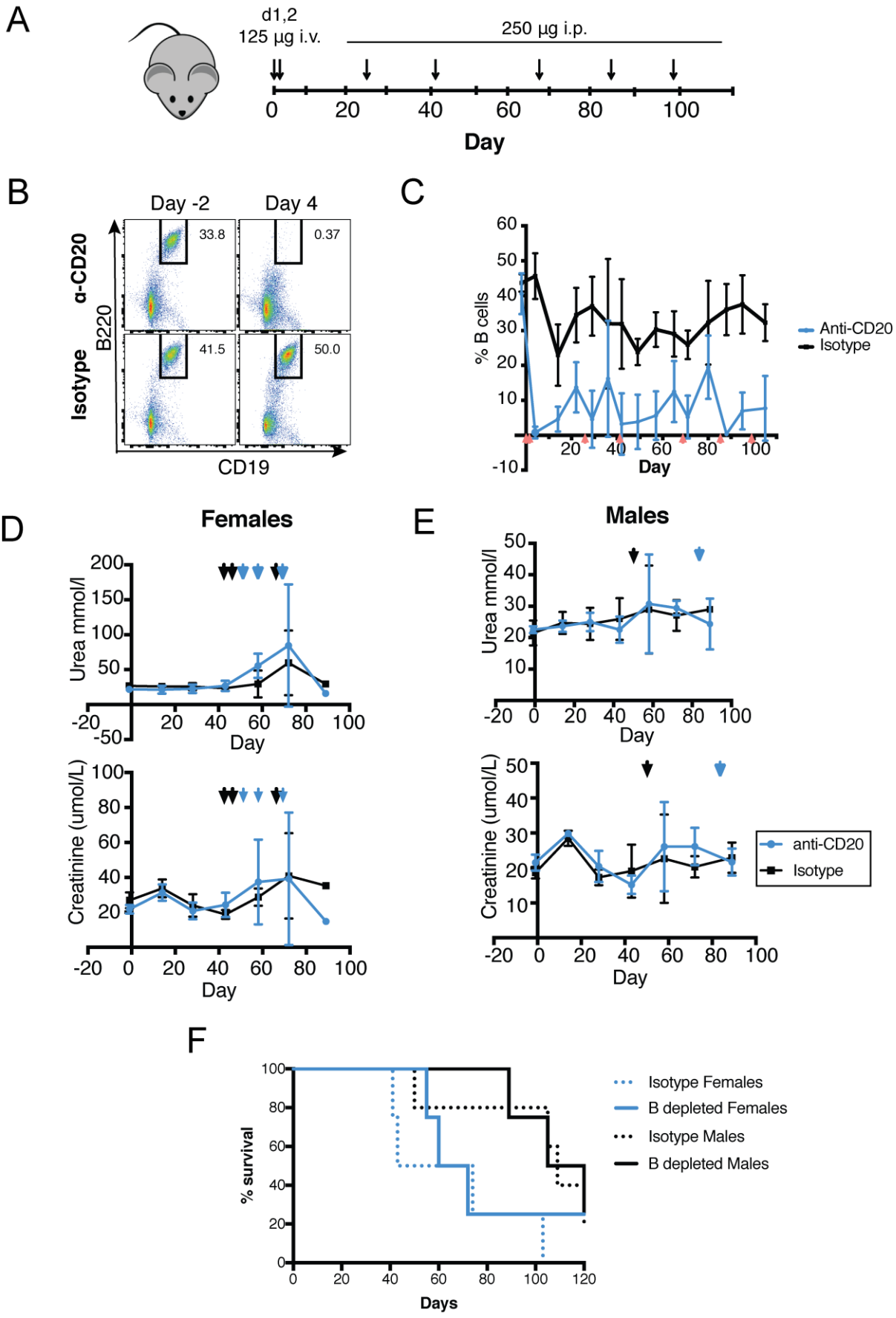

A
d1,2
125 µg i.v.
250 µg i.p.
0
20
40
60
80
100
Day
B
Day -2
Day 4
α-CD20
B220
Isotype
33.8
0.37
41.5
50.0
CD19
C
% B cells
Anti-CD20
Isotype
Day
D
Females
Urea mmol/l
Creatinine (umol/L)
Day
E
Males
Urea mmol/l
Creatinine (umol/L)
anti-CD20
Isotype
Day
F
% survival
Days
Isotype Females
B depleted Females
Isotype Males
B depleted Males

Fig. 6.7 B cell depletion does not rescue *Gimap6*$^{-/-}$ mice. *Gimap6*$^{-/-}$ mice were injected with 125 μg of anti-CD20 (clone SA271G2, Biolegend) or rat IgG2b isotype control i.v. on days 0 and 1 of the experiment, and then every 2-3 weeks afterwards with 250 μg of anti-CD20 (clone 18B12) or mouse IgG2a isotype control i.p. **A)** Schematic showing injections. **B**) Blood was analyzed weekly to check for B cell depletion by flow cytometry. Gating strategy is shown in **Fig. A.6.2** with an example of depletion in mice injected with the anti-CD20 antibodies in **B**. **C**) Quantification of **B**, showing the percent of B cells in peripheral blood leukocytes. Arrows show anti-CD20 treatment days**. D,E**) Plasma was collected every other week and analyzed for blood urea and creatinine levels for females (**D**) and males (**E**). Blue arrows represent times when B-depleted mice died, and black arrows represent when control mice died. **F**) Kaplan-Meier survival curve of B cell-depleted and control mice. $n_{B\ Depleted\ Females}$=4, $n_{Isotype\ Females}$=4, $n_{B\ Depleted\ Males}$=4, $n_{Isotype\ Males}$=5. Shown are mean + SD.

We also carried out the reciprocal experiment adoptively transferring KO bone marrow into irradiated WT hosts (**Fig. 6.8A**). Plasma urea and creatinine levels in KO engrafted mice remained normal through 30 weeks post-irradiation, implying unimpaired kidney function **(Fig. 6.8B,C**). We have since extended these studies to seven months since the bone marrow transfer, and all chimeric mice are alive with no signs of illness. Therefore, the kidney disease in KO mice does not seem to be transferrable through hematopoietic cells. Within the limits of the experiment, the reverse transfer of WT bone marrow did not save the irradiated KO mice. Together with the failure of the anti-CD20 experiment to prevent the renal disease, we do not have any evidence that this problem is mediated by immune cells or products.

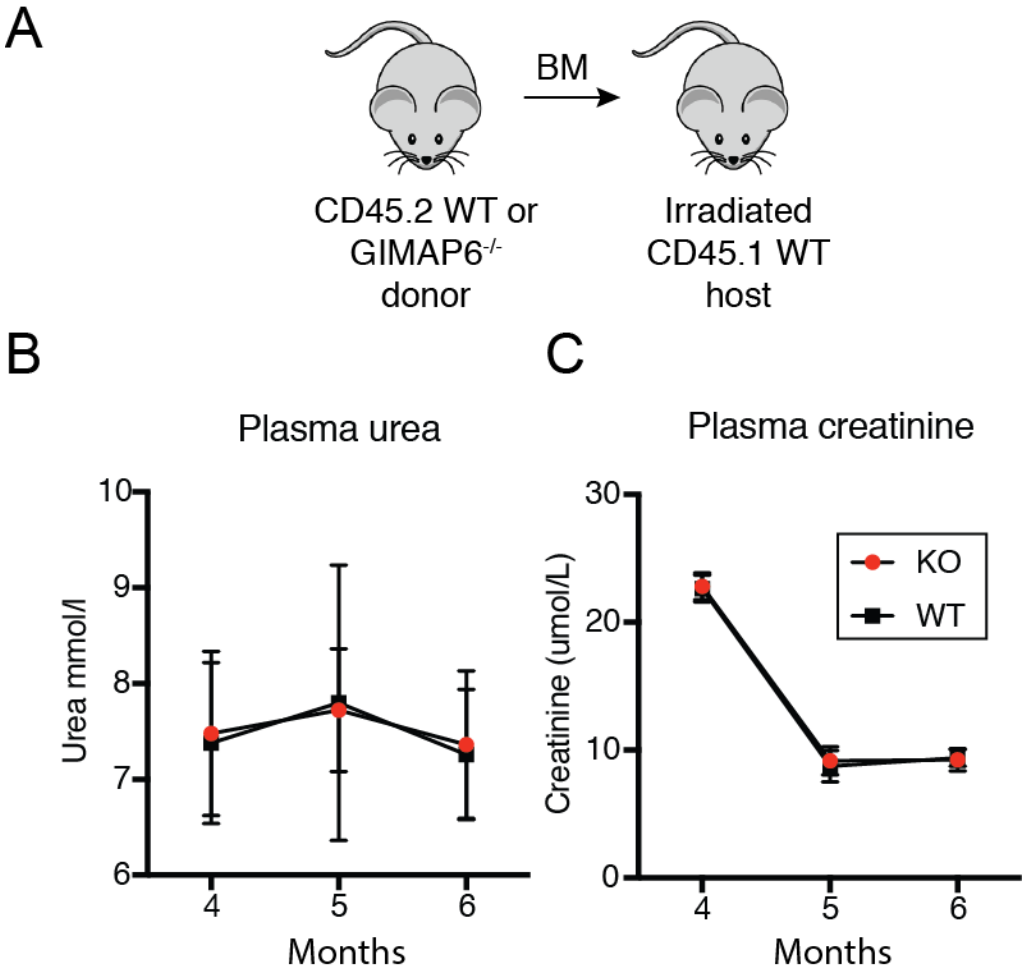


Fig. 6.8 Transfer of *Gimap6*$^{-/-}$ bone marrow is not sufficient to cause kidney disease. Bone marrow (BM) from CD45.2 *Gimap6*$^{-/-}$ (KO) or littermate controls was transferred to lethally irradiated CD45.1 WT mice were lethally irradiated. **A**) Schematic of experimental design**. B,C**) Plasma urea (**B)** and creatinine (**C**) levels after transfer. Data shown is mean +/- standard deviation. n=10 for both groups.

Because of the findings above, we wondered whether the kidney disease may be due to a primary rather than secondary cause. Therefore we asked whether GIMAP6 was expressed in kidneys. To reduce possible contamination from blood lymphocytes, we extracted mRNA from perfused kidneys of WT, KO, and Rag mice, which lack B and T cells. Rag mice still had *Gimap6* expression in spleens, albeit at greatly reduced levels compared to WT, suggesting low levels of GIMAP6 expression in cells such as NK or myeloid cells (**Fig. 6.9**). Surprisingly, kidneys of both Rag and WT mice had low levels of *Gimap6* mRNA, supporting the possibility that a population of renal cells express GIMAP6. Disruption of GIMAP6

expression and function in one or more critical renal cell populations would give a direct explanation of the severe renal pathology in the KO mice.

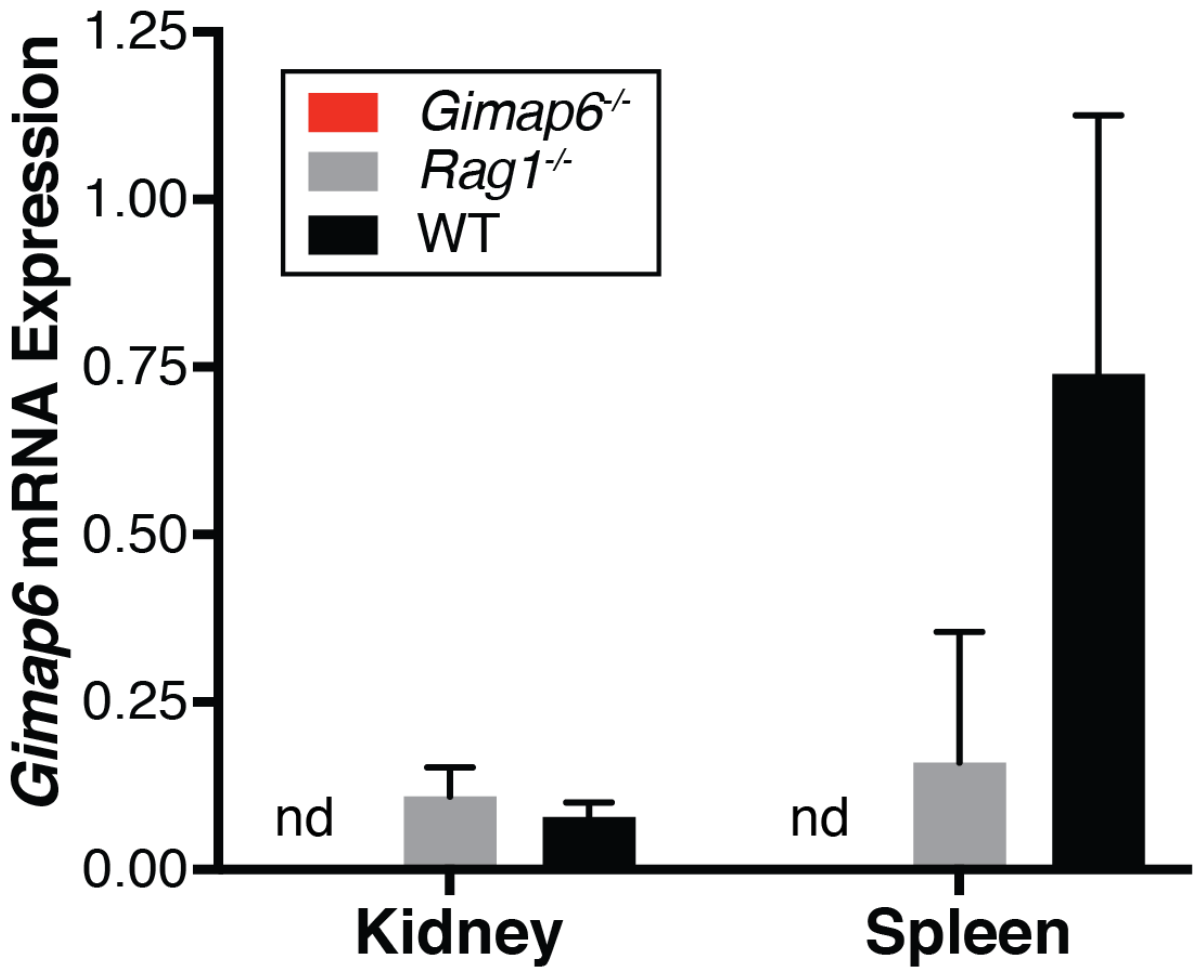


Fig.6.9 *Gimap6* mRNA is lowly expressed in kidney. mRNA was extracted from organs collected from perfused mice. *Gimap6* mRNA was assessed by RT-PCR with *HRPT1* used as the reference gene. Shown is relative expression, with a WT spleen sample set as 1. n=3. nd= not detected.

6.3 Discussion

In this chapter, I discuss the discovery of early mortality likely due to complications from kidney disease in KO mice. This dramatic effect of a germline deletion of *Gimap6* demonstrates the importance of GIMAP6 in kidney function and murine health. However,

there has been no renal disease found in the human patient, and I considered several possible explanations for this difference.

6.3.1 Early mortality in KO mice

KO mice have decreased survival starting at about four and six months for females and males, respectively. I showed that these mice have a complete genetic ablation of GIMAP6 expression. Interestingly, females succumb earlier and more rapidly than males, suggesting a sex-specific effect. Gender biases exist in many diseases due in part to differences in hormones; kidney and heart disease, for example, are typically more severe amongst males, whereas autoimmune disease is more prevalent in females (Ngo, Han, Patten).

Gross examination of tissues showed that the most obvious and consistent phenotypic traits in both male and female KO mice were enlarged hearts and pale, scarred kidneys; damage in either or both could easily explain the survival defect. Heart and kidney diseases are intricately linked. Kidneys regulate blood pressure; renal dysfunction causes hypertension, anemia, inflammation, and alterations in blood properties such as pH and electrolyte levels all of which can damage the heart (*580*, *581*). Heart disease, on the other hand, reduces the blood supply to the kidneys which can both damage the kidneys and cause them to produce more renin, a hormone that further increases blood volume and pressure, leading to a vicious feedback loop (*582*, *583*). Additionally, several factors like diabetes, hypertension, and endothelial dysfunction are risk factors of both (*581*, *595*).

This chicken and egg-like nature of heart and kidney disease can make it difficult to parse out the root cause of the KO mouse's disease. However, the evidence we have gathered thus far leads us to believe that KO mice have microangiopathy leading to kidney disease, and that heart enlargement is secondary to the microangiopathy, kidney disease, or both. First,

kidneys were consistently and severely affected in histological samples, whereas the hearts only occasionally showed histological abnormalities. H&E, PAS, and TEM findings were consistent with microangiopathy. Additionally, markers of renal function showed elevations in plasma urea and creatinine and increased leakage of protein into the urine, indicating damaged kidneys several weeks before the animals died. Plasma urea and creatinine levels only rise after the loss of 50% renal function so it is likely that the kidney damage was already well established by 9 weeks of age (*596*).

We also observed microcytic anemia in KO mice, which is consistent with kidney disease. Peritubular cells in the kidneys are the main producers of the erythropoietin which promotes RBC production (*597*). While an ELISA would be needed to test for erythropoietin levels in the KO mice, it is likely that their kidney damage results in a deficiency in the hormone, partially leading to anemia. Additionally, chronic renal failure is associated with inflammation, which can exacerbate anemia by promoting death in erythroblasts, further inhibiting erythropoiesis, and stimulating release of hepcidin, a liver hormone that regulates iron levels, which can lead to iron deficiency as seen in the KO mice (*584*, *598*). Anemia can result in heart enlargement as it forces the heart to exert more pressure to maintain oxygen levels, as can the other conditions discussed above that are associated with kidney damage (*581*). This leads us to believe heart damage is a secondary complication in KO mice. We hypothesize that the deaths in mice that showed no obvious signs of illness may have been due to cardiomyopathy secondary to kidney disease, whereas those that did show symptoms were likely suffering from advanced renal failure amongst other complications, including anemia.

6.3.2 Etiology of microangiopathy and other potential GIMAP6-expressing cells

As discussed in Section 6.2.3, microangiopathy can be caused by a myriad of different conditions. Because of the lupus-like nature of the patient's disease and the known expression of GIMAP6 in lymphocytes, an antibody-mediated kidney disease seemed at first to be the most likely explanation. However, antibody staining did not show the characteristic granular pattern of immune-complex mediated-kidney damage, though this does not exclude the possibility of contribution from a systemic autoimmune condition. Microangiopathies can be caused by several antibody-mediated diseases, including APS and SLE (*591*). This possibility is especially intriguing as it could tie together the mouse and patient phenotypes. However, there is no evidence that the patient has renal disease and the KO mice were ANA-negative, with similar numbers of KO and controls ACA-positive by ELISA.

Anti-CD20 antibody therapies such as rituximab and ocrelizumab have proven effective in the treatment of multiple autoimmune diseases, including rheumatoid arthritis and relapsing multiple sclerosis (*599*, *600*). Though the benefit of rituximab treatment for SLE is unclear, it is used off-label for SLE treatment (*601*). Thus, we used an anti-CD20 therapy to see if B cell depletion improved mouse outcome both to determine whether B cells might mediate disease and to see whether it should be considered as a potential therapy in human GIMAP6 patients. However, anti-CD20 therapy had no effect on KO mouse disease severity, and the disease progression under treatment was similar to that without treatment. This is consistent with a primary renal problem rather than a primary humoral one.

More telling were the results from the transfer of KO bone marrow into WT mice. KO mice show significant renal dysfunction by 9 weeks of age. The chimeras have shown no signs of kidney disease in over half a year since the transfer. They may later develop renal failure

but even if that were to occur, the delay in clinical onset is marked. The results thus far suggest that a lack of GIMAP6 in the hematopoietic system is not sufficient for renal disease. This is not to say that hematopoietic cells may not contribute to disease, but it does suggest another factor is needed to initiate disease. Intriguingly, this implies a cell of non-hematopoietic origin likely expresses GIMAP6. Supporting this hypothesis, no kidney disease or survival defects are reported for mice with a conditional deletion of *Gimap6* in T and B cells (Geoff Butcher, University of Cambridge, UK, correspondence).

Innumerable gene expression studies have been done previously on many different tissues and cell types. Because of the involvement of the kidney, we interrogated the GenitoUrinary Development Molecular Anatomy Project (GUDMAP) database to query whether GIMAP6 might be expressed in mouse kidneys (*602*, *603*). Along with expression in some urinary tract and gonadal cells, GIMAP6 was highly expressed in endothelium of embryonic and adult kidneys. Further, a recent single-cell transcriptomics study of murine kidneys found high levels of *Gimap6* expression in five cell types: in T and B cells as expected, but also in an undefined subset, NK, and endothelial cells (*539*). Examination of some other publicly available databases (LungGens, Angiogenes, Immgen, Expression Atlas) supported the possibility that GIMAP6 is expressed in at least some mouse and human endothelial cell types, as well as possibly in other immune cells (*604–608*). Expression in endothelial cells and/or non-lymphocytes, would explain the *Gimap6* mRNA expression in the *Rag1*$^{-/-}$ spleen and kidneys. Additionally, a microarray study in human endothelial cells suggested that GIMAP6 is an endothelial-restricted gene, and in fact saw higher expression of *GIMAP6* mRNA in all examined primary endothelial cells than in their T cell dataset (*609*). Indeed, human *GIMAP6* was most highly expressed in microvascular endothelial cells, which if similar in mice, would be consistent with the microvascular disease described in this chapter. Lending further

credence to *GIMAP6* as an endothelial gene, human umbilical vein endothelial cells (HUVEC) have already been verified as expressing human *GIMAP6* (*332*).

Though GIMAP6 expression in endothelial and other immune cells needs to be verified through western blot, RT-PCR, and immunohistochemical staining, this finding it could explain several observations made over the course of this study. First, vascular injury is one of the hallmarks of microangiopathy. The glomerulus consists of a network of capillaries supported by mesangial cells. Thus, loss of GIMAP6 could impair endothelial and glomerular function, serving as the trigger necessary to induce kidney disease that is missing in the bone marrow chimeric and CD2 conditional knockout mice. This could be tested in the future by making a conditional knockout of GIMAP6 in endothelial cells to see whether this would cause kidney disease in mice. Further, these conditional knockouts could be given KO bone marrow to determine the contribution of hematopoietic cells to the disease.

Based on the various databases and papers discussed above, it seems highly likely that human GIMAP6 is expressed in at least some endothelial cell subsets, and likely in microvascular cells. Identification of the similarities and differences between GIMAP6 expression in mouse and human endothelial cells could be informative in explaining some of the potential differences in phenotype seen between the *Gimap6* KO mice and PID1467. It would also be interesting to determine if loss of its expression affects function. Knockout of GIMAP6 in endothelial cell lines could be used to test for function. If GIMAP6 does affect human endothelial cells, it is quite likely that it could contribute to the patient's vasculitis, although her anti-phospholipid antibodies could also contribute. Amongst other functions, endothelial cells participate in inflammatory responses, both recruiting immune cells and releasing pro-inflammatory cytokines (*610*). Indeed, endothelial cells contribute to inflammatory conditions like rheumatoid arthritis and inflammatory bowel syndrome (*611*,

612). Furthermore, if GIMAP6 proves important to endothelial function, it could suggest other GIMAP6 deficiency phenotypes that might be worth searching for, potentially expanding our cohort. It could also suggest other therapies that might benefit our patient PID1467 if her disease is partly driven by endothelial dysfunction. As endothelial injury is common in cardiovascular disease, several drugs exist to treat endothelial defects, including endothelial NO synthase enhancers, beta blockers, Sphingosine-1-phosphate, ACE inhibitors, and more (*613*). Identification of the pathway disrupted by GIMAP6 loss could allow treatment with a drug that would exert a protective effect on endothelium.

Chapter 7. Discussion

In this thesis, I examined three patients with PIDs of unknown etiology and investigated the molecular function of a newly identified PID-associated gene. The majority of my work focused on a single patient whose disease we believe is caused by a novel GIMAP6 deficiency caused by a point mutation that reduces expression of this protein. The patient has a disease pattern that includes splenomegaly, immune thrombocytopenia, autoimmunity, increased susceptibility to certain infections, pulmonary hypertension, and vasculitis. To elucidate the activity of GIMAP6 and the molecular underpinnings of the patient's disease, I carried out detailed studies on mice with a germline *Gimap6* deletion. These mice showed a major clinical phenotype: premature death from renal disease. In this respect, the KO mice differ from the human patient who had no apparent kidney disease. In this final chapter, I will discuss the human-mouse differences in GIMAP6 deficiency, our current understanding of the gene, the PID it may cause, as well as how this may influence clinical practice.

7.1 GIMAP6: mouse vs human differences

PID1467 and the *Gimap6* KO mice have distinct variations in phenotype: autoimmunity and antibody abnormalities are present in the patient and not mice; and conversely, kidney disease is observed in mice and not patient (**Table 7.1**). There are several potential explanations for these discrepancies, the most obvious of which is the possibility of mouse-human differences. As discussed in Chapter 1, while much of the mouse genome does have direct homologues in humans, there are also clear differences than can affect phenotypes (*14–16*, *614*, *615*). Species variation exists even in just the *GIMAP* family: *GIMAP2* is present in humans and not mice, and *Gimap3* and *Gimap9* are expressed in mice but not

humans (*452*, *460*). Because GIMAPs are thought to homo- and hetero-dimerize and possibly function in the same or similar pathways, it is possible that members may be able to partially compensate for another's loss (*460*, *463*). For example, GIMAP3 may be involved in GIMAP5 activity in mice (*463*). Alternatively, loss of one GIMAP could adversely affect another's activity. This is particularly relevant for GIMAP6 as thesis work from a member of the Daumke lab has shown that GIMAP6 can bind to GIMAP7 and inhibit its GTPase activity *in vitro* (*451*, *531*). GIMAP7 in turn can stimulate GTP hydrolysis in GIMAP2, which forms scaffolds on lipid droplets; therefore, GIMAP6 might be an upstream regulator of GIMAP7 and GIMAP2 activity (*460*, *461*, *531*). Additionally, mice and humans have differences in expression that may account for some differences in phenotype. In particular, GIMAP6 is expressed in murine B cells, but does not appear to be expressed in human B cells (*518*).

Another possibility is that the patient does have a similar phenomenon that is presenting differently due to the aforementioned differences. Our current hypothesis is that the loss of *Gimap6* expression in murine microvascular endothelial cells causes damage leading to microangiopathies. The patient, on the other hand, has vasculitis, presumably due to APS. The "two hit" model suggests that thrombosis in APS requires both the presence of autoantibodies and an injury to the endothelium; endothelial-cell priming is required to bind β_2-glycoprotein I, a complement regulator that is the major target in APS (*616*–*618*). A microarray of human primary cells has suggested that *GIMAP6* is an endothelial cell-restricted gene, with higher expression observed in endothelial cells than even in T cells (*609*). Of note, the greatest expression was in microvascular endothelial cells. If human and mouse GIMAP6 are both indeed present in the endothelium, it is tempting to postulate that GIMAP6 dysfunction in the patient's blood vessels contributes to her disease.

Phenotypic variation between different *Gimap6* mouse models provides yet another possible explanation. Three transgenic *Gimap6* strains have been characterized: B6N(Cg)-*Gimap6*$^{tm1b(KOMP)Wtsi}$/J (tm1b), which have a complete excision of *Gimap6* exons 2 and 3; its parental strain, B6N(Cg)-*Gimap6*$^{tm1a(KOMP)Wtsi}$/J (tm1a), which have a selection cassette inserted upstream of exon 2 but maintain the coding sequence (see **Fig. 2.1***)*; and GIMAP6$^{fl/fl}$CD2Cre (CD2Cre), which have a conditional knockout of *Gimap6* in T and B cells (**Table 7.1)** (*316–318*, *517*). My colony (referred to as "Oxford tm1b" in **Table 7.1**) and its sister colony at Jackson Laboratories ("Jax tm1b"), which was phenotyped by the IMPC, have traits consistent with kidney dysfunction, i.e. anemia, abnormal renal parameters, and increased heart weight (*317*). There is no indication of renal disease in the CD2Cre mice, supporting our hypothesis that the renal disease has a non-immunological etiology as discussed in Chapter 6 (*517*). However, the most telling difference is that between the tm1b mice and their parental tm1a strain. Though distinguished from the tm1b strain only by the continued presence of *Gimap6* coding exons, the tm1a mice do not share the tm1b's kidney disease (*317*). The KOMP generates the "knockout-first" tm1a mice through insertion of a cassette containing a splice acceptor and polyadenylation sequence to create a knockout of the targeted gene at the RNA level (*319*, *619*). These tm1a mice sometimes have leaky expression due to incomplete use of the splice acceptor, which we postulate to also be the case in the *Gimap6* tm1a mice (*620–623*). Notably, the patient also appeared to have small quantities of GIMAP6 protein detectable by western blot. Therefore, while this requires verification, the presence of residual GIMAP6 protein, if expressed and stable, could explain the lack of kidney disease in the tm1a mice and the patient: endothelial cells may require only low levels of GIMAP6 for normal function compared to immune cells.

Lastly, genetic and environmental factors might also partially account for the clinical presentations observed. Because we are examining a single patient, we cannot be certain how much heterogeneity in clinical symptoms there may be amongst other patients with GIMAP6 deficiency. After all, even five GIMAP5 patients from the same family, four of whom were siblings, had variations in presentation, with autoantibodies, specific lymphopenias, and hypogammaglobulinemia in some but not others (**Table 3.5**). Multiple factors, including environmental exposures, lifestyle, and genetics, affect disease manifestation (*624–627*). As an example of environmental influences, in the case of Mendelian susceptibility to mycobacterial disease (MSMD), a patient may never present symptoms if they are never exposed to mycobacteria. The clinical care patients receive may also mask symptoms or cause side effects due to drug treatment. PID1467 has been on multiple medications, including the glucocorticoid prednisolone from a young age; prednisolone use can affect multiple organ systems and cause conditions including hypertension, cardiomyopathy, secondary opportunistic infections, and osteoporosis (*628*). Alternatively, corticosteroid therapy may have reduced any inflammation involved in the development of microangiopathy, thus preventing or reducing kidney disease. She has also had a splenectomy, which increases the risk of thrombosis and sepsis (*629*). Any of these factors, or a combination of them, could alter the susceptibility to kidney disease.

Similarly, genetic factors greatly impact disease. The nature of the specific mutation can lead to variable presentation, as exemplified by *Rag1* deficiencies, in which patients can present with SCID, Omenn syndrome, or CID associated with granulomas and/or autoimmunity depending on their mutation's consequence on protein function or expression (*630*, *631*). The patient's genetic background may also contribute to her phenotype. Though not from a reportedly consanguineous family, we cannot exclude that she has other genomic

variants that may act as modifying genes. Even just from the list of homozygous recessive candidate genes (**Table A.5)**, there are several genes that could conceivably contribute to her disease: CHIA, for example, is involved in inflammatory pathways and AGO1 is involved in transcriptional regulation (*489*, *492*). Of particular note, the patient also has a synonymous mutation in the IL-6 receptor (*IL6R*), which has been implicated in autoimmunity and both the pro- and anti- inflammatory responses (*632*). While synonymous mutations were filtered from our list of candidate genes, there is an increasing appreciation that they might also contribute to disease (*633*). The effect of the patient's *IL6R* variant and these other gene variants to her phenotype must therefore be examined.

Table 7.1 Comparison between patient and mouse phenotypes					
	PID1467	**Oxford tm1b**	**Jax tm1b[1]**	**Tm1a[1]**	**CD2 conditional[2]**
Lymphadenopathy	Yes				
Splenomegaly	Yes[3]	Yes[4]			No[5]
Autoantibodies	Direct Coombs test (+); Anti-Cardiolipin (+); anti-Phospholipid (+)	ANA(-)		ANA(-)	
Antibody abnormalities	Yes (hyper-IgM, hypo-IgA, borderline hypo-IgG)	No			
Anemia	Yes (AIHA)	Yes	Yes[6]	No	
Thrombocytopenia	Yes	No	No	No	
Lymphocyte abnormalities	**Blood**: Mild and transient lymphopenia	**Spleen**: Increased B cell #; decreased NKT #; Decreased percentage of T cells		**Blood**: increased monocytes **Spleen**: Decreased NKT # **Bone marrow**: Decreased T cells	**Spleen**: Increased splenic B cells; decreased T cells # and frequency
Renal dysfunction	No	Yes	Yes[7]	No	
Vasculature phenotype	Vasculitis of lungs; livedoid vasculitis; femoral artery pseudoaneurysm; pulmonary hypertension	Increased heart weight; suspected microangiopathy	Increased heart weight	No	
Increased susceptibility to infection	Yes			Yes[8]	
Other	Failure to thrive		Decreased total body fat		

Blank spaces= not tested

[1]Data from (http://www.mousephenotype.org/data/genes/MGI:1918876)(*317*) ;[2]Data from (*517*); [3]Received splenectomy; [4]variable, not statistically significant; [5]No difference in counts, did not weight; [6]Decreased MCV, decreased MCH, increased BUN; [7]Increased plasma blood urea nitrogen; [8]Salmonella challenge (Dr. Simon Clare, Wellcome Sanger Institute, personal correspondence); AIHA= autoimmune hemolytic anemia; ANA= anti-nuclear antibodies. Blank= not tested

7.2 GIMAP6—Current understanding and working models

While much remains to be discovered about the function of GIMAP6 and the GIMAP proteins in general, there is compelling evidence that GIMAP6 is associated in some way with the autophagic process. Though the investigation of autophagy is complicated by the possibility that examined proteins can both regulate or be regulated by autophagy, two independent groups have identified GABARAPL2, an ATG8 homologue, as a strong binding partner of GIMAP6 (*332*, *531*). One possibility is that GABARAPL2 regulates GIMAP6. Indeed, the Butcher group did observe degradation of GIMAP6 after starvation, albeit at a slower rate than that of GABARAPL2 itself, as well as a dependence on the GIMAP6:GABARAPL2 interaction for GIMAP6 recruitment to autophagosomes (*332*). However, the work presented in Chapter 5, in conjunction with that published by the Butcher laboratory, also suggests the reverse is true (*332*, *517*). While GIMAP6 KO Jurkat lines showed no consistent autophagic defect, perhaps due to compensatory mechanisms, T cells from GIMAP6 KO mice and the patient appeared to have a late-stage block. The Butcher group further showed that inducible knockout of murine GIMAP6 in resting T cells leads to an accumulation of p62/SQSTM1 phosphorylated at S405, which is associated with defective autophagy. However, LC3-II levels were not affected, possibly due to the experimental conditions (*517*). Though members of the Atg8 subfamily likely have some functional redundancy, the GABARAP family appears to be particularly important in regulating autophagosome-lysosome fusion, likely, in part, through preferential recruitment of specific effectors (*535*, *536*, *634*). Therefore, the autophagy defect observed during GIMAP6 deficiency seems consistent with a potential role of GIMAP6 as a GABARAPL2 positive regulator. However, one caveat to this hypothesis is that murine GIMAP6 binds only weakly to GABARAPL2, though it is also recruited to the

autophagosome upon autophagy induction (*332*, *517*). It is unknown whether murine GIMAP6 may have a different GABARAP binding partner. Therefore, further studies will be needed to determine GIMAP6's exact role in autophagy and its connection to the ATG8 family.

While there is a clear link between GIMAP6 and autophagy, what remains to be clarified is the functionality of this association in the immune system and, moreover, what the pathological consequences of its disruption are that lead to the patient and mouse phenotypes. The GIMAP family is thought to be involved in immune cell development, survival, and homeostasis (*635*). A role in autophagy could be consistent with this, as autophagy is known to have many roles in lymphocyte survival, maintenance, and differentiation as discussed in Chapter 1. Autophagy also regulates several important endothelial functions, including clearance of intracellular lipid substrates, cell alignment, protection against oxidative stress, reduced inflammation, and increased endothelial nitric oxide synthase expression (*636*, *637*). Therefore, it will be interesting to determine whether autophagy and autophagy-regulated processes are also affected in GIMAP6-deficient endothelial cells.

A straightforward role for GIMAP6 in autophagy, however, is complicated by the discrepancy in phenotype between knockouts models of GIMAP6 and of core autophagy proteins. T cell-specific ablation of core autophagy genes results in severe lymphopenia; the CD2-Cre *Gimap6* knockouts also had lymphopenia, which the authors suggested was due to an increased amount of apoptotic cells leading to higher cell turnover (*256–259*, *517*). Furthermore, a recent paper suggested increased apoptosis after activation in *GIMAP6* knockout cell lines (*518*). However, neither the tm1b nor the tm1a mice had clear lymphophenia and the splenic B cell population was expanded in homozygous mice in my colony. Similarly, PID1467 has had only mild, transient lymphopenia. Also, while autophagy-

deficient T cells have reduced proliferation after *in vitro* activation, no such defect was seen in *Gimap6* KO T cells despite the block in autophagic flux. So the role of GIMAP6 in immune cell survival is not clear at present.

These discrepancies may point towards redundancy in function or a selective role for GIMAP6. If GIMAP6 regulates specific GABARAP proteins, it is possible other family members could compensate for that member's function. Alternatively, GIMAP6 might be involved in selective autophagy. The ATG8 homologues have varying affinities for different adaptor proteins, conferring specificity to cargo (*537*, *538*). GIMAP6 could conceivably affect binding of certain proteins with GABARAPL2, thus regulating its function. Additionally, GIMAP6 has a tentative link to lipophagy and lipid droplets through its interaction with GIMAP7. This could be relevant to GIMAP6's function in T cells as autophagy and lipid metabolism both play a role in T cell differentiation, as discussed in previous chapters (*256*, *257*, *272*, *371*, *638–640*). It would thus be interesting to look further at T cell differentiation, particularly CD4 helper T cell subsets which could contribute to inflammatory responses.

Although GIMAP6 has not been definitively demonstrated in a phagocytic cell, it has been implicated in antimicrobial immunity. A study examining Johne's disease, a chronic infection with *Mycobacterium avium* subsp. *paratuberculosis* (MAP), in ruminants demonstrated downregulation of GIMAP6 (*480*). Infection with a different intracellular parasite, *Toxoplasma gondii*, showed upregulated *Gimap6* expression in peritoneal cells of resistant rats. GIMAP6 appeared to inhibit parasitic growth through localization to the parasitoporous vacuole membrane (PVM) and promotion of lysosomal fusion (*641*). Further, preliminary data suggests *Gimap6* knockout mice have increased susceptibility to *Salmonella typhimurium* (Dr. Simon Clare, Wellcome Sanger, UK, personal correspondence). Interestingly, a recent study showed that specific deletion of *GABARAPL2* in mice also led to

a decreased interferon-γ-mediated clearance of *Toxoplasma* due to dysregulated distribution of interferon-inducible GTPases (*642*). In a database of interferon-regulated genes (Interferome v2.01), human macrophages and monocyte-derived macrophages increase *GIMAP6* transcription in response to interferon-γ (*643*). Confirming these data, a recent paper showed that GIMAP6 is one of the top one hundred genes upregulated by IFN-γ in human macrophages, though its overexpression could not inhibit HIV replication (*644*). Together, these studies implicate GIMAP6 in innate immunity through xenophagy, LC3-associated phagocytosis (LAP), and/or interferon responses. It is interesting to note, however, that deficiencies in interferon-γ signaling typically present as MSMD (*62*).

7.3 Therapeutic prospects

Identification of the molecules and pathways involved in PIDs allows for mechanism-based therapeutic options. In collaboration with other members of the Lenardo laboratory, I helped demonstrate that GIMAP5 interacts with components of the Ragulator complex. Along with functions in lysosomal positioning, the Ragulator, and thus potentially GIMAP5, is involved in metabolism and mTORC1 signaling (*645–649*). Though anecdotal, one GIMAP5 patient has been successfully treated with sirolimus (rapamycin), an inhibitor of mTORC1 signaling, and has had less severe disease than other patients. If this can be replicated in other patients, it would both serve as a proof of principle that GIMAP5 does regulate the mTORC1 pathway and mTOR inhibitors can serve as an effective way to treat our current and future patients.

On the other hand, GIMAP6 appears to be involved in autophagy, which can be modulated by multiple therapeutics (*650*). Hydroxychloroquine is an autophagy inhibitor currently used by our patient. This is important because GIMAP6 deficiency seems to cause a

block in autophagic flux, so further pharmacological inhibition might exacerbate disease pathology. Nor can we currently exclude the possibility that the observed autophagic defect in the patient cells is in fact caused by the hydroxychloroquine treatment. However, predicting the advantages of autophagy induction or inhibition is somewhat complex. In the case of LATAIE disease, LRBA deficiency reduces autophagy in B cells, but hydroxychloroquine has been suggested as a therapy because patients' symptoms are caused partly by increased lysosomal degradation of CTLA4 in T cells (*25*, *290*). In general, blockade of autophagy could lead to further buildup of undegraded vesicles and damaged organelles, as well as affect processes such as cell metabolism. However, autophagy promotion could paradoxically cause the same problem if GIMAP6 is involved in the late-stages of autophagy such as in autophagosome-lysosome fusion and thereby creates a bottleneck effect. Autophagy-modulating drugs typically influence multiple cellular pathways and current autophagy-enhancing drugs that target processes upstream of autophagy like mTORC1 signaling that have broad effects that could be harmful or helpful (*650*). mTORC1 inhibition through treatment with sirolimus, for example, would enhance autophagy initiation but also promote lysosome biogenesis through increased TFEB activity, which could aid autophagosomal clearance (*213*, *214*). Alternatively, if we elucidate the functional effects of GIMAP6 deficiency, such as its potential role in endothelial cell function or in cytokine production, other drugs that target these downstream consequences could be utilized instead, similar to how abatacept treatment is currently being tested for LATAIE disease (*25*). Therefore, further molecular understanding of GIMAP6 deficiency is needed to determine which drugs would be most advantageous for our patient.

Along with improving patient care with the immunodeficiencies that we have described, GIMAP5 and GIMAP6 might be interesting targets for other drug therapies. Though

the GIMAPs are expressed in cells outside the immune system, such as endothelial cells, they still appear to be relatively narrowly cell-type restricted. Yet, both appear to be involved in quite ubiquitously important pathways (i.e. metabolism and autophagy), suggesting that they may regulate functions of those metabolic processes to operate appropriately for cell-specific needs. Therefore, drugs that modulate GIMAP activity may allow for specifically targeted therapies in conditions like autoimmune or vascular disease, and may have the benefit of less severe or fewer systemic side effects.

7.4 Identification of novel PIDs

The identification of monogenic diseases in single patients is extremely valuable, but requires stringent measures to avoid false identification of new PIDs. J. Casanova has published guidelines for the criteria necessary to establish a genotype-phenotype connection in single patients (*1*). Though I verified a known PID in PID1294, these guidelines have served as a useful checklist in the other two single patient cases examined in this thesis, and as well as in the multi-patient GIMAP5 cohort.

The first guideline is that the patients' candidate genotype is monogenic and present in only the affected individual (*1*). This held true for the homozygous missense mutation in *GIMAP6* seen in PID1467; she alone in her family has a homozygous genotype and manifests disease. Additionally, the variant is novel in all examined databases. Similarly, only family members with homozygous or compound heterozygous *GIMAP5* genotypes were affected in that cohort. On the other hand, this criterion was not met for PID1414, whose younger brother appears to be affected but has a wildtype *TICAM2* allele, thus leading us to reject *TICAM2* as causal.

The second guideline requires demonstration of impaired expression or function of the gene product (*1*). The identified GIMAP5 variants as well as GIMAP6^{G153V} also seem to fulfill this requirement: in both patient cells and in overexpression experiments, there is lower protein expression of the patient's variant. Interestingly, TICAM2^{K166Q} does meet this guideline as *in vitro* luciferase assays suggested that the variant has reduced functional activity. Therefore, it may be a potential modifier gene in the patient.

The last guideline is to correlate the genotype with the putative phenotype in relevant models, such as animals or appropriate cell lines. GIMAP5 deficiency causes the same phenotype, particularly lymphopenia, in patients and animal (both mouse and rat) models (*389*–*391*). On the other hand, though promising, the data presented in this thesis does not yet meet the last criterion for GIMAP6. Along with phenotypic differences discussed above, a functional mechanism is still lacking. While T cells from *Gimap6* KO mice have reduced autophagy and preliminary studies suggest the same for patient T cells, knockout in Jurkat lines did not reproduce this. Studies such as the rescue of autophagic flux by addition of wildtype but not the patient's GIMAP6 allele in deficient cells are needed to support causality. Further, the autophagy reduction has not been tied to a cellular or molecular mechanism that could provide a reasonable pathogenic mechanism for the patient and mouse disease. Autoimmune and inflammatory conditions often result from failures of immune tolerance, impaired clearance of cellular debris, or dysregulation of inflammatory responses (*651*). Therefore, we would expect a defect in one or more of these or a similar pathway that could account for the GIMAP6 phenotypes. Until the genotype-phenotype relationship is further established, we cannot be fully confident that the patient's GIMAP6 mutation is truly causal of her disease.

In summary, I have further characterized GIMAP5 and GIMAP6, two proteins in the poorly understood GIMAP family, and shown potential functions in metabolism and autophagy. In phenotyping a novel mouse model for GIMAP6 deficiency, I identified a severe survival defect. By determining that early mortality likely stems from a primary defect in endothelial cells leading to microangiopathic renal disease, I highlight a previously undescribed potential importance for GIMAP proteins in not only the immune system, but also the vasculature. Through the evidence presented in this thesis, I suggest that *GIMAP6* is a promising candidate for a PID-associated gene.

References

1. J.-L. Casanova, M. E. Conley, S. J. Seligman, L. Abel, L. D. Notarangelo, Guidelines for genetic studies in single patients: lessons from primary immunodeficiencies. *J. Exp. Med.* **211**, 2137–49 (2014).
2. A. A. Bousfiha *et al.*, Primary Immunodeficiency Diseases Worldwide: More Common than Generally Thought. *J. Clin. Immunol.* **33**, 1–7 (2013).
3. C. Picard *et al.*, International Union of Immunological Societies: 2017 Primary Immunodeficiency Diseases Committee Report on Inborn Errors of Immunity. *J. Clin. Immunol.* **38**, 96–128 (2018).
4. L. R. Forbes, J. Milner, E. Haddad, Signal transducer and activator of transcription 3: a year in review. *Curr. Opin. Hematol.* **23**, 23–7 (2016).
5. M. Margulies *et al.*, Genome sequencing in microfabricated high-density picolitre reactors. *Nature*. **437**, 376–380 (2005).
6. J. Shendure *et al.*, Accurate multiplex polony sequencing of an evolved bacterial genome. *Science*. **309**, 1728–32 (2005).
7. D. R. Bentley, Whole-genome re-sequencing. *Curr. Opin. Genet. Dev.* **16**, 545–552 (2006).
8. D. A. Wheeler *et al.*, The complete genome of an individual by massively parallel DNA sequencing. *Nature*. **452**, 872–876 (2008).
9. R. S. Geha *et al.*, Primary immunodeficiency diseases: an update from the International Union of Immunological Societies Primary Immunodeficiency Diseases Classification Committee. *J. Allergy Clin. Immunol.* **120**, 776–94 (2007).
10. R. Watanabe-Fukunaga, C. I. Brannan, N. G. Copeland, N. A. Jenkins, S. Nagata, Lymphoproliferation disorder in mice explained by defects in Fas antigen that mediates apoptosis. *Nature*. **356**, 314–317 (1992).
11. F. Rieux-Laucat *et al.*, Mutations in Fas associated with human lymphoproliferative syndrome and autoimmunity. *Science*. **268**, 1347–9 (1995).
12. F. Le Deist *et al.*, Clinical, immunological, and pathological consequences of Fas-deficient conditions. *Lancet*. **348**, 719–723 (1996).
13. G. H. Fisher *et al.*, Dominant interfering Fas gene mutations impair apoptosis in a human autoimmune lymphoproliferative syndrome. *Cell*. **81**, 935–46 (1995).
14. D. M. Church *et al.*, Lineage-Specific Biology Revealed by a Finished Genome Assembly of the Mouse. *PLoS Biol.* **7**, e1000112 (2009).
15. J.-L. Guénet, Animal models of human genetic diseases: do they need to be faithful to be useful? *Mol. Genet. Genomics*. **286**, 1–20 (2011).
16. H. Su, Studying human immunodeficiencies in humans: advances in fundamental concepts and therapeutic interventions. *F1000Research*. **6**, 318 (2017).
17. V. E. Kelley, J. B. Roths, Interaction of mutant lpr gene with background strain influences renal disease. *Clin. Immunol. Immunopathol.* **37**, 220–229 (1985).
18. T. D. Andrews, G. Sjollema, C. C. Goodnow, Understanding the immunological impact of the human mutation explosion. *Trends Immunol.* **34**, 99–106 (2013).
19. L. D. Notarangelo, M.-S. Kim, J. E. Walter, Y. Nee Lee, Human RAG mutations: biochemistry and clinical implications (2016), doi:10.1038/nri.2016.28.
20. N. C. Walsh *et al.*, Humanized Mouse Models of Clinical Disease. *Annu. Rev. Pathol.* **12**, 187–215 (2017).

21. J.-L. Casanova, L. Abel, The human model: a genetic dissection of immunity to infection in natural conditions. *Nat. Rev. Immunol.* **4**, 55–66 (2004).
22. C. McCusker, R. Warrington, Primary immunodeficiency. *Allergy Asthma. Clin. Immunol.* **7 Suppl 1**, S11 (2011).
23. G. Azizi *et al.*, Approach to the Management of Autoimmunity in Primary Immunodeficiency. *Scand. J. Immunol.* **85**, 13–29 (2017).
24. M. Ballow *et al.*, Immunodeficiencies. *Clin. Exp. Immunol.* **158**, 14–22 (2009).
25. B. Lo *et al.*, AUTOIMMUNE DISEASE. Patients with LRBA deficiency show CTLA4 loss and immune dysregulation responsive to abatacept therapy. *Science*. **349**, 436–40 (2015).
26. L. D. Notarangelo, T. A. Fleisher, Targeted strategies directed at the molecular defect: Toward precision medicine for select primary immunodeficiency disorders. *J. Allergy Clin. Immunol.* **139**, 715–723 (2017).
27. A. J. Thrasher, D. A. Williams, Evolving Gene Therapy in Primary Immunodeficiency. *Mol. Ther.* **25**, 1132–1141 (2017).
28. G. Bajic, S. E. Degn, S. Thiel, G. R. Andersen, Complement activation, regulation, and molecular basis for complement-related diseases. *EMBO J.* **34**, 2735–57 (2015).
29. S. Gordon, Phagocytosis: An Immunobiologic Process. *Immunity*. **44**, 463–475 (2016).
30. A. Mandal, C. Viswanathan, Natural killer cells: In health and disease. *Hematol. Oncol. Stem Cell Ther.* **8**, 47–55 (2015).
31. K. Newton, V. M. Dixit, Signaling in innate immunity and inflammation. *Cold Spring Harb. Perspect. Biol.* **4** (2012), doi:10.1101/cshperspect.a006049.
32. J. S. Blum, P. A. Wearsch, P. Cresswell, Pathways of Antigen Processing. *Annu. Rev. Immunol.* **31**, 443–473 (2013).
33. B. Lemaitre, E. Nicolas, L. Michaut, J. M. Reichhart, J. A. Hoffmann, The dorsoventral regulatory gene cassette spätzle/Toll/cactus controls the potent antifungal response in Drosophila adults. *Cell*. **86**, 973–83 (1996).
34. A. Poltorak *et al.*, Defective LPS signaling in C3H/HeJ and C57BL/10ScCr mice: mutations in Tlr4 gene. *Science*. **282**, 2085–8 (1998).
35. R. Medzhitov, P. Preston-Hurlburt, C. A. Janeway, A human homologue of the Drosophila Toll protein signals activation of adaptive immunity. *Nature*. **388**, 394–397 (1997).
36. C. A. Janeway, Approaching the asymptote? Evolution and revolution in immunology. *Cold Spring Harb. Symp. Quant. Biol.* **54 Pt 1**, 1–13 (1989).
37. M. U. Gack, Mechanisms of RIG-I-like receptor activation and manipulation by viral pathogens. *J. Virol.* **88**, 5213–6 (2014).
38. V. Motta, F. Soares, T. Sun, D. J. Philpott, NOD-Like Receptors: Versatile Cytosolic Sentinels. *Physiol. Rev.* **95**, 149–178 (2015).
39. J. Tang, G. Lin, W. Y. Langdon, L. Tao, J. Zhang, Regulation of C-Type Lectin Receptor-Mediated Antifungal Immunity. *Front. Immunol.* **9**, 123 (2018).
40. J. K. Bell *et al.*, Leucine-rich repeats and pathogen recognition in Toll-like receptors. *Trends Immunol.* **24**, 528–533 (2003).
41. R. Medzhitov *et al.*, MyD88 Is an Adaptor Protein in the hToll/IL-1 Receptor Family Signaling Pathways. *Mol. Cell*. **2**, 253–258 (1998).
42. M. Yamamoto *et al.*, Cutting edge: a novel Toll/IL-1 receptor domain-containing adapter that preferentially activates the IFN-beta promoter in the Toll-like receptor signaling. *J. Immunol.* **169**, 6668–72 (2002).

43. L.-H. Bin, L.-G. Xu, H.-B. Shu, TIRP, a novel Toll/interleukin-1 receptor (TIR) domain-containing adapter protein involved in TIR signaling. *J. Biol. Chem.* **278**, 24526–32 (2003).
44. K. A. Fitzgerald *et al.*, Mal (MyD88-adapter-like) is required for Toll-like receptor-4 signal transduction. *Nature*. **413**, 78–83 (2001).
45. M. Carty *et al.*, The human adaptor SARM negatively regulates adaptor protein TRIF–dependent Toll-like receptor signaling. *Nat. Immunol.* **7**, 1074–1081 (2006).
46. T. Horng, G. M. Barton, R. Medzhitov, TIRAP: an adapter molecule in the Toll signaling pathway. *Nat. Immunol.* **2**, 835–841 (2001).
47. M. Yamamoto *et al.*, Essential role for TIRAP in activation of the signalling cascade shared by TLR2 and TLR4. *Nature*. **420**, 324–329 (2002).
48. T. Kawagoe *et al.*, Sequential control of Toll-like receptor–dependent responses by IRAK1 and IRAK2. *Nat. Immunol.* **9**, 684–691 (2008).
49. K. B. Narayanan, H. H. Park, Toll/interleukin-1 receptor (TIR) domain-mediated cellular signaling pathways. *Apoptosis*. **20**, 196–209 (2015).
50. H. Oshiumi, M. Matsumoto, K. Funami, T. Akazawa, T. Seya, TICAM-1, an adaptor molecule that participates in Toll-like receptor 3–mediated interferon-β induction. *Nat. Immunol.* **4**, 161–167 (2003).
51. M. Yamamoto *et al.*, TRAM is specifically involved in the Toll-like receptor 4-mediated MyD88-independent signaling pathway. *Nat. Immunol.* **4**, 1144–50 (2003).
52. S. Sato *et al.*, Toll/IL-1 receptor domain-containing adaptor inducing IFN-beta (TRIF) associates with TNF receptor-associated factor 6 and TANK-binding kinase 1, and activates two distinct transcription factors, NF-kappa B and IFN-regulatory factor-3, in the Toll-like receptor signaling. *J. Immunol.* **171**, 4304–10 (2003).
53. E. Meylan *et al.*, RIP1 is an essential mediator of Toll-like receptor 3–induced NF-κB activation. *Nat. Immunol.* **5**, 503–507 (2004).
54. B. Guo, G. Cheng, Modulation of the interferon antiviral response by the TBK1/IKKi adaptor protein TANK. *J. Biol. Chem.* **282**, 11817–26 (2007).
55. S. Liu *et al.*, Phosphorylation of innate immune adaptor proteins MAVS, STING, and TRIF induces IRF3 activation. *Science*. **347**, aaa2630 (2015).
56. T. H. Mogensen, Pathogen recognition and inflammatory signaling in innate immune defenses. *Clin. Microbiol. Rev.* **22**, 240–73, Table of Contents (2009).
57. A. Fischer, A. Rausell, What do primary immunodeficiencies tell us about the essentiality/redundancy of immune responses? *Semin. Immunol.* **36**, 13–16 (2018).
58. C. Picard, J.-L. Casanova, A. Puel, Infectious diseases in patients with IRAK-4, MyD88, NEMO, or IκBα deficiency. *Clin. Microbiol. Rev.* **24**, 490–7 (2011).
59. H. von Bernuth *et al.*, Pyogenic bacterial infections in humans with MyD88 deficiency. *Science*. **321**, 691–6 (2008).
60. F. Altare *et al.*, Inherited interleukin 12 deficiency in a child with bacille Calmette-Guérin and Salmonella enteritidis disseminated infection. *J. Clin. Invest.* **102**, 2035–40 (1998).
61. R. de Jong *et al.*, Severe mycobacterial and Salmonella infections in interleukin-12 receptor-deficient patients. *Science*. **280**, 1435–8 (1998).
62. J. Bustamante, S. Boisson-Dupuis, L. Abel, J.-L. Casanova, Mendelian susceptibility to mycobacterial disease: genetic, immunological, and clinical features of inborn errors of IFN-γ immunity. *Semin. Immunol.* **26**, 454–70 (2014).
63. M. J. Newport *et al.*, A Mutation in the Interferon-γ –Receptor Gene and

Susceptibility to Mycobacterial Infection. *N. Engl. J. Med.* **335**, 1941–1949 (1996).
64. E. Jouanguy *et al.*, Interferon-gamma-receptor deficiency in an infant with fatal bacille Calmette-Guérin infection. *N. Engl. J. Med.* **335**, 1956–61 (1996).
65. S. Hambleton *et al.*, IRF8 mutations and human dendritic-cell immunodeficiency. *N. Engl. J. Med.* **365**, 127–38 (2011).
66. M. A. Lee-Kirsch, The Type I Interferonopathies. *Annu. Rev. Med.* **68**, 297–315 (2017).
67. E. D. Batu, Monogenic systemic lupus erythematosus: insights in pathophysiology. *Rheumatol. Int.*, 1–13 (2018).
68. H. H. Uhlig, Monogenic diseases associated with intestinal inflammation: implications for the understanding of inflammatory bowel disease. *Gut*. **62**, 1795–805 (2013).
69. G. P. Parnell, D. R. Booth, The Multiple Sclerosis (MS) Genetic Risk Factors Indicate both Acquired and Innate Immune Cell Subsets Contribute to MS Pathogenesis and Identify Novel Therapeutic Opportunities. *Front. Immunol.* **8**, 425 (2017).
70. Y. J. Lee *et al.*, Genome-wide association study identifies GIMAP as a novel susceptibility locus for Behcet's disease. *Ann. Rheum. Dis.* **72**, 1510–6 (2013).
71. B. Verstockt, K. G. Smith, J. C. Lee, Genome-wide association studies in Crohn's disease: Past, present and future. *Clin. Transl. Immunol.* **7**, e1001 (2018).
72. J. Bentham *et al.*, Genetic association analyses implicate aberrant regulation of innate and adaptive immunity genes in the pathogenesis of systemic lupus erythematosus. *Nat. Genet.* **47**, 1457–1464 (2015).
73. J. C. Knight, Genomic modulators of the immune response. *Trends Genet.* **29**, 74–83 (2013).
74. F. Moghaddas, S. L. Masters, The classification, genetic diagnosis and modelling of monogenic autoinflammatory disorders. *Clin. Sci. (Lond).* **132**, 1901–1924 (2018).
75. A. Bousfiha *et al.*, The 2017 IUIS Phenotypic Classification for Primary Immunodeficiencies. *J. Clin. Immunol.* **38**, 129–143 (2018).
76. C. Picard *et al.*, Primary Immunodeficiency Diseases: an Update on the Classification from the International Union of Immunological Societies Expert Committee for Primary Immunodeficiency 2015. *J. Clin. Immunol.* **35**, 696–726 (2015).
77. J. F. Miller, G. F. Mitchell, Cell to cell interaction in the immune response. I. Hemolysin-forming cells in neonatally thymectomized mice reconstituted with thymus or thoracic duct lymphocytes. *J. Exp. Med.* **128**, 801–20 (1968).
78. G. F. Mitchell, J. F. Miller, Cell to cell interaction in the immune response. II. The source of hemolysin-forming cells in irradiated mice given bone marrow and thymus or thoracic duct lymphocytes. *J. Exp. Med.* **128**, 821–37 (1968).
79. T. W. LeBien, T. F. Tedder, B lymphocytes: how they develop and function. *Blood*. **112**, 1570–80 (2008).
80. N. D. Pennock *et al.*, T cell responses: naïve to memory and everything in between. *Adv. Physiol. Educ.* **37**, 273–283 (2013).
81. N. Manolios, F. Letourneur, J. S. Bonifacino, R. D. Klausner, Pairwise, cooperative and inhibitory interactions describe the assembly and probable structure of the T-cell antigen receptor. *EMBO J.* **10**, 1643–51 (1991).
82. Y. Yanagi *et al.*, A human T cell-specific cDNA clone encodes a protein having extensive homology to immunoglobulin chains. *Nature*. **308**, 145–149 (1984).
83. S. M. Hedrick, D. I. Cohen, E. A. Nielsen, M. M. Davis, Isolation of cDNA clones encoding T cell-specific membrane-associated proteins. *Nature*. **308**, 149–153 (1984).
84. S. Tonegawa, Somatic generation of antibody diversity. *Nature*. **302**, 575–581 (1983).

85. D. G. Hesslein, D. G. Schatz, Factors and forces controlling V(D)J recombination. *Adv. Immunol.* **78**, 169–232 (2001).
86. D. G. Schatz, M. A. Oettinger, D. Baltimore, The V(D)J recombination activating gene, RAG-1. *Cell*. **59**, 1035–48 (1989).
87. M. A. Oettinger, D. G. Schatz, C. Gorka, D. Baltimore, RAG-1 and RAG-2, adjacent genes that synergistically activate V(D)J recombination. *Science*. **248**, 1517–23 (1990).
88. P. G. Ashton-Rickardt *et al.*, Evidence for a differential avidity model of T cell selection in the thymus. *Cell*. **76**, 651–663 (1994).
89. R. M. ZINKERNAGEL, G. N. CALLAHAN, J. KLEIN, G. DENNERT, Cytotoxic T cells learn specificity for self H–2 during differentiation in the thymus. *Nature*. **271**, 251–253 (1978).
90. H. Takaba, H. Takayanagi, The Mechanisms of T Cell Selection in the Thymus. *Trends Immunol.* **38**, 805–816 (2017).
91. S. Zuklys *et al.*, Normal thymic architecture and negative selection are associated with Aire expression, the gene defective in the autoimmune-polyendocrinopathy-candidiasis-ectodermal dystrophy (APECED). *J. Immunol.* **165**, 1976–83 (2000).
92. J. W. Kappler, N. Roehm, P. Marrack, T cell tolerance by clonal elimination in the thymus. *Cell*. **49**, 273–80 (1987).
93. N. LE Douarin *et al.*, Evidence for a Thymus-Dependent Form of Tolerance that is Not Based on Elimination or Anergy of Reactive T cells. *Immunol. Rev.* **149**, 35–53 (1996).
94. D. A. Chisolm, A. S. Weinmann, TCR-Signaling Events in Cellular Metabolism and Specialization. *Front. Immunol.* **6**, 292 (2015).
95. E. M. Kuklina, Molecular mechanisms of T-cell anergy. *Biochem.* **78**, 144–156 (2013).
96. M. K. Jenkins, J. D. Ashwell, R. H. Schwartz, Allogeneic non-T spleen cells restore the responsiveness of normal T cell clones stimulated with antigen and chemically modified antigen-presenting cells. *J. Immunol.* **140**, 3324–30 (1988).
97. D. L. Mueller, M. K. Jenkins, R. H. Schwartz, An accessory cell-derived costimulatory signal acts independently of protein kinase C activation to allow T cell proliferation and prevent the induction of unresponsiveness. *J. Immunol.* **142**, 2617–28 (1989).
98. J. M. Curtsinger *et al.*, Inflammatory cytokines provide a third signal for activation of naive CD4+ and CD8+ T cells. *J. Immunol.* **162**, 3256–62 (1999).
99. J. H. Esensten, Y. A. Helou, G. Chopra, A. Weiss, J. A. Bluestone, CD28 Costimulation: From Mechanism to Therapy. *Immunity*. **44**, 973–88 (2016).
100. K. V Prasad *et al.*, T-cell antigen CD28 interacts with the lipid kinase phosphatidylinositol 3-kinase by a cytoplasmic Tyr(P)-Met-Xaa-Met motif. *Proc. Natl. Acad. Sci. U. S. A.* **91**, 2834–8 (1994).
101. F. Pagès *et al.*, Binding of phosphatidyl-inositol-3-OH kinase to CD28 is required for T-cell signalling. *Nature*. **369**, 327–329 (1994).
102. L. Chen, D. B. Flies, Molecular mechanisms of T cell co-stimulation and co-inhibition. *Nat. Rev. Immunol.* **13**, 227–42 (2013).
103. P. S. Linsley *et al.*, CTLA-4 is a second receptor for the B cell activation antigen B7. *J. Exp. Med.* **174**, 561–9 (1991).
104. J. J. Engelhardt, T. J. Sullivan, J. P. Allison, CTLA-4 overexpression inhibits T cell responses through a CD28-B7-dependent mechanism. *J. Immunol.* **177**, 1052–61 (2006).
105. M. F. Krummel, J. P. Allison, CD28 and CTLA-4 have opposing effects on the response of T cells to stimulation. *J. Exp. Med.* **182**, 459–65 (1995).

106. T. L. Walunas *et al.*, CTLA-4 can function as a negative regulator of T cell activation. *Immunity*. **1**, 405–13 (1994).
107. M. E. Keir, M. J. Butte, G. J. Freeman, A. H. Sharpe, PD-1 and Its Ligands in Tolerance and Immunity. *Annu. Rev. Immunol.* **26**, 677–704 (2008).
108. J. M. Curtsinger, J. O. Valenzuela, P. Agarwal, D. Lins, M. F. Mescher, Type I IFNs provide a third signal to CD8 T cells to stimulate clonal expansion and differentiation. *J. Immunol.* **174**, 4465–9 (2005).
109. N. Zhang, M. J. Bevan, CD8(+) T cells: foot soldiers of the immune system. *Immunity*. **35**, 161–8 (2011).
110. H. Cantor, E. A. Boyse, Functional subclasses of T-lymphocytes bearing different Ly antigens. I. The generation of functionally distinct T-cell subclasses is a differentiative process independent of antigen. *J. Exp. Med.* **141**, 1376–89 (1975).
111. P. Golstein, H. Wigzell, H. Blomgren, E. A. Svedmyr, Cells mediating specific in vitro cytotoxicity. II. Probable autonomy of thymus-processed lymphocytes (T cells) for the killing of allogeneic target cells. *J. Exp. Med.* **135**, 890–906 (1972).
112. N. Schmitt, H. Ueno, Regulation of human helper T cell subset differentiation by cytokines. *Curr. Opin. Immunol.* **34**, 130–6 (2015).
113. T. R. Mosmann, H. Cherwinski, M. W. Bond, M. A. Giedlin, R. L. Coffman, Two types of murine helper T cell clone. I. Definition according to profiles of lymphokine activities and secreted proteins. *J. Immunol.* **136**, 2348–57 (1986).
114. F. Y. Liew, TH1 and TH2 cells: a historical perspective. *Nat. Rev. Immunol.* **2**, 55–60 (2002).
115. S. J. Szabo *et al.*, A Novel Transcription Factor, T-bet, Directs Th1 Lineage Commitment. *Cell*. **100**, 655–669 (2000).
116. W. Zheng, R. A. Flavell, The transcription factor GATA-3 is necessary and sufficient for Th2 cytokine gene expression in CD4 T cells. *Cell*. **89**, 587–96 (1997).
117. M. H. Kaplan, U. Schindler, S. T. Smiley, M. J. Grusby, Stat6 is required for mediating responses to IL-4 and for development of Th2 cells. *Immunity*. **4**, 313–9 (1996).
118. G. Le Gros, S. Z. Ben-Sasson, R. Seder, F. D. Finkelman, W. E. Paul, Generation of interleukin 4 (IL-4)-producing cells in vivo and in vitro: IL-2 and IL-4 are required for in vitro generation of IL-4-producing cells. *J. Exp. Med.* **172**, 921–9 (1990).
119. C. S. Hsieh *et al.*, Development of TH1 CD4+ T cells through IL-12 produced by Listeria-induced macrophages. *Science*. **260**, 547–9 (1993).
120. I. Raphael, S. Nalawade, T. N. Eagar, T. G. Forsthuber, T cell subsets and their signature cytokines in autoimmune and inflammatory diseases. *Cytokine*. **74**, 5–17 (2015).
121. L. A. Stephens, C. Mottet, D. Mason, F. Powrie, Human CD4(+)CD25(+) thymocytes and peripheral T cells have immune suppressive activity in vitro. *Eur. J. Immunol.* **31**, 1247–54 (2001).
122. C. Baecher-Allan, J. A. Brown, G. J. Freeman, D. A. Hafler, CD4+CD25high regulatory cells in human peripheral blood. *J. Immunol.* **167**, 1245–53 (2001).
123. S. Sakaguchi, N. Sakaguchi, M. Asano, M. Itoh, M. Toda, Immunologic self-tolerance maintained by activated T cells expressing IL-2 receptor alpha-chains (CD25). Breakdown of a single mechanism of self-tolerance causes various autoimmune diseases. *J. Immunol.* **155**, 1151–64 (1995).
124. M. Kanamori, H. Nakatsukasa, M. Okada, Q. Lu, A. Yoshimura, Induced Regulatory T Cells: Their Development, Stability, and Applications. *Trends Immunol.* **37**, 803–811

(2016).
125. J. D. Fontenot, M. A. Gavin, A. Y. Rudensky, Foxp3 programs the development and function of CD4+CD25+ regulatory T cells. *Nat. Immunol.* **4**, 330–336 (2003).
126. S. Sakaguchi, N. Sakaguchi, M. Asano, M. Itoh, M. Toda, Immunologic self-tolerance maintained by activated T cells expressing IL-2 receptor alpha-chains (CD25). Breakdown of a single mechanism of self-tolerance causes various autoimmune diseases. *J. Immunol.* **155**, 1151–64 (1995).
127. S. Hori, T. Nomura, S. Sakaguchi, Control of Regulatory T Cell Development by the Transcription Factor Foxp3. *Science (80-.).* **299**, 1057–1061 (2003).
128. A. Arce-Sillas *et al.*, Regulatory T Cells: Molecular Actions on Effector Cells in Immune Regulation. *J. Immunol. Res.* **2016**, 1–12 (2016).
129. S. K. Tripathi, R. Lahesmaa, Transcriptional and epigenetic regulation of T-helper lineage specification. *Immunol. Rev.* **261**, 62–83 (2014).
130. K. S. Campbell, E. J. Hager, R. J. Friedrich, J. C. Cambier, IgM antigen receptor complex contains phosphoprotein products of B29 and mb-1 genes. *Proc. Natl. Acad. Sci. U. S. A.* **88**, 3982–6 (1991).
131. B. Treanor, B-cell receptor: from resting state to activate. *Immunology*. **136**, 21–7 (2012).
132. C. Brack, M. Hirama, R. Lenhard-Schuller, S. Tonegawa, A complete immunoglobulin gene is created by somatic recombination. *Cell*. **15**, 1–14 (1978).
133. G. J. NOSSAL, J. LEDERBERG, Antibody production by single cells. *Nature*. **181**, 1419–20 (1958).
134. R. H. Zubler, Naive and memory B cells in T-cell-dependent and T-independent responses. *Springer Semin. Immunopathol.* **23**, 405–419 (2001).
135. T. Defrance, M. Taillardet, L. Genestier, T cell-independent B cell memory. *Curr. Opin. Immunol.* **23**, 330–336 (2011).
136. E. J. Pone, Z. Xu, C. A. White, H. Zan, P. Casali, B cell TLRs and induction of immunoglobulin class-switch DNA recombination. *Front. Biosci. (Landmark Ed.* **17**, 2594–615 (2012).
137. W. Hoffman, F. G. Lakkis, G. Chalasani, B Cells, Antibodies, and More. *Clin. J. Am. Soc. Nephrol.* **11**, 137–54 (2016).
138. P. I. Lobo, Role of Natural Autoantibodies and Natural IgM Anti-Leucocyte Autoantibodies in Health and Disease. *Front. Immunol.* **7**, 198 (2016).
139. A. Cerutti, M. Cols, I. Puga, Marginal zone B cells: virtues of innate-like antibody-producing lymphocytes. *Nat. Rev. Immunol.* **13**, 118–32 (2013).
140. T. I. Arnon, R. M. Horton, I. L. Grigorova, J. G. Cyster, Visualization of splenic marginal zone B-cell shuttling and follicular B-cell egress. *Nature*. **493**, 684–688 (2012).
141. R. Hoogeboom, P. Tolar, (Springer, Cham, 2015; http://link.springer.com/10.1007/82_2015_476), pp. 45–63.
142. A. Lanzavecchia, Antigen-specific interaction between T and B cells. *Nature*. **314**, 537–9.
143. Y. Zhang, L. Garcia-Ibanez, K.-M. Toellner, Regulation of germinal center B-cell differentiation. *Immunol. Rev.* **270**, 8–19 (2016).
144. M. Muramatsu *et al.*, Class switch recombination and hypermutation require activation-induced cytidine deaminase (AID), a potential RNA editing enzyme. *Cell*. **102**, 553–63 (2000).
145. J. Stavnezer, C. E. Schrader, IgH chain class switch recombination: mechanism and

regulation. *J. Immunol.* **193**, 5370–8 (2014).
146. P. W. Kincade, A. R. Lawton, D. E. Bockman, M. D. Cooper, Suppression of immunoglobulin G synthesis as a result of antibody-mediated suppression of immunoglobulin M synthesis in chickens. *Proc. Natl. Acad. Sci. U. S. A.* **67**, 1918–25 (1970).
147. D. Suan, C. Sundling, R. Brink, Plasma cell and memory B cell differentiation from the germinal center. *Curr. Opin. Immunol.* **45**, 97–102 (2017).
148. W. Ratajczak, P. Niedźwiedzka-Rystwej, B. Tokarz-Deptuła, W. Deptuła, Immunological memory cells. *Cent. J. Immunol.* **43**, 194–203 (2018).
149. F. Sallusto, D. Lenig, R. Förster, M. Lipp, A. Lanzavecchia, Two subsets of memory T lymphocytes with distinct homing potentials and effector functions. *Nature*. **401**, 708–712 (1999).
150. X. Liu *et al.*, Regulatory T cells trigger effector T cell DNA damage and senescence caused by metabolic competition. *Nat. Commun.* **9**, 249 (2018).
151. Y. Wang, Bulky DNA Lesions Induced by Reactive Oxygen Species. *Chem. Res. Toxicol.* **21**, 276–281 (2008).
152. A. N. Akbar, S. M. Henson, A. Lanna, Series: Lifetime Immunity Senescence of T Lymphocytes: Implications for Enhancing Human Immunity (2016), doi:10.1016/j.it.2016.09.002.
153. E. J. Wherry, M. Kurachi, Molecular and cellular insights into T cell exhaustion. *Nat. Rev. Immunol.* **15**, 486–99 (2015).
154. H. M. Zarour, Reversing T-cell Dysfunction and Exhaustion in Cancer. *Clin. Cancer Res.* **22**, 1856–64 (2016).
155. A. Fischer, A. Rausell, What do primary immunodeficiencies tell us about the essentiality/redundancy of immune responses? *Semin. Immunol.* **36**, 13–16 (2018).
156. O. C. BRUTON, Agammaglobulinemia. *Pediatrics*. **9**, 722–8 (1952).
157. C. McCusker, R. Warrington, Primary immunodeficiency. *Allergy Asthma. Clin. Immunol.* **7 Suppl 1**, S11 (2011).
158. E. R. Giblett, J. E. Anderson, F. Cohen, B. Pollara, H. J. Meuwissen, Adenosine-deaminase deficiency in two patients with severely impaired cellular immunity. *Lancet (London, England)*. **2**, 1067–9 (1972).
159. M. R. Blackburn, L. F. Thompson, Adenosine deaminase deficiency: unanticipated benefits from the study of a rare immunodeficiency. *J. Immunol.* **188**, 933–5 (2012).
160. I. Dikic, Proteasomal and Autophagic Degradation Systems. *Annu. Rev. Biochem.* **86**, 193–224 (2017).
161. J. Ahlberg, L. Marzella, H. Glaumann, Uptake and degradation of proteins by isolated rat liver lysosomes. Suggestion of a microautophagic pathway of proteolysis. *Lab. Invest.* **47**, 523–32 (1982).
162. R. Sahu *et al.*, Microautophagy of Cytosolic Proteins by Late Endosomes. *Dev. Cell*. **20**, 131–139 (2011).
163. W. Li, J. Li, J. Bao, Microautophagy: lesser-known self-eating. *Cell. Mol. Life Sci.* **69**, 1125–1136 (2012).
164. J. Fred Dice, Peptide sequences that target cytosolic proteins for lysosomal proteolysis. *Trends Biochem. Sci.* **15**, 305–309 (1990).
165. S. Kaushik, A. M. Cuervo, The coming of age of chaperone-mediated autophagy. *Nat. Rev. Mol. Cell Biol.* **19**, 365–381 (2018).
166. U. Bandyopadhyay, S. Kaushik, L. Varticovski, A. M. Cuervo, The chaperone-mediated

autophagy receptor organizes in dynamic protein complexes at the lysosomal membrane. *Mol. Cell. Biol.* **28**, 5747–63 (2008).
167. A. M. Cuervo, J. F. Dice, A receptor for the selective uptake and degradation of proteins by lysosomes. *Science*. **273**, 501–3 (1996).
168. A. Stolz, A. Ernst, I. Dikic, Cargo recognition and trafficking in selective autophagy. *Nat. Cell Biol.* **16**, 495–501 (2014).
169. L. Yu *et al.*, Autophagic programmed cell death by selective catalase degradation. *Proc. Natl. Acad. Sci.* **103**, 4952–4957 (2006).
170. D. Gatica, V. Lahiri, D. J. Klionsky, Cargo recognition and degradation by selective autophagy. *Nat. Cell Biol.* **20**, 233–242 (2018).
171. I. Kissová, M. Deffieu, S. Manon, N. Camougrand, Uth1p is involved in the autophagic degradation of mitochondria. *J. Biol. Chem.* **279**, 39068–74 (2004).
172. M. Mortensen *et al.*, Loss of autophagy in erythroid cells leads to defective removal of mitochondria and severe anemia in vivo. *Proc. Natl. Acad. Sci. U. S. A.* **107**, 832–7 (2010).
173. W. Wu *et al.*, PINK1-Parkin-Mediated Mitophagy Protects Mitochondrial Integrity and Prevents Metabolic Stress-Induced Endothelial Injury. *PLoS One*. **10**, e0132499 (2015).
174. V. Kirkin *et al.*, A Role for NBR1 in Autophagosomal Degradation of Ubiquitinated Substrates. *Mol. Cell*. **33**, 505–516 (2009).
175. J. A. Olzmann *et al.*, Parkin-mediated K63-linked polyubiquitination targets misfolded DJ-1 to aggresomes via binding to HDAC6. *J. Cell Biol.* **178**, 1025–38 (2007).
176. E. Karanasios *et al.*, Dynamic association of the ULK1 complex with omegasomes during autophagy induction. *J. Cell Sci.* **126**, 5224–38 (2013).
177. J. H. Hurley, L. N. Young, Mechanisms of Autophagy Initiation. *Annu. Rev. Biochem.* **86**, 225–244 (2017).
178. H. C. Dooley *et al.*, WIPI2 Links LC3 Conjugation with PI3P, Autophagosome Formation, and Pathogen Clearance by Recruiting Atg12–5-16L1. *Mol. Cell*. **55**, 238–252 (2014).
179. E. L. Axe *et al.*, Autophagosome formation from membrane compartments enriched in phosphatidylinositol 3-phosphate and dynamically connected to the endoplasmic reticulum. *J. Cell Biol.* **182**, 685–701 (2008).
180. T. Proikas-Cezanne, Z. Takacs, P. Dönnes, O. Kohlbacher, WIPI proteins: essential PtdIns3P effectors at the nascent autophagosome. *J. Cell Sci.* **128**, 207–17 (2015).
181. Y. Feng, D. J. Klionsky, Autophagic membrane delivery through ATG9. *Cell Res.* **27**, 161–162 (2017).
182. A. Kuma, N. Mizushima, N. Ishihara, Y. Ohsumi, Formation of the approximately 350-kDa Apg12-Apg5.Apg16 multimeric complex, mediated by Apg16 oligomerization, is essential for autophagy in yeast. *J. Biol. Chem.* **277**, 18619–25 (2002).
183. N. Mizushima *et al.*, A protein conjugation system essential for autophagy. *Nature*. **395**, 395–398 (1998).
184. I. Tanida, E. Tanida-Miyake, T. Ueno, E. Kominami, The Human Homolog of *Saccharomyces cerevisiae* Apg7p Is a Protein-activating Enzyme for Multiple Substrates Including Human Apg12p, GATE-16, GABARAP, and MAP-LC3. *J. Biol. Chem.* **276**, 1701–1706 (2001).
185. Y. Ichimura *et al.*, A ubiquitin-like system mediates protein lipidation. *Nature*. **408**, 488–492 (2000).
186. T. Kirisako *et al.*, The reversible modification regulates the membrane-binding state

of Apg8/Aut7 essential for autophagy and the cytoplasm to vacuole targeting pathway. *J. Cell Biol.* **151**, 263–76 (2000).
187. T. N. Nguyen *et al.*, Atg8 family LC3/GABARAP proteins are crucial for autophagosome-lysosome fusion but not autophagosome formation during PINK1/Parkin mitophagy and starvation. *J. Cell Biol.* **215**, 857–874 (2016).
188. N. Fujita *et al.*, An Atg4B mutant hampers the lipidation of LC3 paralogues and causes defects in autophagosome closure. *Mol. Biol. Cell*. **19**, 4651–9 (2008).
189. N. Mizushima *et al.*, Dissection of autophagosome formation using Apg5-deficient mouse embryonic stem cells. *J. Cell Biol.* **152**, 657–68 (2001).
190. S. Nakamura, T. Yoshimori, New insights into autophagosome–lysosome fusion, doi:10.1242/jcs.196352.
191. T. E. Rusten *et al.*, ESCRTs and Fab1 Regulate Distinct Steps of Autophagy. *Curr. Biol.* **17**, 1817–1825 (2007).
192. M. Filimonenko *et al.*, Functional multivesicular bodies are required for autophagic clearance of protein aggregates associated with neurodegenerative disease. *J. Cell Biol.* **179**, 485–500 (2007).
193. Y. Takahashi *et al.*, An autophagy assay reveals the ESCRT-III component CHMP2A as a regulator of phagophore closure. *Nat. Commun.* **9**, 2855 (2018).
194. M. G. Gutierrez, D. B. Munafó, W. Berón, M. I. Colombo, Rab7 is required for the normal progression of the autophagic pathway in mammalian cells. *J. Cell Sci.* **117**, 2687–97 (2004).
195. S. Pankiv *et al.*, FYCO1 is a Rab7 effector that binds to LC3 and PI3P to mediate microtubule plus end-directed vesicle transport. *J. Cell Biol.* **188**, 253–69 (2010).
196. I. Jordens *et al.*, The Rab7 effector protein RILP controls lysosomal transport by inducing the recruitment of dynein-dynactin motors. *Curr. Biol.* **11**, 1680–1685 (2001).
197. R. H. Wijdeven *et al.*, Cholesterol and ORP1L-mediated ER contact sites control autophagosome transport and fusion with the endocytic pathway. *Nat. Commun.* **7**, 11808 (2016).
198. S. Jäger *et al.*, Role for Rab7 in maturation of late autophagic vacuoles. *J. Cell Sci.* **117**, 4837–48 (2004).
199. T. Kirisako *et al.*, Formation process of autophagosome is traced with Apg8/Aut7p in yeast. *J. Cell Biol.* **147**, 435–46 (1999).
200. M. Hamasaki *et al.*, Autophagosomes form at ER–mitochondria contact sites. *Nature*. **495**, 389–393 (2013).
201. E. Itakura, C. Kishi-Itakura, N. Mizushima, The Hairpin-type Tail-Anchored SNARE Syntaxin 17 Targets to Autophagosomes for Fusion with Endosomes/Lysosomes. *Cell*. **151**, 1256–1269 (2012).
202. M. Cicchini, V. Karantza, B. Xia, Molecular pathways: autophagy in cancer--a matter of timing and context. *Clin. Cancer Res.* **21**, 498–504 (2015).
203. R. A. Saxton, D. M. Sabatini, mTOR Signaling in Growth, Metabolism, and Disease. *Cell*. **168**, 960–976 (2017).
204. R. Zoncu *et al.*, mTORC1 Senses Lysosomal Amino Acids Through an Inside-Out Mechanism That Requires the Vacuolar H+-ATPase. *Science (80-.).* **334** (2011).
205. Y. Sancak *et al.*, The Rag GTPases bind raptor and mediate amino acid signaling to mTORC1. *Science*. **320**, 1496–501 (2008).
206. Y. Sancak *et al.*, Ragulator-Rag complex targets mTORC1 to the lysosomal surface and

is necessary for its activation by amino acids. *Cell*. **141**, 290–303 (2010).
207. L. Bar-Peled, L. D. Schweitzer, R. Zoncu, D. M. Sabatini, Ragulator is a GEF for the rag GTPases that signal amino acid levels to mTORC1. *Cell*. **150**, 1196–208 (2012).
208. H. Stocker *et al.*, Rheb is an essential regulator of S6K in controlling cell growth in Drosophila. *Nat. Cell Biol.* **5**, 559–566 (2003).
209. L. J. Saucedo *et al.*, Erratum: Rheb promotes cell growth as a component of the insulin/TOR signalling network. *Nat. Cell Biol.* **5**, 566–571 (2003).
210. K. Inoki, Y. Li, T. Xu, K.-L. Guan, Rheb GTPase is a direct target of TSC2 GAP activity and regulates mTOR signaling. *Genes Dev.* **17**, 1829–34 (2003).
211. X. Long, Y. Lin, S. Ortiz-Vega, K. Yonezawa, J. Avruch, Rheb binds and regulates the mTOR kinase. *Curr. Biol.* **15**, 702–13 (2005).
212. J. Kim, M. Kundu, B. Viollet, K.-L. Guan, AMPK and mTOR regulate autophagy through direct phosphorylation of Ulk1. *Nat. Cell Biol.* **13**, 132–141 (2011).
213. J. A. Martina, Y. Chen, M. Gucek, R. Puertollano, MTORC1 functions as a transcriptional regulator of autophagy by preventing nuclear transport of TFEB. *Autophagy*. **8**, 903–14 (2012).
214. S. Peña-Llopis *et al.*, Regulation of TFEB and V-ATPases by mTORC1. *EMBO J.* **30**, 3242–58 (2011).
215. D. G. Hardie, F. A. Ross, S. A. Hawley, AMPK: a nutrient and energy sensor that maintains energy homeostasis. *Nat. Rev. Mol. Cell Biol.* **13**, 251–62 (2012).
216. D. M. Gwinn *et al.*, AMPK Phosphorylation of Raptor Mediates a Metabolic Checkpoint. *Mol. Cell*. **30**, 214–226 (2008).
217. I. H. Lee *et al.*, A role for the NAD-dependent deacetylase Sirt1 in the regulation of autophagy. *Proc. Natl. Acad. Sci. U. S. A.* **105**, 3374–9 (2008).
218. N. L. Price *et al.*, SIRT1 is required for AMPK activation and the beneficial effects of resveratrol on mitochondrial function. *Cell Metab.* **15**, 675–90 (2012).
219. A. Salminen, K. Kaarniranta, SIRT1: Regulation of longevity via autophagy. *Cell. Signal.* **21**, 1356–1360 (2009).
220. C. Cantó *et al.*, AMPK regulates energy expenditure by modulating NAD+ metabolism and SIRT1 activity. *Nature*. **458**, 1056–60 (2009).
221. A. Brunet, Stress-Dependent Regulation of FOXO Transcription Factors by the SIRT1 Deacetylase. *Science (80-.).* **303**, 2011–2015 (2004).
222. N. Tia *et al.*, Role of Forkhead Box O (FOXO) transcription factor in aging and diseases. *Gene*. **648**, 97–105 (2018).
223. E. L. Greer *et al.*, The energy sensor AMP-activated protein kinase directly regulates the mammalian FOXO3 transcription factor. *J. Biol. Chem.* **282**, 30107–19 (2007).
224. N. B. Ruderman *et al.*, AMPK and SIRT1: a long-standing partnership? *Am. J. Physiol. Endocrinol. Metab.* **298**, E751-60 (2010).
225. D. F. Egan *et al.*, Phosphorylation of ULK1 (hATG1) by AMP-Activated Protein Kinase Connects Energy Sensing to Mitophagy. *Science (80-.).* **331**, 456–461 (2011).
226. J. Kim *et al.*, Differential Regulation of Distinct Vps34 Complexes by AMPK in Nutrient Stress and Autophagy. *Cell*. **152**, 290–303 (2013).
227. T. Y. Li, S.-Y. Lin, S.-C. Lin, Mechanism and Physiological Significance of Growth Factor-Related Autophagy. *Physiology*. **28**, 423–431 (2013).
228. H. Dudek *et al.*, Regulation of neuronal survival by the serine-threonine protein kinase Akt. *Science*. **275**, 661–5 (1997).
229. T. Y. Li, S.-Y. Lin, S.-C. Lin, Mechanism and Physiological Significance of Growth Factor-

Related Autophagy. *Physiology*. **28**, 423–431 (2013).
230. K. Inoki, T. Zhu, K.-L. Guan, TSC2 mediates cellular energy response to control cell growth and survival. *Cell*. **115**, 577–90 (2003).
231. E. Vander Haar, S. Lee, S. Bandhakavi, T. J. Griffin, D.-H. Kim, Insulin signalling to mTOR mediated by the Akt/PKB substrate PRAS40. *Nat. Cell Biol.* **9**, 316–323 (2007).
232. A. Brunet *et al.*, Akt promotes cell survival by phosphorylating and inhibiting a Forkhead transcription factor. *Cell*. **96**, 857–68 (1999).
233. G. J. P. L. Kops *et al.*, Direct control of the Forkhead transcription factor AFX by protein kinase B. *Nature*. **398**, 630–634 (1999).
234. L. H. Travassos *et al.*, Nod1 and Nod2 direct autophagy by recruiting ATG16L1 to the plasma membrane at the site of bacterial entry. *Nat. Immunol.* **11**, 55–62 (2010).
235. D. Tang, R. Kang, C. B. Coyne, H. J. Zeh, M. T. Lotze, PAMPs and DAMPs: signal 0s that spur autophagy and immunity. *Immunol. Rev.* **249**, 158–75 (2012).
236. L. H. Franco *et al.*, Autophagy downstream of endosomal Toll-like receptor signaling in macrophages is a key mechanism for resistance to *Leishmania major* infection. *J. Biol. Chem.* **292**, 13087–13096 (2017).
237. R. O. Watson, P. S. Manzanillo, J. S. Cox, Extracellular M. tuberculosis DNA Targets Bacteria for Autophagy by Activating the Host DNA-Sensing Pathway. *Cell*. **150**, 803–815 (2012).
238. X. Sun *et al.*, MAVS maintains mitochondrial homeostasis via autophagy. *Cell Discov.* **2**, 16024 (2016).
239. Y. Xu *et al.*, Toll-like receptor 4 is a sensor for autophagy associated with innate immunity. *Immunity*. **27**, 135–44 (2007).
240. N. Jounai *et al.*, NLRP4 negatively regulates autophagic processes through an association with beclin1. *J. Immunol.* **186**, 1646–55 (2011).
241. Q. Zhang *et al.*, DAMPs and autophagy: cellular adaptation to injury and unscheduled cell death. *Autophagy*. **9**, 451–8 (2013).
242. A. Trocoli, M. Djavaheri-Mergny, The complex interplay between autophagy and NF-κB signaling pathways in cancer cells. *Am. J. Cancer Res.* **1**, 629–49 (2011).
243. J. Harris, Autophagy and cytokines. *Cytokine*. **56**, 140–144 (2011).
244. E. D. Smith *et al.*, Rapamycin and interleukin-1β impair brain-derived neurotrophic factor-dependent neuron survival by modulating autophagy. *J. Biol. Chem.* **289**, 20615–29 (2014).
245. M.-Y. Fu *et al.*, Transforming growth factor‐β1 reduces apoptosis via autophagy activation in hepatic stellate cells. *Mol. Med. Rep.* **10**, 1282–8 (2014).
246. J. Korah, L. Canaff, J.-J. Lebrun, The Retinoblastoma Tumor Suppressor Protein (pRb)/E2 Promoter Binding Factor 1 (E2F1) Pathway as a Novel Mediator of TGFβ-induced Autophagy. *J. Biol. Chem.* **291**, 2043–54 (2016).
247. G. Sharma *et al.*, IL-27 inhibits IFN-γ induced autophagy by concomitant induction of JAK/PI3 K/Akt/mTOR cascade and up-regulation of Mcl-1 in Mycobacterium tuberculosis H37Rv infected macrophages. *Int. J. Biochem. Cell Biol.* **55**, 335–347 (2014).
248. T. Wu, W.-M. Li, Y.-M. Yao, Interactions between Autophagy and Inhibitory Cytokines. *Int. J. Biol. Sci.* **12**, 884–897 (2016).
249. J. Harris *et al.*, T Helper 2 Cytokines Inhibit Autophagic Control of Intracellular Mycobacterium tuberculosis. *Immunity*. **27**, 505–517 (2007).
250. S. Il Kim *et al.*, Autophagy promotes intracellular degradation of type I collagen

induced by transforming growth factor (TGF)-β1. *J. Biol. Chem.* **287**, 11677–88 (2012).
251. Y. Xu *et al.*, Tgf-β1 induces autophagy and promotes apoptosis in renal tubular epithelial cells. *Int. J. Mol. Med.* **29**, 781–90 (2012).
252. S. Iovino *et al.*, PED/PEA-15 induces autophagy and mediates TGF-beta1 effect on muscle cell differentiation. *Cell Death Differ.* **19**, 1127–1138 (2012).
253. C. C. Pan *et al.*, Endoglin Regulation of Smad2 Function Mediates Beclin1 Expression and Endothelial Autophagy. *J. Biol. Chem.* **290**, 14884–14892 (2015).
254. B. Levine, N. Mizushima, H. W. Virgin, Autophagy in immunity and inflammation. *Nature*. **469**, 323–35 (2011).
255. H. Zhang, D. J. Puleston, A. K. Simon, Autophagy and Immune Senescence. *Trends Mol. Med.* **22**, 671–686 (2016).
256. D. J. Puleston *et al.*, Autophagy is a critical regulator of memory CD8(+) T cell formation. *Elife*. **3** (2014), doi:10.7554/eLife.03706.
257. H. H. Pua, I. Dzhagalov, M. Chuck, N. Mizushima, Y.-W. He, A critical role for the autophagy gene Atg5 in T cell survival and proliferation. *J. Exp. Med.* **204**, 25–31 (2007).
258. V. V Parekh *et al.*, Impaired autophagy, defective T cell homeostasis, and a wasting syndrome in mice with a T cell-specific deletion of Vps34. *J. Immunol.* **190**, 5086–101 (2013).
259. T. Willinger, R. A. Flavell, Canonical autophagy dependent on the class III phosphoinositide-3 kinase Vps34 is required for naive T-cell homeostasis. *Proc. Natl. Acad. Sci. U. S. A.* **109**, 8670–5 (2012).
260. H. H. Pua, J. Guo, M. Komatsu, Y.-W. He, Autophagy is essential for mitochondrial clearance in mature T lymphocytes. *J. Immunol.* **182**, 4046–55 (2009).
261. W. Jia, H. H. Pua, Q.-J. Li, Y.-W. He, Autophagy regulates endoplasmic reticulum homeostasis and calcium mobilization in T lymphocytes. *J. Immunol.* **186**, 1564–74 (2011).
262. L. M. Stephenson *et al.*, Identification of Atg5-dependent transcriptional changes and increases in mitochondrial mass in Atg5-deficient T lymphocytes. *Autophagy*. **5**, 625–35 (2009).
263. Y. Botbol, B. Patel, F. Macian, Common γ-chain cytokine signaling is required for macroautophagy induction during CD4+ T-cell activation. *Autophagy*. **11**, 1864–77 (2015).
264. V. M. Hubbard *et al.*, Macroautophagy regulates energy metabolism during effector T cell activation. *J. Immunol.* **185**, 7349–57 (2010).
265. C. Li *et al.*, Autophagy is induced in CD4+ T cells and important for the growth factor-withdrawal cell death. *J. Immunol.* **177**, 5163–8 (2006).
266. W. Jia *et al.*, Autophagy regulates T lymphocyte proliferation through selective degradation of the cell-cycle inhibitor CDKN1B/p27Kip1. *Autophagy*. **11**, 2335–45 (2015).
267. D. Murera *et al.*, CD4 T cell autophagy is integral to memory maintenance. *Sci. Rep.* **8**, 5951 (2018).
268. X. Xu *et al.*, Autophagy is essential for effector CD8(+) T cell survival and memory formation. *Nat. Immunol.* **15**, 1152–61 (2014).
269. N. Patsoukis *et al.*, The role of metabolic reprogramming in T cell fate and function. *Curr. Trends Immunol.* **17**, 1–12 (2016).
270. D. O'Sullivan *et al.*, Memory CD8(+) T cells use cell-intrinsic lipolysis to support the

metabolic programming necessary for development. *Immunity*. **41**, 75–88 (2014).
271. G. J. W. van der Windt *et al.*, Mitochondrial respiratory capacity is a critical regulator of CD8+ T cell memory development. *Immunity*. **36**, 68–78 (2012).
272. R. D. Michalek *et al.*, Cutting edge: distinct glycolytic and lipid oxidative metabolic programs are essential for effector and regulatory CD4+ T cell subsets. *J. Immunol.* **186**, 3299–303 (2011).
273. L. Le Texier *et al.*, Autophagy-dependent regulatory T cells are critical for the control of graft-versus-host disease. *JCI insight*. **1**, e86850 (2016).
274. A. M. Kabat *et al.*, The autophagy gene Atg16l1 differentially regulates Treg and TH2 cells to control intestinal inflammation. *Elife*. **5**, e12444 (2016).
275. J. Wei *et al.*, Autophagy enforces functional integrity of regulatory T cells by coupling environmental cues and metabolic homeostasis. *Nat. Immunol.* **17**, 277–285 (2016).
276. J. R. Kovacs *et al.*, Autophagy promotes T-cell survival through degradation of proteins of the cell death machinery. *Cell Death Differ.* **19**, 144–52 (2012).
277. T. Rivera Vargas *et al.*, Selective degradation of PU.1 during autophagy represses the differentiation and antitumour activity of TH9 cells. *Nat. Commun.* **8**, 559 (2017).
278. B. C. Miller *et al.*, The autophagy gene ATG5 plays an essential role in B lymphocyte development. *Autophagy*. **4**, 309–14 (2008).
279. I. Arsov *et al.*, A role for autophagic protein beclin 1 early in lymphocyte development. *J. Immunol.* **186**, 2201–9 (2011).
280. N. Martinez-Martin *et al.*, A switch from canonical to noncanonical autophagy shapes B cell responses. *Science*. **355**, 641–647 (2017).
281. J. M. B. Prieto, M. J. B. Felippe, Development, phenotype, and function of non-conventional B cells. *Comp. Immunol. Microbiol. Infect. Dis.* **54**, 38–44 (2017).
282. A. J. Clarke, T. Riffelmacher, D. Braas, R. J. Cornall, A. K. Simon, B1a B cells require autophagy for metabolic homeostasis and self-renewal. *J. Exp. Med.* **215**, 399–413 (2018).
283. K. Hayakawa, R. R. Hardy, A. M. Stall, L. A. Herzenberg, L. A. Herzenberg, Immunoglobulin-bearing B cells reconstitute and maintain the murine Ly-1 B cell lineage. *Eur. J. Immunol.* **16**, 1313–1316 (1986).
284. I. Krop *et al.*, Self-renewal of B-1 lymphocytes is dependent on CD19. *Eur. J. Immunol.* **26**, 238–242 (1996).
285. N. Pengo *et al.*, Plasma cells require autophagy for sustainable immunoglobulin production. *Nat. Immunol.* **14**, 298–305 (2013).
286. M. Chen *et al.*, Essential role for autophagy in the maintenance of immunological memory against influenza infection. *Nat. Med.* **20**, 503–10 (2014).
287. M. Chen, S. Kodali, A. Jang, L. Kuai, J. Wang, Requirement for autophagy in the long-term persistence but not initial formation of memory B cells. *J. Immunol.* **194**, 2607–15 (2015).
288. D. Ebrahimi-Fakhari *et al.*, Congenital disorders of autophagy: an emerging novel class of inborn errors of neuro-metabolism. *Brain*. **139**, 317–37 (2016).
289. Y. Hua, M. Shen, C. McDonald, Q. Yao, Autophagy dysfunction in autoinflammatory diseases. *J. Autoimmun.* **88**, 11–20 (2018).
290. G. Lopez-Herrera *et al.*, Deleterious mutations in LRBA are associated with a syndrome of immune deficiency and autoimmunity. *Am. J. Hum. Genet.* **90**, 986–1001 (2012).
291. T. Cullup *et al.*, Recessive mutations in EPG5 cause Vici syndrome, a multisystem

disorder with defective autophagy. *Nat. Genet.* **45**, 83–87 (2013).
292. S. Byrne *et al.*, EPG5-related Vici syndrome: a paradigm of neurodevelopmental disorders with defective autophagy. *Brain*. **139**, 765–81 (2016).
293. I. Hori *et al.*, Defects in autophagosome-lysosome fusion underlie Vici syndrome, a neurodevelopmental disorder with multisystem involvement. *Sci. Rep.* **7**, 3552 (2017).
294. Z. Wang *et al.*, The Vici Syndrome Protein EPG5 Is a Rab7 Effector that Determines the Fusion Specificity of Autophagosomes with Late Endosomes/Lysosomes. *Mol. Cell*. **63**, 781–795 (2016).
295. W. Lu *et al.*, Dual proteolytic pathways govern glycolysis and immune competence. *Cell*. **159**, 1578–90 (2014).
296. X. Liu, H. Qin, J. Xu, The role of autophagy in the pathogenesis of systemic lupus erythematosus. *Int. Immunopharmacol.* **40**, 351–361 (2016).
297. H. H. Uhlig, A. M. Muise, Clinical Genomics in Inflammatory Bowel Disease. *Trends Genet.* **33**, 629–641 (2017).
298. T. Kawai, S. Akira, Regulation of innate immune signalling pathways by the tripartite motif (TRIM) family proteins. *EMBO Mol. Med.* **3**, 513–27 (2011).
299. C.-S. Shi *et al.*, Activation of autophagy by inflammatory signals limits IL-1β production by targeting ubiquitinated inflammasomes for destruction. *Nat. Immunol.* **13**, 255–63 (2012).
300. J. Harris *et al.*, Autophagy controls IL-1beta secretion by targeting pro-IL-1beta for degradation. *J. Biol. Chem.* **286**, 9587–97 (2011).
301. M. Zhang, S. J. Kenny, L. Ge, K. Xu, R. Schekman, Translocation of interleukin-1β into a vesicle intermediate in autophagy-mediated secretion. *Elife*. **4** (2015), doi:10.7554/eLife.11205.
302. N. Dupont *et al.*, Autophagy-based unconventional secretory pathway for extracellular delivery of IL-1β. *EMBO J.* **30**, 4701–11 (2011).
303. M. Xia *et al.*, Mitophagy enhances oncolytic measles virus replication by mitigating DDX58/RIG-I-like receptor signaling. *J. Virol.* **88**, 5152–64 (2014).
304. Y. Lei *et al.*, The mitochondrial proteins NLRX1 and TUFM form a complex that regulates type I interferon and autophagy. *Immunity*. **36**, 933–46 (2012).
305. Y. Zhao *et al.*, COX5B Regulates MAVS-mediated Antiviral Signaling through Interaction with ATG5 and Repressing ROS Production. *PLoS Pathog.* **8**, e1003086 (2012).
306. M. A. Delgado, R. A. Elmaoued, A. S. Davis, G. Kyei, V. Deretic, Toll-like receptors control autophagy. *EMBO J.* **27**, 1110–21 (2008).
307. P. P. Lee *et al.*, Wiskott-Aldrich syndrome protein regulates autophagy and inflammasome activity in innate immune cells. *Nat. Commun.* **8**, 1576 (2017).
308. T. J. Vece *et al.*, Copa Syndrome: a Novel Autosomal Dominant Immune Dysregulatory Disease. *J. Clin. Immunol.* **36**, 377–387 (2016).
309. T. Schwerd *et al.*, Impaired antibacterial autophagy links granulomatous intestinal inflammation in Niemann-Pick disease type C1 and XIAP deficiency with NOD2 variants in Crohn's disease. *Gut*. **66**, 1060–1073 (2017).
310. M. J. Massaad, N. Ramesh, R. S. Geha, Wiskott-Aldrich syndrome: a comprehensive review. *Ann. N. Y. Acad. Sci.* **1285**, 26–43 (2013).
311. Y. Zhang *et al.*, Autosomal recessive phosphoglucomutase 3 (PGM3) mutations link glycosylation defects to atopy, immune deficiency, autoimmunity, and neurocognitive impairment. *J. Allergy Clin. Immunol.* **133**, 1400–9, 1409.e1–5 (2014).

312. H. Li, R. Durbin, Fast and accurate short read alignment with Burrows-Wheeler transform. *Bioinformatics*. **25**, 1754–60 (2009).
313. A. McKenna *et al.*, The Genome Analysis Toolkit: a MapReduce framework for analyzing next-generation DNA sequencing data. *Genome Res.* **20**, 1297–303 (2010).
314. K. Wang, M. Li, H. Hakonarson, ANNOVAR: functional annotation of genetic variants from high-throughput sequencing data. *Nucleic Acids Res.* **38**, e164 (2010).
315. D. T. Vistica *et al.*, Therapeutic vulnerability of an in vivo model of alveolar soft part sarcoma (ASPS) to antiangiogenic therapy. *J. Pediatr. Hematol. Oncol.* **31**, 561–70 (2009).
316. C. P. Austin *et al.*, The knockout mouse project. *Nat. Genet.* **36**, 921–4 (2004).
317. M. E. Dickinson *et al.*, High-throughput discovery of novel developmental phenotypes. *Nature*. **537**, 508–514 (2016).
318. W. C. Skarnes *et al.*, A conditional knockout resource for the genome-wide study of mouse gene function. *Nature*. **474**, 337–42 (2011).
319. G. Testa *et al.*, A reliable lacZ expression reporter cassette for multipurpose, knockout-first alleles. *genesis*. **38**, 151–158 (2004).
320. J. E. Moyron-Quiroz, L. Lin, T. Oida, S. Garcia-Mojica, X. Yang, Kinetic study of B cell-depletion with a novel mAb anti-mouse CD20, clone SA271G2. *J. Immunol.* **196** (2016).
321. E. L. Williams *et al.*, Immunotherapy targeting inhibitory Fcγ receptor IIB (CD32b) in the mouse is limited by monoclonal antibody consumption and receptor internalization. *J. Immunol.* **191**, 4130–40 (2013).
322. P. D. Hsu *et al.*, DNA targeting specificity of RNA-guided Cas9 nucleases. *Nat. Biotechnol.* **31**, 827–32 (2013).
323. P. Perez-Pinera *et al.*, RNA-guided gene activation by CRISPR-Cas9-based transcription factors. *Nat. Methods*. **10**, 973–6 (2013).
324. E. K. Brinkman, T. Chen, M. Amendola, B. van Steensel, Easy quantitative assessment of genome editing by sequence trace decomposition. *Nucleic Acids Res.* **42**, e168–e168 (2014).
325. J. Schindelin *et al.*, Fiji: an open-source platform for biological-image analysis. *Nat. Methods*. **9**, 676–682 (2012).
326. C. T. Rueden *et al.*, ImageJ2: ImageJ for the next generation of scientific image data. *BMC Bioinformatics*. **18**, 529 (2017).
327. V. W. Wong *et al.*, The autoimmunity-related GIMAP5 GTPase is a lysosome-associated protein. *Self. Nonself.* **1**, 259–268 (2010).
328. R. Lin, P. Génin, Y. Mamane, J. Hiscott, Selective DNA binding and association with the CREB binding protein coactivator contribute to differential activation of alpha/beta interferon genes by interferon regulatory factors 3 and 7. *Mol. Cell. Biol.* **20**, 6342–53 (2000).
329. I. T. Lamborn *et al.*, Recurrent rhinovirus infections in a child with inherited MDA5 deficiency. *J. Exp. Med.* **214**, 1949–1972 (2017).
330. I. T. Lamborn *et al.*, Recurrent rhinovirus infections in a child with inherited MDA5 deficiency. *J. Exp. Med.* **214**, 1949–1972 (2017).
331. L. M. C. Webb *et al.*, Generation and characterisation of mice deficient in the multi-GTPase domain containing protein, GIMAP8. *PLoS One*. **9**, e110294 (2014).
332. J. C. Pascall *et al.*, The immune system GTPase GIMAP6 interacts with the Atg8 homologue GABARAPL2 and is recruited to autophagosomes. *PLoS One*. **8**, e77782

(2013).
333. R. Chen, H. Im, M. Snyder, Whole-Exome Enrichment with the Agilent SureSelect Human All Exon Platform. *Cold Spring Harb. Protoc.* **2015**, 626–33 (2015).
334. B. Rabbani, N. Mahdieh, K. Hosomichi, H. Nakaoka, I. Inoue, Next-generation sequencing: impact of exome sequencing in characterizing Mendelian disorders. *J. Hum. Genet.* **57**, 621–632 (2012).
335. I. Meyts *et al.*, Exome and genome sequencing for inborn errors of immunity. *J. Allergy Clin. Immunol.* **138**, 957–969 (2016).
336. S. Chakravorty, M. Hegde, Gene and Variant Annotation for Mendelian Disorders in the Era of Advanced Sequencing Technologies. *Annu. Rev. Genomics Hum. Genet.* **18**, 229–256 (2017).
337. N. Krumm *et al.*, Excess of rare, inherited truncating mutations in autism. *Nat. Genet.* **47**, 582–588 (2015).
338. D. G. MacArthur *et al.*, Guidelines for investigating causality of sequence variants in human disease. *Nature*. **508**, 469–476 (2014).
339. R. Blekhman *et al.*, Natural selection on genes that underlie human disease susceptibility. *Curr. Biol.* **18**, 883–9 (2008).
340. M. Kircher *et al.*, A general framework for estimating the relative pathogenicity of human genetic variants. *Nat. Genet.* **46**, 310–315 (2014).
341. I. A. Adzhubei *et al.*, A method and server for predicting damaging missense mutations. *Nat. Methods*. **7**, 248–9 (2010).
342. V. Ramensky, P. Bork, S. Sunyaev, Human non-synonymous SNPs: server and survey. *Nucleic Acids Res.* **30**, 3894–900 (2002).
343. L. A. Miosge *et al.*, Comparison of predicted and actual consequences of missense mutations. *Proc. Natl. Acad. Sci. U. S. A.* **112**, E5189-98 (2015).
344. M. E. Conley, J.-L. Casanova, Discovery of single-gene inborn errors of immunity by next generation sequencing. *Curr. Opin. Immunol.* **30**, 17–23 (2014).
345. D. Cibrián, F. Sánchez-Madrid, CD69: from activation marker to metabolic gatekeeper. *Eur. J. Immunol.* **47**, 946–953 (2017).
346. M. Reddy, E. Eirikis, C. Davis, H. M. Davis, U. Prabhakar, Comparative analysis of lymphocyte activation marker expression and cytokine secretion profile in stimulated human peripheral blood mononuclear cell cultures: an in vitro model to monitor cellular immune function. *J. Immunol. Methods*. **293**, 127–142 (2004).
347. J. M. Brenchley *et al.*, Expression of CD57 defines replicative senescence and antigen-induced apoptotic death of CD8+ T cells. *Blood*. **101**, 2711–2720 (2003).
348. M. Okano, D. W. Bell, D. A. Haber, E. Li, DNA Methyltransferases Dnmt3a and Dnmt3b Are Essential for De Novo Methylation and Mammalian Development. *Cell*. **99**, 247–257 (1999).
349. C. Wijmenga *et al.*, Genetic variation in ICF syndrome: Evidence for genetic heterogeneity. *Hum. Mutat.* **16**, 509–517 (2000).
350. Y. Ueda *et al.*, Roles for Dnmt3b in mammalian development: a mouse model for the ICF syndrome. *Development*. **133**, 1183–92 (2006).
351. M. Ehrlich *et al.*, ICF, an immunodeficiency syndrome: DNA methyltransferase 3B involvement, chromosome anomalies, and gene dysregulation. *Autoimmunity*. **41**, 253–71 (2008).
352. M. Roth, S. Helm-Kruse, T. Friedrich, A. Jeltsch, Functional roles of conserved amino acid residues in DNA methyltransferases investigated by site-directed mutagenesis of

the EcoRV adenine-N6-methyltransferase. *J. Biol. Chem.* **273**, 17333–42 (1998).
353. E. J. Bj◆ck, T.-H. Bui, C. Wijmenga, U. Grandell, M. Nordenskj◆d, Early prenatal diagnosis of the ICF syndrome. *Prenat. Diagn.* **20**, 828–831 (2000).
354. E. Li, T. H. Bestor, R. Jaenisch, Targeted mutation of the DNA methyltransferase gene results in embryonic lethality. *Cell*. **69**, 915–926 (1992).
355. G.-L. Xu *et al.*, Chromosome instability and immunodeficiency syndrome caused by mutations in a DNA methyltransferase gene. *Nature*. **402**, 187–191 (1999).
356. D. C. M. Smeets *et al.*, ICF syndrome: a new case and review of the literature. *Hum. Genet.* **94**, 240–246 (1994).
357. C. Turleau *et al.*, Multibranched chromosomes in the ICF syndrome: Immunodeficiency, centromeric instability, and facial anomalies. *Am. J. Med. Genet.* **32**, 420–424 (1989).
358. P. Maraschio, O. Zuffardi, T. Dalla Fior, L. Tiepolo, Immunodeficiency, centromeric heterochromatin instability of chromosomes 1, 9, and 16, and facial anomalies: the ICF syndrome. *J. Med. Genet.* **25**, 173–80 (1988).
359. M. Ehrlich, DNA Hypomethylation, Cancer, the Immunodeficiency, Centromeric Region Instability, Facial Anomalies Syndrome and Chromosomal Rearrangements. *J. Nutr.* **132**, 2424S–2429S (2002).
360. P. J. Flor *et al.*, Molecular Cloning, Functional Expression and Pharmacological Characterization of the Human Metabotropic Glutamate Receptor Type 2. *Eur. J. Neurosci.* **7**, 622–629 (1995).
361. S. D. Dib-Hajj, L. Tyrrell, J. A. Black, S. G. Waxman, NaN, a novel voltage-gated Na channel, is expressed preferentially in peripheral sensory neurons and down-regulated after axotomy. *Proc. Natl. Acad. Sci. U. S. A.* **95**, 8963–8 (1998).
362. K. Nakabayashi *et al.*, Genomic imprinting of PPP1R9A encoding neurabin I in skeletal muscle and extra-embryonic tissues. *J. Med. Genet.* **41**, 601–8 (2004).
363. J. Patrakka *et al.*, Expression and subcellular distribution of novel glomerulus-associated proteins dendrin, ehd3, sh2d4a, plekhh2, and 2310066E14Rik. *J. Am. Soc. Nephrol.* **18**, 689–97 (2007).
364. T. C. Hart *et al.*, Novel ENAM mutation responsible for autosomal recessive amelogenesis imperfecta and localised enamel defects. *J. Med. Genet.* **40**, 900–6 (2003).
365. P. Lorès *et al.*, Homozygous missense mutation L673P in adenylate kinase 7 (AK7) leads to primary male infertility and multiple morphological anomalies of the flagella but not to primary ciliary dyskinesia. *Hum. Mol. Genet.* **27**, 1196–1211 (2018).
366. M. Yokoi *et al.*, Impairment of hippocampal mossy fiber LTD in mice lacking mGluR2. *Science*. **273**, 645–7 (1996).
367. B. T. Priest *et al.*, Contribution of the tetrodotoxin-resistant voltage-gated sodium channel NaV1.9 to sensory transmission and nociceptive behavior. *Proc. Natl. Acad. Sci. U. S. A.* **102**, 9382–7 (2005).
368. J. C.-C. Hu *et al.*, Enamel defects and ameloblast-specific expression in Enam knock-out/lacz knock-in mice. *J. Biol. Chem.* **283**, 10858–71 (2008).
369. H. Masuya *et al.*, Enamelin (Enam) is essential for amelogenesis: ENU-induced mouse mutants as models for different clinical subtypes of human amelogenesis imperfecta (AI). *Hum. Mol. Genet.* **14**, 575–583 (2005).
370. A. Fernandez-Gonzalez, S. Kourembanas, T. A. Wyatt, S. A. Mitsialis, Mutation of Murine Adenylate Kinase 7 Underlies a Primary Ciliary Dyskinesia Phenotype. *Am. J.*

Respir. Cell Mol. Biol. **40**, 305–313 (2009).
371. E. L. Pearce *et al.*, Enhancing CD8 T-cell memory by modulating fatty acid metabolism. *Nature*. **460**, 103–7 (2009).
372. A. M. Intlekofer *et al.*, Effector and memory CD8+ T cell fate coupled by T-bet and eomesodermin. *Nat. Immunol.* **6**, 1236–1244 (2005).
373. A. Banerjee *et al.*, Cutting edge: The transcription factor eomesodermin enables CD8+ T cells to compete for the memory cell niche. *J. Immunol.* **185**, 4988–92 (2010).
374. S.-Y. Zhang *et al.*, TLR3 Deficiency in Patients with Herpes Simplex Encephalitis. *Science (80-.).* **317**, 1522–1527 (2007).
375. A. P. Russ *et al.*, Eomesodermin is required for mouse trophoblast development and mesoderm formation. *Nature*. **404**, 95–99 (2000).
376. S. J. Arnold *et al.*, The T-box transcription factor Eomes/Tbr2 regulates neurogenesis in the cortical subventricular zone. *Genes Dev.* **22**, 2479–84 (2008).
377. L. Baala *et al.*, Homozygous silencing of T-box transcription factor EOMES leads to microcephaly with polymicrogyria and corpus callosum agenesis. *Nat. Genet.* **39**, 454–456 (2007).
378. L. E. Gralinski *et al.*, Allelic Variation in the Toll-Like Receptor Adaptor Protein Ticam2 Contributes to SARS-Coronavirus Pathogenesis in Mice. *G3 (Bethesda).* **7**, 1653–1663 (2017).
379. Y. Enokizono *et al.*, Structures and interface mapping of the TIR domain-containing adaptor molecules involved in interferon signaling. *Proc. Natl. Acad. Sci. U. S. A.* **110**, 19908–13 (2013).
380. E. M. Palsson-McDermott *et al.*, TAG, a splice variant of the adaptor TRAM, negatively regulates the adaptor MyD88-independent TLR4 pathway. *Nat. Immunol.* **10**, 579–86 (2009).
381. S. L. Doyle *et al.*, The GOLD domain-containing protein TMED7 inhibits TLR4 signalling from the endosome upon LPS stimulation. *Nat. Commun.* **3**, 707 (2012).
382. J. Stack *et al.*, TRAM is required for TLR2 endosomal signaling to type I IFN induction. *J. Immunol.* **193**, 6090–102 (2014).
383. E. Shevlin, S. M. Miggin, The TIR-domain containing adaptor TRAM is required for TLR7 mediated RANTES production. *PLoS One*. **9**, e107141 (2014).
384. K. A. Fitzgerald *et al.*, LPS-TLR4 signaling to IRF-3/7 and NF-kappaB involves the toll adapters TRAM and TRIF. *J. Exp. Med.* **198**, 1043–55 (2003).
385. M. Yamamoto *et al.*, Role of adaptor TRIF in the MyD88-independent toll-like receptor signaling pathway. *Science*. **301**, 640–3 (2003).
386. D. C. Rowe *et al.*, The myristoylation of TRIF-related adaptor molecule is essential for Toll-like receptor 4 signal transduction. *Proc. Natl. Acad. Sci. U. S. A.* **103**, 6299–304 (2006).
387. H. Oshiumi *et al.*, TIR-containing adapter molecule (TICAM)-2, a bridging adapter recruiting to toll-like receptor 4 TICAM-1 that induces interferon-beta. *J. Biol. Chem.* **278**, 49751–62 (2003).
388. M. Michalkiewicz *et al.*, Transgenic rescue demonstrates involvement of the Ian5 gene in T cell development in the rat. *Physiol. Genomics*. **19**, 228–32 (2004).
389. A. J. MacMurray *et al.*, Lymphopenia in the BB rat model of type 1 diabetes is due to a mutation in a novel immune-associated nucleotide (Ian)-related gene. *Genome Res.* **12**, 1029–39 (2002).
390. M. J. Barnes *et al.*, Loss of T cell and B cell quiescence precedes the onset of microbial

flora-dependent wasting disease and intestinal inflammation in Gimap5-deficient mice. *J. Immunol.* **184**, 3743–54 (2010).
391. R. D. Schulteis *et al.*, Impaired survival of peripheral T cells, disrupted NK/NKT cell development, and liver failure in mice lacking Gimap5. *Blood*. **112**, 4905–14 (2008).
392. T. Sandal, L. Aumo, L. Hedin, B. T. Gjertsen, S. O. Døskeland, Irod/Ian5: an inhibitor of gamma-radiation- and okadaic acid-induced apoptosis. *Mol. Biol. Cell*. **14**, 3292–304 (2003).
393. T. Nitta *et al.*, IAN family critically regulates survival and development of T lymphocytes. *PLoS Biol.* **4**, e103 (2006).
394. U. Dalberg, H. Markholst, L. Hornum, Both Gimap5 and the diabetogenic BBDP allele of Gimap5 induce apoptosis in T cells. *Int. Immunol.* **19**, 447–53 (2007).
395. L. Dahéron, T. Zenz, L. D. Siracusa, C. Brenner, B. Calabretta, Molecular cloning of Ian4: a BCR/ABL-induced gene that encodes an outer membrane mitochondrial protein with GTP-binding activity. *Nucleic Acids Res.* **29**, 1308–16 (2001).
396. F. Guerra, C. Bucci, Multiple Roles of the Small GTPase Rab7. *Cells*. **5** (2016), doi:10.3390/cells5030034.
397. S. G. Roy, M. W. Stevens, L. So, A. L. Edinger, Reciprocal effects of rab7 deletion in activated and neglected T cells. *Autophagy*. **9**, 1009–23 (2013).
398. A. Yamamoto *et al.*, Bafilomycin A1 Prevents Maturation of Autophagic Vacuoles by Inhibiting Fusion between Autophagosomes and Lysosomes in Rat Hepatoma Cell Line, H-4-II-E Cells. *Cell Struct. Funct.* **23**, 33–42 (1998).
399. C. Mauvezin, P. Nagy, G. Juhász, T. P. Neufeld, S. Patel, Autophagosome–lysosome fusion is independent of V-ATPase-mediated acidification. *Nat. Commun.* **6**, 7007 (2015).
400. L. Bar-Peled *et al.*, A Tumor suppressor complex with GAP activity for the Rag GTPases that signal amino acid sufficiency to mTORC1. *Science*. **340**, 1100–6 (2013).
401. S. Bagchi, R. Fredriksson, Å. Wallén-Mackenzie, (Humana Press, New York, NY, 2015; http://link.springer.com/10.1007/978-1-4939-2742-5_15), pp. 149–159.
402. A. Aoki *et al.*, Enzymatic properties of de novo-type mouse DNA (cytosine-5) methyltransferases. *Nucleic Acids Res.* **29**, 3506–12 (2001).
403. H. Gowher, A. Jeltsch, Enzymatic properties of recombinant Dnmt3a DNA methyltransferase from mouse: the enzyme modifies DNA in a non-processive manner and also methylates non-CpA sites. *J. Mol. Biol.* **309**, 1201–1208 (2001).
404. J. R. Edwards, O. Yarychkivska, M. Boulard, T. H. Bestor, DNA methylation and DNA methyltransferases. *Epigenetics Chromatin*. **10**, 23 (2017).
405. R. Kosaki, H. Terashima, M. Kubota, K. Kosaki, Acute myeloid leukemia-associated *DNMT3A* p.Arg882His mutation in a patient with Tatton-Brown-Rahman overgrowth syndrome as a constitutional mutation. *Am. J. Med. Genet. Part A*. **173**, 250–253 (2017).
406. K. Tatton-Brown *et al.*, Mutations in the DNA methyltransferase gene DNMT3A cause an overgrowth syndrome with intellectual disability. *Nat. Genet.* **46**, 385–8 (2014).
407. C. J. Klein *et al.*, Mutations in DNMT1 cause hereditary sensory neuropathy with dementia and hearing loss. *Nat. Genet.* **43**, 595–600 (2011).
408. J. Winkelmann *et al.*, Mutations in DNMT1 cause autosomal dominant cerebellar ataxia, deafness and narcolepsy. *Hum. Mol. Genet.* **21**, 2205–10 (2012).
409. C. M. R. Weemaes *et al.*, Heterogeneous clinical presentation in ICF syndrome: correlation with underlying gene defects. *Eur. J. Hum. Genet.* **21**, 1219–25 (2013).

410. A. Pezzolo *et al.*, A novel case of immunodeficiency, centromeric instability, and facial anomalies (the ICF syndrome): immunologic and cytogenetic studies. *Haematologica*. **87**, 329–31 (2002).
411. C. M. Tuck-Muller *et al.*, DNA hypomethylation and unusual chromosome instability in cell lines fromICF syndrome patients. *Cytogenet. Genome Res.* **89**, 121–128 (2000).
412. B. Jin *et al.*, DNA methyltransferase 3B (DNMT3B) mutations in ICF syndrome lead to altered epigenetic modifications and aberrant expression of genes regulating development, neurogenesis and immune function. *Hum. Mol. Genet.* **17**, 690–709 (2008).
413. E. Lana *et al.*, DNA replication is altered in Immunodeficiency Centromeric instability Facial anomalies (ICF) cells carrying DNMT3B mutations. *Eur. J. Hum. Genet.* **20**, 1044–50 (2012).
414. S. M. Kahan, E. J. Wherry, A. J. Zajac, T cell exhaustion during persistent viral infections. *Virology*. **479**–**480**, 180–193 (2015).
415. A. W. Goldrath, L. Y. Bogatzki, M. J. Bevan, Naive T cells transiently acquire a memory-like phenotype during homeostasis-driven proliferation. *J. Exp. Med.* **192**, 557–64 (2000).
416. C. E. Blanco-Betancourt *et al.*, Defective B-cell-negative selection and terminal differentiation in the ICF syndrome. *Blood*. **103**, 2683–90 (2004).
417. N. Wong *et al.*, Hypomethylation of chromosome 1 heterochromatin DNA correlates with q-arm copy gain in human hepatocellular carcinoma. *Am. J. Pathol.* **159**, 465–71 (2001).
418. D. Gisselsson *et al.*, Interphase chromosomal abnormalities and mitotic missegregation of hypomethylated sequences in ICF syndrome cells. *Chromosoma*. **114**, 118–126 (2005).
419. K. L. Sheaffer, E. N. Elliott, K. H. Kaestner, DNA Hypomethylation Contributes to Genomic Instability and Intestinal Cancer Initiation. *Cancer Prev. Res. (Phila).* **9**, 534–46 (2016).
420. A. Almeida *et al.*, Hypomethylation of classical satellite DNA and chromosome instability in lymphoblastoid cell lines. *Hum. Genet.* **91**, 538–546 (1993).
421. C. P. Walsh, J. R. Chaillet, T. H. Bestor, Transcription of IAP endogenous retroviruses is constrained by cytosine methylation. *Nat. Genet.* **20**, 116–117 (1998).
422. B. Panning, R. Jaenisch, DNA hypomethylation can activate Xist expression and silence X-linked genes. *Genes Dev.* **10**, 1991–2002 (1996).
423. T. Caspary, M. A. Cleary, C. C. Baker, X. J. Guan, S. M. Tilghman, Multiple mechanisms regulate imprinting of the mouse distal chromosome 7 gene cluster. *Mol. Cell. Biol.* **18**, 3466–74 (1998).
424. D. Bourc'his, G. L. Xu, C. S. Lin, B. Bollman, T. H. Bestor, Dnmt3L and the establishment of maternal genomic imprints. *Science*. **294**, 2536–9 (2001).
425. A. Wutz *et al.*, Imprinted expression of the Igf2r gene depends on an intronic CpG island. *Nature*. **389**, 745–749 (1997).
426. L. D. Moore, T. Le, G. Fan, DNA methylation and its basic function. *Neuropsychopharmacology*. **38**, 23–38 (2013).
427. S. Gatto *et al.*, ICF-specific DNMT3B dysfunction interferes with intragenic regulation of mRNA transcription and alternative splicing. *Nucleic Acids Res.* **45**, 5739–5756 (2017).
428. M. Ehrlich, K. Jackson, C. Weemaes, Immunodeficiency, centromeric region

instability, facial anomalies syndrome (ICF). *Orphanet J. Rare Dis.* **1**, 2 (2006).
429. O. Takeuchi, S. Akira, Pattern recognition receptors and inflammation. *Cell*. **140**, 805–20 (2010).
430. N. J. Nilsen *et al.*, A role for the adaptor proteins TRAM and TRIF in toll-like receptor 2 signaling. *J. Biol. Chem.* **290**, 3209–22 (2015).
431. A. Fischer, A. Rausell, Primary immunodeficiencies suggest redundancy within the human immune system. *Sci. Immunol.* **1**, eaah5861 (2016).
432. A. Rausell *et al.*, Analysis of stop-gain and frameshift variants in human innate immunity genes. *PLoS Comput. Biol.* **10**, e1003757 (2014).
433. A. Rausell, P. J. McLaren, A. Telenti, HIV and innate immunity - a genomics perspective. *F1000Prime Rep.* **5**, 29 (2013).
434. V. Sancho-Shimizu *et al.*, Herpes simplex encephalitis in children with autosomal recessive and dominant TRIF deficiency. *J. Clin. Invest.* **121**, 4889–902 (2011).
435. N. J. Nilsen *et al.*, A role for the adaptor proteins TRAM and TRIF in toll-like receptor 2 signaling. *J. Biol. Chem.* **290**, 3209–22 (2015).
436. D. G. MacArthur *et al.*, A systematic survey of loss-of-function variants in human protein-coding genes. *Science*. **335**, 823–8 (2012).
437. P. Sulem *et al.*, Identification of a large set of rare complete human knockouts. *Nat. Genet.* **47**, 448–452 (2015).
438. V. M. Narasimhan *et al.*, Health and population effects of rare gene knockouts in adult humans with related parents. *Science*. **352**, 474–7 (2016).
439. R. Chen *et al.*, Analysis of 589,306 genomes identifies individuals resilient to severe Mendelian childhood diseases. *Nat. Biotechnol.* **34**, 531–538 (2016).
440. M. A. Kovach, T. J. Standiford, Toll like receptors in diseases of the lung. *Int. Immunopharmacol.* **11**, 1399–406 (2011).
441. A. R. Patterson *et al.*, Gimap5-dependent inactivation of GSK3β is required for CD4+ T cell homeostasis and prevention of immune pathology. *Nat. Commun.* **9**, 430 (2018).
442. M. Keita, C. Leblanc, D. Andrews, S. Ramanathan, GIMAP5 regulates mitochondrial integrity from a distinct subcellular compartment. *Biochem. Biophys. Res. Commun.* **361**, 481–486 (2007).
443. D. Serrano *et al.*, GTPase of the Immune-Associated Nucleotide Protein 5 Regulates the Lysosomal Calcium Compartment in T Lymphocytes. *Front. Immunol.* **8**, 94 (2017).
444. S. C. Pino *et al.*, CHOP Mediates Endoplasmic Reticulum Stress-Induced Apoptosis in Gimap5-Deficient T Cells. *PLoS One*. **4**, e5468 (2009).
445. M. Pandarpurkar *et al.*, Ian4 is required for mitochondrial integrity and T cell survival. *Proc. Natl. Acad. Sci. U. S. A.* **100**, 10382–7 (2003).
446. X. L. Chen *et al.*, GTPase of the immune-associated nucleotide-binding protein 5 (GIMAP5) regulates calcium influx in T-lymphocytes by promoting mitochondrial calcium accumulation. *Biochem. J.* **449**, 353–64 (2013).
447. S. G. Roy, M. W. Stevens, L. So, A. L. Edinger, Reciprocal effects of rab7 deletion in activated and neglected T cells. *Autophagy*. **9**, 1009–23 (2013).
448. J. M. T. Hyttinen, M. Niittykoski, A. Salminen, K. Kaarniranta, Maturation of autophagosomes and endosomes: A key role for Rab7. *Biochim. Biophys. Acta - Mol. Cell Res.* **1833**, 503–510 (2013).
449. X.-L. Chen *et al.*, GIMAP5 Deficiency Is Associated with Increased AKT Activity in T Lymphocytes. *PLoS One*. **10**, e0139019 (2015).
450. G. M. Poirier *et al.*, Immune-associated nucleotide-1 (IAN-1) is a thymic selection

marker and defines a novel gene family conserved in plants. *J. Immunol.* **163**, 4960–9 (1999).
451. T. Nitta *et al.*, IAN family critically regulates survival and development of T lymphocytes. *PLoS Biol.* **4**, e103 (2006).
452. J. Krücken *et al.*, Comparative analysis of the human gimap gene cluster encoding a novel GTPase family. *Gene*. **341**, 291–304 (2004).
453. C. Liu, T. Wang, W. Zhang, X. Li, Computational identification and analysis of immune-associated nucleotide gene family in Arabidopsis thaliana. *J. Plant Physiol.* **165**, 777–787 (2008).
454. T. Nitta, Y. Takahama, The lymphocyte guard-IANs: regulation of lymphocyte survival by IAN/GIMAP family proteins. *Trends Immunol.* **28**, 58–65 (2007).
455. T. L. Reuber, F. M. Ausubel, Isolation of Arabidopsis genes that differentiate between resistance responses mediated by the RPS2 and RPM1 disease resistance genes. *Plant Cell*. **8**, 241–9 (1996).
456. A. Saunders *et al.*, Expression of GIMAP1, a GTPase of the immunity-associated protein family, is not up-regulated in malaria. *Malar. J.* **8**, 53 (2009).
457. C. Dion *et al.*, Expression of the Ian family of putative GTPases during T cell development and description of an Ian with three sets of GTP/GDP-binding motifs. *Int. Immunol.* **17**, 1257–68 (2005).
458. A. Saunders *et al.*, Putative GTPase GIMAP1 is critical for the development of mature B and T lymphocytes. *Blood*. **115**, 3249–57 (2010).
459. J.-J. Filén *et al.*, Quantitative proteomics reveals GIMAP family proteins 1 and 4 to be differentially regulated during human T helper cell differentiation. *Mol. Cell. Proteomics*. **8**, 32–44 (2009).
460. D. Schwefel *et al.*, Structural insights into the mechanism of GTPase activation in the GIMAP family. *Structure*. **21**, 550–9 (2013).
461. D. Schwefel *et al.*, Structural basis of oligomerization in septin-like GTPase of immunity-associated protein 2 (GIMAP2). *Proc. Natl. Acad. Sci. U. S. A.* **107**, 20299–304 (2010).
462. R. Jokinen *et al.*, Quantitative changes in Gimap3 and Gimap5 expression modify mitochondrial DNA segregation in mice. *Genetics*. **200**, 221–35 (2015).
463. K. Yano *et al.*, Gimap3 and Gimap5 cooperate to maintain T-cell numbers in the mouse. *Eur. J. Immunol.* **44**, 561–72 (2014).
464. C. Carter *et al.*, A natural hypomorphic variant of the apoptosis regulator Gimap4/IAN1. *J. Immunol.* **179**, 1784–95 (2007).
465. S. Schnell, C. Démollière, P. van den Berk, H. Jacobs, Gimap4 accelerates T-cell death. *Blood*. **108**, 591–9 (2006).
466. M. A. Mouthon *et al.*, Expression of tal-1 and GATA-binding proteins during human hematopoiesis. *Blood*. **81**, 647–55 (1993).
467. Z. Li *et al.*, MicroRNA-146a Overexpression Impairs the Positive Selection during T Cell Development. *Front. Immunol.* **8**, 2006 (2017).
468. K. A. Duthie, L. C. Osborne, L. J. Foster, N. Abraham, Proteomics analysis of interleukin (IL)-7-induced signaling effectors shows selective changes in IL-7Ralpha449F knock-in T cell progenitors. *Mol. Cell. Proteomics*. **6**, 1700–10 (2007).
469. M. Cambot, S. Aresta, B. Kahn-Perlès, J. de Gunzburg, P.-H. Roméo, Human immune associated nucleotide 1: a member of a new guanosine triphosphatase family expressed in resting T and B cells. *Blood*. **99**, 3293–301 (2002).

470. M. T. Heinonen, K. Kanduri, H. J. Lähdesmäki, R. Lahesmaa, T. A. Henttinen, Tubulin- and actin-associating GIMAP4 is required for IFN-γ secretion during Th cell differentiation. *Immunol. Cell Biol.* **93**, 158–66 (2015).
471. F. Payne *et al.*, Haplotype tag single nucleotide polymorphism analysis of the human orthologues of the rat type 1 diabetes genes Ian4 (Lyp/Iddm1) and Cblb. *Diabetes*. **53**, 505–9 (2004).
472. M. Lim *et al.*, IAN5 polymorphisms are associated with systemic lupus erythematosus. *Lupus*. **18**, 1045–1052 (2009).
473. J.-H. Shin *et al.*, IA-2 autoantibodies in incident type I diabetes patients are associated with a polyadenylation signal polymorphism in GIMAP5. *Genes Immun.* **8**, 503–12 (2007).
474. A. Hellquist *et al.*, The human GIMAP5 gene has a common polyadenylation polymorphism increasing risk to systemic lupus erythematosus. *J. Med. Genet.* **44**, 314–21 (2007).
475. M. T. Heinonen *et al.*, GIMAP GTPase family genes: potential modifiers in autoimmune diabetes, asthma, and allergy. *J. Immunol.* **194**, 5885–94 (2015).
476. D. H. Moralejo *et al.*, BB rat Gimap gene expression in sorted lymphoid T and B cells. *Life Sci.* **89**, 748–54 (2011).
477. Z. Huang *et al.*, Dysregulation of GTPase IMAP family members in hepatocellular cancer. *Mol. Med. Rep.* (2016), doi:10.3892/mmr.2016.5764.
478. Y.-M. Shiao *et al.*, Dysregulation of GIMAP genes in non-small cell lung cancer. *Lung Cancer*. **62**, 287–294 (2008).
479. K. Hosokawa *et al.*, T Cell Transcriptomes from Paroxysmal Nocturnal Hemoglobinuria Patients Reveal Novel Signaling Pathways. *J. Immunol.* **199**, 477–488 (2017).
480. S. Thirunavukkarasu *et al.*, Expression of genes associated with cholesterol and lipid metabolism identified as a novel pathway in the early pathogenesis of Mycobacterium avium subspecies paratuberculosis-infection in cattle. *Vet. Immunol. Immunopathol.* **160**, 147–157 (2014).
481. N. Sanati, O. D. Iancu, G. Wu, J. E. Jacobs, S. K. McWeeney, Network-Based Predictors of Progression in Head and Neck Squamous Cell Carcinoma. *Front. Genet.* **9**, 183 (2018).
482. D. Schwefel, C. Fröhlich, O. Daumke, Purification, crystallization and preliminary X-ray analysis of human GIMAP2. *Acta Crystallogr. Sect. F. Struct. Biol. Cryst. Commun.* **66**, 725–9 (2010).
483. E. A. Rutledge *et al.*, Sequence variation and expression of the Gimap gene family in the BB rat. *Exp. Diabetes Res.* **2009**, 835650 (2009).
484. A. I. Su *et al.*, A gene atlas of the mouse and human protein-encoding transcriptomes. *Proc. Natl. Acad. Sci.* **101**, 6062–6067 (2004).
485. B. A. Muhammad *et al.*, *Mol. Cancer Res.*, in press, doi:10.1158/1541-7786.MCR-18-0262.
486. S. Nicole *et al.*, Perlecan, the major proteoglycan of basement membranes, is altered in patients with Schwartz-Jampel syndrome (chondrodystrophic myotonia). *Nat. Genet.* **26**, 480–3 (2000).
487. E. Arikawa-Hirasawa *et al.*, Dyssegmental dysplasia, Silverman-Handmaker type, is caused by functional null mutations of the perlecan gene. *Nat. Genet.* **27**, 431–434 (2001).
488. E. Arikawa-Hirasawa, H. Watanabe, H. Takami, J. R. Hassell, Y. Yamada, Perlecan is

essential for cartilage and cephalic development. *Nat. Genet.* **23**, 354–8 (1999).
489. B. A. Janowski *et al.*, Involvement of AGO1 and AGO2 in mammalian transcriptional silencing. *Nat. Struct. Mol. Biol.* **13**, 787–792 (2006).
490. D. Völler *et al.*, Argonaute Family Protein Expression in Normal Tissue and Cancer Entities. *PLoS One*. **11**, e0161165 (2016).
491. R. G. Boot *et al.*, Identification of a Novel Acidic Mammalian Chitinase Distinct from Chitotriosidase. *J. Biol. Chem.* **276**, 6770–6778 (2001).
492. C. G. Lee *et al.*, Role of Chitin and Chitinase/Chitinase-Like Proteins in Inflammation, Tissue Remodeling, and Injury. *Annu. Rev. Physiol.* **73**, 479–501 (2011).
493. Z. Zhu *et al.*, Acidic Mammalian Chitinase in Asthmatic Th2 Inflammation and IL-13 Pathway Activation. *Science (80-.).* **304**, 1678–1682 (2004).
494. N. Qamar, R. L. Fuleihan, The Hyper IgM Syndromes. *Clin. Rev. Allergy Immunol.* **46**, 120–130 (2014).
495. B. J. C. Quah, C. R. Parish, New and improved methods for measuring lymphocyte proliferation in vitro and in vivo using CFSE-like fluorescent dyes. *J. Immunol. Methods*. **379**, 1–14 (2012).
496. M. Roederer, Interpretation of cellular proliferation data: Avoid the panglossian. *Cytom. Part A*. **79A**, 95–101 (2011).
497. B. E. Tomkinson, D. K. Wagner, D. L. Nelson, J. L. Sullivan, Activated lymphocytes during acute Epstein-Barr virus infection. *J. Immunol.* **139**, 3802–7 (1987).
498. J. F. Viallard *et al.*, HLA-DR expression on lymphocyte subsets as a marker of disease activity in patients with systemic lupus erythematosus. *Clin. Exp. Immunol.* **125**, 485–91 (2001).
499. Y. Agata *et al.*, Expression of the PD-1 antigen on the surface of stimulated mouse T and B lymphocytes. *Int. Immunol.* **8**, 765–72 (1996).
500. B. E. Palmer, N. Blyveis, A. P. Fontenot, C. C. Wilson, Functional and phenotypic characterization of CD57+CD4+ T cells and their association with HIV-1-induced T cell dysfunction. *J. Immunol.* **175**, 8415–23 (2005).
501. S. M. Henson *et al.*, KLRG1 signaling induces defective Akt (ser473) phosphorylation and proliferative dysfunction of highly differentiated CD8+ T cells. *Blood*. **113**, 6619–28 (2009).
502. F. J. Plunkett *et al.*, The loss of telomerase activity in highly differentiated CD8+CD28-CD27- T cells is associated with decreased Akt (Ser473) phosphorylation. *J. Immunol.* **178**, 7710–9 (2007).
503. A. Larbi, T. Fulop, From “truly naïve” to “exhausted senescent” T cells: When markers predict functionality. *Cytom. Part A*. **85**, 25–35 (2014).
504. A. Jäger, V. K. Kuchroo, Effector and regulatory T-cell subsets in autoimmunity and tissue inflammation. *Scand. J. Immunol.* **72**, 173–84 (2010).
505. S. Crotty, T Follicular Helper Cell Differentiation, Function, and Roles in Disease. *Immunity*. **41**, 529–542 (2014).
506. R. Khattri, T. Cox, S.-A. Yasayko, F. Ramsdell, An essential role for Scurfin in CD4+CD25+ T regulatory cells. *Nat. Immunol.* **4**, 337–342 (2003).
507. D. Baumjohann, D. Baumjohann, K. M. Ansel, Identification of T follicular helper (Tfh) cells by flow cytometry. *Protoc. Exch.* (2013), doi:10.1038/protex.2013.060.
508. N. Beyersdorf, X. Ding, J. K. Tietze, T. Hanke, Characterization of mouse CD4 T cell subsets defined by expression of KLRG1. *Eur. J. Immunol.* **37**, 3445–3454 (2007).
509. W. W. Reiley *et al.*, Distinct functions of antigen-specific CD4 T cells during murine

Mycobacterium tuberculosis infection. *Proc. Natl. Acad. Sci. U. S. A.* **107**, 19408–13 (2010).
510. M. L. Hermiston, Z. Xu, A. Weiss, CD45: A Critical Regulator of Signaling Thresholds in Immune Cells. *Annu. Rev. Immunol.* **21**, 107–137 (2003).
511. T. M. McIntyre *et al.*, Transforming growth factor beta 1 selectivity stimulates immunoglobulin G2b secretion by lipopolysaccharide-activated murine B cells. *J. Exp. Med.* **177**, 1031–7 (1993).
512. C. M. Snapper, W. Waegell, H. Beernink, J. R. Dasch, Transforming growth factor-beta 1 is required for secretion of IgG of all subclasses by LPS-activated murine B cells in vitro. *J. Immunol.* **151**, 4625–36 (1993).
513. M. Endale, H. I. Aksoylar, K. Hoebe, Central role of gimap5 in maintaining peripheral tolerance and T cell homeostasis in the gut. *Mediators Inflamm.* **2015**, 436017 (2015).
514. H. I. Aksoylar, K. Lampe, M. J. Barnes, D. R. Plas, K. Hoebe, Loss of immunological tolerance in Gimap5-deficient mice is associated with loss of Foxo in CD4+ T cells. *J. Immunol.* **188**, 146–54 (2012).
515. H. J. Fischer *et al.*, Distinct roles of T-cell lymphopenia and the microbial flora for gastrointestinal and CNS autoimmunity. *FASEB J.* (2016), doi:10.1096/fj.15-277384.
516. L. Ortiz-Fernández *et al.*, GIMAP and Behçet disease: no association in the European population. *Ann. Rheum. Dis.* **73**, 1433–4 (2014).
517. J. C. Pascall *et al.*, GIMAP6 is required for T cell maintenance and efficient autophagy in mice. *PLoS One*. **13**, e0196504 (2018).
518. C.-H. Ho, S.-F. Tsai, Functional and biochemical characterization of a T cell-associated anti-apoptotic protein, GIMAP6. *J. Biol. Chem.* **292**, 9305–9319 (2017).
519. J. Mestas, C. C. W. Hughes, Of Mice and Not Men: Differences between Mouse and Human Immunology (2004).
520. G. K. Wong, A. P. Huissoon, T-cell abnormalities in common variable immunodeficiency: the hidden defect. *J. Clin. Pathol.* **69**, 672–6 (2016).
521. E. F. McKinney, J. C. Lee, D. R. W. Jayne, P. A. Lyons, K. G. C. Smith, T-cell exhaustion, co-stimulation and clinical outcome in autoimmunity and infection. *Nature*. **523**, 612–6 (2015).
522. M. Honda *et al.*, Telomere Shortening and Decreased Replicative Potential, Contrasted by Continued Proliferation of Telomerase-Positive CD8+CD28lo T Cells in Patients with Systemic Lupus Erythematosus. *Clin. Immunol.* **99**, 211–221 (2001).
523. C. J. Hedeskov, Early effects of phytohaemagglutinin on glucose metabolism of normal human lymphocytes. *Biochem. J.* **110**, 373–80 (1968).
524. J. C. Rathmell, M. G. V. Heiden, M. H. Harris, K. A. Frauwirth, C. B. Thompson, In the Absence of Extrinsic Signals, Nutrient Utilization by Lymphocytes Is Insufficient to Maintain Either Cell Size or Viability. *Mol. Cell*. **6**, 683–692 (2000).
525. K. Araki *et al.*, mTOR regulates memory CD8 T-cell differentiation. *Nature*. **460**, 108–112 (2009).
526. R. R. Rao, Q. Li, K. Odunsi, P. A. Shrikant, The mTOR kinase determines effector versus memory CD8+ T cell fate by regulating the expression of transcription factors T-bet and Eomesodermin. *Immunity*. **32**, 67–78 (2010).
527. G. Cui *et al.*, IL-7-Induced Glycerol Transport and TAG Synthesis Promotes Memory CD8+ T Cell Longevity. *Cell*. **161**, 750–61 (2015).
528. D. D. Leipe, Y. I. Wolf, E. V Koonin, L. Aravind, Classification and evolution of P-loop GTPases and related ATPases. *J. Mol. Biol.* **317**, 41–72 (2002).

529. E. T. Spiliotis, Spatial effects - site-specific regulation of actin and microtubule organization by septin GTPases. *J. Cell Sci.* **131**, jcs207555 (2018).
530. C. Andrès, B. Agne, F. Kessler, The TOC complex: Preprotein gateway to the chloroplast. *Biochim. Biophys. Acta - Mol. Cell Res.* **1803**, 715–723 (2010).
531. A. Balasubramaniyam Sivanandam, Structural and Biochemical Analysis of GTPases of IMmunity-Associated Proteins (GIMAPs) and their Interaction Partners (2015).
532. T. Shpilka, H. Weidberg, S. Pietrokovski, Z. Elazar, Atg8: an autophagy-related ubiquitin-like protein family. *Genome Biol.* **12**, 226 (2011).
533. H. Weidberg *et al.*, LC3 and GATE-16 N termini mediate membrane fusion processes required for autophagosome biogenesis. *Dev. Cell*. **20**, 444–54 (2011).
534. H. Weidberg *et al.*, LC3 and GATE-16/GABARAP subfamilies are both essential yet act differently in autophagosome biogenesis. *EMBO J.* **29**, 1792–802 (2010).
535. T. N. Nguyen *et al.*, Atg8 family LC3/GABARAP proteins are crucial for autophagosome-lysosome fusion but not autophagosome formation during PINK1/Parkin mitophagy and starvation. *J. Cell Biol.* **215**, 857–874 (2016).
536. L. Pontano Vaites, J. A. Paulo, E. L. Huttlin, J. W. Harper, Systematic analysis of human cells lacking ATG8 proteins uncovers roles for GABARAPs and the CCZ1/MON1 regulator C18orf8/RMC1 in macro and selective autophagic flux. *Mol. Cell. Biol.* **38**, e00392-17 (2017).
537. V. V Rogov *et al.*, Structural and functional analysis of the GABARAP interaction motif (GIM). *EMBO Rep.* **18**, 1382–1396 (2017).
538. Å. B. Birgisdottir, T. Lamark, T. Johansen, The LIR motif - crucial for selective autophagy. *J. Cell Sci.* **126**, 3237–47 (2013).
539. J. Park *et al.*, Single-cell transcriptomics of the mouse kidney reveals potential cellular targets of kidney disease. *Science*. **360**, 758–763 (2018).
540. H. H. Pua, J. Guo, M. Komatsu, Y.-W. He, Autophagy is essential for mitochondrial clearance in mature T lymphocytes. *J. Immunol.* **182**, 4046–55 (2009).
541. Y. Z. Zhang, Novel fluorescent acidic organelle-selective dyes and mitochondrion-selective dyes that are well retained during cell fixation and permeabilization. *Mol. Biol. Cell*. **5**, 113a (1994).
542. D. P. Narendra *et al.*, PINK1 is selectively stabilized on impaired mitochondria to activate Parkin. *PLoS Biol.* **8**, e1000298 (2010).
543. K. Okatsu *et al.*, PINK1 autophosphorylation upon membrane potential dissipation is essential for Parkin recruitment to damaged mitochondria. *Nat. Commun.* **3**, 1016 (2012).
544. M. Lazarou *et al.*, The ubiquitin kinase PINK1 recruits autophagy receptors to induce mitophagy. *Nature*. **524**, 309–314 (2015).
545. J.-M. Heo, A. Ordureau, J. A. Paulo, J. Rinehart, J. W. Harper, The PINK1-PARKIN Mitochondrial Ubiquitylation Pathway Drives a Program of OPTN/NDP52 Recruitment and TBK1 Activation to Promote Mitophagy. *Mol. Cell*. **60**, 7–20 (2015).
546. R. L. Schweers *et al.*, NIX is required for programmed mitochondrial clearance during reticulocyte maturation. *Proc. Natl. Acad. Sci. U. S. A.* **104**, 19500–5 (2007).
547. M. C. Tal *et al.*, Absence of autophagy results in reactive oxygen species-dependent amplification of RLR signaling. *Proc. Natl. Acad. Sci. U. S. A.* **106**, 2770–5 (2009).
548. P. Mukhopadhyay *et al.*, Simultaneous detection of apoptosis and mitochondrial superoxide production in live cells by flow cytometry and confocal microscopy. *Nat. Protoc.* **2**, 2295–301 (2007).

549. N. Pengo *et al.*, Plasma cells require autophagy for sustainable immunoglobulin production. *Nat. Immunol.* **14**, 298–305 (2013).
550. C. Ponticelli, G. Moroni, Hydroxychloroquine in systemic lupus erythematosus (SLE). *Expert Opin. Drug Saf.* **16**, 411–419 (2017).
551. C. A. Homewood, D. C. Warhurst, W. Peters, V. C. Baggaley, Lysosomes, pH and the anti-malarial action of chloroquine. *Nature*. **235**, 50–2 (1972).
552. R. I. Fox, Mechanism of action of hydroxychloroquine as an antirheumatic drug. *Semin. Arthritis Rheum.* **23**, 82–91 (1993).
553. D. E. Furst, Pharmacokinetics of hydroxychloroquine and chloroquine during treatment of rheumatic diseases. *Lupus*. **5 Suppl 1**, S11-5 (1996).
554. S. Nielsen, Y. Yuzenkova, N. Zenkin, Mechanism of eukaryotic RNA polymerase III transcription termination. *Science*. **340**, 1577–80 (2013).
555. R. D. Mashal, J. Koontz, J. Sklar, Detection of mutations by cleavage of DNA heteroduplexes with bacteriophage resolvases. *Nat. Genet.* **9**, 177–183 (1995).
556. D. J. Klionsky *et al.*, Guidelines for the use and interpretation of assays for monitoring autophagy. *Autophagy*. **8**, 445–544 (2012).
557. P. Codogno, M. Mehrpour, T. Proikas-Cezanne, Canonical and non-canonical autophagy: variations on a common theme of self-eating? *Nat. Rev. Mol. Cell Biol.* **13**, 7–12 (2012).
558. L. M. Lindqvist, J. R. Hospital, E. H. Baehrecke, L. M. ; Lindqvist, A. K. ; Simon, Current questions and possible controversies in autophagy A K. Simon Repository Citation (2058), doi:10.1038/cddiscovery.2015.36.
559. O. Florey, N. Gammoh, S. E. Kim, X. Jiang, M. Overholtzer, V-ATPase and osmotic imbalances activate endolysosomal LC3 lipidation. *Autophagy*. **11**, 88–99 (2015).
560. G. Matsumoto, K. Wada, M. Okuno, M. Kurosawa, N. Nukina, Serine 403 Phosphorylation of p62/SQSTM1 Regulates Selective Autophagic Clearance of Ubiquitinated Proteins. *Mol. Cell*. **44**, 279–289 (2011).
561. U. Schneider, H.-U. Schwenk, G. Bornkamm, Characterization of EBV-genome negative “null” and “T” cell lines derived from children with acute lymphoblastic leukemia and leukemic transformed non-Hodgkin lymphoma. *Int. J. Cancer*. **19**, 621–626 (1977).
562. R. T. Abraham, A. Weiss, Jurkat T cells and development of the T-cell receptor signalling paradigm. *Nat. Rev. Immunol.* **4**, 301–308 (2004).
563. A. Weiss, R. L. Wiskocil, J. D. Stobo, The role of T3 surface molecules in the activation of human T cells: a two-stimulus requirement for IL 2 production reflects events occurring at a pre-translational level. *J. Immunol.* **133**, 123–8 (1984).
564. R. T. Abraham, A. Weiss, Jurkat T cells and development of the T-cell receptor signalling paradigm. *Nat. Rev. Immunol.* **4**, 301–308 (2004).
565. W. A. Nelson-Rees, D. W. Daniels, R. R. Flandermeyer, Cross-contamination of cells in culture. *Science*. **212**, 446–52 (1981).
566. E. Astoul, C. Edmunds, D. A. Cantrell, S. G. Ward, PI 3-K and T-cell activation: limitations of T-leukemic cell lines as signaling models. *Trends Immunol.* **22**, 490–6 (2001).
567. M. A. Keibler *et al.*, Metabolic requirements for cancer cell proliferation. *Cancer Metab.* **4**, 16 (2016).
568. M. Obinata, The immortalized cell lines with differentiation potentials: Their establishment and possible application. *Cancer Sci.* **98**, 275–283 (2007).

569. L. Gioia, A. Siddique, S. R. Head, D. R. Salomon, A. I. Su, A genome-wide survey of mutations in the Jurkat cell line. *BMC Genomics*. **19**, 334 (2018).
570. P. Hughes, D. Marshall, Y. Reid, H. Parkes, C. Gelber, The costs of using unauthenticated, over-passaged cell lines: How much more data do we need? *Biotechniques* (2007), , doi:10.2144/000112598.
571. A. I. Penzo-Méndez, Y.-J. Chen, J. Li, E. S. Witze, B. Z. Stanger, Spontaneous Cell Competition in Immortalized Mammalian Cell Lines. *PLoS One*. **10**, e0132437 (2015).
572. M. A. Nowak, F. Michor, Y. Iwasa, Genetic instability and clonal expansion. *J. Theor. Biol.* **241**, 26–32 (2006).
573. X. Wang *et al.*, Unbiased detection of off-target cleavage by CRISPR-Cas9 and TALENs using integrase-defective lentiviral vectors. *Nat. Biotechnol.* **33**, 175–178 (2015).
574. C. Kuscu, S. Arslan, R. Singh, J. Thorpe, M. Adli, Genome-wide analysis reveals characteristics of off-target sites bound by the Cas9 endonuclease. *Nat. Biotechnol.* **32**, 677–683 (2014).
575. X. Shan *et al.*, Deficiency of PTEN in Jurkat T cells causes constitutive localization of Itk to the plasma membrane and hyperresponsiveness to CD3 stimulation. *Mol. Cell. Biol.* **20**, 6945–57 (2000).
576. R. W. Freeburn *et al.*, Evidence That SHIP-1 Contributes to Phosphatidylinositol 3,4,5-Trisphosphate Metabolism in T Lymphocytes and Can Regulate Novel Phosphoinositide 3-Kinase Effectors. *J. Immunol.* **169**, 5441–5450 (2002).
577. A. Sakai, C. Thieblemont, A. Wellmann, E. S. Jaffe, M. Raffeld, PTEN gene alterations in lymphoid neoplasms. *Blood*. **92**, 3410–5 (1998).
578. C. C. Dibble, L. C. Cantley, Regulation of mTORC1 by PI3K signaling. *Trends Cell Biol.* **25**, 545–555 (2015).
579. A. Seki, S. Rutz, Optimized RNP transfection for highly efficient CRISPR/Cas9-mediated gene knockout in primary T cells. *J. Exp. Med.* **215**, 985–997 (2018).
580. D. Silverberg, D. Wexler, M. Blum, D. Schwartz, A. Iaina, The association between congestive heart failure and chronic renal disease. *Curr. Opin. Nephrol. Hypertens.* **13**, 163–70 (2004).
581. C. Tuegel, N. Bansal, Heart failure in patients with kidney disease. *Heart*. **103**, 1848–1853 (2017).
582. K. Damman, J. M. Testani, The kidney in heart failure: an update. *Eur. Heart J.* **36**, 1437–1444 (2015).
583. A. Ahmed, R. C. Campbell, Epidemiology of chronic kidney disease in heart failure. *Heart Fail. Clin.* **4**, 387–99 (2008).
584. G. Tsagalis, Renal anemia: a nephrologist's view. *Hippokratia*. **15**, 39–43 (2011).
585. P. R. Sarma, *Red Cell Indices* (Butterworths, 1990; http://www.ncbi.nlm.nih.gov/pubmed/21250103).
586. F. H. Wians, J. E. Urban, J. H. Keffer, S. H. Kroft, "Discriminating Between Iron Deficiency Anemia and Anemia of Chronic Disease Using Traditional Indices of Iron Status vs Transferrin Receptor Concentration" (2001), (available at https://pdfs.semanticscholar.org/5782/8d552fcd177061afe45771dad7068276ea33.pdf).
587. J. David Bessman, P. Ridgway Gilmer, F. H. Gardner, "Improved Classification of Anemias by MCV and RDW," (available at https://academic.oup.com/ajcp/article-abstract/80/3/322/1803902).
588. J. L. Meredith, N. S. Rosenthal, "CE U P D A T E-A N E M I A S II," (available at

https://academic.oup.com/labmed/article-abstract/30/8/538/2504280).
589. K. Amann, C. S. Haas, What you should know about the work-up of a renal biopsy. *Nephrol. Dial. Transplant.* **21**, 1157–1161 (2006).
590. I. Shore, J. Moss, Electron microscopy in diagnostic renal pathology. *Curr. Diagnostic Pathol.* **8**, 207–215 (2002).
591. V. Brocklebank, K. M. Wood, D. Kavanagh, Thrombotic Microangiopathy and the Kidney. *Clin. J. Am. Soc. Nephrol.* **13**, 300–317 (2018).
592. R. Duran-Struuck, R. C. Dysko, Principles of bone marrow transplantation (BMT): providing optimal veterinary and husbandry care to irradiated mice in BMT studies. *J. Am. Assoc. Lab. Anim. Sci.* **48**, 11–22 (2009).
593. A. Safwat, O. S. Nielsen, H. abd el-Bakky, J. Overgaard, Renal damage after total body irradiation in a mouse model for bone marrow transplantation: effect of radiation dose rate. *Radiother. Oncol.* **34**, 203–9 (1995).
594. E. Korpela, S. K. Liu, Endothelial perturbations and therapeutic strategies in normal tissue radiation damage. *Radiat. Oncol.* **9**, 266 (2014).
595. N. Shiba, H. Shimokawa, Chronic kidney disease and heart failure—Bidirectional close link and common therapeutic goal. *J. Cardiol.* **57**, 8–17 (2011).
596. N. Baum, C. C. Dichoso, C. E. Carlton, Blood urea nitrogen and serum creatinine. *Urology*. **5**, 583–588 (1975).
597. C. Lacombe *et al.*, Erythropoietin: sites of synthesis and regulation of secretion. *Am. J. Kidney Dis.* **18**, 14–9 (1991).
598. A. J. Madu, M. D. Ughasoro, Anaemia of Chronic Disease: An In-Depth Review. *Med. Princ. Pract.* **26**, 1–9 (2017).
599. M. D. Cohen, E. Keystone, Rituximab for Rheumatoid Arthritis. *Rheumatol. Ther.* **2**, 99–111 (2015).
600. X. Montalban *et al.*, Ocrelizumab versus Placebo in Primary Progressive Multiple Sclerosis. *N. Engl. J. Med.* **376**, 209–220 (2017).
601. T. Schioppo, F. Ingegnoli, Current perspective on rituximab in rheumatic diseases. *Drug Des. Devel. Ther.* **11**, 2891–2904 (2017).
602. A. P. McMahon *et al.*, GUDMAP: The Genitourinary Developmental Molecular Anatomy Project. *J. Am. Soc. Nephrol.* **19**, 667–671 (2008).
603. S. D. Harding *et al.*, The GUDMAP database - an online resource for genitourinary research. *Development*. **138**, 2845–2853 (2011).
604. R. Müller *et al.*, ANGIOGENES: knowledge database for protein-coding and noncoding RNA genes in endothelial cells. *Sci. Rep.* **6**, 32475 (2016).
605. Y. Du *et al.*, Lung Gene Expression Analysis (LGEA): an integrative web portal for comprehensive gene expression data analysis in lung development. *Thorax*. **72**, 481–484 (2017).
606. Y. Du, M. Guo, J. A. Whitsett, Y. Xu, 'LungGENS': a web-based tool for mapping single-cell gene expression in the developing lung: Figure 1. *Thorax*. **70**, 1092–1094 (2015).
607. T. S. P. Heng *et al.*, The Immunological Genome Project: networks of gene expression in immune cells. *Nat. Immunol.* **9**, 1091–1094 (2008).
608. R. Petryszak *et al.*, Expression Atlas update—an integrated database of gene and protein expression in humans, animals and plants. *Nucleic Acids Res.* **44**, D746–D752 (2016).
609. M. Bhasin *et al.*, Bioinformatic identification and characterization of human endothelial cell-restricted genes. *BMC Genomics*. **11**, 342 (2010).

610. C. Michiels, Endothelial cell functions. *J. Cell. Physiol.* **196**, 430–443 (2003).
611. A. G. Gravina *et al.*, Vascular Endothelial Dysfunction in Inflammatory Bowel Diseases: Pharmacological and Nonpharmacological Targets. *Oxid. Med. Cell. Longev.* **2018**, 2568569 (2018).
612. R. Bordy *et al.*, Microvascular endothelial dysfunction in rheumatoid arthritis. *Nat. Rev. Rheumatol.* **14**, 404–420 (2018).
613. J. B. Su, Vascular endothelial dysfunction and pharmacological treatment. *World J. Cardiol.* **7**, 719–41 (2015).
614. J. Mestas, C. C. W. Hughes, Of mice and not men: differences between mouse and human immunology. *J. Immunol.* **172**, 2731–8 (2004).
615. R. L. Perlman, Mouse models of human disease: An evolutionary perspective. *Evol. Med. public Heal.* **2016**, 170–6 (2016).
616. C. Agostinis *et al.*, In vivo distribution of 2 glycoprotein I under various pathophysiologic conditions. *Blood*. **118**, 4231–4238 (2011).
617. F. Fischetti *et al.*, Thrombus formation induced by antibodies to 2-glycoprotein I is complement dependent and requires a priming factor. *Blood*. **106**, 2340–2346 (2005).
618. B. Giannakopoulos, S. A. Krilis, The Pathogenesis of the Antiphospholipid Syndrome. *N. Engl. J. Med.* **368**, 1033–1044 (2013).
619. W. C. Skarnes *et al.*, A conditional knockout resource for the genome-wide study of mouse gene function. *Nature*. **474**, 337–42 (2011).
620. Y. Pan *et al.*, Insertion of a knockout-first cassette in Ampd1 gene leads to neonatal death by disruption of neighboring genes expression. *Sci. Rep.* **6**, 35970 (2016).
621. J. Chen *et al.*, Spinster homolog 2 (spns2) deficiency causes early onset progressive hearing loss. *PLoS Genet.* **10**, e1004688 (2014).
622. T. V Novoselova *et al.*, 230:1 Mrap2 deficiency in obesity. *J. Endocrinol.* **230**, 13–26 (2016).
623. T. L. Nguyen *et al.*, Functional characterization of the lysosomal membrane protein TMEM192 in mice. *Oncotarget*. **8**, 43635–43652 (2017).
624. R. M. Shawky, Reduced penetrance in human inherited disease. *Egypt. J. Med. Hum. Genet.* **15**, 103–111 (2014).
625. S. E. Castel *et al.*, Modified penetrance of coding variants by cis-regulatory variation contributes to disease risk. *Nat. Genet.* **50**, 1327–1334 (2018).
626. D. N. Cooper, M. Krawczak, C. Polychronakos, C. Tyler-Smith, H. Kehrer-Sawatzki, Where genotype is not predictive of phenotype: towards an understanding of the molecular basis of reduced penetrance in human inherited disease. *Hum. Genet.* **132**, 1077–130 (2013).
627. V. Vu *et al.*, Natural Variation in Gene Expression Modulates the Severity of Mutant Phenotypes. *Cell*. **162**, 391–402 (2015).
628. O. Breuer, A. Schultz, Side effects of medications used to treat childhood interstitial lung disease. *Paediatr. Respir. Rev.* (2018), doi:10.1016/J.PRRV.2018.03.002.
629. L.-H. Thai *et al.*, Long-term complications of splenectomy in adult immune thrombocytopenia. *Medicine (Baltimore).* **95**, e5098 (2016).
630. L. D. Notarangelo, Immunodeficiency and immune dysregulation associated with proximal defects of T cell receptor signaling. *Curr. Opin. Immunol.* **31**, 97–101 (2014).
631. S. S. De Ravin *et al.*, Hypomorphic Rag mutations can cause destructive midline granulomatous disease. *Blood*. **116**, 1263–71 (2010).
632. C. A. Hunter, S. A. Jones, IL-6 as a keystone cytokine in health and disease. *Nat.*

Immunol. **16**, 448–457 (2015).
633. Z. E. Sauna, C. Kimchi-Sarfaty, in *eLS* (John Wiley & Sons, Ltd, Chichester, UK, 2013; http://doi.wiley.com/10.1002/9780470015902.a0025173).
634. H. Wang *et al.*, GABARAPs regulate PI4P-dependent autophagosome:lysosome fusion. *Proc. Natl. Acad. Sci. U. S. A.* **112**, 7015–20 (2015).
635. T. Ciucci, R. Bosselut, Gimap and T cells: a matter of life or death. *Eur. J. Immunol.* **44**, 348–51 (2014).
636. A.-C. Vion *et al.*, Autophagy is required for endothelial cell alignment and atheroprotection under physiological blood flow. *Proc. Natl. Acad. Sci. U. S. A.* **114**, E8675–E8684 (2017).
637. F. Jiang, Autophagy in vascular endothelial cells. *Clin. Exp. Pharmacol. Physiol.* **43**, 1021–1028 (2016).
638. S. D. Dowling, F. Macian, Autophagy and T cell metabolism. *Cancer Lett.* (2018), doi:10.1016/j.canlet.2018.01.033.
639. E. Jacquin, L. Apetoh, Cell-Intrinsic Roles for Autophagy in Modulating CD4 T Cell Functions. *Front. Immunol.* **9**, 1023 (2018).
640. M. Lochner, L. Berod, T. Sparwasser, Fatty acid metabolism in the regulation of T cell function. *Trends Immunol.* **36**, 81–91 (2015).
641. C. Y. Kim, X. Zhang, W. H. Witola, Small GTPase Immunity-Associated Proteins Mediate Resistance to Toxoplasma gondii Infection in Lewis Rat. *Infect. Immun.* **86** (2018), doi:10.1128/IAI.00582-17.
642. M. Sasai *et al.*, Essential role for GABARAP autophagy proteins in interferon-inducible GTPase-mediated host defense. *Nat. Immunol.* (2017), doi:10.1038/ni.3767.
643. I. Rusinova *et al.*, Interferome v2.0: an updated database of annotated interferon-regulated genes. *Nucleic Acids Res.* **41**, D1040-6 (2013).
644. T. Kueck, E. Cassella, J. Holler, B. Kim, P. D. Bieniasz, The aryl hydrocarbon receptor and interferon gamma generate antiviral states via transcriptional repression. *Elife*. **7** (2018), doi:10.7554/eLife.38867.
645. J. Pu, T. Keren-Kaplan, J. S. Bonifacino, A Ragulator-BORC interaction controls lysosome positioning in response to amino acid availability. *J. Cell Biol.* **216**, 4183–4197 (2017).
646. P. A. Filipek *et al.*, LAMTOR/Ragulator is a negative regulator of Arl8b- and BORC-dependent late endosomal positioning. *J. Cell Biol.* **216**, 4199–4215 (2017).
647. G. F. Vogel *et al.*, Ultrastructural Morphometry Points to a New Role for LAMTOR2 in Regulating the Endo/Lysosomal System. *Traffic*. **16**, 617–634 (2015).
648. C.-S. Zhang *et al.*, The Lysosomal v-ATPase-Ragulator Complex Is a Common Activator for AMPK and mTORC1, Acting as a Switch between Catabolism and Anabolism. *Cell Metab.* **20**, 526–540 (2014).
649. L. Bar-Peled, L. D. Schweitzer, R. Zoncu, D. M. Sabatini, Ragulator is a GEF for the rag GTPases that signal amino acid levels to mTORC1. *Cell*. **150**, 1196–208 (2012).
650. L. Galluzzi, J. M. Bravo-San Pedro, B. Levine, D. R. Green, G. Kroemer, Pharmacological modulation of autophagy: therapeutic potential and persisting obstacles. *Nat. Rev. Drug Discov.* **16**, 487–511 (2017).
651. O. Zharkova *et al.*, Pathways leading to an immunological disease: systemic lupus erythematosus. *Rheumatology*. **56**, i55–i66 (2017).
652. J. G. Doench *et al.*, Rational design of highly active sgRNAs for CRISPR-Cas9-mediated gene inactivation. *Nat. Biotechnol.* **32**, 1262–7 (2014).

653. H. Wang *et al.*, One-step generation of mice carrying mutations in multiple genes by CRISPR/Cas-mediated genome engineering. *Cell*. **153**, 910–8 (2013).
654. T. Wang, J. J. Wei, D. M. Sabatini, E. S. Lander, Genetic screens in human cells using the CRISPR-Cas9 system. *Science*. **343**, 80–4 (2014).

Appendix

Table A.1 Homozygous candidate variants in patient 1294.

Gene		Mutation				Allele Frequency			Severity Prediction					Genotypes					
Gene	Chr	Pos	Ref	Alt	Type	1000	ExAC	GnomAD	Polyphen	Sift	Mtaster	Fathmm	CADD	P	F	M	S	B	YB
PLXNA4	7	131878934	C	A	Mis	0.00	1.52E-05	0.00	PoD	D	DC	T	34	A/A	C/A	C/A	C/C	C/A	C/C
DNMT3B	20	31387129	C	T	Mis	0.00	0.00	0.00	PrD	D	DC	D	34	T/T	C/T	C/T	C/T	C/C	C/T
TULP4	6	158927641	C	T	Mis	0.00	4.32E-04	2.19E-04	PrD	D	DC	D	33	T/T	C/T	C/T	T/T	C/T	C/C
TMEM232	5	109976595	C	T	Mis	0.00	0.00	7.13E-06	PoD	D	DC		32	T/T	C/T	C/T	C/T	C/T	C/C
ALDH3A1	17	19641649	G	A	Mis	0.00	9.65E-05	4.07E-06	PoD	D	DC	D	26.7	A/A	G/A	G/A	A/A	G/A	G/A
OTP	5	76926541	G	A	Syn	0.00	0.00	0.00					17.77	A/A	G/A	G/A	G/A	G/A	G/G
GNL2	1	38048467	T	C	Mis	0.00	0.00	0.00			DC		16.03	C/C	T/C	T/C	T/T	T/C	C/C
ASB16	17	42248374	G	A	Mis	0.00	0.00	0.00	B	T	DC	T	15.76	A/A	G/A	G/A	A/A	G/A	G/A
ASAP3	1	23762476	C	T	Syn	0.00	0.00	8.12E-06					15.64	T/T	C/T	C/T	C/C	C/T	T/T
NKAIN2	6	125112527	A	G	Mis	0.00	0.00	0.00	B	T	DC	T	14.83	G/G	A/G	A/G	A/A	A/G	A/A
BFSP1	20	17489549	C	T	Syn	0.00	0.00	0.00					14.76	T/T	C/T	C/T	C/T	C/C	C/C
ANK2	4	114239791	A	C	Other	0.00	3.04E-04	8.30E-05					14.58	C/C	A/C	A/C	A/C	A/A	A/A
OTUD7B/ MTMR11	1	149907427	C	T	Other	0.00	3.31E-04	2.01E-04					13.89	T/T	C/T	C/T	C/T	C/T	T/T
RALGAPB	20	37146253	C	T	Mis	0.00	0.00	0.00	B	T	DC		13.43	T/T	C/T	C/T	C/T	C/C	C/T
YTHDF2	1	29069671	G	C	Mis	0.00	0.00	0.00E+00	B	T	DC	T	10.5	C/C	G/C	G/C	G/G	G/C	C/C
ATG12	5	115177324	C	T	Mis	0.00	0.00	4.06E-06	B	T	P		8.727	T/T	C/T	C/T	C/T	C/T	C/T
RGMB	5	98115266	T	G	Other	0.00	0.00	0.00					7.061	G/G	T/G	T/G	T/G	T/G	T/T
ABHD12	20	25304076	A	T	Other	0.00	9.65E-05	1.22E-05					7.013	T/T	A/T	A/T	A/T	A/A	A/T
UTRN	6	144750684	T	C	Other	0.00	1.52E-05	4.43E-06					6.284	C/C	T/C	T/C	T/C	T/C	T/T
CMYA5	5	79058857	C	T	Other	0.00	4.34E-04	2.37E-04					5.302	T/T	C/T	C/T	C/T	C/T	C/C
LYZL6	17	34263709	G	A	Other	0.00	1.52E-05	4.16E-06					3.017	A/A	G/A	G/A	A/A	G/A	G/A

Table A.1 Homozygous candidate variants in patient 1294.

Gene		Mutation				Allele Frequency			Severity Prediction					Genotypes					
Gene	Chr	Pos	Ref	Alt	Type	1000	ExAC	GnomAD	Polyphen	Sift	Mtaster	Fathmm	CADD	P	F	M	S	B	YB
CACNB1	17	37341122	G	A	Ext. Sp.	0.00	1.08E-04	1.02E-04					2.024	A/A	G/A	G/A	A/A	G/A	G/A
ANKRD50	4	125593707	A	C	Other	0.00	8.27E-04	1.18E-04					1.99	C/C	A/C	A/C	A/C	A/A	A/A
SLC18B1	6	133093243	A	G	Other	0.00	2.44E-04	4.03E-05					0.682	G/G	A/G	A/G	A/A	A/G	A/A
HSPG2	1	22203107	G	A	Syn	0.00	1.82E-04	4.87E-05					0.561	A/A	G/A	G/A	G/G	G/A	A/A
MPRIP	17	17069408	C	T	Syn	0.00	1.47E-04	1.45E-05					0.052	T/T	C/T	C/T	T/T	C/T	C/T
CDH9	5	26881698	T	C	Syn	0.00	0.00	0.00					0.006	C/C	T/C	T/C	T/C	T/C	T/C

Chr= Chromosome; Pos= Position; Ref= Genomic reference nucleotide; Alt= Altered nucleotide

Mut. Type (Mutation type): Mis= Missense; Syn= Synonymous; Ext. Sp.= Extended splice site

1000= 1000 Genome database

Polyphen: PoD= Possibly Damaging; PrD= Probably damaging; B=Benign

Sift: D= Damaging; T= Tolerated

Mtaster (Mutation Taster): DC= Disease causing; P= Polymorphism

Fathmm: D= Damaging; T= Tolerated

Genotypes: P= Patient; F= Father; M= Mother; S= Sister; B= Brother; YB= Younger brother

Table A.2 Karyotyping of patient 1294[1]				
Cell #	**Chr #**	**Description**	**Analysis**	**Notes**
1	44	44,XY,-5,del(9),del(12)	SKY	
2	46	46,XY	SKY	
3	46	46,XY	SKY	
4	46	46,XY	SKY	
5	46	46,XY	SKY	
6	46	46,XY	SKY	
7	47	47,XY,+del(1)	SKY	Entire p arm
8	46	46,XY,-1,del(1p)	SKY	Entire p arm
9	46	46,XY	SKY	
10	46	46,XY	SKY	
11	46	46,XY,-1,del(1p)	SKY	Partial p arm
12	46	46,XY	SKY	
13	46	46,XY	SKY	
14	49	49,XY,+1p-,+1q-,del(4),+der(4)t(4;14),del(16)	SKY	
15	46	46,XY	SKY	
16	46	46,XY,del(1),+X	SKY	Entire p arm
17	46	46,XY	SKY	
18	46	46,XY	SKY	
19	46	46XY	SKY	
20	46	46,XY	SKY	
21	46	46,XY	SKY	
22	46	46,XY,der(1),del(13)	Gband	Band difference p arm
23	46	46,XY	Gband	
24	47	47,XY,+1,cen(9),del(9p),+t(15;?16),-16	Gband	
25	46	46,XY	Gband	
26	46	46,XY,cen(1)	Gband	Fragile
27	46	46,XY	Gband	
28	47	47,+21	Gband	
29	46	46,XY	Gband	
30	46	46,XY	Gband	
31	46	46,XY	Gband	16 stretched fragile
32	46	46,XY	Gband	
33	46	46,XY	Gband	
34	46	46,XY	Gband	
35	46	46,XY	Gband	

[1]Each line represents analysis done on an individual metaphase-arrested cell. Twenty-one were analyzed with SKY analysis and fourteen with G-banding. Chr=chromosome

Table A.3 Homozygous variants in patient 1414.

Gene		Mutation				Allele Frequency			Severity Prediction					Genotypes			
Gene	**Chr**	**Pos**	**Ref**	**Alt**	**Type**	**1000**	**ExAC**	**GnomAD**	**Polyphen**	**Sift**	**Mtaster**	**Fathmm**	**CADD**	**1414**	**1415**	**1416**	**1417**
GRM2	3	185155301	C	T	Mis	1.00E-03	1.16E-04	1.63E-05	PrD	D	DC	D	34	T/T	C/T	C/T	C/T
AK7	14	96864440	C	T	Mis	0.00	4.50E-05	1.63E-05	PrD	D	DC	T	34	T/T	C/T	C/T	C/T
KCNK10	14	88652306	C	T	Mis	0.00	6.06E-05	8.13E-06	PrD	D	DC	D	33	T/T	C/T	C/T	C/T
SCN11A	3	38936100	G	A	Mis	0.00	1.73E-04	6.50E-05	PoD	D	DC	D	31	A/A	G/A	G/A	G/A
ENTPD3	3	40456270	G	A	Mis	0.00	1.50E-05	8.13E-06	PrD	D	DC	T	28.2	A/A	G/A	G/A	G/A
TMED7-TICAM2, TICAM2	5	114916458	T	G	Mis	0.00	0.00	0.00	PrD	D	DC	T	28.2	G/G	T/G	T/G	T/G
MCF2L2	3	183027551	C	T	Mis	0.00	1.05E-04	4.47E-05	PrD	D	DC	T	26.2	T/T	C/T	C/T	C/T
ENAM	4	71503556	G	C	Mis	1.00E-03	9.61E-05	3.66E-05	PrD	D	P	T	23.7	C/C	G/C	G/C	G/C
PPP1R9A	7	94827760	A	C	Mis	0.00	0.00	0.00	PrD	D	DC	T	23.5	C/C	A/C	A/C	A/A
PLEKHH2	2	43934658	C	T	Mis	0.00	3.63E-04	4.88E-05	PoD	T	DC	T	22.7	T/T	C/T	C/T	C/T
EOMES	3	27758892	C	T	Mis	0.00	0.00E+00	0.00E+00	B	D	DC	D	20.5	T/T	C/T	C/T	C/T
PPP2R5C	14	102391485	A	G	Mis	0.00	3.30E-04	2.91E-04	B	T	DC	T	19.95	G/G	A/G	A/G	A/G
RASA1	5	86565087	T	G	Syn	0.00	0.00	0.00					19.19	G/G	T/G	T/G	T/T
CXCL11	4	76956486	A	G	Mis	0.00	0.00E+00	0.00	PoD	T	DC	T	17.77	G/G	A/G	A/G	A/G
PLEKHH2	2	43934602	C	G	Mis	0.00	3.63E-04	4.87E-05	B	T	DC	T	16.48	G/G	C/G	C/G	C/G
ZAN	7	100391555	G	A	Mis	0.00	2.05E-04	4.48E-05			DC	D	15.12	A/A	G/A	G/A	G/G
BAIAP2L1	7	97933582	C	T	Mis	0.00	1.28E-04	7.75E-05	B	T	P	T	13.48	T/T	C/T	C/T	C/C
C20orf129	20	3299061	G	A	Other	0.00	0.00	0.00					13.17	A/A	G/A	G/A	G/A
GRM2	3	51747141	G	A	Mis	8.00E-04	2.96E-04	2.44E-05	B	T	P	D	11.26	A/A	G/A	G/A	G/A
TRIM3	11	6478976	C	T	Syn	0.00	0.00	0.00					9.595	T/T	C/T	C/T	C/T

Table A.3 Homozygous variants in patient 1414.

Gene		Mutation				Allele Frequency			Severity Prediction					Genotypes			
Gene	**Chr**	**Pos**	**Ref**	**Alt**	**Type**	**1000**	**ExAC**	**GnomAD**	**Polyphen**	**Sift**	**Mtaster**	**Fathmm**	**CADD**	**1414**	**1415**	**1416**	**1417**
DCLK3	3	36778676	T	A	Other	0.00	2.21E-04	6.23E-05					9.347	A/A	T/A	T/A	T/A
SGO1	3	20202738	A	C	Other	0.00	0.00	0.00E+00					8.563	C/C	A/C	A/C	A/C
HEATR3/ AC007610.1	16	50100256	C	G	Other	0.00	6.76E-04	4.24E-04					7.513	G/G	C/G	C/G	C/G
ZCCHC2	18	60242410	C	T	Syn	0.00	3.00E-05	2.03E-05					7.138	T/T	C/T	C/T	C/T
KLHL6	3	183245837	C	T	Other	0.00	0.00	0.00					6.815	T/T	C/T	C/T	C/T
NES	1	156639075	G	A	Other	0.00	0.00	1.18E-05					5.591	A/A	G/A	G/A	G/A
ATP8B2	1	154304072	G	A	Other	0.00	9.61E-05	2.03E-05					2.226	A/A	G/A	G/A	G/A
PPP4R3CP	X	27480851	G	A	Other	0.00	2.16E-04	4.90E-05					1.679	A/A	G/G	G/A	G/A
ADAMTS3	4	73414336	G	A	Syn	1.00E-03	4.84E-04	1.34E-04					0.998	A/A	G/A	G/A	G/A
ACTL6B	7	100244734	C	T	Other	0.00	1.06E-04	6.11E-05					0.744	T/T	C/T	C/T	C/C
FAM122C	X	133981452	A	C	Mis	0.00	0.00	0.00E+00	B	D	P		0.707	C/C	A/A	A/C	A/C
ARHGEF2	1	155931881	G	C	Other	0.00	0.00	0.00					0.578	C/C	G/C	G/C	G/C
AHNAK2	14	105410967	A	G	Syn	0.00	1.02E-04	8.17E-06					0.056	G/G	A/G	A/G	A/G
OR6K6	1	158724606	A	G	Mis	0.00	0.00	4.22E-06	B	T	P	T	0.001	G/G	A/G	A/G	A/G
SLAMF7	1	160721230	C	T	Mis	0.00	3.00E-05	2.03E-05	B	D	P	T	0.001	T/T	C/T	C/T	C/T
SLC26A6/ TMEM89	3	48658877	AAAG	A	Other	0.00	0.00	0.00						A/A	AAAG/A	AAAG/A	AAAG/A

Chr= Chromosome; Pos= Position; Ref= Genomic reference nucleotide; Alt= Altered nucleotide

Mut. Type (Mutation type): Mis= Missense; Syn= Synonymous; Ext. Sp.= Extended splice site

1000= 1000 Genome database

Polyphen: PoD= Possibly Damaging; PrD= Probably damaging; B=Benign

Sift: D= Damaging; T= Tolerated; Mtaster (Mutation Taster): DC= Disease causing; P= Polymorphism; Fathmm: D= Damaging; T= Tolerated

Table A.4 Tracking of Indels by Decomposition (TIDE) analysis of GIMAP5 CRISPR lines	
Clone ID	**Identified Indel**
4_D7	+1/+8
7_E4	+1
7_E10	+1/+8
7_E12	+1
10_B7	+2/+4
16_F10	-5/+5
25_F10	-1/+4
1_E21	+1/+7

Table A.5 Candidate variants in patient 1467																	
Homozygous variants																	
Gene		Mutation				Allele Frequency			Severity Prediction					Genotypes				
Gene	Chr	Pos	Ref	Alt	Type	1000	ExAC	GnomAD	Polyphen	Sift	Mtaster	Fathmm	CADD	1467	1468	1469	1470	1471
C4orf45	4	159894373	T	A	Mis	0.00	0.00	0.00	PrD	D	DC	T	28.5	A/A	T/A	T/A	T/T	T/A
CHIA	1	111854818	C	T	Mis	0.00	0.00	0.00	PoD	D	DC	T	27.2	T/T	C/T	C/T	C/C	C/C
AGO1	1	36354076	G	A	Mis	0.00	0.00	0.00	PoD	T	DC	T	26.3	A/A	G/A	G/A	G/A	G/A
FLYWCH1	16	2988407	C	G	Mis	1.00E-03	0.00	1.65E-04	PrD	D	DC		25.4	G/G	C/G	C/G	C/G	C/C
HSPG2	1	22169930	A	C	Mis	0.00	2.07E-04	2.49E-05	PrD	T	DC	T	23.3	C/C	A/C	A/C	A/C	A/C
GIMAP6	7	150325228	C	A	Mis	0.00	0.00	0.00	PoD	D	P	T	22.9	A/A	C/A	C/A	C/A	C/A
IL6R	1	154437754	C	T	Syn	0.00	0.00	0.00					16	T/T	C/T	C/T	C/C	C/C
MAB21L3	1	116670172	C	T	Syn	0.00	0.00	0.00					11.94	T/T	C/T	C/T	C/C	C/C
PITX2, PANCR	4	111541221	C	T	other	1.00E-03	0.00	1.06E-04					11.92	T/T	C/T	C/T	C/C	C/T
PHACTR4	1	28816307	T	G	other	0.00	0.00	0.00		D	P		11.76	G/G	T/G	T/G	T/G	T/G
PKLR	1	155263349	T	A	Syn	0.00	0.00	0.00					8.045	A/A	T/A	T/A	T/T	T/T
EPHA1	7	143098746	C	A	other	0.00	7.89E-05	8.86E-06					6.068	A/A	C/A	C/A	C/A	C/A
RUSC1, FDPS, RUSC1-AS1	1	155294983	G	T	other	1.00E-03	7.07E-04	4.92E-04					5.536	T/T	G/T	G/T	G/G	G/G
NOTCH2	1	120491594	T	C	other	0.00	0.00	0.00					5.42	C/C	T/C	T/C	T/T	T/T
RBM39	20	34317335	T	A	other	0.00	0.00	2.16E-04					2.068	A/A	T/A	T/A	T/A	T/T

Table A.5 Candidate variants in patient 1467																	
PHTF1	1	114252924	G	T	Syn	1.00 E-03	0.00	5.28E-05				2.041	T/T	G/T	G/T	G/G	G/G
EPB41L1	20	34794968	G	A	other	0.00	0.00	0.00	B	T	P	1.753	A/A	G/A	G/A	G/A	G/G
Gene		**Mutation**				**Allele Frequency**			**Severity Prediction**				**Genotypes**				
Gene	**Chr**	**Pos**	**Ref**	**Alt**	**Type**	**1000**	**ExAC**	**GnomAD**	**Polyphen**	**Sift**	**Mtaster**	**Fathmm**	**CADD**	**1467**	**1468**	**1469**	**1470**	**1471**
Compound heterozygous variants																	
FOXRED2, FAM118B, SRPRA	11	126134446	A	G	Oth	0.00	0.00	0.00					9.252	A/G	A/A	A/A	A/A	A/A
FOXRED1, FAM118B, SRPRA	11	126134447	A	T	Oth	0.00	0.00	0.00					6.547	A/T	A/A	A/A	A/A	A/A
LAMA3	18	21390514	G	T	Oth	0.00	8.66E-05	2.85E-05					1.316	G/T	G/G	G/T	G/T	G/G
LAMA3	18	21464858	C	T	Oth	0.00	0.00	8.58E-05					9.162	C/T	C/T	C/C	C/C	C/T
***De novo* variants**																	
Gene		**Mutation**				**Allele Frequency**			**Severity Prediction**				**Genotypes**				
Gene	**Chr**	**Pos**	**Ref**	**Alt**	**Type**	**1000**	**ExAC**	**GnomAD**	**Polyphen**	**Sift**	**Mtaster**	**Fathmm**	**CADD**	**1467**	**1468**	**1469**	**1470**	**1471**
KMT2C	7	151970752	T	A	Oth	0.00	8.50E-04	0.00					3.025	T/A	T/T	T/T	T/T	T/T
SCARNA9, CEP295, Y_RNA	11	93454837	T	C	Oth	0.00	0.00	0.00						T/C	T/T	T/T	T/T	T/T
FOXRED1, FAM118B, SRPRA	11	126134446	A	G	Oth	0.00	0.00	0.00					9.252	A/G	A/A	A/A	A/A	A/A

Table A.5 Candidate variants in patient 1467															
FOXRED1, FAM118B, SRPRA	11	126134447	A	T	Oth	0.00	0.00	0.00		6.527	A/T	A/A	A/A	A/A	A/A
CACNA1G	17	48646346	A	AG TGT GT GT GT	Oth	0.00	0.00	0.00			A/A GTG TGT GTG T	A/A	A/A	A/A	A/A
TTC3	21	38498341	G	GTT TT	Oth	0.00	0.00	0.00			G/G TTTT	G/G	G/G	G/G	G/G
MED15	22	20920816	G	A	Syn	0.00	0.00	0.00		5.821	G/A	G/G	G/G	G/G	G/G

Chr= Chromosome; Pos= Position; Ref= Genomic reference nucleotide; Alt= Altered nucleotide

Mut. Type (Mutation type): Mis= Missense; Syn= Synonymous; Oth=Other

1000= 1000 Genome database

Polyphen: PoD= Possibly Damaging; PrD= Probably damaging; B=Benign

Sift: D= Damaging; T= Tolerated

Mtaster (Mutation Taster): DC= Disease causing; P= Polymorphism

Fathmm: D= Damaging; T= Tolerated

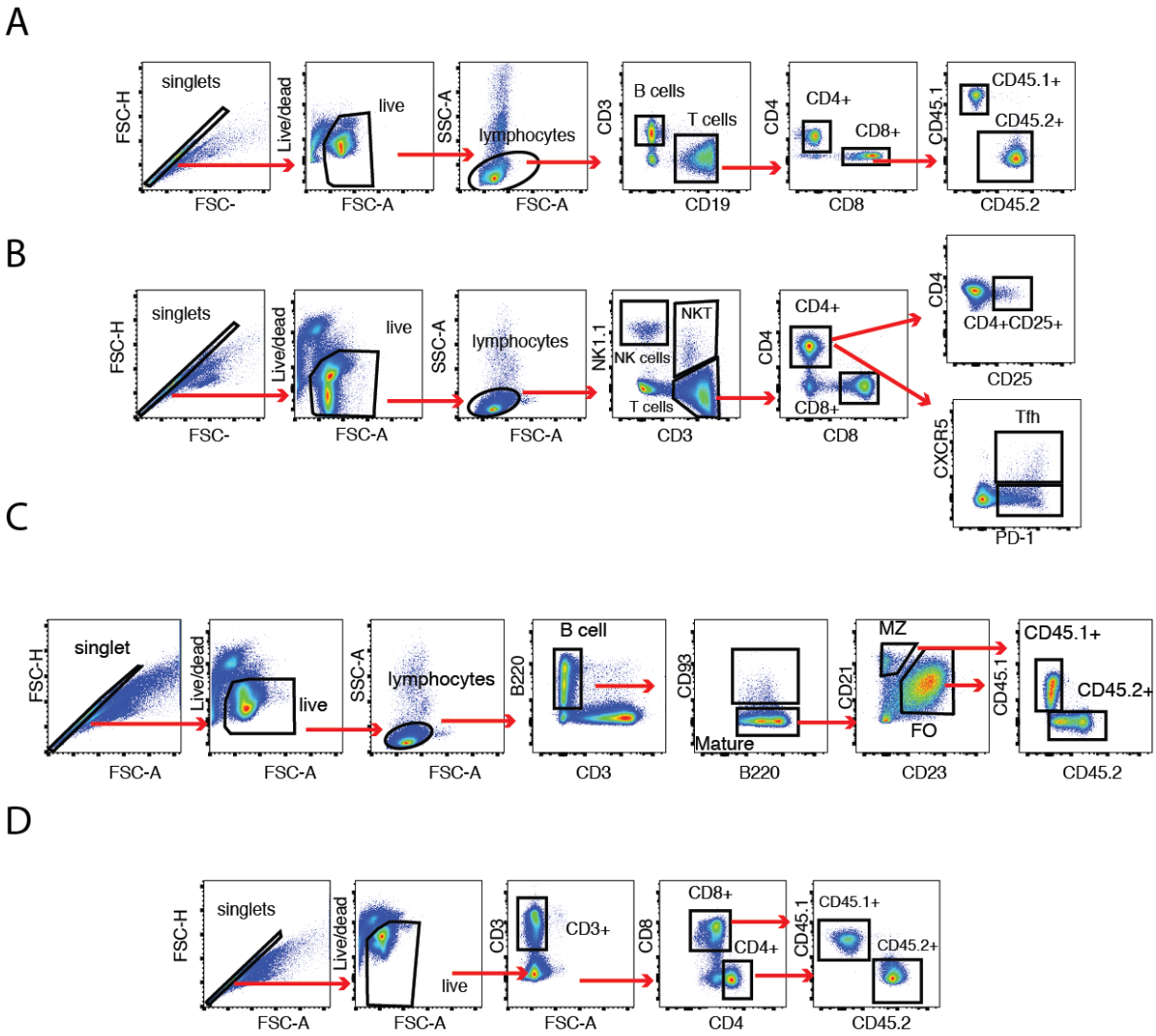


Fig. A.1 Gating strategies for Chapter 4 flow cytometry. A) Gating strategy for Fig. 4.8B,C. **B**) Gating strategy for Fig. 4.8.E and Fig. 4.9A-J **C)** Gating strategy for Fig. 4.8F **D**) Gating strategy for Fig. 4.9K,L. FSC-A= forward scatter-area; FSC-H= forward scatter-height; SSC-A= side scatter-area; MZ= marginal zone B cell; FO= follicular B cell; mature= mature B cell

Table A.6 Top 10 gRNAs[1]								
Guide ID #	Guide rank	Guide Sequence (+PAM)	# Genic Off-Targets[2]	# Intergenic Off-Targets[2]	Favorable PAM? [3]	3' NT to PAM: A, C, or T?[4]	% GC Content [5]	Cas9 Loading Score[6]
1	1	CTGAGGCTCATTCTCATGGGG	0	8		Yes	50	42
2	2	ATGAGCCTCAGTCTCCTTGGG	0	15			50	30
	3	ACTGAGGCTCATTCTCATGGG	1	10			44.44	32.5
	4	GACTGAGGCTCATTCTCATGG	0	7	Avoid		50	43
	5	AATGAGCCTCAGTCTCCTTGG	2	27	Avoid		50	27.5
3	6	AAGACCCCAAGGAGACTGAGG	0	17		Yes	55.55	44
	7	TGAGCCTCAGTCTCCTTGGGG	0	17		Yes	55.55	37
	8	ATGGGGAAAACAGGGAGTGGG	1	19		Yes	50	44
	9	AAAGAACAGAAGACCCCAAGG	1	20		Yes	44.44	51
	10	CATGGGGAAAACAGGGAGTGG	1	24	Avoid		55.55	59

[1]Data and description of rules from MIT CRISPR design tool (http://crispr.mit.edu)(*322*)
[2]Off-targets as determined by (*573*, *574*)
[3]CGG motifs are favorable and TGG motifs are disfavorable (*652*)
[4]G as 3' NT adjacent to PAM is disfavorable (*652*)
[5]40-60% GC content favorable (*653*)
[6]gRNA preference for loading onto Cas9 (*654*); Scores in red were among the top third highest
PAM= Protospacer adjacent motif; NT=nucleotide

Table A.7. Tracking of Indels by Decomposition (TIDE) analysis of GIMAP6 CRISPR lines	
Clone ID	**Identified Indel**
3G11	+5/+5
4C6	+4/+14
4D3	+1/+4
5F7	+2/+2
9F5	-4/-4

Table A.8. Histological findings of KO tissues			
Age (weeks)	**Sex**	**Organ**	**Findings**
23.1	F	Thymus	smaller, lower thymocytes density in medulla
		Spleen	extensive extramedullatory hematopoiesis, poor myeloid maturation, poorly defined white pulp, with few secondary B cell follicles
		Lymph node	poorly defined B-cell follicles, big increase in sinus histiocytosis, possible increase in marginal zone B cells
		Intestines	more leucocytes in lamina propria of small intestine
		Lung	peribronchial and perivascular infiltrates
		Liver	Small hepatocytes, possibly more prominent Kupffer cells
		Kidney	widespread cortical infiltrate (though possibly crushed myeloid cells)
		Heart	Dilated
21.7	F	Lymph node	poorly defined B-cell follicles
18.3	F	Spleen	some residual expanded white pulp without obvious B cell follicles, diffuse infiltrate of lymphplasmacytic cells or dysplastic extramedullary hematopoiesis
		Lymph node	possibly poorly defined B-cell follicles
		Intestines	possible myeloid cells expanding lamina propria, shorter and wider vili,
		Lung	small amount of peribronchial and perivascular cuffing by cells that might be myeloid
		Liver	smaller hepatocytes, possibly more prominent Kupffer cells
		Kidney	extensive glomerulosclerosis and possible amyloid deposits, thickened blood vessel walls, interstitial infiltrate, sever tubular atrophy, protein cases in tubules,
		Heart	Dilated and hypertrophic
16	F	Spleen	ill defined infiltrate of lymphocytes/lymphoplasmacytic cells
		Kidney	Very abnormal glomeruli with thickened capillary loops and some crescent. Minor loss of tubules. Occasional foci of acute and chronic inflammatory cells adjacent to gloms

Table A.8. Histological findings of KO tissues			
16	F	Lung	marked oedema (suggests left ventricular failure)
		Liver	Small irregular hepatocytes, circulating megakaryocytes, bilary dilation
		Kidney	severly abnormal with very thick capillary loops, some capsular adhesions, some glomeruloscloeriss, significant loss of tubules, thickened artery and arteriole walls, perivascular fibrosis with some inflammation
		Heart	severely dilated atria
17-18	M	Thymus	possible increase in medulla:cortex
		Kidney	Very abnormal glomeruli with thickened capillary loops and some crescent. Minor loss of tubules. Occasional foci of acute and chronic inflammatory cells adjacent to gloms
17-18	M	Thymus	possible increase in medulla:cortex
		Kidney	Very abnormal glomeruli with thickened capillary loops and some crescent. Minor loss of tubules. Occasional foci of acute and chronic inflammatory cells adjacent to gloms

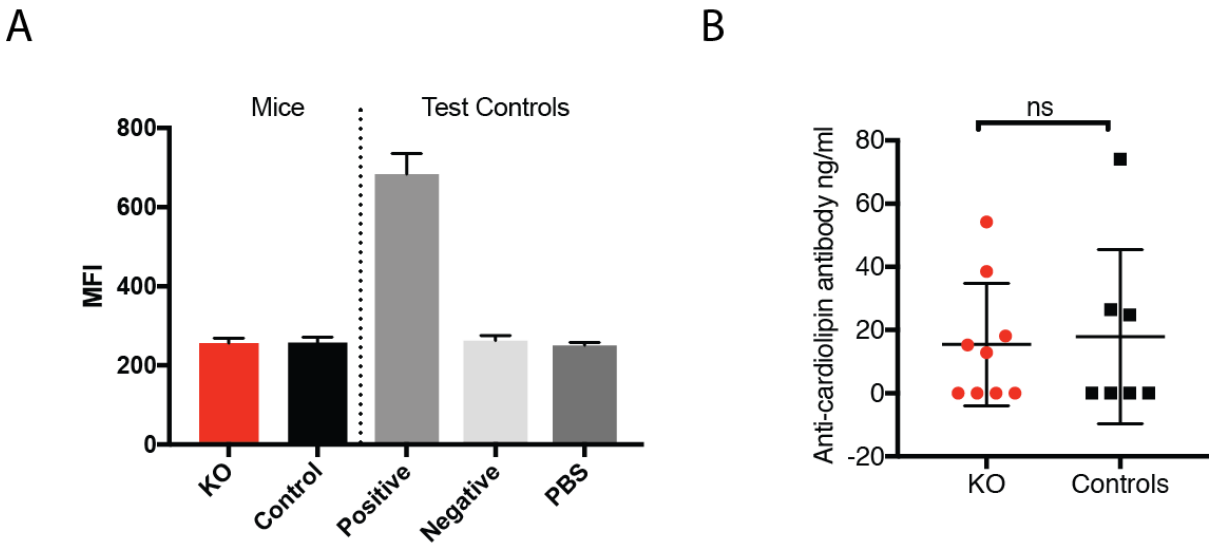


Fig.A.2. *Gimap6* KO mice do not have anti-nuclear or -cardiolipin antibodies in serum. Serum of *Gimap6*$^{-/-}$ (KO) mice or controls was tested for anti-nuclear antibodies using Hep-2000 substrate slides (**A)** or for anti-cardiolipin antibodies using an anti-cardiolipin antibody-IgG ELISA kit. For A, n_{KO}=10; $n_{Control\ mice}$=9; $n_{test\ controls}$=3. For B, n_{KO}=9; $n_{Control}$=7. KO=knockout; MFI= mean fluorescent intensity.

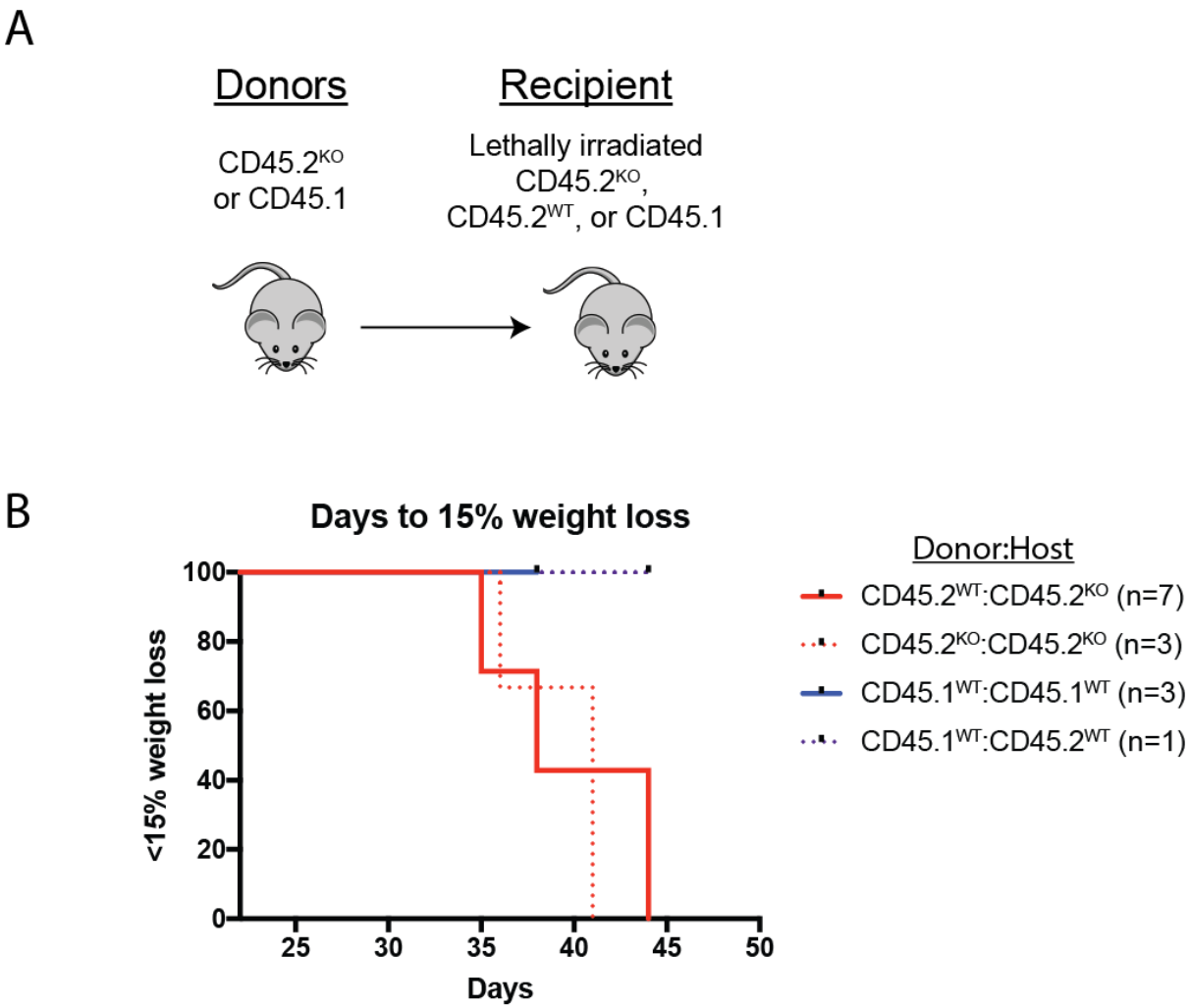


Fig. A.3 Transfer of WT bone marrow into *Gimap6*$^{-/-}$ mice. Bone marrow from CD45.1.B6 or KO mice were transferred to lethally irradiated KO, heterozygous, or CD45.1.B6 as shown in **A**. **B**) Days post-transfer for each mouse to reach endpoint of >15% weight loss. N numbers are as shown in the figure legend.

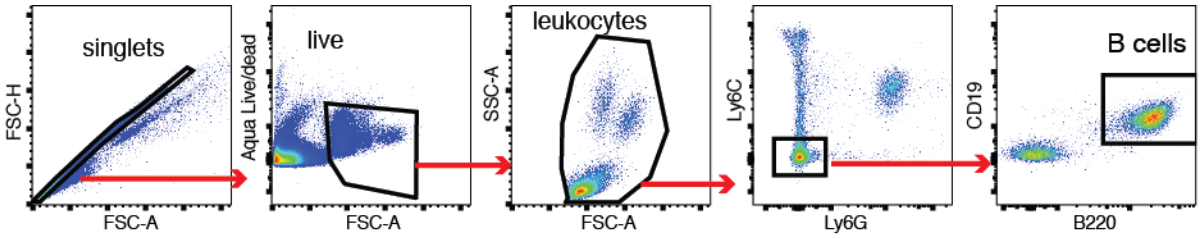


Fig. A.4 Gating Strategy for monitoring B cell depletion in anti-CD20 antibody treated mice. Gating strategy for Fig. 6.7B. FSC-A= forward scatter-area; FSC-H= forward scatter-height; SSC-A= side scatter-area